Contributi innovativi nel campo dell'Analisi Modale Operazionale finalizzati all'identificazione, al monitoraggio e alla damage detection in applicazioni ingegneristiche di

Department of Mechanics, Mathematics and Management
Mechanical and Management Engineering
Ph.D. Program
SSD: ING-IND/13 - Applied Mechanics

Final dissertation

Novel contributions in the field of Operational Modal Analysis aimed at system identification, monitoring, and damage detection in challenging engineering applications

---

by
Simone De Carolis

Supervisor:
Prof. Leonardo Soria

Coordinator of the Ph.D. Program:
Prof. Giuseppe P. Demelio

Course n° 34, 01/11/2018 - 31/12/2021

Department of Mechanics, Mathematics and Management
MECHANICAL AND MANAGEMENT ENGINEERING
PH.D. PROGRAM
SSD: ING-IND/13 - APPLIED MECHANICS

Final dissertation

Novel contributions in the field of Operational Modal Analysis aimed at system identification, monitoring, and damage detection in challenging engineering applications

---

by
SIMONE DE CAROLIS

Referees:
Prof. Elsa CAETANO
Prof. Jean Philippe NÖEL

Supervisor:
Prof. Leonardo SORIA

Coordinator of the Ph.D. Program:
Prof. Giuseppe P. Demelio

Course n° 34, 01/11/2018 - 31/12/2021

Approved by the Guidance Committee:

Major: Applied Mechanics

Leonardo Soria
Associate Professor of
Applied Mechanics

Date

Acknowledgements

"Un bel posto dove coltivare vecchi dubbi e raccogliere nuovi interrogativi", con le tasche svuotate di citazioni, a seguito di tutto il navigare che mi porta ad oggi, forse risponderei come tra quelle virgolette ad un passante disposto a chiedermi cos'è un dottorato di ricerca (assunto che io l'abbia capito!). Sono stati anni che passeggiano nel disordine di una scrivania, spostano la polvere di un laboratorio, riempiono l'agenda di inchiostro e date, afferrano spunti dalle chiacchierate ed anche un po' di conforto diluito in numerosi caffè. Sono state sfide e crisi, come tra creste e valli di quell'oscillazione su cui ti senti naturalmente libero con in mano il sogno di un orizzonte stabile e nel cuore la paura che insorga una disastrosa instabilità: comunque vada è stato divertente come solo la dinamica può esserlo!

E allora... Grazie, caro professor Soria, per avermi concesso il timone, per quella mano sempre pronta a disegnare una rotta insieme, per l'esempio di umiltà e umanità nei confronti di studenti e collaboratori ma, soprattutto, della scienza. *"Siccome non siamo abbastanza intelligenti, dobbiamo compensare con il duro lavoro"* (dovrebbe suonare più o meno così), ti sarò riconoscente per il tempo e lo spazio che mi hai offerto in cambio di conquiste e delusioni, sperando che le prime siamo sempre almeno pari alle seconde.

Grazie a chi è entrato nel percorso come compagno di una squadra in cui si preparano articoli come fossero partite, quelle tante spalle con cui ci siamo sostenuti tra conti e conversazioni, menti eccezionali da cui rubare consigli in cambio della promessa di un assist per il prossimo obiettivo da raggiungere.

Ringrazio, poi, tutte quelle altre anime coraggiose su navi diverse in oceani diversi, colleghi con cui condividere angosce e meraviglie che ogni ramo della conoscenza riserva. Prima del prossimo viaggio, mettete nel sacco il ricordo sereno di quelle fughe dalla scrivania per ritrovarsi insieme in un brindisi o in una risata.

Grazie a tutta quella parte di vita con cui non occorre indossare le vesti del dottorando,

quel posto sicuro che è la mia famiglia, fatta di mani che lavorano, occhi che ti curano e valori che porto sul petto nelle scelte giuste o sbagliate che faccio. A quegli amici che mi regalano leggerezza, che mi fanno sentire fortunato come mi fosse capitata un'eredità da spendere in abbracci e tempo per dividere il bello o il brutto che facciamo capitare.

A te, Marinella, coperta e faro di molte tempeste, grazie per quell'incredibile capacità di rovesciare il mio mondo con tutta la sua scienza, di rompere la simmetria della mia logica e fare spazio ad un posto dove pasticciare insieme, in cui si può smettere di inseguire quello che si illude di essere perfetto e cominciare a sorridere a braccetto con i propri difetti... a cui oggi si aggiunge quello di essere un dottore di ricerca.

Bari, Martedì 29 Marzo 2022

"E' nella crisi che sorge l'inventiva, le scoperte e le grandi strategie. Chi supera la crisi supera sé stesso senza essere superato. Chi attribuisce alla crisi i suoi fallimenti e difficoltà, violenta il suo stesso talento e dà più valore ai problemi che alle soluzioni. [...] *Senza crisi non ci sono sfide, senza sfide la vita è una routine, una lenta agonia. Senza crisi non c'è merito. E' nella crisi che emerge il meglio di ognuno, perché senza crisi tutti i venti sono solo lievi brezze."*

Mein Weltbild, Albert Einstein, 1934

Ai venti tempostosi di questi anni ed al coraggio di continuare a ricercare.

ABSTRACT

Novel contributions in the field of Operational Modal Analysis aimed at system identification, monitoring, and damage detection in challenging engineering applications

by

Simone De Carolis

Advisor: Prof. Leonardo Soria, Ph.D.

January 2022

In this dissertation, novel contributions in the field of Operational Modal analysis are presented in two principal branches. The former focuses on a vibro-acoustical OMA formulations as a simple and effective methodology for microsystems dynamic characterization. The particular output-only modal analysis methodology, that includes acoustical excitation via speakers and response measurements through a laser interferometer and microphone, is illustrated through the in-plane and out-of-plane flexural mode identification by experiment on high-quality factor quartz tuning fork (QTF). Additionally, a generalized OMA framework is proposed with the aim to overcome the main drawback of OMA approach consisting in the NExT assumption of uncorrelated white noises excitations. These hypotheses, in fact, are violated in all those cases in which the exerted environmental loads exhibit coloration, harmonic content or some kind of correlation, as in the cases of mechanical engineering

systems like vehicles or wind turbines. Specifically, the proposed OMA technique requires some knowledge about the inputs acting on the system and, thus, it is applicable to systems for which something about the inputs is somehow known. The generalized modal structures of the output cross-correlation functions and power spectral densities are derived, as models showing the dependence not only by the modal parameters, but also by the input spectral characteristics, and employed in a customized identification technique. The second research offshoot is dedicated to a specific class of transmissibility functions, here called Response-based Frequency-Response-Functions (R-FRFs), and it comprises a first investigation on the estimation process of R-FRFs followed by a derivation of the relevant modal model, suitable for being tackled through frequency-domain estimators from the field of experimental and operational modal analysis, which let these additional modal parameters to be identified. It is demonstrated how modes retrieved from R-FRFs are related to the system under investigation, but, virtually, with a different set of boundary conditions. The particular properties give this additional modal parameters the advantage of being local, in turn confirming the significance of response-based frequency response functions in the field of damage detection. Both the research lines are corroborated by numerical and real-world experimental case studies that offer a number of application scenarios for results discussion.

Contents

List of Figures

List of Tables

List of Symbols

$*$	convolution product
$\delta(.)$	Dirac delta
$E[.]$	expected value
$(.)^{\mathrm{T}}$	transpose of a matrix
$(.)^{*}$	conjugate of a matrix
$(.)^{\mathrm{H}}$	conjugate transpose of a matrix
$(.)^{-1}$	inverse of a matrix
i	imaginary unit
tr[.]	matrix trace
Re(.)	real part
$\otimes$	Kronecker product
$h(.)$	Heaviside step function
ln(.)	natural logarithm
$\mathrm{e}^{(.)}$	exponential function
s	Laplace variable
ω	radian frequency
Δt	sampling period
$\mathbb{R}$	real number
$\mathbb{C}$	complex number

Introduction

Research Context

Operational modal analysis belongs to the field of structural identification techniques employed to extract dynamic properties of vibrating systems which comprise the so-called modal models [16, 17, 22, 23]. As an extension of the classical input-output experimental modal analysis [32, 61, 80, 114], OMA retrieves resonance frequencies, damping ratios, and modes (i.e. the modal parameters) moving from the only measured output signals of in-operation structures in turn subjected to ambient excitations like wind, traffic, road roughness induced forces, and waves [37, 68, 99, 123]. The output-only formulations rely on the Natural Excitation Technique (NExT) assumptions [81, 83] which states that unknown loads acting on the system have to fit the form of white noise sequences and, in case of multi-point excitation, the external inputs are required to be strictly uncorrelated. This hypothesis is regrettably violated in all those cases in which the operational environment encompasses harmonic forces generated by rotating parts (machine tools, engines or wind turbines) [98, 149], or assist with the occurrence of spatial and/or time correlated inputs (road and rail vehicles) [48, 84, 146]. The attractiveness of OMA in aerospace and mechanical engineering still persists due to many advantages, such as: cheap and fast operating testing, no elaborate excitation equipment and boundary condition simulation needed, modal parameters' estimate at much more representative working points, the model characteristics under real loading are linearized due to broad band random excitation [163]. For these reasons in the recent years, the development

of methods aiming at overcoming the NExT assumption limitations has become a challenging topic that can be tackled by the coming of innovative approaches which introduces tools (i.e. data pre-processing, coordinate transformation, enhanced identification models) able to put aside the poor force description like uncorrelated white noises [33, 53, 59, 87, 154].

Secondly, structural dynamics of microelectromechanical systems (MEMS) plays a crucial role in determining their performance and reliability. Classically, experimental modal analysis is used to characterize the dynamic behavior of large scale structures, as well as to derive, and validate analytical and numerical models. It would be crucial, thus, to derive and adapt EMA techniques to the case of microsystems: in this case, this approach would be helpful to model and validate multi-physics phenomena, such as the interaction between electrostatic forces or gas damping and structural dynamics, or to evaluate manufacturing processes, assessing changes in the fabrication features, diagnosing structural faults and defects before and during the operation, and carrying out in situ performance measurements. When dealing with MEMS, excitation and measurement methods from EMA field may turn out to be challenging [112]. In fact, conventional modal testing techniques involve attaching accelerometers which substantially alter the dynamic characteristics of microstructures, and providing transient input with an impulse hammer or attaching a shaker to the structure is often unfeasible. Therefore, both the excitation and measurement must be conducted through non-contact instruments [40] opening different experimental scenarios where the vibro-acoustical OMA formulation [124], in which both acoustical and structural responses are taken into account by a fluid-structure coupled dynamical system description, could play a key role.

Changing into the areas of the damage detection and continuous monitoring of structures, the importance and the role of a specific class of global transmissibility matrices (global TFs) [160], here named response-based frequency response functions (R-FRFs), is worth discussing for their ability to enrich the intrinsic modal database of the system under study and to allow for analyzing the system in a local sense. In fact, the R-FRFs, as specialized

frequency response functions, have been recently introduced in the literature [102, 103], and, as originally proved, they are able to inherently provide local poles, related to the system under investigation, but, virtually, with a different set of boundary conditions; i.e. as if some of the original degrees of freedom, arbitrarily chosen by the analyst, were constrained to ground. The peculiarity of the R-FRFs to incorporate modal data essentially related to subparts of a system makes these functions deserving of being measured through suitable estimators, whose definition and performance analysis comprise one of the objective of this dissertation. The specific formal representation of the R-FRFs generally requires a simultaneous measurement of groups of these functions arranged in response-based transfer matrices from which additional local poles and modes are extractable and employable to detect structural modifications, in turn confirming the significance of response-based frequency response functions in the field of damage detection [39, 42, 62].

Focus and Outline of the Thesis

The research presented in this doctoral thesis is mainly addressed to the analysis and resolution of specific challenging aforementioned problems, belonging to the field of structural identification: (i) the pairing of vibro-acoustical OMA formulation with microsystems dynamic characterization; (ii) the development of a generalized OMA framework aimed at overcoming the NExT assumption; (iii) the definition of nonparametric R-FRFs estimators and the derivation of the relevant modal decomposition embedding local modes as remarkable features for damage detection. As a consequence, the dissertation is divided into two parts whose outlines are reported in Figure 1, with regards to Part I, and in Figure 2, as concerns Part II.

Part I: Operational Modal Analysis: classical and novel frameworks

The goal of the research here presented is to provide novel identification approaches in the field of OMA. Before the definition of innovative frameworks, Chapter 1 offers an overview of

the discipline starting from fundamental modal formulation of the cross-correlation and power spectral density (PSD) matrix. A brief description of the standard PolyMAX method is then carried out by investigating its two main steps: a poly-reference Least Squares Complex Frequency (pLSCF) algorithm, based on a Right Matrix Fraction Description (RMFD), addressed to poles and operational reference vectors (ORV) estimation and a Least Squares Frequency Domain (LSFD) estimator for mode shapes extraction. In addition, practical tools and procedures for model order selection and modal parameter validation are given being concepts invoked during the following analyses.

After becoming familiar with in-operation modal analysis context, Chapter 2 develops on a particular OMA methodology that includes acoustical excitation via speakers and response measurements through a laser interferometer and microphone. A simple setup marks this approach: it relies on the analytical modal model of the cross-power spectra between the structural and acoustical system outputs and, when a fluid-structure coupling is exploited, modal parameter estimation (MPE) techniques are applied from the OMA field. The effectiveness of the methodology is illustrated through the in-plane and out-of-plane flexural mode identification by experiment on high-quality factor quartz tuning fork (QTF).

In Chapter 3, a novel output-only modal formulation, not based on the NExT assumptions, is described. As made for classical OMA, a modal model of the output cross-correlation and PSD matrix is derived revealing its dependence not only by modal parameters, but also by input correlation terms. In the effort to implement a frequency domain estimator, the generalized PSD modal model is accompanied by an extended Left Matrix Description, employed in a pLSCF-like solution aimed at retrieving poles and mode shapes, and a LSFD estimator for extended ORV fitting. Examples of the usage of this approach are illustrated in the identification process involving a lumped parameter system numerical simulations and experimental testing on a PTFE beam. Both the numerical and experimental vibrating systems are studied in the presence of environmental forces which exhibit definite infringements

of the NExT assumption (i.e. coloration, time correlation, coherence).

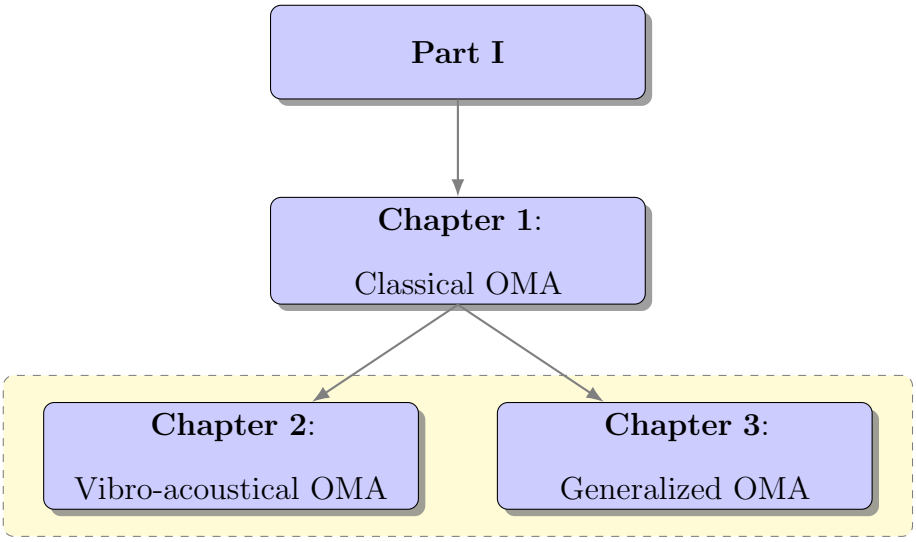

Figure 1: Outline of the thesis, Part I

Part II: On the role of a particular class of global transmissibility functions: the RFRFs

The main goal of Part II is to specifically tackle the problem of estimation and identification by R-FRFs. The latter enter in the global transmissibility matrices scenario and embed additional modal information which could play an appealing role in the area of structural health monitoring and damage localization.

In particular, Chapter 4 offers the problem of R-FRFs assessment by investigating estimators for MIMO linear systems, extending known concepts and introducing new ideas. Specifically, it is proposed the definition of output-only and input-output estimators, including, in the latter case, the advantage of using the measured exciting forces, when available. Therefore, a detailed performance comparison of the proposed estimators is presented by making usage of data from simulated and experimental case studies. The analysis carried out leads to conclusions aimed at identifying the best estimators for the measurement of R-FRFs.

Chapter 5 focuses on the modal analysis of this special class of transfer matrices revealing

the meaning of modes that compose them. In this regard, a parametric model of the R-FRFs matrix is provided, suitable for being tackled through frequency-domain estimators from the field of experimental and operational modal analysis, which let these additional modal parameters to be identified. Such a conceptual extension is carried out by both a theoretical and a numerical point of view. Data sets from numerical and real-world experimental case studies are processed and the corresponding results are brought under discussion with the view to show the R-FRFs potential in the damage detection field.

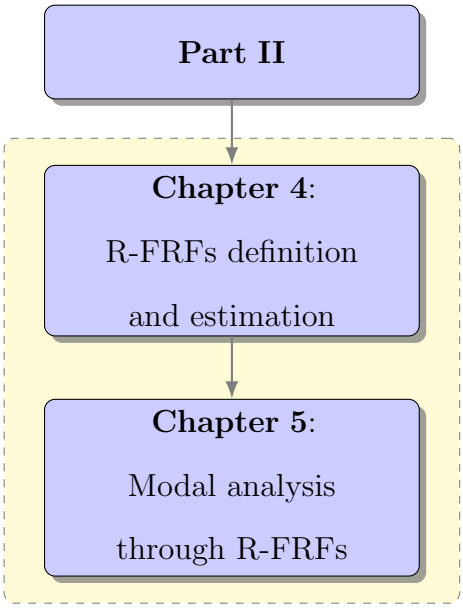

Figure 2: Outline of the thesis, Part II

Ultimately, it is worth mentioning that the solution and results of the novel approaches analysed in this dissertation, presented, specifically, in Parts I and II, have been published, respectively, in [28, 43, 44] and [45].

Part I

Operational Modal Analysis: classical and novel formulations

Chapter 1

Classical OMA: obeying the NExT assumption

Contents

1.1 Introduction

In this chapter, the concepts of operational modal analysis (OMA), and modal structures employed in output-only identification algorithms are introduced. These methods are an extension to the framework of classic input-output experimental modal analysis (EMA) which consists of well established phases: set-up building, data acquisition (e.g. estimation of frequency response functions), system identification, i.e. determination of modal parameters from measured input-output data, and results' validation [61, 80].

Modes, as characteristics collecting natural frequencies, damping ratios, and mode shapes, are inherent properties of a structure: modes change if geometrical properties, material properties or the boundary conditions vary. They are independent of the loads acting on and fully determine the dynamic behavior of structures.

Many fields of industry such as automotive, aerospace, rotational machinery, robotics, civil engineering need research on experimental techniques aimed at identifying the dynamic structural behavior. In this respect, modal analysis can be used for troubleshooting, validation of FE model, structural dynamic modification, load estimation, sensitivity analysis, substructure coupling, structural heath monitoring (SHM), prediction of dynamic strain, damage detection, quantification and locating damage, etc. [16, 35, 161]. Numerical methods, for instance, have drawback in modeling the structures in its real condition particularly for the complicated ones. The main challenges of FEM (as a capable numerical method in dynamic analysis of structures) are replicating the exact nonlinear and damping properties, modeling the real boundary and operational conditions and so on. To overcome the problem, model updating by results from EMA can be utilized.

Since the middle of the 20^{th} century, EMA methods estimate the modal parameters of structures based on the application of known artificial input forces (reproduced by shakers or impact hammers) and the recording of output responses (generally measured by accelerometers

sensors). As an approach performed in laboratory condition, the experimental equipment and data signal processing algorithms are crucial in modal parameter estimation (MPE).

Some shortcomings within EMA processes arise especially for huge engineering structures (such as bridges, buildings, towers, off-shore platforms, etc) for which generating vibration by shaker or impact hammer results expensive and difficult (if not impossible). Exploiting ambient loads like wind, traffic, pedestrian remains still challenging since these loads are immeasurable, that's why researchers became motivated to identify the structures characteristics by considering just the response of the structure, regardless of input loads. Consequently, output-only modal analysis or ambient vibration analysis or in-operation modal analysis or, in a word, OMA took its first steps as an ensemble of algorithms extracting the modal parameters just based on the output responses [77, 120].

Primary studies about OMA, particularly dedicated to civil engineering structures [5, 19, 119], were established in 1990s and evolved into an autonomous discipline [22, 126] able to attract great research even in mechanical engineering. OMA makes its debut in mechanics with successful MPE of wind turbines at different rotation rates [30]. Some later applications include on-the-road modal analysis of cars and in-flight modal analysis of airplanes, modal testing of spacecraft during launch, and modal testing of engines during startup and shutdown [41, 78, 89].

In output-only identification methods, the deterministic knowledge of the input signals is replaced by the assumption that the forces are realizations of stochastic processes (stationary Gaussian white noises): this is called natural excitation hypothesis and it names NExT techniques [26, 83] which uses the cross-correlation functions (CFs) of measured responses demonstrating how CFs, due to their modal structure, can be employed as impulse response functions [142] in conventional time-domain identification procedures developed in traditional EMA. In general, MPE algorithms dedicated to EMA and OMA range from Single-Input/Single-Output (SISO), Single-Input/Multiple-Output (SIMO) to Multiple-Input/Multiple-Output (MIMO)

techniques in time domain, frequency domain and spatial domain [3, 70]. Time domain MIMO algorithms are generally classified as:

- NExT-type procedures: they include polyreference complex exponential (MIMO version of the SIMO Least Squares Complex Exponential, LSCE) [3], eigensystem realization algorithm (ERA) imported from system realization theory [26, 81, 85, 96], extended Ibrahim time domain [82]. These methods start from the estimation of time response functions such as impulse response function, free decay responses, correlation function, random decrement signature from which they extract modal parameters. For the specific case of OMA, CF matrix is the basis for identification in its modal decomposition or stochastic state-space representation;

- ARMA-type procedures: a multi-dimensional auto-regression moving average model [5, 27, 108, 109], which correspond to multiple natural excitations, is the foundation of these techniques. In this case, the estimation can be carried out by Prediction-Error methods as a data-driven approach, or by Instrument Variable methods based on covariance matrices of the output data (hence the name covariance-driven approach);

- Stochastic Realization-based procedures: stochastic system realization approaches are based on discrete-time stochastic state-space equation. They introduce, as a key feature, singular value decomposition (SVD) of covariance matrix and can also be taken as subspace system identification method [9]. For this reason, these procedures are often called as Covariance-driven Stochastic Subspace Identification (SSI) methods [94];

- Stochastic Subspace-based procedures: subspace-based state-space system identification (SSI) differs from stochastic realization-based approach, since the state vector is substituted by its prediction, and the two input/noise processes are converted into one [20, 36]. SSI, also called data-driven SSI, makes direct use of stochastic response data to identify modal parameters employing innovation state-space equation model.

Frequency domain approaches rely on input/output power spectrum density (PSD) relationship for stochastic processes [29, 67]. By assuming natural excitation hypothesis, modal decomposition of the output PSD matrix is derived and employed by the following methods:

- FDD-type procedures: the Peak-picking method (PP) is a basic approach to find the eigenfrequencies as the peaks of non-parametric spectrum estimates but it works well as long as modes are well separated and frequency resolution is high. Frequency Domain Decomposition (FDD) technique exploits SVD at discrete frequencies but can only estimate modal frequencies and mode shapes [23]. A second generation of FDD, which is called as Enhanced FDD or EFDD, has been followed for estimation of not only modal frequencies and mode shapes, but damping ratios [76, 104, 125].

- LSCF-type procedures: in EMA this approach is based on parametric transfer function model represented by rational fraction polynomial (RFP) [54, 126] involved in least squares solution problems or in maximum likelihood estimators [59, 60, 79]. The least-squares complex frequency-domain (LSCF) estimation method is based on common-denominator model or scalar matrix-fraction description and has shortcomings in mode shapes and modal participation factors extraction, especially with closely spaced poles. Its polyreference version (pLSCF) [73], based on right matrix-fraction model (RMFD), overcomes these limitations. In the case of OMA, these methods adopt the so-called positive spectra (i.e. FFT of the correlation functions with positive time lags) due to the similarity between their modal decomposition and that of the FRF matrix [152].

The rest of the chapter is organized as follows. In Section 1.2, the key modal structures of OMA are presented such as modal decomposition of correlation and PSD matrix commonly employed in several identification techniques. In Section 1.3, a particular two stage procedure, commercially known as PolyMAX method [121, 122], is introduced in its relevant steps such as a pLSCF estimator based on the RMFD, the corresponding state-space realization and a least squares frequency domain algorithm for mode shapes estimation. Data pre-processing,

the model order selection (i.e. the usage of stabilisation diagrams), and tools for modal parameter validation are dealt with in Section 1.4.

1.2 Development of the Natural Excitation Technique

The well-known set of second order motion equations equations for a linear, time-invariant, damped, vibrating system having N degrees of freedom (dofs), is formulated in a matrix notation as

$$\mathbf{M}\ddot{\boldsymbol{q}}(t) + \mathbf{C}\dot{\boldsymbol{q}}(t) + \mathbf{K}\boldsymbol{q}(t) = \boldsymbol{f}(t), \tag{1.1}$$

where t is the time variable, $\mathbf{M}$, $\mathbf{C}$, and $\mathbf{K} \in \mathbb{R}^{N\times N}$ are the mass, damping, stiffness matrices, $\boldsymbol{q}(t) \in \mathbb{R}^{N\times 1}$ denotes the vector of Lagrangian coordinates and $\boldsymbol{f}(t) \in \mathbb{R}^{N\times 1}$ that of external loads. One can recast the system dynamics equations in Eq. (1.1) into an equivalent set of $2N$ first-order differential equations

$$\begin{cases} \mathbf{M}\dot{\boldsymbol{q}}(t) - \mathbf{M}\dot{\boldsymbol{q}}(t) = \mathbf{0}^{N\times 1} \\ \mathbf{M}\ddot{\boldsymbol{q}}(t) + \mathbf{C}\dot{\boldsymbol{q}}(t) + \mathbf{K}\boldsymbol{q}(t) = \boldsymbol{f}(t) \end{cases}, \tag{1.2}$$

and by introducing the state vector $\boldsymbol{x}(t) \in \mathbb{R}^{2N\times 1}$

$$\boldsymbol{x}(t) = \begin{bmatrix} \boldsymbol{q}(t) \\ \dot{\boldsymbol{q}}(t) \end{bmatrix}, \tag{1.3}$$

the equations of motion are represented in state-space form [142]

$$\mathbf{P}\dot{\boldsymbol{x}}(t) + \mathbf{Q}\boldsymbol{x}(t) = \boldsymbol{u}(t), \tag{1.4}$$

where $\mathbf{P} \in \mathbb{R}^{2N\times 2N}$, $\mathbf{Q} \in \mathbb{R}^{2N\times 2N}$, and vector $\boldsymbol{u}(t)$ are defined as

$$\mathbf{P} = \begin{pmatrix} \mathbf{C} & \mathbf{M} \\ \mathbf{M} & \mathbf{0}^{N\times N} \end{pmatrix} \quad \mathbf{Q} = \begin{pmatrix} \mathbf{K} & \mathbf{0}^{N\times N} \\ \mathbf{0}^{N\times N} & -\mathbf{M} \end{pmatrix} \quad \boldsymbol{u}(t) = \begin{pmatrix} \boldsymbol{f}(t) \\ \mathbf{0}^{N\times 1} \end{pmatrix}. \tag{1.5}$$

Specifically, the so-called state matrix $\mathbf{A} = -\mathbf{P}^{-1}\mathbf{Q}$, is introduced along with its eigenvalue decomposition

$$\mathbf{A} = \mathbf{V}\boldsymbol{\Lambda}\mathbf{V}^{-1}, \tag{1.6}$$

where $\boldsymbol{\Lambda}$ is a diagonal matrix, containing the $2N$ complex conjugate system poles λ_n, while $\mathbf{V} \in \mathbb{C}^{2N\times 2N}$ is the modal matrix structured as

$$\mathbf{V} = \begin{bmatrix} \boldsymbol{\psi}_1 & \cdots & \boldsymbol{\psi}_N & \boldsymbol{\psi}_1^* & \cdots & \boldsymbol{\psi}_N^* \\ \lambda_1\boldsymbol{\psi}_1 & \cdots & \lambda_N\boldsymbol{\psi}_N & \lambda_1^*\boldsymbol{\psi}_1^* & \cdots & \lambda_N^*\boldsymbol{\psi}_N^* \end{bmatrix} = \begin{bmatrix} \boldsymbol{\Psi} \\ \boldsymbol{\Psi}\boldsymbol{\Lambda} \end{bmatrix}, \tag{1.7}$$

in which $(.)^*$ stands for the conjugate operation and $\boldsymbol{\psi}_n = \begin{bmatrix} \psi_{1,n} & \cdots & \psi_{N,n} \end{bmatrix}^{\mathrm{T}} \in \mathbb{C}^{N\times 1}$ are the mode shape vectors referred to the n-th pole and collected in $\boldsymbol{\Psi} \in \mathbb{C}^{N\times 2N}$. The motion equations in Eq. (1.4) can be decoupled through the coordinates transformation given by the matrix $\mathbf{V}$ in Eq. (1.7) obtaining

$$\boldsymbol{x}(t) = \mathbf{V}\boldsymbol{p}(t) = \sum_{n=1}^{2N} \begin{bmatrix} \boldsymbol{\psi}_n \\ \lambda_n\boldsymbol{\psi}_n \end{bmatrix} p_n(t), \tag{1.8}$$

where $\boldsymbol{p}(t) = \begin{bmatrix} p_1(t) & \cdots & p_{2N}(t) \end{bmatrix}^{\mathrm{T}} \in \mathbb{R}^{2N\times 1}$ is the modal state vector. Pre-multiplying both sides of Eq. (1.4) by $\mathbf{V}^{\mathrm{T}}$ and substituting $\boldsymbol{x}(t)$ and $\dot{\boldsymbol{x}}(t)$ with expression in Eq. (1.8), it is derived

$$\mathbf{M}_a\dot{\boldsymbol{p}}(t) + \mathbf{M}_b\boldsymbol{p}(t) = \mathbf{V}^{\mathrm{T}}\boldsymbol{u}(t), \tag{1.9}$$

indicating by $\mathbf{M}_a = \mathbf{V}^{\mathrm{T}}\mathbf{P}\mathbf{V}$ and $\mathbf{M}_b = \mathbf{V}^{\mathrm{T}}\mathbf{Q}\mathbf{V}$ the so-called modal A and modal B diagonal matrices. The generic system motion scalar equation of set Eq. (1.9) is

$$\dot{p}_n(t) - \lambda_n p_n(t) = \frac{1}{m_{an}} \boldsymbol{\psi}_n{}^{\mathrm{T}} \boldsymbol{f}(t), \tag{1.10}$$

with $\lambda_n = -m_{bn}/m_{an}$. The solution of Eq. (1.10) is retrieved from Duhamel integral assuming zero initial conditions

$$p_n(t) = \frac{\boldsymbol{\psi}_n^{\mathrm{T}}}{m_{an}} \int_{-\infty}^{t} \boldsymbol{f}(\theta)\, \mathrm{e}^{\lambda_n (t-\theta)} \mathrm{d}\theta. \tag{1.11}$$

Combining the solutions from Eq. (1.11) as stated in Eq (1.8), the system responses are obtained in terms of the physical Lagrangian coordinates

$$\boldsymbol{q}(t) = \sum_{n=1}^{2N} \boldsymbol{\psi}_n p_n(t) = \sum_{n=1}^{2N} \frac{1}{m_{an}} \boldsymbol{\psi}_n \boldsymbol{\psi}_n^{\mathrm{T}} \int_{-\infty}^{t} \boldsymbol{f}(\theta) \mathrm{e}^{\lambda_n (t-\theta)} \mathrm{d}\theta, \tag{1.12}$$

which can be interpreted as a convolution integral encompassing the impulse response matrix of the system and the generic system of external forces. The generic output $q_i(t)$ from the vector in Eq. (1.12) is considered as

$$q_i(t) = \sum_{g=1}^{L} \sum_{n=1}^{2N} \frac{1}{m_{an}} \psi_{in} \psi_{gn} \int_{-\infty}^{t} f_g(\theta)\, \mathrm{e}^{\lambda_n (t-\theta)} \mathrm{d}\theta = \sum_{g=1}^{L} \tilde{q}_{ig}(t), \tag{1.13}$$

where L ($L \leq N$) is the number of non-null forces included in the external load vector $\boldsymbol{f}(t)$ and $\tilde{q}_{ig}(t)$ indicates the response contribution related to the single force $f_g(t)$.

1.2.1 Output cross-correlation modal decomposition

Considering two different outputs evaluated at the separated time instants $t+T$ and t, respectively,

$$\tilde{q}_{ig}(t+T) = \sum_{n=1}^{2N} \frac{1}{m_{an}} \psi_{in} \psi_{gn} \int_{-\infty}^{t+T} f_g(\theta_1)\, \mathrm{e}^{\lambda_n (t+T-\theta_1)} \mathrm{d}\theta_1, \tag{1.14}$$

and

$$\tilde{q}_{jl}(t) = \sum_{m=1}^{2N} \frac{1}{m_{am}} \psi_{jm} \psi_{lm} \int_{-\infty}^{t} f_l(\theta_2)\, \mathrm{e}^{\lambda_m (t-\theta_2)} \mathrm{d}\theta_2, \tag{1.15}$$

the resulting output cross-correlation function is derived as [110]

$$\begin{aligned} &R_{ig,jl}^{\tilde{q}}(T) = \mathrm{E}\left[\tilde{q}_{ig}(t+T)\, \tilde{q}_{jl}(t)\right] = \\ &= \sum_{n=1}^{2N} \sum_{m=1}^{2N} \frac{\psi_{in} \psi_{jm} \psi_{gn} \psi_{lm}}{m_{an} m_{am}} \int_{-\infty}^{t+T} \int_{-\infty}^{t} \mathrm{d}\theta_1 \mathrm{d}\theta_2 \mathrm{e}^{\lambda_n (t+T-\theta_1)} \mathrm{e}^{\lambda_m (t-\theta_2)} \mathrm{E}\left[f_g(\theta_1)\, f_l(\theta_2)\right], \end{aligned} \tag{1.16}$$

where E[·] stands for the expectation computed over the ensemble and

$$\mathrm{E}\left[f_g(\theta_1)\, f_l(\theta_2)\right] = R_{gl}^{f}(\theta_2 - \theta_1), \tag{1.17}$$

is the correlation function between two generic forces. At this stage, the NExT techniques assume inputs as white uncorrelated noises in order to solve the integral in Eq. (1.16) [83]

$$\mathbf{R}^{f}(\theta_2 - \theta_1) = \begin{bmatrix} \alpha_1 \delta(\theta_2 - \theta_1) & \cdots & 0 \\ \vdots & \ddots & \vdots \\ 0 & \cdots & \alpha_L \delta(\theta_2 - \theta_1) \end{bmatrix}, \tag{1.18}$$

where $\mathbf{R}^{f}(\theta_2 - \theta_1) \in \mathbb{R}^{L \times L}$ is the input correlation matrix and α_i is a real-valued constant. Substituting the particular expression of the input correlation term $R_{gg}^{f}(\theta_2 - \theta_1)$ of Eq. (1.18) in Eq. (1.16), you obtain

$$R_{ig,jg}^{\tilde{q}}(T) = \sum_{n=1}^{2N} \sum_{m=1}^{2N} \frac{\psi_{in} \psi_{jm} \psi_{gn} \psi_{gm}}{m_{an} m_{am}} \left(\frac{\alpha_g \mathrm{e}^{\lambda_n T}}{-(\lambda_m + \lambda_n)} h(T) + \frac{\alpha_g \mathrm{e}^{-\lambda_m T}}{-(\lambda_m + \lambda_n)} h(-T) \right), \tag{1.19}$$

where $h(\cdot)$ indicates the proper Heaviside step function. For the multi-input, multi-output, and multi-mode case, the cross-correlation between two outputs $q_i(t)$ and $q_j(t)$ is reached by

summing the different contributions as

$$R_{ij}^{q}(T) = \sum_{n=1}^{2N} \psi_{in} \left(\sum_{g=1}^{L} \alpha_g \frac{\psi_{gn}}{m_{an}} \sum_{m=1}^{2N} \frac{\psi_{gm}}{m_{am}(-\lambda_n - \lambda_m)} \psi_{jm} \right) \mathrm{e}^{\lambda_n T} h(T) + \\ + \sum_{m=1}^{2N} \left(\sum_{g=1}^{L} \alpha_g \frac{\psi_{gm}}{m_{am}} \sum_{n=1}^{2N} \frac{\psi_{gn}}{m_{an}(-\lambda_n - \lambda_m)} \psi_{in} \right) \psi_{jm} \mathrm{e}^{-\lambda_m T} h(-T), \tag{1.20}$$

that corresponds to the whole output correlation matrix $\mathbf{R}^{q}(T) \in \mathbb{R}^{N \times N}$ expressed by

$$\mathbf{R}^{q}(T) = \sum_{n=1}^{2N} \boldsymbol{\psi}_n \boldsymbol{\rho}_n^{\mathrm{T}} \mathrm{e}^{\lambda_n T} h(T) + \boldsymbol{\rho}_n \boldsymbol{\psi}_n^{\mathrm{T}} \mathrm{e}^{-\lambda_n T} h(-T), \tag{1.21}$$

embedding the following definition of operational reference vector referred to the n-th pole

$$\boldsymbol{\rho}_n = \sum_{g=1}^{L} \alpha_g \frac{\psi_{gn}}{m_{an}} \sum_{m=1}^{2N} \frac{\psi_{gm}}{m_{am}(-\lambda_n - \lambda_m)} \boldsymbol{\psi}_m. \tag{1.22}$$

In Eq. (1.21) the strong similarity between cross-correlation function and impulse response function arises [18]. In fact, a sum of complex exponential functions characterizes their modal models giving the go-ahead for the application of conventional time-domain identification procedures, developed in traditional EMA, to the output-only modal analysis [142, 153].

1.2.2 Output PSD modal decomposition

Changing into the frequency domain models, the transfer function matrix for the system in Eq. (1.1) is defined as the inverse of the dynamic stiffness $\mathbf{B}(s)$

$$\mathbf{H}(s) = (s^2\mathbf{M} + s\mathbf{C} + \mathbf{K})^{-1} = \mathbf{B}(s)^{-1}, \tag{1.23}$$

with s the Laplace variable. From the modal analysis theory [80], the modal decomposition of the frequency response function matrix, FRF, is

$$\mathbf{H}(\mathrm{i}\omega) = \sum_{n=1}^{N} \frac{\boldsymbol{\psi}_n \boldsymbol{L}_n^{\mathrm{T}}}{\mathrm{i}\omega - \lambda_n} + \frac{\boldsymbol{\psi}_n^* \boldsymbol{L}_n^{\mathrm{H}}}{\mathrm{i}\omega - \lambda_n^*} = \sum_{n=1}^{2N} \frac{\boldsymbol{\psi}_n \boldsymbol{L}_n^{\mathrm{T}}}{\mathrm{i}\omega - \lambda_n}, \tag{1.24}$$

where a translate into the Fourier domain is done by imposing $s = \mathrm{i}\omega$, and with $\boldsymbol{L}_n = Q_n \begin{bmatrix} \psi_{1,n} & \cdots & \psi_{L,n} \end{bmatrix} \in \mathbb{C}^{L\times 1}$ indicating the modal participation vector related to the n-th pole containing the L components of the n-th mode shape where the L external forces act ($Q_n = 1/m_{an}$ is referred as scale factor). The power spectral density (PSD) matrix $\mathbf{S}^q(\mathrm{i}\omega)$ referred to the system ouputs, i.e. the Fourier transform of matrix $\mathbf{R}^q(T)$, can be evaluated by using the following implicit analytical expression, the well-known input-output formula, holding in the frequency domain [110]

$$\mathbf{S}^q(\mathrm{i}\omega) = \mathbf{H}(\mathrm{i}\omega)\mathbf{S}^f(\mathrm{i}\omega)\mathbf{H}(\mathrm{i}\omega)^{\mathrm{H}}, \tag{1.25}$$

where $\mathbf{S}^f(\mathrm{i}\omega) \in \mathbb{C}^{L\times L}$ is the Fourier transform of the input correlation matrix $\mathbf{R}^f(T)$. Substituting in Eq. (1.25) the modal decomposition of Eq. (1.24), one obtains

$$\mathbf{S}^q(\mathrm{i}\omega) = \left(\sum_{n=1}^{2N} \frac{\boldsymbol{\psi}_n \boldsymbol{L}_n^{\mathrm{T}}}{\mathrm{i}\omega - \lambda_n} \right) \mathbf{S}^f(\omega) \left(\sum_{m=1}^{2N} \frac{\boldsymbol{L}_m \boldsymbol{\psi}_m^{\mathrm{T}}}{-\mathrm{i}\omega - \lambda_m} \right). \tag{1.26}$$

So, from that perspective, the assumption of inputs as white uncorrelated noises, described in the time lag domain as in Eq. (1.18), here becomes

$$\mathbf{S}^f(\mathrm{i}\omega) = \begin{bmatrix} \alpha_1 & \cdots & 0 \\ \vdots & \ddots & \vdots \\ 0 & \cdots & \alpha_L \end{bmatrix}, \tag{1.27}$$

implying the following partial fraction decomposition the matrix in Eq. (1.26)

$$\mathbf{S}^{q}\left(\mathrm{i}\omega\right)=\sum_{n=1}^{2N}\frac{\mathbf{R}_{n}^{+}}{\mathrm{i}\omega-\lambda_{n}}+\frac{\mathbf{R}_{n}^{-}}{-\mathrm{i}\omega-\lambda_{n}}, \tag{1.28}$$

where the resulting residue matrix is

$$\mathbf{R}_{n}^{+}(\mathrm{i}\omega)=\boldsymbol{\psi}_{n}\boldsymbol{\rho}_{n}^{\mathrm{T}}, \tag{1.29}$$

and the definition of operational reference vector coming up again as

$$\boldsymbol{\rho}_{n}(\mathrm{i}\omega)^{\mathrm{T}}=\boldsymbol{L}_{n}^{\mathrm{T}}\mathbf{S}^{f}\left(\mathrm{i}\omega\right)\left(\sum_{m=1}^{2N}\frac{\boldsymbol{L}_{m}\boldsymbol{\psi}_{m}^{\mathrm{T}}}{-\lambda_{n}-\lambda_{m}}\right)=\sum_{g=1}^{L}\alpha_{g}\boldsymbol{g}_{n}^{gg\mathrm{T}}, \tag{1.30}$$

with

$$\boldsymbol{g}_{n}^{gg}=\frac{\psi_{gn}}{m_{an}}\sum_{m=1}^{2N}\frac{\psi_{gm}}{m_{am}\left(-\lambda_{n}-\lambda_{m}\right)}\boldsymbol{\psi}_{m}, \tag{1.31}$$

Therefore, by assuming the operational forces to be white noise uncorrelated sequences, the output PSD matrix $\mathbf{S}_{q}(\mathrm{i}\omega)\in\mathbb{C}^{N\times N}$ can be modally decomposed as follows [142]:

$$\mathbf{S}^{q}\left(\mathrm{i}\omega\right)=\sum_{n=1}^{2N}\frac{\boldsymbol{\psi}_{n}\boldsymbol{\rho}_{n}^{\mathrm{T}}}{\mathrm{i}\omega-\lambda_{n}}+\frac{\boldsymbol{\rho}_{n}\boldsymbol{\psi}_{n}^{\mathrm{T}}}{-\mathrm{i}\omega-\lambda_{n}}, \tag{1.32}$$

where the operational participation vectors, Eq. (1.30), result being a combination of the system modal parameters and the unknown (i.e. forces are not measured) input correlation terms. For this reason, the modal participation factors and by consequence the modal scale factors cannot be determined from a single OMA test but they need appropriate methods for scaling [15, 64, 88, 141].

Usually, the so-called positive power spectra are employed in the output-only identification techniques for their algebraic similarity to FRFs [131]. Indeed, positive power spectra matrix is defined as the Fourier transform of the causal part of the correlation matrix in Eq. (1.21)

resulting

$$\mathbf{S}^{q+}(\mathrm{i}\omega) = \sum_{n=1}^{2N} \frac{\boldsymbol{\psi}_n \boldsymbol{\rho}_n^{\mathrm{T}}}{\mathrm{i}\omega - \lambda_n}, \tag{1.33}$$

or in a compact form

$$\mathbf{S}^{q+}(\mathrm{i}\omega) = \boldsymbol{\Psi}(\mathrm{i}\omega\mathbf{I} - \boldsymbol{\Lambda})^{-1}\mathbf{G}^{\mathrm{T}}, \tag{1.34}$$

with the $2N$ ORV collected in $\mathbf{G} \in \mathbb{C}^{N\times 2N}$, representing a modal decomposition similar to that of Eq. (1.24) except for the definition of operational reference vectors $\boldsymbol{\rho}_n$.

1.3 Frequency domain procedure for MPE

In the OMA field, identification algorithms are generally divided into two categories depending on the domain, time or frequency, where they operate. Regarding frequency-domain output-only estimators [22, 126], they are generally PSD-based identification methods that first estimate power spectral densities between O responses and certain r reference responses in order to fit them by means of a parametric model. In the following, some details of a particular two step procedure, commonly called PolyMAX technique, are provided in terms of polynomial description, least squares solution for coefficient matrices calculation and realization into an equivalent state-space model for determining modal parameters.

1.3.1 Classical Right Matrix Fraction Description

Right Matrix Fraction Description (RMFD) parametrizes the o-th row of $\mathbf{S}^{q+}(\mathrm{i}\omega) \in \mathbb{C}^{O\times r}$ in Eq. (1.33) at each radian frequency ω_k as a right division of two polynomial matrices [73]:

$$\mathbf{S}_o^{q+}(\omega_k) \simeq \mathbf{N}_o(k)\mathbf{D}(k)^{-1}, \tag{1.35}$$

where

$$\mathbf{D}(k) = \sum_{r=0}^{p} z_k^{-r} \boldsymbol{\alpha}_r \tag{1.36}$$

$$\mathbf{N}_o(k) = \sum_{r=0}^{p} z_k^{-r} \boldsymbol{\beta}_{o,r} \tag{1.37}$$

are the denominator $\mathbf{D}(k) \in \mathbb{C}^{r\times r}$ and the numerator $\mathbf{N}_o(k) \in \mathbb{C}^{1\times r}$ p-order matrix polynomial containing the unknown matrix real valued coefficients $\boldsymbol{\alpha}_r$ and $\boldsymbol{\beta}_{o,r}$, grouped in the vectors $\boldsymbol{\alpha} = \begin{pmatrix} \boldsymbol{\alpha}_0 & \cdots & \boldsymbol{\alpha}_p \end{pmatrix}^{\mathrm{T}} \in \mathbb{R}^{r(p+1)\times r}$ and $\boldsymbol{\beta}_o = \begin{pmatrix} \boldsymbol{\beta}_{o,0} & \cdots & \boldsymbol{\beta}_{o,p} \end{pmatrix}^{\mathrm{T}} \in \mathbb{R}^{(p+1)\times r}$. The transform variable z_k, named as complex polynomial basis function, is formulated in the z-domain being equal to $\mathrm{e}^{\mathrm{i}\omega_\mathrm{k}\Delta\mathrm{t}}$ where Δt is the sampling period.

1.3.2 Polyreference Least Squares Complex Frequency

To find the unknown coefficient matrices $\boldsymbol{\alpha}$ and $\boldsymbol{\beta}_o$ by solving a least squares problem, the following scalar cost function has to be minimized

$$l\left(\boldsymbol{\beta}_o, \boldsymbol{\alpha}\right) = \sum_{o=1}^{O} \sum_{k=1}^{N_f} \mathrm{tr}\left[\boldsymbol{\eta}_o^{\mathrm{H}}\left(\omega_k, \boldsymbol{\beta}_o, \boldsymbol{\alpha}\right) \boldsymbol{\eta}_o\left(\omega_k, \boldsymbol{\beta}_o, \boldsymbol{\alpha}\right)\right], \tag{1.38}$$

where $\mathrm{tr}\left[.\right]$ is the trace of matrix operator, and a linear-in-variables error is defined for each o-th row in $\mathbf{S}^{q+}(\mathrm{i}\omega)$ and for each k-th frequency (N_f is the number of frequency lines) as:

$$\boldsymbol{\eta}_o(\omega_k, \boldsymbol{\beta}_o, \boldsymbol{\alpha}) = \mathbf{N}_o(k, \boldsymbol{\beta}_o) - \mathbf{D}(k, \boldsymbol{\alpha})\mathbf{S}_o^{q+}(\omega_k). \tag{1.39}$$

Extending for all the N_f frequency lines, and reformulating in matrix notation as

$$\boldsymbol{\eta}_o\left(\boldsymbol{\beta}_o, \boldsymbol{\alpha}\right) = \begin{pmatrix} \boldsymbol{\eta}_o\left(\omega_1, \boldsymbol{\beta}_o, \boldsymbol{\alpha}\right) \\ \vdots \\ \boldsymbol{\eta}_o\left(\omega_{N_f}, \boldsymbol{\beta}_o, \boldsymbol{\alpha}\right) \end{pmatrix} = \begin{bmatrix} \mathbf{X} & \boldsymbol{v}_o \end{bmatrix} \begin{bmatrix} \boldsymbol{\beta}_o \\ \boldsymbol{\alpha} \end{bmatrix}, \tag{1.40}$$

where the two matrices, $\mathbf{X}$ and $\boldsymbol{\upsilon}_o$, are given by

$$\mathbf{X} = \begin{bmatrix} \begin{bmatrix} z_1^0 & \cdots & z_1^{-p} \end{bmatrix} \\ \vdots \\ \begin{bmatrix} z_{N_f}^0 & \cdots & z_{N_f}^{-p} \end{bmatrix} \end{bmatrix} \in \mathbb{C}^{N_f \times (p+1)}, \tag{1.41}$$

$$\boldsymbol{\upsilon}_o = \begin{bmatrix} -\begin{bmatrix} z_1^0 & \cdots & z_1^{-p} \end{bmatrix} \otimes \mathbf{S}_o^{q+}(\omega_1) \\ \vdots \\ -\begin{bmatrix} z_{N_f}^0 & \cdots & z_{N_f}^{-p} \end{bmatrix} \otimes \mathbf{S}_o^{q+}(\omega_{N_f}) \end{bmatrix} \in \mathbb{C}^{N_f \times (p+1)r}, \tag{1.42}$$

with $\otimes$ denoting the Kronecker product. In such a matrix formulation, the linear least-squares cost function of Eq. (1.38) can be rewritten as

$$l(\boldsymbol{\beta}_o, \boldsymbol{\alpha}) = \sum_{o=1}^{O} \operatorname{tr}\left[\left(\begin{bmatrix} \boldsymbol{\beta}_o^{\mathrm{T}} & \boldsymbol{\alpha}^{\mathrm{T}} \end{bmatrix} \begin{bmatrix} \mathbf{R} & \boldsymbol{\Upsilon}_o \\ \boldsymbol{\Upsilon}_o^{\mathrm{T}} & \mathbf{T}_o \end{bmatrix} \begin{bmatrix} \boldsymbol{\beta}_o \\ \boldsymbol{\alpha} \end{bmatrix} \right) \right], \tag{1.43}$$

where the following matrices need to be built

$$\mathbf{R} = \operatorname{Re}\left[\mathbf{X}^{\mathrm{H}}\mathbf{X}\right] \in \mathbb{R}^{(p+1)\times(p+1)}, \tag{1.44}$$

$$\boldsymbol{\Upsilon}_o = \operatorname{Re}\left[\mathbf{X}^{\mathrm{H}}\boldsymbol{\upsilon}_o\right] \in \mathbb{R}^{(p+1)\times(p+1)r}, \tag{1.45}$$

$$\mathbf{T}_o = \operatorname{Re}\left[\boldsymbol{\upsilon}_o^{\mathrm{H}}\boldsymbol{\upsilon}_o\right] \in \mathbb{R}^{(p+1)r\times(p+1)r}, \tag{1.46}$$

with Re[·] denoting the real part because of the real valued coefficients assumption. In the minimum of the cost function the derivatives of with respect to the unknown matrix

coefficients $\boldsymbol{\beta}_o$ and $\boldsymbol{\alpha}$ have to be zero

$$\frac{\partial l\left(\boldsymbol{\beta}_o, \boldsymbol{\alpha}\right)}{\partial \boldsymbol{\beta}_o} = 2\left(\mathbf{R}\boldsymbol{\beta}_o + \boldsymbol{\Upsilon}_o\boldsymbol{\alpha}\right) = \mathbf{0}^{(p+1)\times r},\ \forall o = 1, \cdots, O \tag{1.47}$$

$$\frac{\partial l\left(\boldsymbol{\beta}_o, \boldsymbol{\alpha}\right)}{\partial \boldsymbol{\alpha}} = 2\left(\boldsymbol{\Upsilon}_o^{\mathrm{T}}\boldsymbol{\beta}_o + \mathrm{T}_o\boldsymbol{\alpha}\right) = \mathbf{0}^{(p+1)\times r}, \tag{1.48}$$

which leads to the so-called reduced normal equations. In fact, the denominator matrix coefficients $\boldsymbol{\alpha}$ can be retrieved by replacing $\boldsymbol{\beta}_o$ with in the second equation as

$$\sum_{o=1}^{O}\left(-\boldsymbol{\Upsilon}_o^{\mathrm{T}}\mathbf{R}^{-1}\boldsymbol{\Upsilon}_o + \mathbf{T_o}\right)\boldsymbol{\alpha} = \mathbf{M}\boldsymbol{\alpha} = \mathbf{0}, \tag{1.49}$$

where the contribution of each o-th row of $\mathbf{S}^{q+}(\mathrm{i}\omega)$ has been taken into account. The typical constraint, $\boldsymbol{\alpha}_p = \mathbf{I}_r$ [34], is imposed in order to remove parameter redundancy of the RMFD [126], and also to avoid trivial solution $\boldsymbol{\alpha} = \mathbf{0}$.

1.3.3 Conversion into a state-space description

Once the denominator matrix coefficients have been determined, the roots of the denominator polynomial $\mathbf{D}(k, \boldsymbol{\alpha})$ can be calculated as the eigenvalues of the companion matrix [58]:

$$\mathbf{A}_c = \begin{pmatrix} \mathbf{0} & \mathbf{I} & \cdots & \mathbf{0} \\ \vdots & \vdots & \ddots & \vdots \\ \mathbf{0} & \mathbf{0} & \cdots & \mathbf{I} \\ -\boldsymbol{\alpha}_0 & -\boldsymbol{\alpha}_1 & \cdots & -\boldsymbol{\alpha}_{p-1} \end{pmatrix} \in \mathbb{R}^{pr\times pr}. \tag{1.50}$$

This eigenvalues, defined in the z-domain, can be converted into the system poles, which are strictly related to the system modal parameters by

$$\lambda_i, \lambda_i^* = -\zeta_i\omega_{u,i} \pm \mathrm{i}\omega_{u,i}\sqrt{1-\zeta_i^2}, \tag{1.51}$$

where $\omega_{u,i} = 2\pi f_{u,i}$ and ζ_i are respectively natural frequency and damping ratio referred to the i-th mode. The eigenvectors of the companion matrix assume the role of the ORV as can be demonstrated deriving the state-space conversion of the system, here described by a matrix polynomial division, adopting the so-called Controllable Canonical state-space Realization [96]. In fact, the RMFD model in Eq. (1.35) corresponds to the following state-space description

$$\begin{cases} \dot{\mathbf{x}}(t) = \begin{bmatrix} \mathbf{0} & \mathbf{I} & \cdots & \mathbf{0} \\ \vdots & \vdots & \ddots & \vdots \\ \mathbf{0} & \mathbf{0} & \cdots & \mathbf{I} \\ -\boldsymbol{\alpha}_0 & -\boldsymbol{\alpha}_1 & \cdots & -\boldsymbol{\alpha}_{p-1} \end{bmatrix} \mathbf{x}(t) + \begin{bmatrix} \mathbf{0} \\ \vdots \\ \mathbf{I}_r \end{bmatrix} \mathbf{u}(t) \\ \mathbf{y}(t) = \begin{bmatrix} \boldsymbol{\beta}_0 - \boldsymbol{\alpha}_0\boldsymbol{\beta}_p & \cdots & \boldsymbol{\beta}_{p-1} - \boldsymbol{\alpha}_{p-1}\boldsymbol{\beta}_p \end{bmatrix} \mathbf{x}(t) + \boldsymbol{\beta}_p \mathbf{u}(t) \end{cases}, \tag{1.52}$$

with the numerator coefficients arranged in $\boldsymbol{\beta}_r = \begin{pmatrix} \boldsymbol{\beta}_{1,r}^{\mathrm{T}} & \cdots & \boldsymbol{\beta}_{O,r}^{\mathrm{T}} \end{pmatrix}^{\mathrm{T}} \in \mathbb{R}^{O\times r}$, the input vector $\mathbf{u}(t) \in \mathbb{R}^{r\times 1}$, the output vector $\mathbf{y}(t) \in \mathbb{R}^{O\times 1}$, and the state variable vector $\mathbf{x}(t) \in \mathbb{R}^{pr\times 1}$ collecting the i-th time derivatives of the displacement vector $\mathbf{q}(t)$

$$\mathbf{x}(t) = \begin{Bmatrix} \mathbf{q}(t) \\ \vdots \\ \mathbf{q}^{(p-1)}(t) \end{Bmatrix}. \tag{1.53}$$

In Eq. (1.52), the four discrete-time system matrices $\bar{\mathbf{A}} \in \mathbb{R}^{pr\times pr}$, $\bar{\mathbf{B}} \in \mathbb{R}^{pr\times r}$, $\bar{\mathbf{C}} \in \mathbb{R}^{O\times pr}$, and $\bar{\mathbf{D}} \in \mathbb{R}^{O\times r}$ need to be converted into the continuous-time domain, in order to define the relevant transfer function $\mathbf{G}(\omega) \in \mathbb{C}^{O\times r}$ as

$$\bar{\mathbf{G}}(\omega) = \bar{\mathbf{C}}(\mathrm{i}\omega\mathbf{I} - \bar{\mathbf{A}})^{-1}\bar{\mathbf{B}} + \bar{\mathbf{D}}. \tag{1.54}$$

By performing the eigenvalue decomposition of the companion matrix $\bar{\mathbf{A}} = \mathbf{V}\boldsymbol{\mu}\mathbf{V}^{-1}$, the system poles, $\boldsymbol{\Lambda} = \ln(\boldsymbol{\mu})/\Delta t$, and the operational reference vectors are extracted, $\mathbf{G} = \mathbf{V}^{-1}\bar{\mathbf{B}}$.

The next step concerns the selection of a certain number of physical modes, among that associated to the polynomial model, by using a stabilization diagram (it will be briefly described in what follows).

1.3.3.1 Stabilization diagram: model order selection

In modal analysis field, the stabilisation analysis assists the analyst in distinguishing the physical system poles from the mathematical or spurious poles and in finding the correct polynomial model order [151] (which remain an unknown value as the number of modes to be identified in the frequency band of interest). The presence of spurious poles can be attributed to many different causes, such as measurement noise, modelling errors, computational issues, etc. A characteristic of the physical system poles is their trend in stabilising when the estimation is performed at different model orders (referring to the polynomial order in Eq. (1.35)). By employing this fundamental idea, the so-called stabilization criteria are defined: modes for which the distance in modal parameters between two consecutive model orders are higher than certain threshold values, are not plotted in the diagram. Accordingly, a graphical tool, the so called stabilisation diagram, allows for visualizing the estimated modal parameters at increasing polynomial orders. As you can see in Figure 1.1, on the x-axis (the frequency axis), the natural frequencies are represented, while the increasing polynomial model orders are given on the left ordinate axis. The analyst sets the thresholds that define the stabilisation in natural frequency, damping factor and Modal Assurance Criterion (MAC) value (MAC definition will be given in Section 1.5). Several situations are labelled with different symbols: the '`o`' denotes no stabilisation in natural frequency, the '`f`' represents stabilisation in natural frequency, the '`d`' and the '`v`' stand for extra stabilisation in damping ratio and in MAC value, the '`s`' refers to fully stabilised solutions. The spurious numerical poles will not stabilize during this process and they can be easily sorted out of the modal parameter data set.

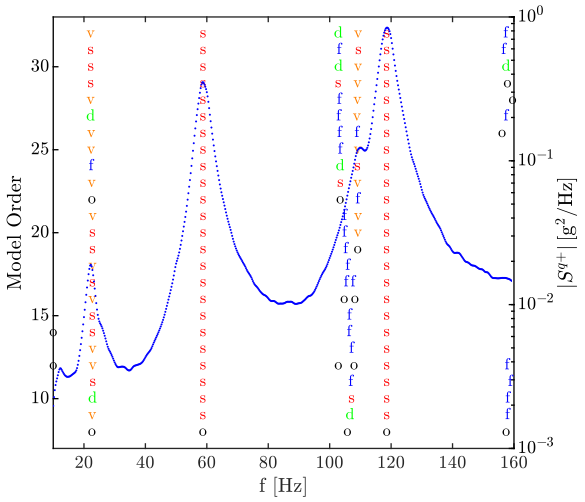

Figure 1.1: Example of stabilisation diagram employed for model order selection: stabilisation diagram along with the magnitude of the PSDs sum function, blue line. The model order is indicated on the left ordinate axis. '`o`': new pole; '`f`' stabilisation in natural frequency; '`f`' extra stabilisation in damping ratio; '`v`' extra stabilisation in MAC value; '`s`' full stabilisation. Stabilisation thresholds for natural frequency, damping ratio, and MAC value are 1%, 5%, and 2%, respectively.

1.3.4 Least Squares Frequency Domain

After the analyst have selected the physical system poles on the stabilisation diagram, the last step concerns mode shape vectors' computation by a linear least squares fitting procedure. This step is also referred to as LSFD based on the partial fraction decomposition representation of Eq. (1.33) which leads to the minimization of the following scatter [126]

$$\boldsymbol{\Gamma}(\boldsymbol{\Psi}, \mathbf{LR}, \mathbf{UR}) = \sum_{k=1}^{N_f} \left(\mathbf{S}^{q+}(\mathrm{i}\omega_k) - \left(\boldsymbol{\Psi}\mathbf{A}(\mathrm{i}\omega_k) + \frac{\mathbf{LR}}{\mathrm{i}\omega_k} + \mathrm{i}\omega_k \mathbf{UR} \right) \right)^2, \tag{1.55}$$

where $\mathbf{A}(\mathrm{i}\omega_k) = (\mathrm{i}\omega_k \mathbf{I} - \boldsymbol{\Lambda})^{-1}\mathbf{G}^{\mathrm{T}}$ embeds the modal parameters selected from the pLSCF step, $\mathbf{LR}$ and $\mathbf{UR}$ are respectively the unknown lower and upper residuals aiming at introducing into the model the influence of the out-of-band modes.

1.4 Data pre-processing

The two step procedure above proposed doesn't directly use the raw output measurements but rely on reduced data such as power spectral densities or cross-correlation functions between signals measured at different locations during several runs (as a number of the output-only MPE methods). The nonparametric estimation of PSDs from time series is quite extensively treated in the literature [10]. Two statistics for the estimation of PSDs, the correlogram and periodogram approaches, are the most popular: the former will be discussed in the following and an efficient numerical implementation of the latter was proposed by Welch in [157].

Regarding the weighted correlogram method, one firstly estimates the CFs matrix $\mathbf{R}(\tau) \in \mathbb{R}^{o\times r}$, with o the number of outputs and r the number of references. The generic CF between the output q_i and the reference q_j, evaluated at the time lag $k\Delta t$ is expressed as:

$$R_{ij}^{q}(k\Delta t) = \frac{1}{N_s}\sum_{t=0}^{N_s-1} q_{i,t}q_{j,t+k}, \tag{1.56}$$

where N_s is the total number of samples, Δt is the sampling period and k is the correlation sample index. It comes up with the output PSD estimate by computing the Discrete Fourier Transform (DFT) of the weighted output correlation function in Eq. (1.56)

$$S_{ij}^{q}(\omega) = \sum_{k=-K}^{K} w_k R_{ij}^{q}(k\Delta t)\mathrm{e}^{-\mathrm{i}\omega k\Delta t}, \tag{1.57}$$

where K is the maximum number of time lags, chosen so that $K < N_s$, and w_k indicates the exponential window used for reducing leakage (same strategy as for the nonparametric estimation of impulse responses), which introduces a known additional damping to the poles. As the correlation samples at negative time lags contain redundant information, several OMA techniques consider only the positive time lags, dealing with the positive power spectrum

computed as

$$S_{ij}^{q+}(\omega) = \frac{w_0 R_{ij}^q(0)}{2} + \sum_{k=1}^{K} w_k R_{ij}^q(k\Delta t)\mathrm{e}^{-\mathrm{i}\omega k\Delta t}. \tag{1.58}$$

1.5 Modal parameters validation

Once the modal parameters are determined, several procedures exist allowing for the modal data (model) validation. All of these methods depend upon the evaluation of an assumption concerning the modal model. Unfortunately, the success of the validation method only defines the validity of the assumption; the failure of the modal validation does not generally define what the cause of the problem is.

1.5.1 Synthesis and MAC

A first validation procedure consists of comparing the data synthesized from the modal model, e.g. Eq. (1.33), with the nonparametric estimates. A quantitative assessment of the agreement between synthesized and measured values of each $\mathbf{S}^{q+}(\mathrm{i}\omega)$ matrix entry is obtained by computing the synthesis correlation coefficient $C_{S_{ij}^q}$ and the normalised error $E_{S_{ij}^q}$, respectively defined as

$$C_{S_{ij}^q} = \frac{\left|\sum_{k=1}^{N_f} S_{ij}^q(\omega_k)\,\hat{S}_{ij}^{q*}(\omega_k)\right|^2}{\sum_{k=1}^{N_f} S_{ij}^q(\omega_k)\,S_{ij}^{q*}(\omega_k)\sum_{k=1}^{N_f}\hat{S}_{oi}^q(\omega_k)\,\hat{S}_{ij}^{q*}(\omega_k)}, \tag{1.59}$$

$$E_{S_{ij}^q} = \frac{\sum_{k=1}^{N_f}\left|S_{ij}^q(\omega_k) - \hat{S}_{ij}^q(\omega_k)\right|^2}{\sum_{k=1}^{N_f}\left|S_{ij}^q(\omega_k)\right|^2}, \tag{1.60}$$

where $S_{ij}^{q}(\omega_k)$ denotes the measured PSD values, $\hat{S}_{ij}^{q}(\omega_k)$ the estimated ones. The two coefficients, defined by Eqs. (1.59) and (1.60), provide a global evaluation, over the whole frequency range, of the linear relationship between the theoretical and estimated PSDs.

Focusing on the individual modal parameters, natural frequencies and damping ratios could be compared with reference values, e.g. from FE analysis or different experimental campaign, by means of relative percentage errors; on the other hand mode shape vectors are usually validated by calculating the relevant MAC, Modal Assurance Criterion, between reference, $\tilde{\boldsymbol{\psi}}_i$, and estimated, $\boldsymbol{\psi}_j$, modal vector sets [115]. The modal assurance criterion is defined as a scalar constant relating the portion of the auto moment of the modal vector that is linearly related to the reference modal vector as follows [2, 150]:

$$\mathrm{MAC}_{ij} = \frac{\left|\tilde{\boldsymbol{\psi}}_i^{\mathrm{H}} \boldsymbol{\psi}_j\right|^2}{\tilde{\boldsymbol{\psi}}_i^{\mathrm{H}} \tilde{\boldsymbol{\psi}}_i \boldsymbol{\psi}_j^{\mathrm{H}} \boldsymbol{\psi}_j}, \tag{1.61}$$

where MAC_{ij} is a scalar constant relating the causal relationship between two modal vectors. The constant takes on values from zero, representing no consistent correspondence, to one, representing a consistent correspondence. In this manner, if the modal vectors under consideration truly exhibit a consistent relationship, the modal assurance criterion should approach unity. Moreover, the MAC is commonly used for measuring the distance between eigenvectors in a stabilization diagram, for comparing identified and forwardly computed modes, and for validating the identified set of modal parameters. However, several other indicators, helpful for validation of the set of modal parameters, exist but they are here omitted for the sake of brevity [80].

In a nutshell

1. *Classical Operational Modal Analysis models: modal decomposition of the ouput CFs and PSDs matrices under the NExT assumption. The right matrix fraction description of positive spectra matrix and its conversion into a state space equivalent model.*
2. *A particular two step procedure for modal parameter estimation: details about the pLSCF solution for poles and operational reference vectors estimation, and the LSFD estimator for mode shapes extraction.*
3. *The role of the stabilisation diagram in physical poles selection and some tools for modal parameters validation: synthesis correlation coefficients, normalized errors and the Modal Assurance Criterion.*

Chapter 2

Vibro-acoustical OMA for MEMS identification

Contents

2.1 Introduction

The need for tools to understand, test, model, and predict microsystems performances inspires the wide framework of multidisciplinary research on MEMS sensor technologies. Compared to regular mechanical structures, these structures possess very high natural frequencies (in the order of kilohertz or megahertz), as made up of components from micrometers to

millimetres in size, and small elastic displacement. Characterization of dynamic properties and testing capabilities is required to guarantee that the microsystems reliably perform their own task and to validate predictive models that enable optimization at the design stage [24, 40, 65, 112, 139].

To this extent, an overview of modal testing techniques for microsystems together with a particular EMA methodology that includes base excitation via a piezoelectric shaker and measurement through a laser interferometer can be found in Ref. [112]. Experimental modal analysis (EMA) techniques are traditionally applied to dynamic characterization of large scale structures (i.e. made up of components sized over a centimeter): this is due to the systems classically employed to produce the structure excitation, measure the input and the associated output [61, 80]. The most of modal testing techniques includes the usage of impact hammers or shakers for exciting the structure via a function of known frequency characteristics (impulse, random, periodic), and measuring the associated response using force or motion sensors (i.e. accelerometers, load cells). When performing EMA on microsystems, such excitation and measurement methods result challenging, due to the system small size: this issue is particularly significant with conventional modal testing techniques. Indeed, attaching accelerometers substantially alters the dynamic characteristics of microstructures: thus, providing transient input with an impulse hammer or attaching a shaker to the structure is unfeasible. Therefore, both the excitation and measurement must be conducted through non-contact instruments [40]. Other issues are related to MEMS characteristic natural frequencies, which are in the order of kilohertz or megahertz, and thus require a specific excitation method: traditional mechanical, electromagnetic, and hydraulic shakers have a limited frequency range. For these reasons, numerous different excitation techniques are employed for modal testing of microsystems [112]. Electrostatic excitation can be applied either by employing the structure itself, or by using a built-in actuator [49, 86]. The excitation can also be established by embedded smart material elements integrated into the structure

[162]. This solution adds complexities to the fabrication methods and, the inclusion of extra materials can significantly alter MEMS dynamic characteristics. Generally, the characteristics of embedded smart materials and electrostatic forces are nonlinear functions of structural motion [112]. Alternatively, magnetic and thermal excitation techniques may adversely impact the structures requiring to add coating material, thus altering the structure dynamics and making difficult to control the input [14]. An alternative, which does not alter the structural characteristics, is the base excitation approach using external elements [31]. Here, a transducer, e.g., a piezoelectric shaker, is used as the source of excitation at high frequencies. Usually, the input is not directly measured since a sensor, such as a load cell, cannot be included. The common issue with all these methods arises from the fact that none of them is truly external and not suitable for measuring inputs [112].

To deal with the measurement problem, techniques from optics, such as video imaging, and interferometry, have been adapted by employing non-contact devices [25, 165]. Among these, it is interesting to recall: (i) stroboscopy, with light emitters able to increase the maximum detectable frequency [75]; (ii) video-imaging techniques, generally costly and complex, which employ ultra-high-speed cameras [129]; (iii) interferometry that requires specular surfaces, i.e. mirror-like reflective, and offer the motion of the whole surface, rather than a single point [164]; (iv) other optical techniques (including holographic interferometry, electronic speckle pattern interferometry (ESPI), blur envelope), most of which measure changes in capacitance arising from structural vibrations (existence of large parasitic capacitance, however, usually results in very poor signal-to-noise ratios and limits the accuracy) [86, 112]. Another attractive non-contact measurement is the laser Doppler vibrometry (LDV) [92, 111]. LDVs measure the out-of-plane velocities of a moving surface with adequate reflectivity. Single-point LDVs require multiple measurements for establishing the mode shapes that need the usage of a common, repeatable reference for correct phase information. Alternatively, scanning LDVs allow automatic measurement of many points in a single test.

In this context, a vibro-acoustical methodology based on OMA is proposed, consisting in acoustical excitation and output-only measurement throughout a single-point LDV and a microphone to access both the acoustical and structural responses. OMA techniques enable to get information on the modal parameters replacing the deterministic knowledge of the input signal with the NExT assumption. In fact, the assessment of the operational input forces turns out to be challenging especially in the case of micro-systems. Furthermore, classical OMA algorithms may be employed for vibro-acoustical systems, where the fluid–structure interaction yields both the acoustical and structural responses, as presented in Ref. [124]. In the following, the vibro-acoustical OMA formulation will be recalled: the specific approach is based on the modal decomposition of cross-power spectra, defined CPs, between structural and acoustical responses assuming to have acoustical excitation obeying NExT assumption. Once this modal decomposition formulation is determined, experimental testing on a specific quartz tuning fork, QTF, vibrating in air is performed. This acousto-electric transducer is employed in trace gas sensing techniques, specifically called quartz-enhanced photoacoustic spectroscopy (QEPAS) [90, 91, 116, 117, 118].

Recently a theoretical-experimental framework for the analysis of QTF dynamic response has been proposed [28]. Specific attention has been paid to the fluid-structure coupling in terms of forces exerted by the fluid on the structure (fluid inertia and viscosity as well as an additional diffusivity term) whose influence is crucial for the correct evaluation of the system response. In this chapter, an alternative approach, based on the vibro-acoustical OMA, is presented as a valid technique to identify the relevant QTF modal parameters, i.e., flexural eigenfrequencies, quality factors, and unscaled mode shapes. An acoustic stationary random field generated by two speakers has been used to acoustically excite the QTF. The resulting structural velocities have been measured and recorded by using a single-point LDV, while an electronic microphone has been employed to measure the acoustic pressure at a specific fixed point close to the QTF. This latter signal represents the acoustical output

reference. Two set-up configurations are proposed in order to access the QTF fundamental in-plane skew-symmetric mode and the two first out-of-plane flexural modes. A comparison of results, obtained by means of the identification performed on the CPs computed by using only structural responses (classical OMA approach) and those got by including both structural and acoustical outputs, referred to as vibro-acoustical OMA, is developed.

2.2 Modal models for vibro-acoustical systems

A linear, time-invariant, damped, vibrating system coupled with a fluid medium is considered, as usually done in a Finite Element (FE) formulation [74]. To assess the equations describing the vibro-acoustical behavior of coupled systems, it is combined the discretized motion equation for the structural vibrational behavior under external structural loading and coupled acoustical loading, with the acoustical problem of the pressure response in the cavity caused by acoustical excitation, as well as by structural vibration on the boundaries. Indeed, the nonsymmetrical set of second order equations of motion for the vibro-acoustical coupled system is expressed in matrix notation as [159]

$$\begin{bmatrix} \mathbf{M}^s & \mathbf{0} \\ \mathbf{M}^c & \mathbf{M}^f \end{bmatrix} \begin{Bmatrix} \ddot{\mathbf{x}}(t) \\ \ddot{\mathbf{p}}(t) \end{Bmatrix} + \begin{bmatrix} \mathbf{C}^s & \mathbf{0} \\ \mathbf{0} & \mathbf{C}^f \end{bmatrix} \begin{Bmatrix} \dot{\mathbf{x}}(t) \\ \dot{\mathbf{p}}(t) \end{Bmatrix} + \begin{bmatrix} \mathbf{K}^s & -\mathbf{K}^c \\ \mathbf{0} & \mathbf{K}^f \end{bmatrix} \begin{Bmatrix} \mathbf{x}(t) \\ \mathbf{p}(t) \end{Bmatrix} = \begin{Bmatrix} \mathbf{f}(t) \\ \rho \dot{\mathbf{q}}(t) \end{Bmatrix}, \quad (2.1)$$

where $\mathbf{M}^s$, $\mathbf{C}^s$, and $\mathbf{K}^s$ are the structural mass, damping, and stiffness matrices, $\mathbf{M}^f$, $\mathbf{C}^f$, and $\mathbf{K}^f$, resulting from an indirect formulation of the acoustical problem, describe the pressure-volume acceleration relation in case of a rigid wall structure; the variables $\mathbf{x}(t)$, $\mathbf{p}(t)$, $\mathbf{f}(t)$, and $\dot{\mathbf{q}}(t)$ are the displacement, pressure, structural force, and volume acceleration vectors as functions of time, ρ is the fluid density. The coupling matrices $\mathbf{K}^c$ and $\mathbf{M}^c$ derive respectively from the acoustical pressure loading on the structure over the boundary surface S_b and the loading due to vibration at the same flexible boundary. According to Ref. [74], the entries of

the coupling matrices can be expressed as follows

$$K_{ij}^{c} = \int_{S_b} \mathbf{n}_i \cdot \mathbf{n} N_j dS \tag{2.2}$$

$$M_{ji}^{c} = \int_{S_b} \rho N_i \mathbf{n}_j \cdot \mathbf{n} dS, \tag{2.3}$$

where $\mathbf{n}$ is the surface normal vector and $\mathbf{n}_i$ is the interpolation function vector in the finite element formulation. These matrices are so interrelated by using the equation $\mathbf{M}^c = \rho(\mathbf{K}^c)^{\mathrm{T}}$. By Laplace-transforming Eq. (2.1), with s being the Laplace variable, the more compact matrix relationship is obtained:

$$\begin{bmatrix} \mathbf{A}^s & -\mathbf{K}^c \\ -\omega^2(\mathbf{K}^c)^{\mathrm{T}} & \mathbf{A}^f/\rho \end{bmatrix} \begin{Bmatrix} \mathbf{x}(s) \\ \mathbf{p}(s) \end{Bmatrix} = \mathbf{B}(s) \begin{Bmatrix} \mathbf{x}(s) \\ \mathbf{p}(s) \end{Bmatrix} = \begin{Bmatrix} \mathbf{f}(s) \\ \dot{\mathbf{q}}(s) \end{Bmatrix}, \tag{2.4}$$

with

$$\mathbf{A}^s = \mathbf{K}^s + s\mathbf{C}^s + s^2\mathbf{M}^s \tag{2.5}$$

$$\mathbf{A}^f = \mathbf{K}^f + s\mathbf{C}^f + s^2\mathbf{M}^f. \tag{2.6}$$

For the special nonsymmetry of $\mathbf{B}(s)$, it can be proven that the left eigenvectors, $\boldsymbol{\phi}_n$, and the right ones, $\boldsymbol{\psi}_n$, are related by

$$\begin{Bmatrix} \boldsymbol{\phi}_n^s \\ \boldsymbol{\phi}_n^f \end{Bmatrix} = \begin{Bmatrix} \boldsymbol{\psi}_n^s \\ \frac{1}{\lambda_n^2}\boldsymbol{\psi}_n^f \end{Bmatrix}, \tag{2.7}$$

where the superscript s is for the structural response locations, f for the acoustical response ones, while the subscript n refers to the system pole λ_n. Conforming to general modal analysis theory [61], we write the coupled system transfer matrix $\mathbf{H}(s) = \mathbf{B}(s)^{-1}$ in the following

partitioned form:

$$\left\{ \begin{array}{c} \mathbf{x}\left(s\right) \\ \mathbf{p}\left(s\right) \end{array} \right\} = \left[\begin{array}{cc} \mathbf{H}_{xf}\left(s\right) & \mathbf{H}_{x\dot{q}}\left(s\right) \\ \mathbf{H}_{pf}\left(s\right) & \mathbf{H}_{p\dot{q}}\left(s\right) \end{array} \right] \left\{ \begin{array}{c} \mathbf{f}\left(s\right) \\ \dot{\mathbf{q}}\left(s\right) \end{array} \right\}, \tag{2.8}$$

where the transfer matrix partitions between the responses and acoustical volume acceleration excitation $\dot{\mathbf{q}}(t)$ can be derived as a function of the right eigenvectors and eigenvalues of the system matrix as

$$\mathbf{H}_{x\dot{q}}\left(s\right) = \sum_{n=1}^{2N} \frac{\boldsymbol{\psi}_n^s \left(P_n \boldsymbol{\psi}_n^f\right)^{\mathrm{T}}}{\lambda_n^2 \left(s-\lambda_n\right)} = \sum_{n=1}^{2N} \frac{\boldsymbol{\psi}_n^s \left(\boldsymbol{\mu}_n^f\right)^{\mathrm{T}}}{s-\lambda_n} \tag{2.9}$$

$$\mathbf{H}_{p\dot{q}}\left(s\right) = \sum_{n=1}^{2N} \frac{\boldsymbol{\psi}_n^f \left(P_n \boldsymbol{\psi}_n^f\right)^{\mathrm{T}}}{\lambda_n^2 \left(s-\lambda_n\right)} = \sum_{n=1}^{2N} \frac{\boldsymbol{\psi}_n^f \left(\boldsymbol{\mu}_n^f\right)^{\mathrm{T}}}{s-\lambda_n}, \tag{2.10}$$

where N is the number of complex-conjugates mode pairs in the range of interest, P_n is a modal scaling factor, the right eigenvectors $\boldsymbol{\psi}_n^{s,f}$ represent the vibro-acoustical mode shapes, and the participation factors $\boldsymbol{\mu}_n^f$ are related to the left eigenvectors with

$$\boldsymbol{\mu}_n^f = \frac{P_n \boldsymbol{\psi}_n^f}{\lambda_n^2} = P_n \boldsymbol{\phi}_n^f. \tag{2.11}$$

Starting from Eqs. (2.9) and (2.10), the modal decomposition of the output PSD for the vibro-acoustical system of Eq. (2.1) is derived in Ref. [124]. In fact, by focusing on the case where there are no structural forces ($\mathbf{f}(t) = \mathbf{0}$) and K refers to the white noise uncorrelated acoustical inputs, such that the corresponding CFs matrix $\mathbf{R}_{\dot{q}}(\tau) \in \mathbb{R}^{K \times K}$ is

$$\mathbf{R}_{\dot{q}}(\tau) = \left[\begin{array}{ccc} \alpha_1 \delta(\tau) & & 0 \\ & \ddots & \\ 0 & & \alpha_K \delta(\tau) \end{array} \right], \tag{2.12}$$

one can employ Duhamel's integrals to calculate

$$\mathbf{x}\left(t\right)=\int_{-\infty}^{t}\mathbf{h}_{x\dot{q}}\left(t-\tau\right)\dot{\mathbf{q}}\left(\tau\right)d\tau \tag{2.13}$$

$$\mathbf{p}\left(t\right)=\int_{-\infty}^{t}\mathbf{h}_{p\dot{q}}\left(t-\sigma\right)\dot{\mathbf{q}}\left(\sigma\right)d\sigma, \tag{2.14}$$

where $\mathbf{h}_{x\dot{q}}(t)$ and $\mathbf{h}_{x\dot{q}}(t)$ represent the inverse Laplace transforms of transfer matrices in Eqs. (2.9) and (2.10), and allow to model the CFs matrix $\mathbf{R}_{xp}(\tau)$ between the acoustical p and structural x responses as

$$\mathbf{R}_{xp}\left(\tau\right)=\mathbf{E}\left[\mathbf{x}\left(t+\tau\right)\mathbf{p}(t)^{\mathrm{T}}\right]=\sum_{n=1}^{2N}\boldsymbol{\psi}_{n}^{s}(\mathbf{Q}_{n}^{xp})^{\mathrm{T}}\mathrm{e}^{\lambda_{n}\tau}h\left(\tau\right)+\mathbf{Q}_{n}^{xp}\left(\boldsymbol{\psi}_{n}^{f}\right)^{\mathrm{T}}\mathrm{e}^{-\lambda_{n}|\tau|}h\left(-\tau\right), \tag{2.15}$$

where $h(\cdot)$ is the well-known Heaviside step function, and the particular output-only reference vector $\mathbf{Q}_{n}^{xp}$ is defined as:

$$\mathbf{Q}_{n}^{xp}=-\sum_{k=1}^{K}\frac{\alpha_{k}P_{n}\psi_{n,k}^{f}}{\lambda_{n}^{2}}\sum_{j=1}^{2N}\left[\frac{P_{j}\psi_{j,k}^{f}\boldsymbol{\psi}_{j}^{f}}{\lambda_{j}^{2}\left(\lambda_{n}+\lambda_{j}\right)}\right]. \tag{2.16}$$

Analogously, the same procedure is followed in Ref. [124] to express the CFs matrix $\mathbf{R}_{xx}(\tau)$ between structural x responses:

$$\mathbf{R}_{xx}\left(\tau\right)=\mathbf{E}\left[\mathbf{x}\left(t+\tau\right)\mathbf{x}(t)^{\mathrm{T}}\right]=\sum_{n=1}^{2N}\boldsymbol{\psi}_{n}^{s}(\mathbf{Q}_{n}^{xx})^{\mathrm{T}}\mathrm{e}^{\lambda_{n}\tau}h\left(\tau\right)+\mathbf{Q}_{n}^{xx}\left(\boldsymbol{\psi}_{n}^{f}\right)^{\mathrm{T}}\mathrm{e}^{-\lambda_{n}|\tau|}h\left(-\tau\right), \tag{2.17}$$

in which the corresponding output-only reference vector $\mathbf{Q}_{n}^{xx}$ is

$$\mathbf{Q}_{n}^{xx}=-\sum_{k=1}^{K}\frac{\alpha_{k}P_{n}\psi_{n,k}^{f}}{\lambda_{n}^{2}}\sum_{j=1}^{2N}\left[\frac{P_{j}\psi_{j,k}^{f}\boldsymbol{\psi}_{j}^{s}}{\lambda_{j}^{2}\left(\lambda_{n}+\lambda_{j}\right)}\right]. \tag{2.18}$$

Given the modal models of cross-power spectra, CPs, that are the matrices representing

the Laplace transforms of Eq. (2.15) and (2.17), a translation into the Fourier domain is done by imposing $s = \mathrm{i}\omega$:

$$\mathbf{G}_{xp}(\mathrm{i}\omega) = \sum_{n=1}^{2N} \frac{\boldsymbol{\psi}_n^s (\mathbf{Q}_n^{xp})^{\mathrm{T}}}{\mathrm{i}\omega - \lambda_n} + \frac{\mathbf{Q}_n^{xp} (\boldsymbol{\psi}_n^f)^{\mathrm{T}}}{-\mathrm{i}\omega - \lambda_n} \tag{2.19}$$

$$\mathbf{G}_{xx}(\mathrm{i}\omega) = \sum_{n=1}^{2N} \frac{\boldsymbol{\psi}_n^s (\mathbf{Q}_n^{xx})^{\mathrm{T}}}{\mathrm{i}\omega - \lambda_n} + \frac{\mathbf{Q}_n^{xx} (\boldsymbol{\psi}_n^f)^{\mathrm{T}}}{-\mathrm{i}\omega - \lambda_n}. \tag{2.20}$$

One can, thus, determine the so-called positive power spectrum, PCPs, as the Fourier transform of the CFs at positive time lags, related to the stable poles λ_n, and here recalled:

$$\mathbf{G}_{xp}^{+}(\mathrm{i}\omega) = \sum_{n=1}^{2N} \frac{\boldsymbol{\psi}_n^s (\mathbf{Q}_n^{xp})^{\mathrm{T}}}{\mathrm{i}\omega - \lambda_n} \tag{2.21}$$

$$\mathbf{G}_{xx}^{+}(\mathrm{i}\omega) = \sum_{n=1}^{2N} \frac{\boldsymbol{\psi}_n^s (\mathbf{Q}_n^{xx})^{\mathrm{T}}}{\mathrm{i}\omega - \lambda_n}. \tag{2.22}$$

By looking at Eqs. (2.21) and (2.22), it is pointed out that the modal decompositions of $\mathbf{G}_{xp}^{+}(\mathrm{i}\omega)$ and $\mathbf{G}_{xx}^{+}(\mathrm{i}\omega)$ depend on the same vibro-acoustical mode shapes and system poles but differ for the definition of the operational reference vectors expressed in Eqs. (2.16) and (2.18). Furthermore, the similarity with the classic OMA modal models [126] allows to apply techniques developed for output-only system identification. The choice falls on a frequency-domain parametric modal method based on the Least Squares Frequency Domain (LSFD) estimator, relied on the modal model in Eqs. (2.21) and (2.22), along with the poly-reference Least Squares Complex Frequency (pLSCF) method [73]. The LSFD method is employed to obtain a global estimate of the mode shapes whilst the pLSCF provides poles and operational reference vectors using a fraction polynomial model, the so-called Right Matrix Fraction Description, equivalent to the modal model in Eqs. (2.21) and (2.22).

In the following, the identification process based on the PCPs matrix $\mathbf{G}_{xx}^{+}(\mathrm{i}\omega)$ will be referred to with the abbreviation OMA, while the one based on $\mathbf{G}_{xp}^{+}(\mathrm{i}\omega)$ will be called VA-OMA. From the experimental perspective, the choice of considering acoustical references for

micro-scale vibro-acoustical structure, like MEMS, may prove to be advantageous for reasons related to simplicity to take a microphone near the acoustical excitation overcoming the need to have multiple sensors located on the structure, often not feasible for these systems.

2.3 Experimental case study

In order to assess the performance of the presented approach, two case studies are offered, employing the data achieved by processing the time records collected through real-world experiments on a QTF. The dimensions of the device under test are listed in Table 2.1 and the main purpose of the test is to validate the theoretical model, proposed in [28], which enhances the intelligibility of the physical parameters governing the dynamics of the QTF by describing the interaction with the surrounding fluid via a specific hydrodynamic function (dominated by a diffusive term that proves to be crucial for damping prediction).

QTF Dimensions, mm		Geometry
Prong Length	$l_p = 9.4$	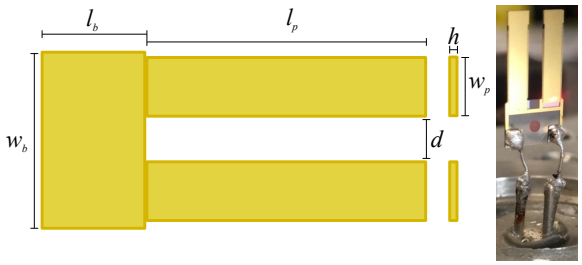
Base Length	$l_b = 3.6$	
Prong Width	$w_p = 2$	
Base Width	$w_b = 6$	
Prong Spacing	$d = 1.5$	
QTF Thickness	$h = 0.25$	

Table 2.1: Dimensions of the device under test, the nomenclature refers to sketch.

Results of structural and vibro-acoustical OMA approach are compared by exploiting experiment on structures at millimeter scale. In this respect, differences emerge from the study case in [124], where vibro-acoustical OMA turns out to be useful for high scale structures, i.e. an helicopter cabin, for reasons related to the usage of moving sensors together with additional acoustical fixed reference ones. In this experimental application, vibro-acoustical

OMA reveals itself attractive also for MEMS testing where the non-contact measurement devices are commonly roving and the usage of fixed acoustical sensors near the structure represents a valid reference signal. The two experimental setup, adopted to completely achieve the in-plane and out-of-plane QTF sensor flexural modes, are sketched in Figure 2.1. Preliminary in-vacuum 3D finite element (FE) analyses [28] are exploited in order to determine a first estimate of the relevant natural frequencies so as to choose the excitation source and measurement parameters. Furthermore, the theoretical model in [28] confirms that the two tin weldings, see picture in Table 2.1, can be treated as a bracket joint positioned on the base cross-section.

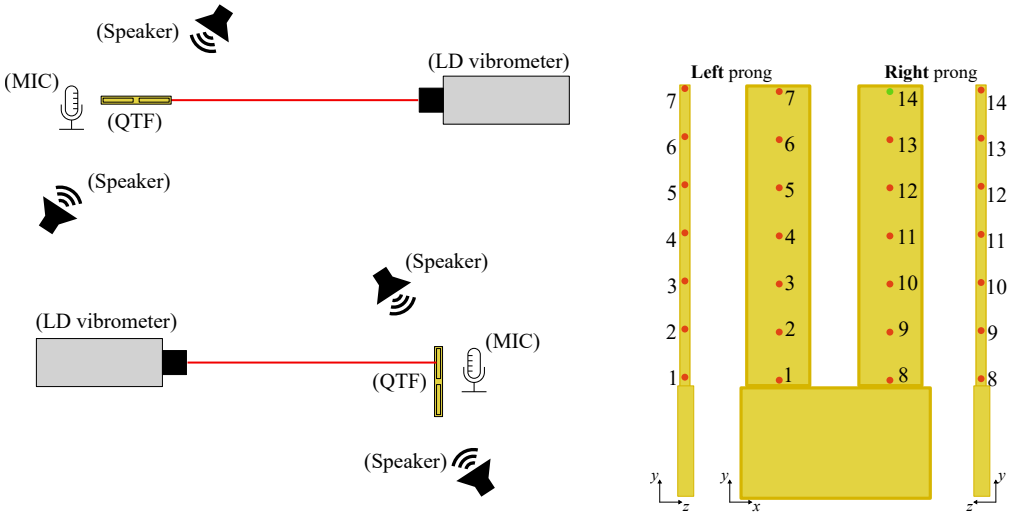

(a) (b)

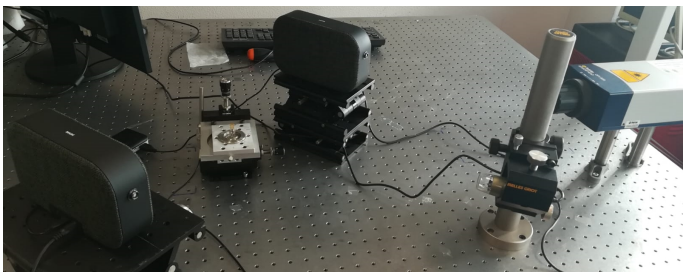

(c)

Figure 2.1: (a) Schematic representation of the two adopted experimental setups: in-plane (top panel), real setup in (c), and out-of-plane configuration (bottom panel). (b) Set-up geometry with the 14 measurement locations: 7 on the left prong and 7 on the right one. The tip point location, `point14`, is depicted in green. It has been used as structural reference.

The QTF is excited in laboratory air by a stochastic, white acoustic field, generated by two speakers. QTF responses are measured, in terms of displacement and velocity, by a single-point LDV pointing at different locations comprising the test layout sketched in Figure 2.1b. In addition to structural responses, a microphone is used to measure acoustical pressure in proximity of the sensor in order to include an acoustical output usable as reference in the PCPs assessment involved in the vibro-acoustical OMA framework.

The setup is composed by: (i) a Polytec OFV-5000 modular LD vibrometer to measure the output response in several points of the QTF, (ii) two speakers to produce a white acoustic random field for exciting the tuning fork structure, (iii) a Microtech Gefell $1/4''$ elecret-measurement microphone M370, (iv) a LMS SCADAS Recorder 09 mobile PC based multichannel analyzer platform, running the LMS Test.Lab 14A software suite for generating the input electric signal to drive the speakers, and to acquire and record the time histories of the output responses measured by the vibrometer and the microphone.

In summary, the differences between the two configurations are mainly made by: (i) the frequency band of white noise input, driving the speakers and the sampling frequency, both related to the predicted natural frequencies of the in-plane and out-of-plane flexural modes; (ii) the measurements points and the sensor orientation with respect to speakers and vibrometers position unchanging in the test campaigns as depicted in Figure 2.1.

In the OMA approach, one of the structural velocities, measured by means of LDV, is considered as reference $q_j(t)$ leading to PCPs matrix whose modal decomposition is derived in Eq. (2.22). On the other hand, the acoustical response, coming from the microphone near the QTF, is chosen in order to reach the PCPs matrix with the modal model expressed in Eq. (2.21). It is stressed the fact that the two modal models in Eqs. (2.22) and (2.21) differ only in the meaning of the second modal vector, indicated by $\mathbf{Q}_n^{xp}$ and $\mathbf{Q}_n^{xx}$ defined in Eqs. (2.16) and (2.18) for the generic n mode, which depends on the choice of reference, structural or acoustical. However, PCPs can be parameterized in exactly the same way and

then the same MPE procedure are used for both OMA and VA-OMA.

2.3.1 MPE strategy

In order to estimate the modal parameters of Eqs. (2.22) and (2.21), a two step procedure derived from OMA field is proposed. The first step involves the pLSCF estimator which is based on a Right Matrix Fraction Description (RMFD) of the PCPs matrix and allows to obtain the system poles, λ_n, and operational reference vectors, $\mathbf{Q}_n^{xx}$ or $\mathbf{Q}_n^{xp}$, by means of a stabilization chart. The latter gives a strong indication of the number of present physical modes and allows to estimate the corresponding physical poles (i.e. eigenfrequencies and damping ratios) and the respective operational reference vectors. As a second step, a frequency domain parametric modal method based on the LSFD estimator is used, relied on the equivalent modal models in Eqs. (2.22) and (2.21). The LSFD method is employed to obtain a global estimate of the mode shapes.

A quantitative assessment of the agreement between the estimated modal model and the measurement of each $\mathbf{G}_{xp}^{+}(\mathrm{i}\omega)$ matrix entry is obtained by computing the synthesis correlation coefficient $C_{S_{oi}}$ and the normalised error $E_{S_{oi}}$, respectively defined in Eqs. (1.59) and (1.60). In the next subsections, results of the identification process, previously described, are proposed for both the case of QFT fundamental in-plane skew-symmetric mode and the two first out-of-plane flexural modes.

2.3.2 In-plane flexural mode identification

The signals are acquired in the time domain with a sampling frequency of 51200 Hz and a time period of 64 s. Seven measurement runs are performed, each characterized by the acquisition of two outputs: the velocity at one of the seven locations depicted in Figure 2.1b and the acoustic pressure in a fixed point close to the sensor. The input electric signal, driving the speakers, is generated as a white noise source in the frequency band from 12 to 18 kHz

with an excitation level of 0.03 V. So, seven structural velocities are independently collected in correspondence of different locations on the right prong as indicated in Figure 2.1b. QTF prong tip, middle, and root velocities are plotted in Figure 2.2 together with the acoustical pressure coming from the microphone. The particular application includes a root mean square, RMS, value of the prong tip velocity of approximately 36 µm/s and of 0.4 nm for the relative displacement.

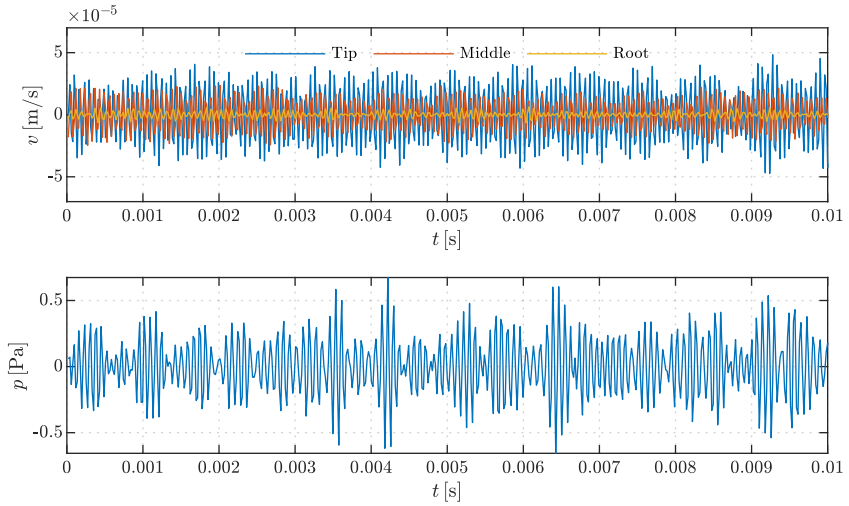

Figure 2.2: Channel throughputs: velocities of the right prong root, middle, and tip locations (top panel), acoustical pressure response coming from the microphone near the loudspeaker (bottom panel).

With regards to the pressure output, Figure 2.3 shows the relevant autoPSD in the whole acquired band, inset at the top right, with a zoom in the excitation region in order to compare the differences between two independent measurement runs. It is underlined the good agreement between the two curves as a sign of consistent repeatability of the microphone acquisition that represents our reference in the vibro-acoustical OMA approach.

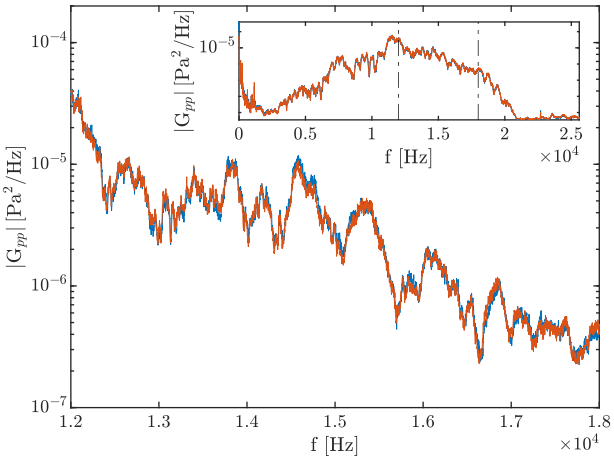

Figure 2.3: In-plane testing: magnitude of pressure PSD in the case of two measurement runs: run 1, blue solid line, and run 2, red solid line, in the bandwidth from 12 to 18 kHz. The inset figure at the top right shows the same spectra in all the acquired frequency band.

In order to apply averaging techniques in PCPs matrix non-parametric estimation, time signals are divided in $M = 32$ blocks, which implies a frequency resolution of the PCPs equal to 0.5 Hz, and a 0.01% exponential window is used to reduce noise contamination, yielding smooth positive-spectra. The weighted correlogram leads to the PCPs matrix estimation, here reported in Figure 2.4, where `point14` velocity is considered as output, $q_i(t)$, and two different reference signals, $q_j(t)$, are employed: the structural, `point14` velocity-reference PCP in the left panel, and the acoustical one, pressure-reference PCP in the right panel. It is noticed the presence of three peaks in both two curves including the fundamental in-plane skew-symmetric flexural eigenfrequency of QTF, which is the mode excited by means of sound waves in the QEPAS application [117], approximately located at 15.8 kHz. The other two peaks, respectively located at 14.590 kHz and 16.170 kHz, are related to the first in-plane symmetric flexural mode and to a torsional mode, having even out-of-plane displacement components, respectively, as demonstrated by performing an in-vacuum 3D finite element (FE) analysis of the tested QTF by the software COMSOL in [28].

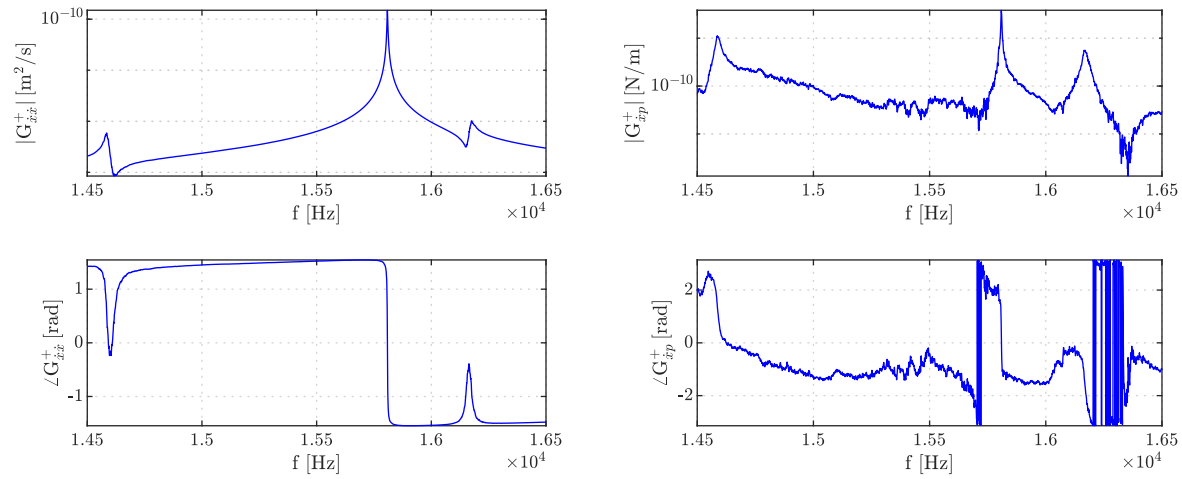

(a) OMA (b) VA-OMA

Figure 2.4: In-plane testing: magnitude and phase angle of the estimated PCP of the velocity measured at the tip of one QTF prong with respect to the structural reference (a) and to the acoustical reference (b).

From the pLSCF, the two stabilization diagrams are reached in Figure 2.5 assuming subsequently an increasing values for the polynomial model order and focusing on the frequency range from 15750 to 15900 Hz, i.e. around the peak of the fundamental in-plane skew-symmetric flexural mode of the QTF. In particular, the PCP-sum, i.e. the complex sum of the PCPs of all the measured structural points together with the system poles estimated by the pLSCF is represented. The stabilization diagram give the indication of one stable pole for both OMA, left panel, and VA-OMA, right panel, processing.

In Table 2.2 the pairs of natural frequencies and damping ratios, computed from the selected stable pole, are reported together with the quality factor calculated as $Q_n = 1/(2\zeta_n)$.

	Natural Frequency (Hz)		Damping Ratio (%)		Quality Factor (-)	
	OMA	VA-OMA	OMA	VA-OMA	OMA	VA-OMA
Mode 1	15808, 5	15808, 7	0.00295	0.00363	16975.6	13769.6

Table 2.2: In-plane flexural modes identification: comparison between modal parameters from OMA and VA-OMA.

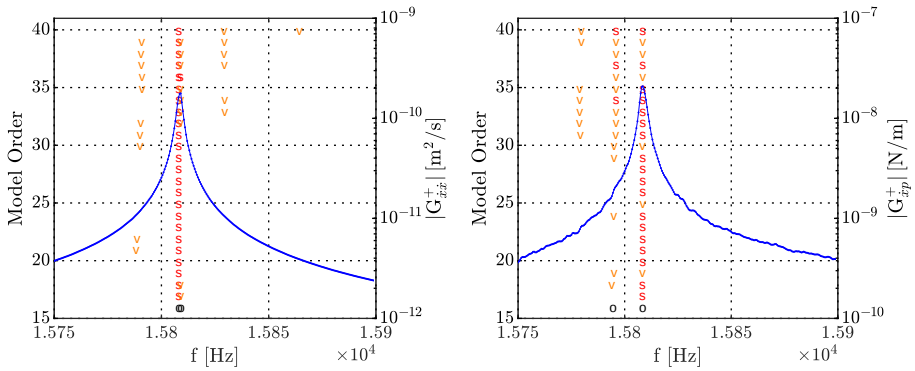

(a) OMA (b) VA-OMA

Figure 2.5: In-plane flexural modes identification: stabilization diagrams along with the magnitude of the PCP sum function, blue line, referred to the structural reference (a) and the acoustical one (b). The stable poles are indicated with '`s`' and the model order is indicated on the left ordinate axis.

It is underline the improved accuracy in the estimate of the quality factor from the vibro-acoustical data, due to the reliability of the acoustic pressure reference. This value is in agreement with the estimate in Ref. [28] where a combined theoretical and experimental approach is employed. On the other hand, damping ratio coming from the OMA data reveals to be underestimated for reasons related to noise due to the usage of a reference signal, `point14` velocity, not simultaneously acquired. Indeed, the relative percentage error with respect to quality factor in Ref. [28] is approximately 5% for the VA-OMA and 30% for that one from OMA.

Achieved poles and operational reference factors from the first step, the MPE is ended up deploying the LSFD estimator in order to compute the unscaled mode shapes. In Figure 2.6, it is shown the mode shape associated to the selected pole suggesting a comparison between that coming from OMA, left panel, and the one from vibro-acoustical OMA, right panel.

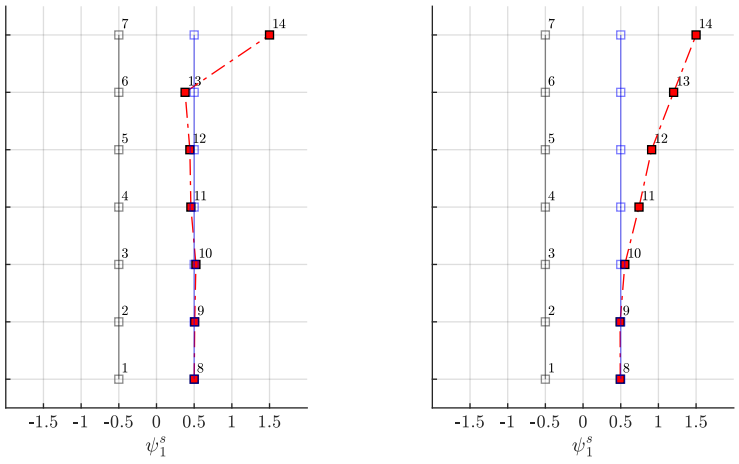

(a) OMA (b) VA-OMA

Figure 2.6: In-plane flexural mode identification: comparison of the mode shape from OMA (a) and VA-OMA (b).

In the OMA case, a distorted mode shape is reached because of the inconsistency of the structural reference in the multi-run measurement process which leads to incorrect phase information. On the other hand, the usage of the acoustic pressure reference reveals to be robust and gives us an accurate estimate of this modal vector in correspondence of the seven structural measurement locations.

Once the modal parameters are computed, the PCPs synthesized from the modal model of Eq. (2.21) are compared with the measured PCPs, as shown in Figure 2.7, referring only to the vibro-acoustical OMA case. The visual match, together with an high correlation coefficient for all the PCPs, proves the goodness of the MPE process results as depicted in Figure 2.8. When looking at the error, it is noticed that the error values remain lower than or equal to approximately 5%. Furthermore, the values of the correlation coefficient, higher than 95%, confirm this assessment, whereby higher values of this quantity corresponds to lower error values and vice-versa. It is pointed out that these improved results are particularly related to the accuracy of the estimation achieved around the resonance peak, see Figure 2.7.

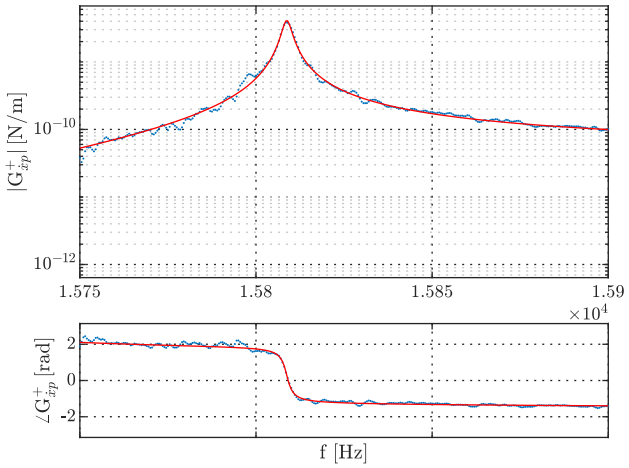

Figure 2.7: In-plane flexural modes identification: comparison between the estimated PCP of the tip velocity referred to the acoustical reference, blue dotted line, and synthesis by modal model, red solid line.

The good correlations and the correctness of the mode chosen corroborate the experimentally verification of the MPE effectiveness obtained considering an acoustical reference in the OMA analysis, as theoretically predicted through the comparison between the formulation derived in Ref. [124], also in the experimental outcomes obtained by means of a vibro-acoustic setup on a millimeter-scale sensor.

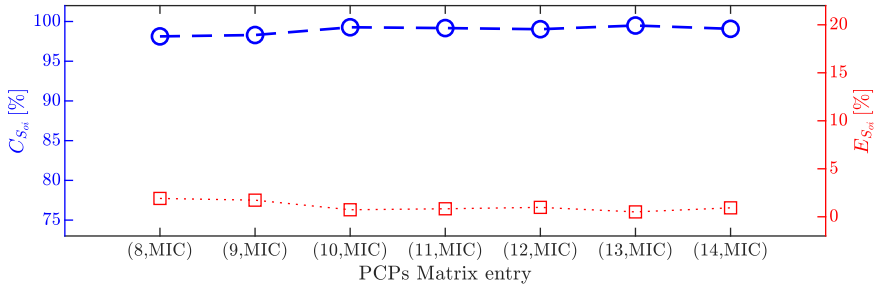

Figure 2.8: In-plane flexural modes identification: correlation coefficients Eq. (1.59) and normalized errors Eq. (1.60) related to the seven PCPs used for the identification with the VA-OMA approach.

2.3.3 Out-of-plane flexural modes identification

In the second case study, the signals are acquired in the time domain with a sampling frequency of 8192 Hz and a time period of 100 s. Fourteen measurement runs are collected, each characterized by the solely acquisition of velocity at one of the fourteen locations, depicted in Figure 2.1b, and the acoustic pressure in a fixed location. In this case, the input electric signal driving the speakers is a white noise source in the frequency band from 1 to 2 kHz with an excitation level of 0.03 V. The RMS value of the prong tips velocity is approximately 10 µm/s and 1 nm regarding the displacement.

In Figure 2.9, the pressure signal autoPSD is shown in the whole acquired band, inset at the left right, with a zoom in the excitation region in order to highlight the good repeatability of the microphone acquisition which plays the role of reference in the PCPs processing.

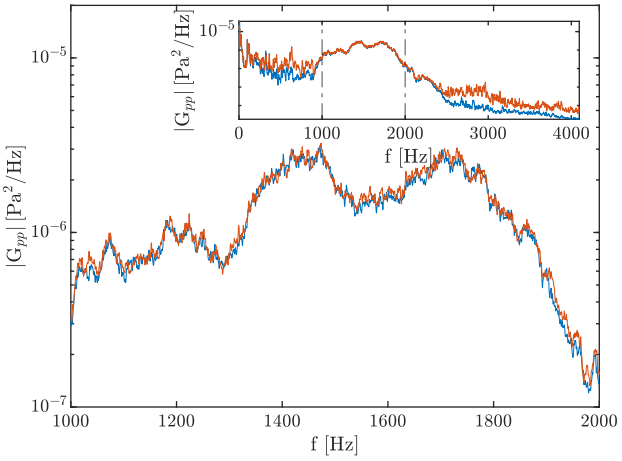

Figure 2.9: Out-of-plane testing: magnitude of pressure PSD in the case of two measurement runs: run 1, blue solid line, and run 2, red solid line, in the bandwidth from 1 to 2 kHz.

Time signals are divided in $M = 40$ blocks, providing a frequency resolution of the PCPs equal to 0.4 Hz, and a 0.01% exponential window is used to reduce noise contamination. In Figure 2.10, it is reported the estimated PCPs between the output, $q_i(t)$, i.e. `point14` velocity, and two different reference signals, $q_j(t)$, i.e. `point14` velocity, in the left panel, and acoustical pressure, in the right panel. Specifically, it is noticed the presence of two peaks in

both two curves including the first out-of-plane symmetric and skew-symmetric modes of the tuning fork, as predicted by the aforementioned 3D FE analysis [28].

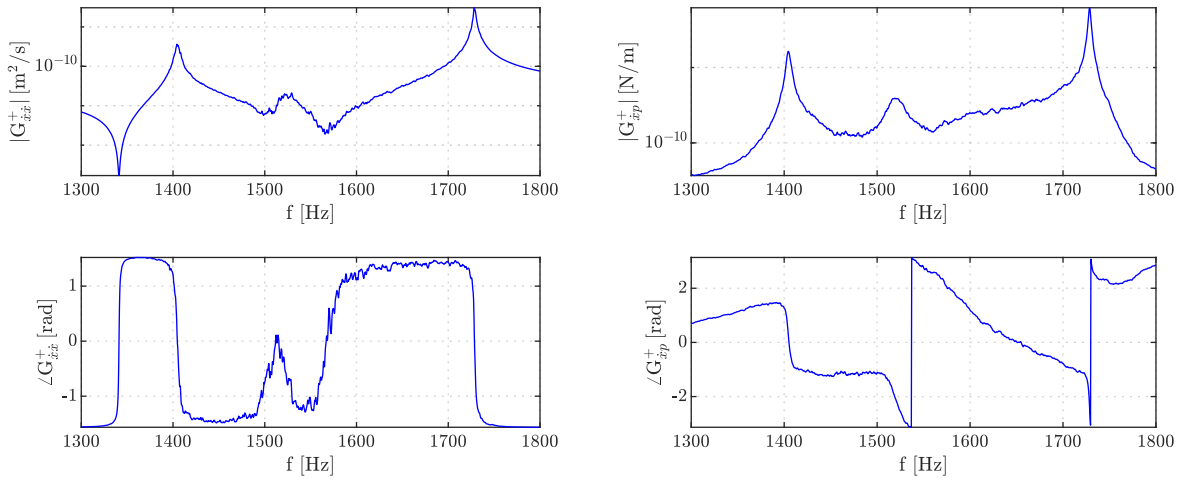

(a) OMA (b) VA-OMA

Figure 2.10: Out-of-plane testing: magnitude and phase angle of the estimated PCPs of the velocity measured at the tip of one QTF prong with respect to the structural reference (a) and to the acoustical reference (b).

From the first identification step, the two stabilization diagrams are obtained in Figure 2.11 focusing on the frequency range from 1300 to 1800 Hz. In the two cases, the stabilization diagram suggests the selection of two stable poles whose corresponding natural frequencies, damping ratios, and quality factors are collected in Table 2.3.

	Natural Frequency (Hz)		Damping Ratio (%)		Quality Factor (-)	
	OMA	VA-OMA	OMA	VA-OMA	OMA	VA-OMA
Mode 1	1405.32	1403.58	0.1557	0.1442	321.1	346.64
Mode 2	1728.53	1728.92	0.0671	0.0561	744.9	891.5

Table 2.3: Out-of-plane flexural modes identification: comparison between modal parameters from OMA and VA-OMA.

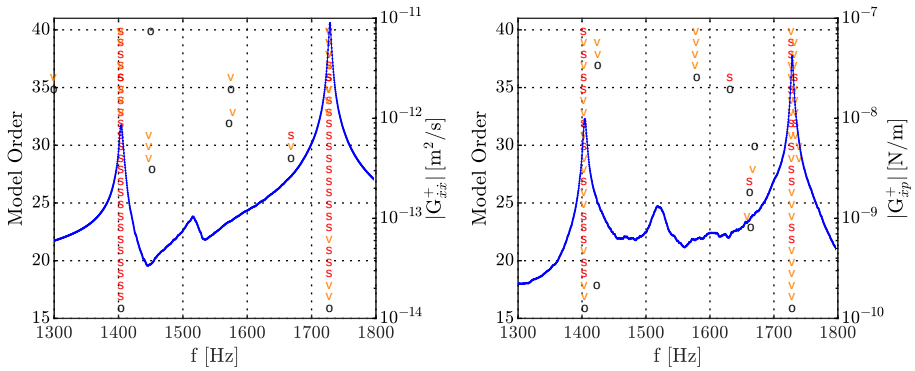

(a) OMA (b) VA-OMA

Figure 2.11: Out-of-plane flexural modes identification: stabilization diagrams along with the magnitude of the PCPs sum function, blue line, referred to the structural reference (a) and the acoustical one (b). The stable poles are indicated with '**s**' and the model order is indicated on the left ordinate axis.

Achieved poles and operational reference factors, one proceed to the MPE deploying the LSFD estimator in order to compute the unscaled mode shapes. In Figure 2.12, it is shown the mode shapes associated to the selected poles suggesting a comparison between that coming from OMA, (a, b) panels, and the ones from VA-OMA, (c, d) panels.

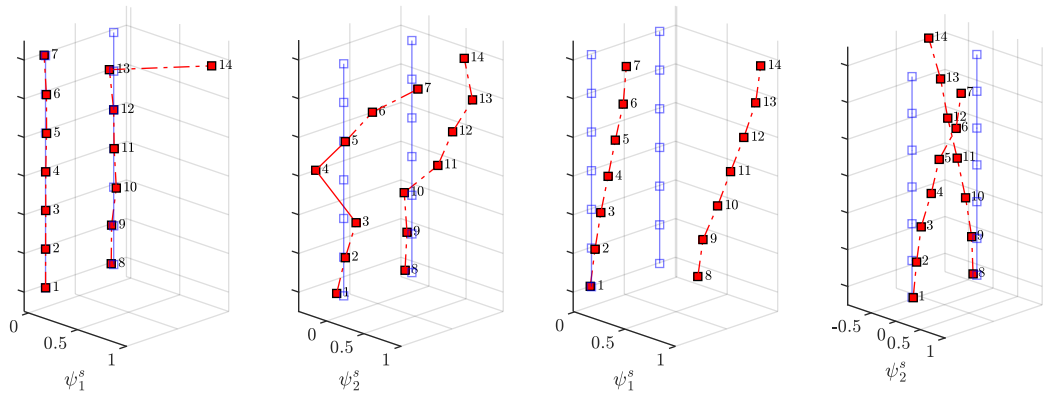

(a) OMA (b) OMA (c) VA-OMA (d) VA-OMA

Figure 2.12: Out-of-plane flexural modes identification: comparison of the mode shapes from OMA (a, b) and VA-OMA (c, d).

As previously mentioned, the OMA identification produces distorted mode shapes because

of the incorrect phase information introduced by the structural reference. For this reason, the acoustic pressure output represents a robust reference returning an accurate estimate of the mode shapes in correspondence of the fourteen structural measurement locations. Regarding the out-of-plane symmetric flexural mode shape coming from VA-OMA, an amplified deformation of points located on the right prong is observed. This discrepancy could be attributed to mass balance of the two weldings, that can be observed in the right panel of Table 2.1, which introduces a differential base compliance: this effect becomes prominent when prongs deflect in-phase. The corresponding autoMAC values are reported in Figure 2.13 for the VA-OMA set of modes showing their orthogonality.

Finally, correlation coefficient and normalized error between the synthesized PCPs and the measured ones are depicted in Figure 2.13, referring only to the VA-OMA case.

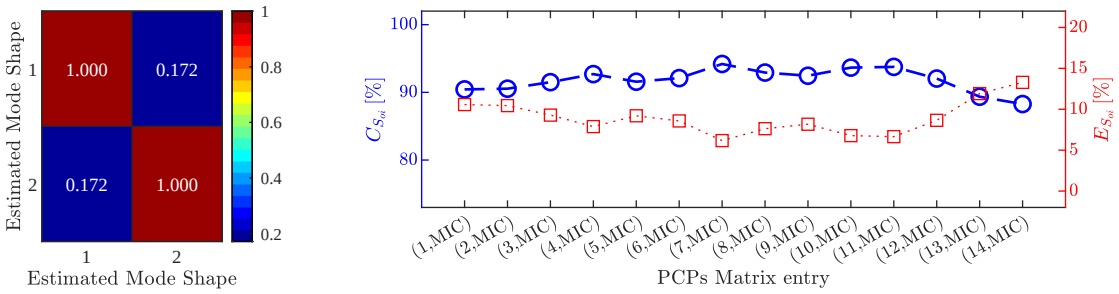

(a) (b)

Figure 2.13: Out-of-plane flexural modes identification: (a) autoMAC from the estimated modal vectors' set and (b) correlation coefficients Eq. (1.59) and normalized errors Eq. (1.60) related to the 14 PCPs used for the identification with the VA-OMA approach.

The high correlation coefficients for all the PCPs, shown in Figure 2.13, prove the goodness of the MPE process results. Error values remain lower than or equal to approximately 15%, and the correlation coefficients are higher than 85%.

In a nutshell

1. *Vibro-acoustical Operational Modal Analysis (VA-OMA) approach: a methodology to perform dynamical identification on micro-devices.*
2. *Cross-power spectra modal decomposition formulation for vibro-acoustical systems: the possibility to adopt acoustical references in the OMA context.*
3. *Vibro-acoustic setup for the experimental evaluation of a quartz tuning fork (QTF) dynamics: acoustical excitation and output-only measurement throughout a single-point LDV and a microphone to access both the acoustical and structural responses.*
4. *Modal parameter estimation based on both the acoustical and structural response measurements: identification of in-plane and out-of-plane QTF flexural modes.*

Chapter 3

Generalized OMA framework: overcoming the NExT assumption

Contents

3.1 Introduction

The NExT assumption is often valid in case of civil engineering structures like buildings, bridges, and towers because they are mainly excited by seismic micro-tremors, wind or traffic, which are faithful to the statistical description of stationary Gaussian uncorrelated white noises. By dealing with mechanical engineering structures, the operational environment could offer ambient forces which infringe classical OMA hypothesis due to the presence of harmonic components (from moving/rotating parts of the machine like gears, shafts, couplings, reciprocating piston in pumps and engines, etc.), non-white excitation [97] (e.g. forces induced on vehicles by road surface roughness [6, 11, 12, 13, 55], wind speed fluctuation, i.e. turbulence, in wind turbines [30]), the existence of temporal and/or spatial correlation between loads (as the wheelbase filtering effect in vehicle dynamics [48, 56, 145]), and time periodic effects in rotating systems [4].

These aspects can give rise to OMA methods' failures: for instance, harmonic components may be identified as spurious resonance modes (also called operational modes) or they can affect the estimation of modal parameters, especially resulting in poor damping ratio estimations. Many approaches have been proposed over the years to address this lack of description in OMA [161]: (i) statistics-driven identification of harmonics where statistical measurement known as probability density function and kurtosis are used to determine whether a peak in a spectrum is an operational or natural mode [21]; (ii) removal of harmonic components from the signal in pre-processing stage [69, 127, 128]; (iii) explicit incorporation of the harmonic component in existing OMA methods for the identification of modal parameters, assuming a prior knowledge of the harmonic frequencies [105, 106]; (iv) input spectrum independent techniques, such as the transmissibility-based OMA (TOMA) and polyreference TOMA (p-TOMA) [51, 155], which handle the problem when ambient excitation is not white. In addition, a hybrid approach using elements of both EMA and OMA was proposed by [71]

called OMAX (i.e. Operational Modal Analysis in presence of eXogenous inputs): it is based on a system model that takes both the measured and the ambient excitation into account directly to the measured signals [130, 132].

In the recent years, the development of methods aiming at overcoming the NExT assumption limitations has become a challenging topic [7, 8, 147]. Looking for a method suitable mechanical application such as vehicle systems running on a straight road with a constant speed and rotating wind turbines [149], authors started to modify the classical OMA methods to achieve specialized techniques or they introduced specific transformations as a data pre-processing aimed at extending operational modal analysis to linear, periodically time-varying systems.

Time periodic effects in wind turbines might arise due to interaction between the flow around the blade and tower or variation in the wind speed with altitude. Forward Coleman transformation (also called multi-blade coordinate transformation, MBC) or harmonic transfer function concept [144] is, for instance, applied to the data measured on the wind turbine blades, then combined with tower responses, in order to apply Operational Modal Analysis to the transformed data. Furthermore, an analytical expression for the output spectrum in terms of the modal parameters was developed and used to interpret the spectra [4]. Further to time periodic effects, the second violated assumption, dealing with wind turbine systems, concerns the nature of excitation spectrum of aerodynamic forces which is characterized by peaks at the frequency of rotor rotation and its harmonics. Besides this, the forces acting at different points of the blades are highly correlated at fundamental frequency and its harmonics [57, 166]. MBC transformation removes periodicity from the system matrix but does not help in removing periodicity from the excitation forces. Application of tone removing methods cannot be considered as a proper solution, and operational modal analysis based on transmissibility functions appears a very attractive approach due to its insensitivity to colored excitation spectra.

Analogously, the idea to perform OMA on vehicles during road tests is prevented by some other infringements of the NExT assumption. In fact, a certain correlation among the road forces acting on the wheels arises: different kinds of correlation exist which describe relation between loads on the front and the rear axle, or inputs on wheels belonging to the left and the right side [48]. This aspect, combined with typical high damped rigid body modes, make challenging the application of standard OMA algorithms. In [133], the smooth orthogonal decomposition, SOD, method is extended to the MPE of lightly damped systems, in which the inputs are time shifted functions (i.e. temporal correlated) of white noise signals. This approach has been proposed to identify the modal parameters of a vehicle during road testing, but, although the assumption of time correlated inputs is well addressed, relatively inaccurate results have been obtained owing to the drawbacks of time-domain techniques when treating highly damped systems. On the other hand, in [57] vertical accelerations of unsprung masses are used as inputs for subspace identification, giving comparably accurate results with the subspace identification method using tyre forces as inputs. Recently, a specialised modal model, referred to as the Track-Vehicle Interaction Modal Model (TVIMM), able to incorporate the character of road/rail inputs acting on vehicles during operation, is developed together with a method for determining the modal parameters of road and rail vehicles [46, 47].

The idea, behind the hereby called generalized OMA (G-OMA), consists in overcoming a number of NExT assumption infringements by including a priori known input correlation features in the OMA modal structures. In this sense, an analytical description of these effects (such as coloration, time correlation, spatial coherence, etc.) is needed and explicated in the models employed by the identification techniques. This way, it is possible to perform "ad hoc" procedures, even in case of completely violation of the classical assumption and still not measuring forces.

The rest of the chapter is organized as follows. In Section 3.2.1, the theoretical background

of G-OMA is presented regarding the modal model of the cross-correlation function. In Section 3.2.2, the discussion focuses on the modal decomposition of the output PSD matrix. In Section 3.3.1, the extended matrix fraction description, employed in a modified pLSCF solution, is established. Section 3.3 supplies the MPE strategy in the two identification steps. In Section 3.4 numerical and experimental case studies are exploited evaluating the performance of the G-OMA procedure with respect to the classical OMA approach.

3.2 Development of a no-NExT technique

3.2.1 Generalized output cross-correlation modal model

By resuming the discussion in Section 1.2 to the point in Eq. (1.16), one can consider the input correlation matrix entries generally expressed as

$$\mathbf{R}^f(\theta_2-\theta_1)=\begin{bmatrix} R^f_{11}(\theta_2-\theta_1) & \cdots & R^f_{1L}(\theta_2-\theta_1) \\ \vdots & \ddots & \vdots \\ R^f_{1L}(-\theta_2+\theta_1) & \cdots & R^f_{LL}(\theta_2-\theta_1) \end{bmatrix}, \tag{3.1}$$

leaving the possibility to include external loads departing from white noise definition and that could be affected by any kind of correlation. In this way, the matrix in Eq. (1.18) becomes a special case of Eq. (3.1). The double integral in Eq. (1.16) is, therefore, expressed as

$$J^{gl}_{nm}(T)=\int_{-\infty}^{t+T}\int_{-\infty}^{t}\mathrm{d}\theta_1\mathrm{d}\theta_2\mathrm{e}^{\lambda_n(t+T-\theta_1)}\mathrm{e}^{\lambda_m(t-\theta_2)}R^f_{gl}(\theta_2-\theta_1), \tag{3.2}$$

whose upper limits can be changed using proper Heaviside step functions as follows

$$J^{gl}_{nm}(T)=\int_{-\infty}^{+\infty}\int_{-\infty}^{+\infty}\mathrm{d}\theta_1\mathrm{d}\theta_2\mathrm{e}^{\lambda_n(t+T-\theta_1)}\mathrm{e}^{\lambda_m(t-\theta_2)}h(t+T-\theta_1)\,h(t-\theta_2)\,R^f_{gl}(\theta_2-\theta_1). \tag{3.3}$$

By supposing the change of variable $z = \theta_2 - \theta_1$, it is derived

$$J_{nm}^{gl}(T) = \int_{-\infty}^{+\infty} \mathrm{d}\theta_1 \int_{-\infty}^{+\infty} \mathrm{d}z \mathrm{e}^{\lambda_n(t+T-\theta_1)} \mathrm{e}^{\lambda_m(t-\theta_1-z)} h(t+T-\theta_1)\, h(t-\theta_1-z)\, R_{gl}^{f}(z), \quad (3.4)$$

and, by looking at the integral with respect to z, one can write

$$\int_{-\infty}^{+\infty} \mathrm{d}z \eta\kappa(t-\theta_1-z)\, R_{gl}^{f}(z) = \left(\eta\kappa * R_{gl}^{f}\right), \quad (3.5)$$

where $\eta = \mathrm{e}^{\lambda_n(t+T-\theta_1)} h(t+T-\theta_1)$ is a scalar with respect to z variable, and the convolution, indicated by $*$, of $\kappa(z) = \mathrm{e}^{\lambda_m z} h(z)$ and $R_{gl}^{f}(z)$ arises. So, the integration property of the convolution product is used in order to express Eq. (3.4) as

$$J_{nm}^{gl}(T) = \int_{-\infty}^{+\infty} \mathrm{d}\theta_1 (\eta\kappa * R_{gl}) = \left(\int_{-\infty}^{+\infty} \mathrm{d}\theta_1 \eta\kappa * R_{gl}\right)(T), \quad (3.6)$$

where the term $\eta\kappa$, in the convolution product of Eq. (3.5), can be rearranged exploiting step functions properties as

$$\begin{aligned}\eta\kappa =& \mathrm{e}^{\lambda_n(t+T-\theta_1)} \mathrm{e}^{\lambda_m(t-\theta_1)} h(t+T-\theta_1)\, h(t-\theta_1) = \\ =& \mathrm{e}^{\lambda_n(t+T-\theta_1)} \mathrm{e}^{\lambda_m(t-\theta_1)} h(t-\theta_1)\, h(T) + \mathrm{e}^{\lambda_n(t+T-\theta_1)} \mathrm{e}^{\lambda_m(t-\theta_1)} h(t+T-\theta_1)\, h(-T), \end{aligned} \quad (3.7)$$

and, by integrating with respect to θ_1 variable, it is accessed

$$\begin{aligned}\int_{-\infty}^{+\infty} \mathrm{d}\theta_1 \eta\kappa =& \mathrm{e}^{\lambda_n T} h(T)\, \mathrm{e}^{(\lambda_m+\lambda_n)t} \int_{-\infty}^{t} \mathrm{d}\theta_1 \mathrm{e}^{-(\lambda_m+\lambda_n)\theta_1} + \\ &+ \mathrm{e}^{\lambda_n T} h(-T)\, \mathrm{e}^{(\lambda_m+\lambda_n)t} \int_{-\infty}^{t+T} \mathrm{d}\theta_1 \mathrm{e}^{-(\lambda_m+\lambda_n)\theta_1} = \\ =& \mathrm{e}^{\lambda_n T} h(T)\, \mathrm{e}^{(\lambda_m+\lambda_n)t} \left[\frac{\mathrm{e}^{-(\lambda_m+\lambda_n)\theta_1}}{-\lambda_m-\lambda_n}\right]_{-\infty}^{t} + \mathrm{e}^{\lambda_n T} h(-T)\, \mathrm{e}^{(\lambda_m+\lambda_n)t} \left[\frac{\mathrm{e}^{-(\lambda_m+\lambda_n)\theta_1}}{-\lambda_m-\lambda_n}\right]_{-\infty}^{t+T}. \end{aligned} \quad (3.8)$$

Since you deal with a stable system, i.e. $\mathrm{Re}(\lambda_{n,m}) < 0$, the integral function evaluated at $t = -\infty$ tends to zero, and using some simple mathematics Eq. (3.8) becomes

$$\int_{-\infty}^{+\infty} \mathrm{d}\theta_1 \eta\kappa = \frac{\mathrm{e}^{\lambda_n T}}{-\left(\lambda_m + \lambda_n\right)} h\left(T\right) + \frac{\mathrm{e}^{-\lambda_m T}}{-\left(\lambda_m + \lambda_n\right)} h\left(-T\right), \tag{3.9}$$

which only depends on the separation time T and leads to the following solution of $J_{nm}^{gl}(T)$ integral from Eq. (3.6)

$$J_{nm}^{gl}\left(T\right) = \frac{\left(g_n * R_{gl}^{f}\right)\left(T\right)}{-\lambda_m - \lambda_n} + \frac{\left(g_m * R_{lg}^{f}\right)\left(-T\right)}{-\lambda_m - \lambda_n}, \tag{3.10}$$

where $g_n = \mathrm{e}^{\lambda_n T} h\left(T\right)$ and the relation between cross-correlation functions, $R_{gl}^{f}(T) = R_{lg}^{f}(-T)$, has been used in order to write the second term depending upon $-T$.

For the multi-input, multi-output, and multi-mode case the cross-correlation between two outputs $q_i(t)$ and $q_j(t)$ is reached by summing the different contributions

$$\begin{aligned} R_{ij}^{q}\left(T\right) &= \sum_{g=1}^{L}\sum_{l=1}^{L} R_{ig,jl}^{\tilde{q}}\left(T\right) = \sum_{n=1}^{2N}\sum_{m=1}^{2N} \frac{\psi_{in}\psi_{jm}}{m_{an}m_{am}} \sum_{g=1}^{L}\sum_{l=1}^{L} J_{nm}^{gl}\left(T\right) = \\ &= \sum_{n=1}^{2N}\sum_{m=1}^{2N} \frac{\psi_{in}\psi_{jm}}{m_{an}m_{am}} \sum_{g=1}^{L}\sum_{l=1}^{L} \frac{\left(g_m * R_{gl}^{f}\right)\left(T\right)}{-\lambda_n - \lambda_m} + \sum_{n=1}^{2N}\sum_{m=1}^{2N} \frac{\psi_{in}\psi_{jm}}{m_{an}m_{am}} \sum_{g=1}^{L}\sum_{l=1}^{L} \frac{\left(g_n * R_{lg}^{f}\right)\left(-T\right)}{-\lambda_n - \lambda_m}, \end{aligned} \tag{3.11}$$

that can be rearranged as

$$\begin{aligned} R_{ij}^{q}\left(T\right) = &\sum_{n=1}^{2N} \psi_{in}\mathrm{e}^{\lambda_n T} h(T) * \left(\sum_{g=1}^{L}\sum_{l=1}^{L} R_{gl}^{f}\left(T\right) \frac{\psi_{gn}}{m_{an}} \sum_{m=1}^{2N} \frac{\psi_{lm}}{m_{am}(-\lambda_n - \lambda_m)} \psi_{jm} \right) + \\ &+ \sum_{m=1}^{2N} \left(\sum_{g=1}^{L}\sum_{l=1}^{L} R_{lg}^{f}\left(-T\right) \frac{\psi_{lm}}{m_{am}} \sum_{n=1}^{2N} \frac{\psi_{gn}}{m_{an}(-\lambda_n - \lambda_m)} \psi_{in} \right) * \mathrm{e}^{-\lambda_m T} h(-T) \psi_{jm}. \end{aligned} \tag{3.12}$$

Finally, the whole output correlation matrix $\mathbf{R}^q(T) \in \mathbb{R}^{N\times N}$ is written as

$$\begin{aligned}\mathbf{R}^q\left(T\right) = &\sum_{n=1}^{2N} \boldsymbol{\psi}_n \mathrm{e}^{\lambda_n T} h\left(T\right) * \left(\sum_{g=1}^{L}\sum_{l=1}^{L} R_{gl}^f\left(T\right) \boldsymbol{g}_n^{gl^{\mathrm{T}}}\right) + \\ &+ \sum_{n=1}^{2N} \left(\sum_{g=1}^{L}\sum_{l=1}^{L} R_{lg}^f\left(-T\right) \boldsymbol{g}_n^{lg}\right) * \mathrm{e}^{-\lambda_n T} h\left(-T\right) \boldsymbol{\psi}_n^{\mathrm{T}},\end{aligned} \tag{3.13}$$

where

$$\boldsymbol{g}_n^{gl} = \frac{\psi_{gn}}{m_{an}} \sum_{m=1}^{2N} \frac{\psi_{lm}}{m_{am}\left(-\lambda_n - \lambda_m\right)} \boldsymbol{\psi}_m, \tag{3.14}$$

is the extended operational reference vector referred to the generic input correlation matrix entry $R_{gl}^f(T)$. One can also embed vectors in Eq. (3.14) defining the time-lag dependent operational vectors (τ-ORV), which can be considered a generalized version of the classical ORV, here written as

$$\boldsymbol{\rho}_n\left(T\right) = \sum_{g=1}^{L}\sum_{l=1}^{L} R_{gl}^f\left(T\right) \boldsymbol{g}_n^{gl}. \tag{3.15}$$

So, the output correlation matrix in Eq. (3.13) is generally indicated as

$$\mathbf{R}^q\left(T\right) = \sum_{n=1}^{2N} \boldsymbol{\psi}_n \mathrm{e}^{\lambda_n T} h\left(T\right) * \boldsymbol{\rho}_n\left(T\right)^{\mathrm{T}} + \boldsymbol{\rho}_n\left(-T\right) * \mathrm{e}^{-\lambda_n T} h\left(-T\right) \boldsymbol{\psi}_n^{\mathrm{T}}, \tag{3.16}$$

and it is called generalized modal model because of the general definition of the input correlation matrix in Eq. (3.1) which allows the modal model to take into account effects such as coloured noises and temporal or spatial correlation between forces. This becomes possible because of the particularized concept of time-lag dependent operational vectors, Eq. (3.15), which collects information about $\mathbf{R}^f(T)$ matrix together with some modal characteristic of the system.

As previously mentioned, the NExT techniques consider the special case of matrix in Eq. (3.1) shown in Eq. (1.18). Substituting this expression in Eq. (3.15) and Eq. (3.16), you

can write

$$\mathbf{R}^{q}\left(T\right)=\sum_{n=1}^{2N}\boldsymbol{\psi}_{n}\boldsymbol{\rho}_{n}^{\mathrm{T}}\mathrm{e}^{\lambda_{n}T}h\left(T\right)+\boldsymbol{\rho}_{n}\boldsymbol{\psi}_{n}^{\mathrm{T}}\mathrm{e}^{-\lambda_{n}T}h\left(-T\right), \tag{3.17}$$

where the Dirac-delta function is the identity for convolution and time-lag dependent operational reference vector collapses in its classical time-independent expression

$$\boldsymbol{\rho}_{n}=\sum_{l=1}^{L}\alpha_{l}\boldsymbol{g}_{n}^{ll}, \tag{3.18}$$

which contains unknown input information, α_i, combined with system scaling factors leaving mode shapes unscaled. Eq. (3.17) is the classical modal model of the output correlation matrix [142] which is a special case of Eq. (3.16). This last is called generalized modal model exploiting the concept of τ-ORV where input correlation matrix entries have a general expression. Forces remain unmeasured but one has the possibility to take into account an a-priori known model of the correlation between external loads.

3.2.2 Generalized output PSD modal model

Analogously to the case of cross-correlation functions and without making any assumption on the particular structure of $\mathbf{S}^{f}(\mathrm{i}\omega)$, the output PSD matrix of Eq. (1.26) can be written in partial fraction by means of the following decomposition [119]

$$\mathbf{S}^{q}\left(\mathrm{i}\omega\right)=\sum_{n=1}^{2N}\frac{\mathbf{R}_{n}^{+}(\mathrm{i}\omega)}{\mathrm{i}\omega-\lambda_{n}}+\frac{\mathbf{R}_{n}^{-}(\mathrm{i}\omega)}{-\mathrm{i}\omega-\lambda_{n}}, \tag{3.19}$$

where the residue referred to the n-th pole is expressed by

$$\mathbf{R}_{n}^{+}(\mathrm{i}\omega)=\boldsymbol{\psi}_{n}\boldsymbol{\rho}_{n}(\mathrm{i}\omega)^{\mathrm{T}}, \tag{3.20}$$

in which the vector $\boldsymbol{\rho}_n(\mathrm{i}\omega)^{\mathrm{T}}$, as well as the Fourier transform of the τ-ORF, is defined as

$$\begin{aligned}\boldsymbol{\rho}_n(\mathrm{i}\omega)^{\mathrm{T}} &= \boldsymbol{L}_n^{\mathrm{T}}\mathbf{S}^f(\mathrm{i}\omega)\left(\sum_{s=1}^{2N}\frac{\boldsymbol{L}_s\boldsymbol{\psi}_s^{\mathrm{T}}}{-\lambda_n-\lambda_s}\right) = \\ &= \sum_{s=1}^{2N}\boldsymbol{L}_n^{\mathrm{T}}\mathbf{S}^f(\mathrm{i}\omega)\frac{\boldsymbol{L}_s\boldsymbol{\psi}_s^{\mathrm{T}}}{-\lambda_n-\lambda_s} = \sum_{s=1}^{2N}\frac{\sum_{g=1}^{L}L_{g,n}\sum_{l=1}^{L}S_{gl}^f(\mathrm{i}\omega)L_{l,s}}{-\lambda_n-\lambda_s}\boldsymbol{\psi}_s^{\mathrm{T}} = \sum_{g=1}^{L}\sum_{l=1}^{L}S_{gl}^f(\mathrm{i}\omega)\,\boldsymbol{g}_n^{gl^{\mathrm{T}}},\end{aligned} \tag{3.21}$$

where the extended operational reference vector $\boldsymbol{g}_n^{gl}$, related to the input correlation matrix entry $S_{gl}^f(\mathrm{i}\omega)$, occurs again as

$$\boldsymbol{g}_n^{gl} = L_{g,n}\sum_{s=1}^{2N}\frac{L_{l,s}}{-\lambda_n-\lambda_s}\boldsymbol{\psi}_s, \tag{3.22}$$

that is the same vector defined in Eq. (3.14) where the modal participation vector components are expounded. Analogously, you notice that

$$\begin{aligned}\mathbf{R}_n^-(\mathrm{i}\omega) &= \left(\sum_{s=1}^{2N}\frac{\boldsymbol{\psi}_s\boldsymbol{L}_s^{\mathrm{T}}}{-\lambda_n-\lambda_s}\right)\mathbf{S}^f(\mathrm{i}\omega)\,\boldsymbol{L}_n\boldsymbol{\psi}_n^{\mathrm{T}} = \\ &= \left(\sum_{s=1}^{2N}\boldsymbol{\psi}_s\frac{\sum_{g=1}^{L}L_{g,s}\sum_{l=1}^{L}S_{gl}^f(\mathrm{i}\omega)L_{l,n}}{-\lambda_n-\lambda_s}\right)\boldsymbol{\psi}_n^{\mathrm{T}} = \\ &= \left(\sum_{g=1}^{L}\sum_{l=1}^{L}S_{lg}^f(-\mathrm{i}\omega)L_{l,n}\sum_{s=1}^{2N}\frac{L_{g,s}}{-\lambda_n-\lambda_s}\boldsymbol{\psi}_s\right)\boldsymbol{\psi}_n^{\mathrm{T}} = \\ &= \left(\sum_{l=1}^{L}\sum_{g=1}^{L}S_{lg}^f(-\mathrm{i}\omega)\,\boldsymbol{g}_n^{lg}\right)\boldsymbol{\psi}_n^{\mathrm{T}} = \boldsymbol{\rho}_n(-\mathrm{i}\omega)\,\boldsymbol{\psi}_n^{\mathrm{T}},\end{aligned} \tag{3.23}$$

and thus Eq. (3.19) can be written as

$$\mathbf{S}^q(\mathrm{i}\omega) = \sum_{n=1}^{2N}\frac{\boldsymbol{\psi}_n\boldsymbol{\rho}_n(\mathrm{i}\omega)^{\mathrm{T}}}{\mathrm{i}\omega-\lambda_n} + \frac{\boldsymbol{\rho}_n(-\mathrm{i}\omega)\,\boldsymbol{\psi}_n^{\mathrm{T}}}{-\mathrm{i}\omega-\lambda_n}, \tag{3.24}$$

which is related to the modal model in Eq. (3.16) by the Fourier transform integral. In the following, $\boldsymbol{g}_n^{gl}$ is referred to as the extended operational reference vectors (eORV) related to the r-th pole and the gl-th entry of matrix $\mathbf{S}^f(\mathrm{i}\omega)$, while $\boldsymbol{\rho}_n(\mathrm{i}\omega)$ is called frequency dependent ORV (ω-ORV). Similar to the classical operational reference factors, these quantities do not represent a scale factor for the modal shape. The modal decomposition in Eq. (3.24) can be called the generalized PSD modal model. Differently from the classical PSD modal model, the dependency on the input PSD functions is clarified and no assumptions about the inputs are used to achieve the formulation.

As shown before for the output correlation matrix $\mathbf{R}^q(T)$, the classical PSD modal model is derived imposing input matrix correlation $\mathbf{S}^f(\mathrm{i}\omega)$ to be

$$\mathbf{S}^f(\mathrm{i}\omega) = \begin{bmatrix} S_1 & \cdots & 0 \\ \vdots & \ddots & \vdots \\ 0 & \cdots & S_L \end{bmatrix}, \tag{3.25}$$

where S_l is a real-valued constant. Substituting this expression in Eq. (3.24), one collapses to the definition of the well-known operational reference factors

$$\boldsymbol{\rho}_n = \sum_{l=1}^{L} S_l \boldsymbol{g}_n^{ll}, \tag{3.26}$$

and so the modal decomposition is derived

$$\mathbf{S}^q(\mathrm{i}\omega) = \sum_{n=1}^{2N} \frac{\boldsymbol{\psi}_n \boldsymbol{\rho}_n^{\mathrm{T}}}{\mathrm{i}\omega - \lambda_n} + \frac{\boldsymbol{\rho}_n \boldsymbol{\psi}_n^{\mathrm{T}}}{-\mathrm{i}\omega - \lambda_n}, \tag{3.27}$$

as a special case of the generalized PSD modal model where the ORF are a combination of input and modal parameters.

3.3 Modal parameter estimation: a two step approach

3.3.1 Extended Left Matrix Fraction Description

In the previous section, the modal decomposition of the output PSD matrix is derived referring to a linear, time-invariant, damped, vibrating system having N dofs and subjected to L external forces. If you generalize to the the multi-input, multi-output, and multi-mode case, Eq. (3.24) can be written into matrix notation as

$$\mathbf{S}^q(\mathrm{i}\omega) = \boldsymbol{\Psi}(\mathrm{i}\omega\mathbf{I} - \boldsymbol{\Lambda})^{-1}\mathbf{P}(\mathrm{i}\omega)^{\mathrm{T}} + \mathbf{P}(-\mathrm{i}\omega)(-\mathrm{i}\omega\mathbf{I} - \boldsymbol{\Lambda})^{-1}\boldsymbol{\Psi}^{\mathrm{T}}, \tag{3.28}$$

where $\mathbf{S}^q(\omega) \in \mathbb{C}^{o\times r}$ relates o outputs and r references, $\boldsymbol{\Lambda} \in \mathbb{C}^{2N_p\times 2N_p}$ is a diagonal matrix, containing the $2N_p$ complex conjugate system poles λ_n in the frequency band of interest, while $\boldsymbol{\Psi} \in \mathbb{C}^{o\times 2N_p}$ collects the mode shape vectors and $\mathbf{P}(\mathrm{i}\omega) \in \mathbb{C}^{r\times 2N_p}$ gathers together the ω-ORV being

$$\mathbf{P}(\mathrm{i}\omega) = \sum_{g=1}^{L}\sum_{l=1}^{L} S_{gl}^f(\mathrm{i}\omega)\,\mathbf{G}_{gl}, \tag{3.29}$$

with the $2N_p$ eORV collected in $\mathbf{G}_{gl} \in \mathbb{C}^{r\times 2N_p}$. The output PSD matrix is considered as $\mathbf{S}^q(\mathrm{i}\omega) = \tilde{\mathbf{S}}^q(\mathrm{i}\omega) + \tilde{\mathbf{S}}^q(\mathrm{i}\omega)^{\mathrm{H}}$, where $\tilde{\mathbf{S}}^q(\mathrm{i}\omega)$ indicates the part of the PSDs related to stable poles

$$\tilde{\mathbf{S}}^q(\mathrm{i}\omega) = \boldsymbol{\Psi}(\mathrm{i}\omega\mathbf{I} - \boldsymbol{\Lambda})^{-1}\sum_{g=1}^{L}\sum_{l=1}^{L} S_{gl}^f(\mathrm{i}\omega)\,\mathbf{G}_{gl}{}^{\mathrm{T}}. \tag{3.30}$$

In order to introduce a matrix fraction description of $\mathbf{S}^q(\omega)$, the well-known input-output relationship is considered in the Fourier domain ω

$$\mathbf{Q}(\omega) = \mathbf{B}(\omega)^{-1}\mathbf{F}(\omega) = \mathbf{H}(\omega)\mathbf{F}(\omega), \tag{3.31}$$

in which $\mathbf{B}(\omega)$ and $\mathbf{H}(\omega) \in \mathbb{C}^{o\times L}$ are respectively the dynamic stiffness and the FRF matrices

relating the displacement $\mathbf{Q}(\omega) \in \mathbb{C}^{o\times 1}$ and force $\mathbf{F}(\omega) \in \mathbb{C}^{L\times 1}$ vectors. Hence, the generic i-component of the displacement vector is

$$Q_i(\omega) = \sum_{g=1}^{L} H_{ig}(\omega)F_g(\omega) = \sum_{g=1}^{L} \frac{\bar{B}_{ig}(\omega)}{\det \mathbf{B}(\omega)} F_g(\omega) = \frac{\sum_{g=1}^{L} N_{ig}(\omega)F_g(\omega)}{D(\omega)}, \tag{3.32}$$

where $\bar{\mathbf{B}}(\omega) = \text{adj}(\mathbf{B}(\omega))$ indicates the classical adjoint of the dynamic stiffness matrix whose il-entry is generally expressed as a polynomial $N_{il}(\omega)$, $\det \mathbf{B}(\omega)$ is the determinant operator which defines the characteristic polynomial $D(\omega)$ of the system. Eq.(3.32) represents the so-called common denominator model which uses rational functions to relate an N-dimensional displacement vector to an L-dimensional force vector. As an alternative general representation of Eq.(3.32), in [109] the authors propose the autoregressive with exogenous excitation, ARX, model represented by

$$\mathbf{A}(d)\boldsymbol{q}(t) = \mathbf{B}(d)\boldsymbol{f}(t), \tag{3.33}$$

where the presence of unmeasured disturbances is neglected, and where the autoregressive AR, $\mathbf{A}(d)$, and exogenous X, $\mathbf{B}(d)$, matrices are respectively

$$\mathbf{A}(d) = \mathbf{I}_o + \mathbf{A}_1 d + \cdots + \mathbf{A}_{na} d^{na} \in \mathbb{R}^{o\times o}, \tag{3.34}$$

$$\mathbf{B}(d) = \mathbf{B}_0 + \mathbf{B}_1 d + \cdots + \mathbf{B}_{nb} d^{nb} \in \mathbb{R}^{o\times L}, \tag{3.35}$$

with d indicating the backshift operator, $\mathbf{I}_o$ indicates the identity matrix of order o, na and nb are the orders of polynomial elements of AR, and X matrices. A diagonal structure, $\mathbf{A}(d) = \text{diag}(A_{11}(d)\cdots A_{ii}(d)\cdots A_{oo}(d))$, is imposed on the AR matrix [109, 113]. The equivalent matrix polynomial model in the frequency domain is derived by taking the z-transform of Eq. (3.33) as

$$\mathbf{A}(k)\mathbf{Q}(\omega_k) = \mathbf{B}(k)\mathbf{F}(\omega_k), \tag{3.36}$$

where $\mathbf{A}(k) = \sum_{r=0}^{na} z_k^{-r}\mathbf{a}_r$, $\mathbf{B}(k) = \sum_{r=0}^{nb} z_k^{-r}\mathbf{b}_r$, with $\mathbf{a}_r \in \mathbb{R}^{o\times o}$ and $\mathbf{b}_r \in \mathbb{R}^{o\times L}$ real-valued coefficient matrices, and the z-domain orthogonal polynomials z_k defined as $z_k = \mathrm{e}^{\mathrm{i}2\pi k/N_s}$, N_s is the number of samples. The i-th multiple-input single-output (MISO) ARX model extracted from Eq. (3.36) is

$$A_{ii}(k)Q_i(\omega_k) = \sum_{g=1}^{L} B_{ig}(k)F_g(\omega_k), \tag{3.37}$$

and by defining the PSD function between two generic outputs according to $S_{ij}^q(\omega_k) = \mathrm{E}\left[Q_i(\omega_k)Q_j^*(\omega_k)\right]$ [10], its relevant ARX model is achieved using Eq. (3.37)

$$A_{ii}(k)A_{jj}^*(k)\mathrm{E}\left[Q_i(\omega_k)Q_j^*(\omega_k)\right] = \sum_{g=1}^{L}\sum_{l=1}^{L} B_{ig}(k)B_{jl}^*(k)\mathrm{E}\left[F_g(\omega_k)F_l^*(\omega_k)\right], \tag{3.38}$$

where polynomial functions can be carried out of the expected value operator, due to their deterministic nature. In Eq. (3.38) the PSD definition is exploited and the polynomial product is performed in order to write

$$D_{ij}(k)S_{ij}^q(\omega_k) = \sum_{g=1}^{L}\sum_{l=1}^{L} N_{ij}^{gl}(k)S_{gl}^f(\omega_k) = N_{ij}^{(e)}(k), \tag{3.39}$$

where [136]

$$D_{ij}(k) = A_{ii}(k)A_{jj}^*(k) = \sum_{r=0}^{2na} z_k^{-r}\left(\sum_{m=0}^{r}(-1)^m a_{ii,m}a_{jj,r-m}\right) = \sum_{r=0}^{p} z_k^{-r}\alpha_{ij,r} \tag{3.40}$$

$$N_{ij}^{gl}(k) = B_{ig}(k)B_{jl}^*(k) = \sum_{r=0}^{2nb} z_k^{-r}\left(\sum_{m=0}^{r}(-1)^m b_{ij,m}b_{jl,r-m}\right) = \sum_{r=0}^{p} z_k^{-r}\beta_{ij,r}^{gl}, \tag{3.41}$$

with $p = 2na = 2nb$ as polynomial order, that results in an extended left matrix fraction

description (eLMFD) when referred to the whole output PSD matrix $\mathbf{S}_q(k)$

$$\mathbf{S}^q(\omega_k) = \mathbf{D}(k)^{-1}\mathbf{N}^{(e)}(k), \tag{3.42}$$

with $\mathbf{N}^{(e)}(k) = \sum_{g=1}^{L}\sum_{l=1}^{L} S_{gl}^f(\omega_k)\mathbf{N}^{gl}(k) \in \mathbb{C}^{o\times r}$ here called extended fitting polynomial numerator matrix and $\mathbf{D}(k) \in \mathbb{C}^{o\times o}$ the denominator matrix, whose coefficient matrices $\boldsymbol{\alpha}_p$ and $\boldsymbol{\beta}_p^{gl}$ represent the parameters to be estimated. Specifically, $\mathbf{N}^{(e)}(k)$ definition incorporates several a-priori known features resulting from loads which explicitly violate the NExT assumption, such as coloured noises, time and spatial correlation among multiple inputs, presence of deterministic loads such as harmonics. One can easily demonstrate how the description in Eq. (3.42) collapses in the classical LMFD description [131] by imposing the associated to the NExT hypothesis. In this latter case, the numerator matrix can be written as

$$\mathbf{N}^{(e)}(k) = \sum_{g=1}^{L} S_{gg}^f \sum_{r=0}^{p} z_k^{-r}\boldsymbol{\beta}_r^{gg} = \sum_{r=0}^{p} z_k^{-r}\sum_{g=0}^{L} S_{gg}^f\boldsymbol{\beta}_r^{gg} = \sum_{r=0}^{p} z_k^{-r}\bar{\boldsymbol{\beta}}_r, \tag{3.43}$$

which corresponds to the single polynomial matrix of Eq. (1.35).

3.3.2 Polyreference Least Squares Complex Frequency

The polynomial coefficient estimation problem of Eq. (3.42) can be solved, in a Least-Square sense, with the poly-reference version of the LSCF estimator that differs from the classical one [73] because of the particular matrix description which includes the definition of an extended fitting polynomial numerator matrix $\mathbf{N}^{(e)}(\omega_k)$. The left MFD is chosen because it considers all r references simultaneously [32], hence, it allows to estimate both system poles and mode shape vectors directly by solving the eigenproblem of the companion matrix associated to the denominator polynomial (as it will be shown in the following). The nonlinear least-squares problem, emerging from Eq. (3.42), can be approximated by a sub-optimal

linear one based on the equation error

$$\boldsymbol{\eta}(\boldsymbol{\beta}^{(e)}, \boldsymbol{\alpha}, \omega_k) = \mathbf{N}^{(e)}(\boldsymbol{\beta}^{(e)}, k) - \mathbf{D}(\boldsymbol{\alpha}, k)\mathbf{S}^q(\omega_k) = \\ = \sum_{g=1}^{L}\sum_{l=1}^{L}\left(\sum_{r=0}^{p} z_k^{-r}\boldsymbol{\beta}_r^{gl}\right) S_{gl}^f(\omega_k) - \left(\sum_{r=0}^{p} z_k^{-r}\boldsymbol{\alpha}_r\right)\mathbf{S}^q(\omega_k), \tag{3.44}$$

with the unknowns $\boldsymbol{\beta}^{(e)} = \begin{pmatrix} \boldsymbol{\beta}_0^{11} & \dots & \boldsymbol{\beta}_p^{11} & \boldsymbol{\beta}_0^{12} & \dots & \boldsymbol{\beta}_p^{12} & \dots & \boldsymbol{\beta}_0^{LL} & \dots & \boldsymbol{\beta}_p^{LL} \end{pmatrix}^{\mathrm{T}} \in \mathbb{R}^{(p+1)L^2 r \times o}$ and $\boldsymbol{\alpha} = \begin{pmatrix} \boldsymbol{\alpha}_0 & \dots & \boldsymbol{\alpha}_p \end{pmatrix}^{\mathrm{T}} \in \mathbb{R}^{(p+1)o \times o}$, where some input features, regarding the input PSD matrix $\mathbf{S}^f(\omega)$, are included as a priori known in the error matrix definition. The error $\boldsymbol{\eta}(\boldsymbol{\beta}^{(e)}, \boldsymbol{\alpha}, \omega_k)$, defined in Eq. (3.44), is extended for all the N_f frequency lines, reformulating in matrix notation as

$$\boldsymbol{\eta}\left(\boldsymbol{\beta}^{(e)}, \boldsymbol{\alpha}\right) = \begin{pmatrix} \boldsymbol{\eta}\left(\omega_1, \boldsymbol{\beta}^{(e)}, \boldsymbol{\alpha}\right) \\ \vdots \\ \boldsymbol{\eta}\left(\omega_{N_f}, \boldsymbol{\beta}^{(e)}, \boldsymbol{\alpha}\right) \end{pmatrix} = \begin{bmatrix} \mathbf{X}^{(e)} & \boldsymbol{\upsilon} \end{bmatrix} \begin{bmatrix} \boldsymbol{\beta}^{(e)} \\ \boldsymbol{\alpha} \end{bmatrix}, \tag{3.45}$$

where the two matrices, $\mathbf{X}^{(e)}$ and $\boldsymbol{\upsilon}$, are given by

$$\mathbf{X}^{(e)} = \begin{bmatrix} \left(\begin{bmatrix} z_1^0 & \dots & z_1^{-p} \end{bmatrix} \otimes \mathbf{I}_r\right) \otimes \begin{bmatrix} S_{11}^f(\omega_1) & \dots & S_{LL}^f(\omega_1) \end{bmatrix} \\ \vdots \\ \left(\begin{bmatrix} z_{N_f}^0 & \dots & z_{N_f}^{-p} \end{bmatrix} \otimes \mathbf{I}_r\right) \otimes \begin{bmatrix} S_{11}^f(\omega_{N_f}) & \dots & S_{LL}^f(\omega_{N_f}) \end{bmatrix} \end{bmatrix} \in \mathbb{C}^{N_f r \times (p+1)L^2 r}, \tag{3.46}$$

$$\boldsymbol{\upsilon} = \begin{bmatrix} -\begin{bmatrix} z_1^0 & \dots & z_1^{-p} \end{bmatrix} \otimes \mathbf{S}^{q\mathrm{T}}(\omega_1) \\ \vdots \\ -\begin{bmatrix} z_{N_f}^0 & \dots & z_{N_f}^{-p} \end{bmatrix} \otimes \mathbf{S}^{q\mathrm{T}}(\omega_{N_f}) \end{bmatrix} \in \mathbb{C}^{N_f r \times (p+1)o}, \tag{3.47}$$

with $\otimes$ denoting the Kronecker product. The following cost function can be formulated based on the linearised error matrix in Eq. (3.45) as

$$\boldsymbol{l}\left(\boldsymbol{\beta}^{(e)},\boldsymbol{\alpha}\right)=\mathrm{tr}\left[\boldsymbol{\eta}^{\mathrm{H}}\left(\boldsymbol{\beta}^{(e)},\boldsymbol{\alpha}\right)\boldsymbol{\eta}\left(\boldsymbol{\beta}^{(e)},\boldsymbol{\alpha}\right)\right]=\mathrm{tr}\left[\begin{bmatrix}\boldsymbol{\beta}^{(e)}\\ \boldsymbol{\alpha}\end{bmatrix}^{\mathrm{T}}\mathrm{Re}\left(\mathbf{J}^{\mathrm{H}}\mathbf{J}\right)\begin{bmatrix}\boldsymbol{\beta}^{(e)}\\ \boldsymbol{\alpha}\end{bmatrix}\right], \tag{3.48}$$

whose minimization with respect to the unknown matrix coefficients, $\boldsymbol{\beta}^{(e)}$ and $\boldsymbol{\alpha}$, consists of the solution of the following so-called normal equations [122]

$$\mathrm{Re}\left[\mathbf{J}^{\mathrm{H}}\mathbf{J}\right]\begin{pmatrix}\boldsymbol{\beta}^{(e)}\\ \boldsymbol{\alpha}\end{pmatrix}=\begin{cases}\mathbf{R}\boldsymbol{\beta}^{(e)}+\boldsymbol{\Upsilon}\boldsymbol{\alpha}=\mathbf{0}\\ \boldsymbol{\Upsilon}^{\mathrm{T}}\boldsymbol{\beta}^{(e)}+\mathbf{T}\boldsymbol{\alpha}=\mathbf{0}\end{cases}, \tag{3.49}$$

with $\mathbf{J}$ the Jacobian matrix, $\mathbf{R}$,$\boldsymbol{\Upsilon}$ and $\mathbf{T}$ defined as

$$\mathbf{R}=\mathrm{Re}\left[\left(\mathbf{X}^{(e)}\right)^{\mathrm{H}}\mathbf{X}^{(e)}\right]\in\mathbb{R}^{(p+1)L^2r\times(p+1)L^2r}, \tag{3.50}$$

$$\boldsymbol{\Upsilon}=\mathrm{Re}\left[\left(\mathbf{X}^{(e)}\right)^{\mathrm{H}}\boldsymbol{\upsilon}\right]\in\mathbb{R}^{(p+1)L^2r\times(p+1)o}, \tag{3.51}$$

$$\mathbf{T}=\mathrm{Re}\left[\boldsymbol{\upsilon}^{\mathrm{H}}\boldsymbol{\upsilon}\right]\in\mathbb{R}^{(p+1)o\times(p+1)o}. \tag{3.52}$$

The computational effort of the solution of equation Eq. (3.49) is further reduced considering the reduced normal equations, obtained by replacing $\boldsymbol{\beta}^{(e)}$ with $-\mathbf{R}^{-1}\boldsymbol{\Upsilon}\boldsymbol{\alpha}$ in the second equation as

$$\left(-\boldsymbol{\Upsilon}^{\mathrm{T}}\mathbf{R}^{-1}\boldsymbol{\Upsilon}+\mathbf{T}\right)\boldsymbol{\alpha}=\mathbf{M}\boldsymbol{\alpha}=\mathbf{0}, \tag{3.53}$$

where the size of $\mathbf{M}$ is $(p+1)o$ resulting much smaller than the size of $\mathrm{Re}\left[\mathbf{J}^{\mathrm{H}}\mathbf{J}\right]$. The typical constraint, $\boldsymbol{\alpha}_p=\mathbf{I}_o$ [34], is imposed in order to remove parameter redundancy of the extended LMFD [126], and also to avoid trivial solution $\boldsymbol{\alpha}=\mathbf{0}$.

From the knowledge of the denominator matrix coefficients one can compute the poles and corresponding mode shape vectors by performing the eigenvalue decomposition of the

so-called companion matrix which finds its definition in the following section about state space realization of the system described by the transfer function matrix $\mathbf{S}^q(\omega)$.

3.3.3 Conversion into a state-space description

In order to perform modal parameter estimation, you need to develop a state-space realization [54] of the transfer matrix $\mathbf{S}^q(\omega)$, modeled by the eLMFD in Eq. (3.42) whose coefficients can be calculated with the pLSCF algorithm previously described. In fact, by recalling the matrix polynomial description of the output PSD matrix as

$$\mathbf{S}^q(\omega) = \left(\sum_{r=0}^{p} z_k^{-r}\boldsymbol{\alpha}_r\right)^{-1}\left(\sum_{g=1}^{L}\sum_{l=1}^{L} S_{gl}^f(\omega)\sum_{r=0}^{p} z_k^{-r}\boldsymbol{\beta}_r^{gl}\right), \tag{3.54}$$

the state-space equation system, represented by the transfer matrix $\mathbf{S}^q(\omega)$ which relates the system output $\mathbf{y}(t) \in \mathbb{R}^{o\times 1}$ with the input $\mathbf{u}(t) \in \mathbb{R}^{r\times 1}$, is needed. Firstly, the state variable vector $\mathbf{x}(t) \in \mathbb{R}^{po\times 1}$ is defined

$$\mathbf{x}(t) = \begin{Bmatrix} \mathbf{q}(t) \\ \vdots \\ \mathbf{q}^{(p-1)}(t) \end{Bmatrix}, \tag{3.55}$$

where $\mathbf{q}^{(i)}(t) \in \mathbb{R}^{o\times 1}$ is the i-th time derivative of the displacement vector $\mathbf{q}(t)$. At this stage, the Observable Canonical Realization (OCR) of $\mathbf{S}^q(\omega)$, described by to the generic p-th order polynomial MFD of Eq. (3.54), is performed into the following state equations

$$\begin{cases} \dot{\mathbf{x}}(t) = \begin{bmatrix} \mathbf{0} & \mathbf{0} & \cdots & \mathbf{0} & -\boldsymbol{\alpha}_0 \\ \mathbf{I} & \mathbf{0} & \cdots & \mathbf{0} & -\boldsymbol{\alpha}_1 \\ \vdots & \vdots & & \vdots & \vdots \\ \mathbf{0} & \mathbf{0} & \cdots & \mathbf{I} & -\boldsymbol{\alpha}_{p-1} \end{bmatrix}\mathbf{x}(t) + \sum_{g=1}^{L}\sum_{l=1}^{L} R_{gl}^f(t) * \begin{bmatrix} \boldsymbol{\beta}_0^{gl} - \boldsymbol{\alpha}_0\boldsymbol{\beta}_p^{gl} \\ \vdots \\ \boldsymbol{\beta}_{p-1}^{gl} - \boldsymbol{\alpha}_{p-1}\boldsymbol{\beta}_p^{gl} \end{bmatrix}\mathbf{u}(t) \\ \mathbf{y}(t) = \begin{bmatrix} \mathbf{0} & \cdots & \mathbf{I}_o \end{bmatrix}\mathbf{x}(t) + \sum_{g=1}^{L}\sum_{l=1}^{L} R_{gl}^f(t) * \boldsymbol{\beta}_p^{gl}\mathbf{u}(t) \end{cases}, \tag{3.56}$$

that could be compactly written in the frequency domain as

$$\begin{cases} z_k\mathbf{X}(k) = \bar{\mathbf{A}}\mathbf{X}(k) + \sum_{g=1}^{L}\sum_{l=1}^{L} S_{gl}^{f}(\omega_k)\,\bar{\mathbf{B}}^{gl}\mathbf{U}(k) \\ \mathbf{Y}(k) = \bar{\mathbf{C}}\mathbf{X}(k) + \sum_{g=1}^{L}\sum_{l=1}^{L} S_{gl}^{f}(\omega_k)\,\bar{\mathbf{D}}^{gl}\mathbf{U}(k) \end{cases}, \tag{3.57}$$

where the four discrete-time system matrices $\bar{\mathbf{A}} \in \mathbb{R}^{po\times po}$, $\bar{\mathbf{B}}^{gl} \in \mathbb{R}^{po\times r}$, $\bar{\mathbf{C}} \in \mathbb{R}^{o\times po}$, and $\bar{\mathbf{D}}^{gl} \in \mathbb{R}^{o\times r}$ need to be converted into the continuous-time domain, in order to define the relevant transfer function $\mathbf{G}(\omega) \in \mathbb{C}^{o\times r}$ as

$$\bar{\mathbf{G}}(\omega) = \bar{\mathbf{C}}(\mathrm{i}\omega\mathbf{I} - \bar{\mathbf{A}})^{-1}\sum_{g=1}^{L}\sum_{l=1}^{L} S_{gl}^{f}(\omega)\,\bar{\mathbf{B}}^{gl} + \sum_{g=1}^{L}\sum_{l=1}^{L} S_{gl}^{f}(\omega)\,\bar{\mathbf{D}}^{gl}. \tag{3.58}$$

By performing the eigenvalue decomposition of the companion matrix $\bar{\mathbf{A}}$, also called similarity transform [131], as a way to find the roots of the denominator polynomial $\mathbf{D}(\boldsymbol{\alpha}, k)$ of Eq. (3.42),

$$\bar{\mathbf{A}} = \mathbf{V}\boldsymbol{\mu}\mathbf{V}^{-1}, \tag{3.59}$$

you achieve the diagonal matrix $\boldsymbol{\mu} \in \mathbb{C}^{po\times po}$ collecting the eigenvalues in the discrete-time domain, convertible into the system poles by $\lambda_i = \ln(\mu_i)/\Delta t$ (Δt indicates the sampling time). While the eigenvalues of $\bar{\mathbf{A}}$ are the system poles, the eigenvectors associated to the poles correspond to the mode shape of the system [32, 96, 151]. In fact, the matrix $\mathbf{V} \in \mathbb{C}^{po\times po}$ results structured as

$$\mathbf{V} = \begin{bmatrix} \mu_1^{p-1}\boldsymbol{\psi}_1 & \cdots & \mu_{po}^{p-1}\boldsymbol{\psi}_{po} \\ \vdots & \cdots & \vdots \\ \mu_1\boldsymbol{\psi}_1 & \cdots & \mu_{po}\boldsymbol{\psi}_{po} \\ \boldsymbol{\psi}_1 & \cdots & \boldsymbol{\psi}_{po} \end{bmatrix}, \tag{3.60}$$

from which the system mode shapes are extracted by $\boldsymbol{\Psi} = \bar{\mathbf{C}}\mathbf{V}$. So, the transfer function matrix in Eq. (3.58) takes into account the solely part of $\mathbf{S}^q(\omega)$ associated to stable poles

and expressed in Eq. (3.30) because of the particular choice of the polynomial basis function $z_k = \mathrm{e}^{\mathrm{i}2\pi k/N_s}$. In the state space time domain of Eq. (3.56), the replacement of z_k with z_k^{-1} translates into the time axis reversing where the unstable poles, include in $\mathbf{S}^q(\omega)^{\mathrm{H}}$, act.

Once the denominator coefficients are calculated, the numerator coefficients $\boldsymbol{\beta}^{(e)}$ can be obtained by the first equation in Eq. (3.49), and they can be theoretically employed for the identification of the extended operational reference vectors $\mathbf{G}_{gl} = \mathbf{V}^{-1}\bar{\mathbf{B}}^{gl}$. In practice, a two-step approach is performed because the MFD doesn't force rank-one residue matrices; the poles and mode shapes, selected by means of a stabilisation diagram, are passed to the LSFD estimator, described in the next section, in order to obtain the eORV by a second least squares problem.

3.3.4 Least Squares Frequency Domain

Once one determines poles and mode shapes, the remaining unknowns can be estimated with a Least-Squares Frequency-Domain estimator (LSFD) minimizing the scatter between the estimated PSD matrix $\tilde{\mathbf{S}}_q(\mathrm{i}\omega)$ and the modeled one:

$$\boldsymbol{\Gamma}(\mathbf{G}_{gl}, \boldsymbol{\Theta}_f) = \sum_{k=1}^{N_f} \left(\tilde{\mathbf{S}}_q(\mathrm{i}\omega_k) - \left(\mathbf{A}^+(\mathrm{i}\omega_k)\mathbf{P}(\mathrm{i}\omega_k)^{\mathrm{T}} + \mathbf{P}(-\mathrm{i}\omega_k)\mathbf{A}^-(\mathrm{i}\omega_k) + \frac{\mathbf{LR}}{(\mathrm{i}\omega_k)^4} + \mathbf{UR} \right) \right)^2, \tag{3.61}$$

where N_f is the number of spectral lines, and we indicate with $\mathbf{A}^+(\mathrm{i}\omega_k) = \boldsymbol{\Psi}(\mathrm{i}\omega_k\mathbf{I} - \boldsymbol{\Lambda})^{-1}$ and $\mathbf{A}^-(\mathrm{i}\omega_k) = (-\mathrm{i}\omega_k\mathbf{I} - \boldsymbol{\Lambda})^{-1}\boldsymbol{\Psi}^{\mathrm{T}}$ the matrices collecting estimated poles and mode shapes. Furthermore, $\mathbf{P}(\mathrm{i}\omega_k)$ contains the L^2 unknown $\mathbf{G}_{gl} \in \mathbb{C}^{r\times 2N_p}$ matrices together with unknown parameters, generally indicated by $\boldsymbol{\Theta}_f^{lg}$, related to the input PSD matrix. Regarding this aspect, the proposed method needs a minimum knowledge about external forces but still without measuring them. Specifically, it incorporates several a-priori known features resulting from loads which explicitly violate the NExT assumption, Eq. (3.25), such as coloured noises, time and spatial correlation among multiple inputs, presence of deterministic loads

(e.g. harmonics). The input PSD matrix model could contain these known characteristic, embedded in $\mathbf{P}(\mathrm{i}\omega_k)$ definition, together with unknown parameters, generally indicated by $\mathbf{\Theta}_f^{lg}$. $\mathbf{LR}$ and $\mathbf{UR} \in \mathbb{R}^{o\times r}$ are the unknown lower and upper residuals for the case of displacement full-spectra [122]. The error in Eq. (3.61) is generally non-linear in the parameters $\mathbf{G}_{lg}$ and $\mathbf{\Theta}_f^{lg}$ but in some cases it can be linearized as it will be shown in the following application.

3.4 Application and results

In order to validate the two steps MPE procedure previously described, different situations are exploited each characterized by a particular the correlation input matrix $\mathbf{S}^f(\mathrm{i}\omega)$. Considering the case of two external loads, $\boldsymbol{f}(t) \in \mathbb{R}^{2\times 1}$, one can generally represent $\mathbf{S}^f(\mathrm{i}\omega) \in \mathbb{C}^{2\times 2}$ as

$$\mathbf{S}^f(\mathrm{i}\omega) = \begin{bmatrix} S_1(\omega) & \Gamma(\omega)\sqrt{S_1(\omega)\,S_2(\omega)}\mathrm{e}^{\mathrm{i}\omega\tau} \\ \Gamma(\omega)\sqrt{S_1(\omega)\,S_2(\omega)}\mathrm{e}^{-\mathrm{i}\omega\tau} & S_2(\omega) \end{bmatrix}, \tag{3.62}$$

where $S_i(\omega)$ is the auto-PSD function referred to i-th force, τ indicates the generic time-lag between two sources, and $\Gamma(\omega)$ stands for the coherence function classically defined as

$$\Gamma(\omega) = \frac{|S_{12}(\omega)|}{\sqrt{S_1(\omega)\,S_2(\omega)}}. \tag{3.63}$$

Two case studies are offered: the former employing the data achieved by numerically simulating a 4-DOF discrete system model, displayed in Figure 3.1, and the latter processing the time records collected through real-world experiments of MIMO environmental testing, performed on a slender beam of known geometry and material properties, shown in Figure 3.16. In both cases, different infringements of the NExT assumption are investigated by varying the quantities $S_i(\omega)$, τ, $\Gamma(\omega)$ of the PSD matrix in Eq. (3.62), and so studying the effect of colored noise excitation, temporal correlation and coherence between forces on the OMA procedures. Each of these statistical features is emblematic of the loading environment in which typical

mechanical structures (such as vehicles and wind turbines) operate, justifying the need to be gradually tackled by employing an entry-level example, i.e. a discrete system model, and then by approaching an experimental subject. In each application, the first and second step of the identification procedure are carried out by classical and generalized operational modal analysis approach. In Table 3.1, a comparison is set up between the classical OMA procedure (described in Chapter 1), as a basis for comparison, and the generalized one.

	OMA	G-OMA
1^{st} Step	pLSCF based on RMFD	pLSCF based on eLMFD
MFD	$\mathbf{S}^q(\omega_k) = \mathbf{N}(k)\mathbf{D}(k)^{-1}$	$\mathbf{S}^q(\omega_k) = \mathbf{D}(k)^{-1}\mathbf{N}^{(e)}(k)$
Results	$\mathbf{\Lambda}$, $\mathbf{G}$	$\mathbf{\Lambda}$, $\mathbf{\Psi}$
2^{nd} Step	LSFD based on classical PSD modal model	LSFD based on generalized PSD modal model
Modal model	$\mathbf{S}^q(\mathrm{i}\omega) = \mathbf{\Psi}(\mathrm{i}\omega\mathbf{I} - \mathbf{\Lambda})^{-1}\mathbf{G}^{\mathrm{T}} + \mathbf{G}(-\mathrm{i}\omega\mathbf{I} - \mathbf{\Lambda})^{-1}\mathbf{\Psi}^{\mathrm{T}}$	$\mathbf{S}^q(\mathrm{i}\omega) = \mathbf{\Psi}(\mathrm{i}\omega\mathbf{I} - \mathbf{\Lambda})^{-1}\mathbf{P}(\mathrm{i}\omega)^{\mathrm{T}} + \mathbf{P}(-\mathrm{i}\omega)(-\mathrm{i}\omega\mathbf{I} - \mathbf{\Lambda})^{-1}\mathbf{\Psi}^{\mathrm{T}}$
Results	$\mathbf{\Psi}$	$\mathbf{P}(\omega)$

Table 3.1: Comparison between the two step identification procedures employed in the OMA and G-OMA approach. In the results line, we indicate the modal parameters coming out from each step.

As one can notice, main differences, regarding the first step, are related to the matrix fraction description used to describe $\mathbf{S}^q(\omega)$, which leads to distinct state-space realization resulting in distinct modal role of the companion matrix eigenvectors (as appreciable in the line of 1^{st} step results). The modal vectors, extracted from the pLSCF algorithm, also depend upon the choice of polynomial basis functions, z_k or z_k^{-1}, which in turn captures the part of $\mathbf{S}^q(\omega)$ bound up with stable poles, $\tilde{\mathbf{S}}^q(\omega)$, or unstable poles, $\tilde{\mathbf{S}}^q(\omega)^{\mathrm{H}}$. In our cases, the option z_k is adopted for both OMA and G-OMA approach. For the experimental case study, positive power spectra are processed, as defined in Eq. (1.58), with the classical OMA which still employs the RMFD in Table 3.1 at the first identification step but needs a model model like $\mathbf{S}^q(\mathrm{i}\omega) = \mathbf{\Psi}(\mathrm{i}\omega\mathbf{I} - \mathbf{\Lambda})^{-1}\mathbf{G}^{\mathrm{T}}$ for the LSFD estimator. In the results discussion, natural frequencies and damping ratios are compared to reference values, the mode shapes are validated by calculating the relevant MAC with respect to a reference modal vector set, and

synthesized modal models are compared with measured spectra through synthesis correlation coefficients and normalised errors.

3.4.1 Numerical example: a lumped-parameter system

Figure 3.1 offers the discrete 4-DOF mechanical system used to simulate the data. The dynamics is reproduced using the Matlab Control System Toolbox to obtain virtual displacements measurements at each dof. Measurement noise is simulated as Gaussian incoherent noise added to all the dofs' displacements, adjusting the variance values to achieve a 40 dB signal-to-noise-ratio (SNR) for all signals. The system parameters are given as $m_i = 2$ kg, $k_i = 10^4$ N m^{-1} and $c_i = 10$ N s m^{-1} and the exact modal parameters are collected in Table 3.2 in terms of natural frequencies and damping ratios. Two random inputs are hypothesized acting on the 1$^{\text{st}}$ mass, $f_1(t)$, and on the 2$^{\text{nd}}$ mass, $f_2(t)$.

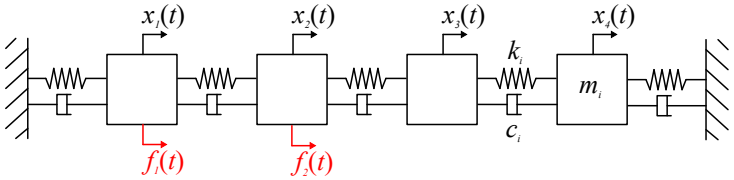

Figure 3.1: 4-DOF system: the pertinent nomenclature for the i-th lumped system is included.

	Natural Frequency (Hz)	Damping Ratio (%)
Mode 1	6.9553	2.1851
Mode 2	13.2298	4.1563
Mode 3	18.2093	5.7206
Mode 4	21.4063	6.7250

Table 3.2: 4-DOF system: theoretical natural frequencies and damping ratios.

Four cases are investigated by varying the nature and correlation of these two noises simulated as a series of cosine functions with weighted amplitudes and random phase angles

[95, 143, 148]. The first case corresponds to the following input PSD matrix

$$\mathbf{S}^f(\omega) = \begin{pmatrix} S_1 & 0 \\ 0 & \dfrac{S_2}{\omega^2} \end{pmatrix}, \tag{3.64}$$

where $f_1(t)$ is realization of a white noise process and $f_2(t)$ that of a red one, the two inputs remain uncorrelated as stated by the NExT assumptions. So, in this case the effect of input coloration is explored and the frequency-dependent operational vector, referred to the n-th pole, can be written as

$$\boldsymbol{\rho}_n(\mathrm{i}\omega) = S_1 \boldsymbol{g}_n^{11} + \frac{S_2}{\omega^2}\boldsymbol{g}_n^{22} = \bar{\boldsymbol{g}}_n^{11} + \frac{1}{\omega^2}\bar{\boldsymbol{g}}_n^{22}, \tag{3.65}$$

where the distribution of $S_2^f(\omega)$ in the frequency domain is assumed a priori known, resulting in the two unknowns $\bar{\boldsymbol{g}}_n^{11}$ and $\bar{\boldsymbol{g}}_n^{22}$ that represent the operational vectors to be estimated by the modified LSFD. As a second case, two white noises characterized by temporal correlation are considered. In this case, the input correlation matrix is expressed by

$$\mathbf{S}^f(\omega) = S_1 \begin{pmatrix} 1 & \mathrm{e}^{-\mathrm{i}\omega\tau} \\ \mathrm{e}^{\mathrm{i}\omega\tau} & 1 \end{pmatrix}, \tag{3.66}$$

where τ is the temporal delay between the loads assumed as a known feature of the inputs. By similarly proceeding for this case, the n-th ω-ORV is expressed in the form

$$\boldsymbol{\rho}_n(\mathrm{i}\omega) = S_1\left(\boldsymbol{g}_n^{11} + \boldsymbol{g}_n^{22}\right) + S_1\mathrm{e}^{-\mathrm{i}\omega\tau}\boldsymbol{g}_n^{12} + S_1\mathrm{e}^{\mathrm{i}\omega\tau}\boldsymbol{g}_n^{21} = \bar{\boldsymbol{g}}_n^{0} + \mathrm{e}^{-\mathrm{i}\omega\tau}\bar{\boldsymbol{g}}_n^{12} + \mathrm{e}^{\mathrm{i}\omega\tau}\bar{\boldsymbol{g}}_n^{21}, \tag{3.67}$$

with the operational vectors $\bar{\boldsymbol{g}}_n^{0}$, $\bar{\boldsymbol{g}}_n^{12}$, and $\bar{\boldsymbol{g}}_n^{21}$ representing the unknowns in the extended LSFD problem. The third case introduces the effect of coherence, represented by the function $\Gamma(\omega) = \mathrm{e}^{-\alpha|\omega|}$ and usually employed in the stochastic modelling of parallel road tracks [13],

between two white noises correlated in accordance with the matrix

$$\mathbf{S}^f(\omega) = S_1 \begin{pmatrix} 1 & \mathrm{e}^{-\alpha|\omega|} \\ \mathrm{e}^{-\alpha|\omega|} & 1 \end{pmatrix}, \tag{3.68}$$

which leads to the operational reference vectors

$$\boldsymbol{\rho}_n(\mathrm{i}\omega) = S_1\left(\boldsymbol{g}_n^{11} + \boldsymbol{g}_n^{21}\right) + S_1\mathrm{e}^{-\alpha|\omega|}\left(\boldsymbol{g}_n^{12} + \boldsymbol{g}_n^{21}\right) = \bar{\boldsymbol{g}}_n^0 + \mathrm{e}^{-\alpha|\omega|}\bar{\boldsymbol{g}}_n^1, \tag{3.69}$$

where the two unknown vectors $\bar{\boldsymbol{g}}_n^0$ and $\bar{\boldsymbol{g}}_n^1$ are accessed by the modified LSFD once assumed a model of $\Gamma(\omega)$, as for the case of noise coloration in Eq. (3.65). Finally, all the three effects (coloration, temporal correlation, and coherence) are combined designing the two inputs according to the PSD matrix

$$\mathbf{S}^f(\omega) = \frac{S_1}{\omega^2} \begin{pmatrix} 1 & \mathrm{e}^{-\alpha|\omega|}\mathrm{e}^{-\mathrm{i}\omega\tau} \\ \mathrm{e}^{-\alpha|\omega|}\mathrm{e}^{\mathrm{i}\omega\tau} & 1 \end{pmatrix}, \tag{3.70}$$

thus the n-th frequency-dependent operational reference vector is rephrased as

$$\begin{aligned} \boldsymbol{\rho}_n(\mathrm{i}\omega) =& \frac{S_1}{\omega^2}\left(\boldsymbol{g}_n^{11} + \boldsymbol{g}_n^{22}\right) + \frac{S_1}{\omega^2}\mathrm{e}^{-\alpha|\omega|}\mathrm{e}^{-\mathrm{i}\omega\tau}\boldsymbol{g}_n^{12} + \frac{S_1}{\omega^2}\mathrm{e}^{\alpha|\omega|}\mathrm{e}^{-\mathrm{i}\omega\tau}\boldsymbol{g}_n^{21} = \\ =& \frac{1}{\omega^2}\bar{\boldsymbol{g}}_n^0 + \frac{1}{\omega^2}\mathrm{e}^{-\alpha|\omega|}\mathrm{e}^{-\mathrm{i}\omega\tau}\bar{\boldsymbol{g}}_n^{12} + \frac{1}{\omega^2}\mathrm{e}^{-\alpha|\omega|}\mathrm{e}^{\mathrm{i}\omega\tau}\bar{\boldsymbol{g}}_n^{21}, \end{aligned} \tag{3.71}$$

where three unknowns $\bar{\boldsymbol{g}}_n^0$, $\bar{\boldsymbol{g}}_n^{12}$, and $\bar{\boldsymbol{g}}_n^{21}$ arise. At this stage, it is underlined how classical operational modal analysis, based on the modal model in Eq. (3.27), approximates the different operational reference vectors in Eqs. (3.65), (3.67), (3.69), and (3.71) by a single constant vector $\boldsymbol{\rho}_n$; on the other hand, by employing the estimator, described in Section 3.3.4, you can embed known characteristic of the input PSD matrix, such as the temporal delay τ and the frequency dependence of coloration and coherence models, in order to estimate the extended operational reference factors related to the r-th pole and the entries of matrix

$\mathbf{S}^f(\mathrm{i}\omega)$. Figure 3.2 shows the input characteristics, chosen in order to not obey the NExT assumptions, recurring in the force design of the four investigated cases.

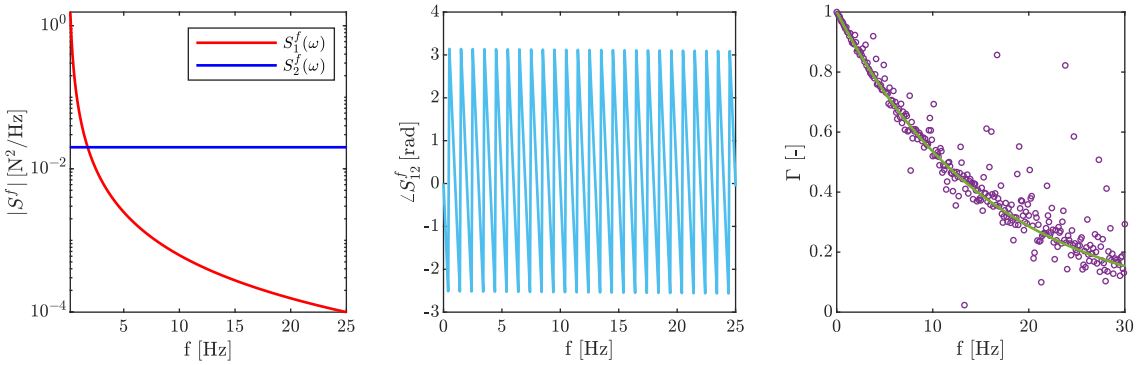

(a) Coloration (b) Temporal correlation (c) Coherence

Figure 3.2: 4-DOF system: characteristic of the simulated forces employed in the four cases. (a) Magnitude of autoPSD functions referred to the white, blue line, and red, red line, noise, (b) phase angle of the cross-PSD term in the case of temporal correlation ($\tau = 1\,\mathrm{s}$), (c) coherence model $\Gamma(\omega)$, green line, compared to the measured coherence, dotted purple line, resulting from the input simulation procedure proposed in [95].

Forces, responses, and additive noises are simulated in the time domain, adopting a sampling frequency, a time period, and a number of repetitions equal to 300 Hz, 10 s, and $M = 25$, respectively. Figure 3.3 offers the first output PSD matrix column, which takes the 1$^{\mathrm{st}}$ DOF displacement as reference signal, obtained by processing the system responses by means of the weighted correlogram recalled in Eq. (1.57). Specifically, no exponential window is applied to all the response signals, while windowing will be employed for the experimental case studies.

The coloration effect is evident and it distinguishes the energy distribution in frequency of the first and fourth loading case with respect to other two ones. Time correlation and coherence of the excitations produce relevant effects in form of distortions of spectra. The time delay between the loads, acting on the 1$^{\mathrm{st}}$ and 2$^{\mathrm{nd}}$ mass, introduces the most significant of these distortions, see the blue and green lines in Figure 3.3. In particular, humps appear in the magnitude of the cross-PSDs and the phase plots, referred to the cross-PSDs, reveal

the typical saw-tooth trend caused by time-delayed signals. It should be expected that the presence in the output spectra of these distortion effects could hamper the correct operation of curve fitting methodologies based on the classical OMA modal model, that specifically relies on the NExT hypotheses.

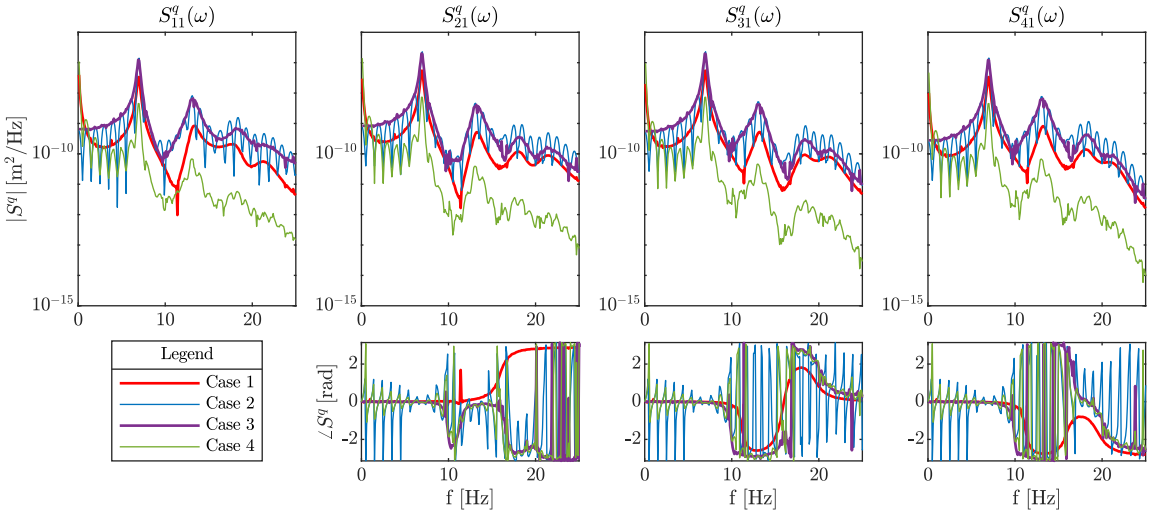

Figure 3.3: 4-DOF system: comparison of the output PSD matrix entries in the four different loading cases. Each case is defined by the input PSD matrix definition. The pertinent legend refers to the case description.

In the following sections, the identification procedure is carried out by classical and generalized operational modal analysis LSFD estimators operating in the frequency band $0 - 25$ Hz that contains the four modes in Table 3.2.

3.4.1.1 Effect of input coloration

3.4.1.1.1 First identification step: pLSCF

As already mentioned, the G-OMA approach requires a minimum knowledge of the input PSD matrix $\mathbf{S}^f(\omega)$. The known characteristics can be embedded into a dedicated eLMFD model properly designing the extended polynomial numerator matrix $\mathbf{N}^{(e)}(k)$ of Eq. (3.42). In the following loading case, it is suppose to know in advance the frequency dependence of

the colored noise so as to define

$$\mathbf{N}^{(e)}(k) = \sum_{r=0}^{p} S_1 z_k^{-r} \boldsymbol{\beta}_r^{11} + \sum_{r=0}^{p} \frac{S_2}{\omega_k^2} z_k^{-r} \boldsymbol{\beta}_r^{22} = \sum_{r=0}^{p} z_k^{-r} \bar{\boldsymbol{\beta}}_r^{11} + \frac{1}{\omega_k^2} \sum_{r=0}^{p} z_k^{-r} \bar{\boldsymbol{\beta}}_r^{22}, \tag{3.72}$$

where $\bar{\boldsymbol{\beta}}_r^{11}$ and $\bar{\boldsymbol{\beta}}_r^{22}$ are the two numerator coefficient matrix unknowns derived by the combination of $L^2 = 4$ (L number of physical system input) matrices in the extended numerator definition. Algebraic manipulation is needed in order to reduce the number of unknowns, as already done with the ω-ORV of Eq. (3.71) to be included into the modal model, and it determines the relevant assembling of matrix $\mathbf{X}^{(e)}$, defined in Eq. (3.46), in the least square solution making. From the pLSCF, two stabilisation diagrams in Figure 3.4 are built up, assuming subsequently an increasing value for the polynomial model order and focusing on the frequency range from 0 to 25 Hz. In particular, the PSD-sum, i.e. the complex sum of the PSDs of all the DOF displacements, together with the poles estimated by the pLSCF are represented. The stabilisation diagram gives the indication of four stable pole for both OMA, left panel, and G-OMA, right panel, processing.

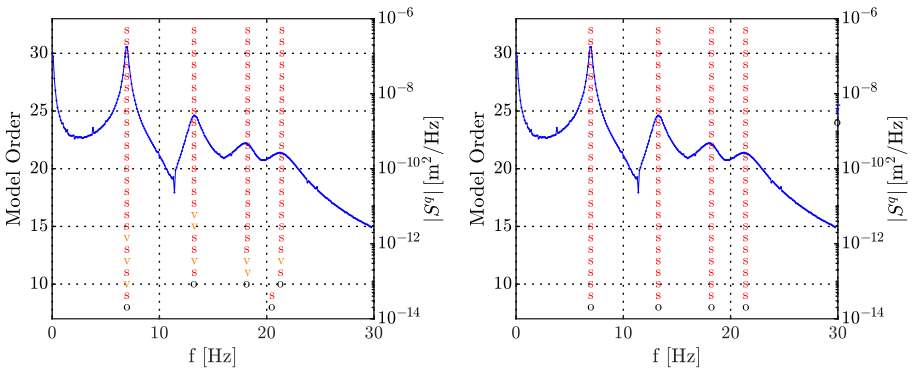

(a) OMA (b) G-OMA

Figure 3.4: Identification of the lumped parameter system: stabilisation diagram along with the magnitude of the PSDs sum function, blue line. The model order is indicated on the left ordinate axis. '`o`': new pole; '`f`' stabilisation in natural frequency; '`f`' extra stabilisation in damping ratio; '`v`' extra stabilisation in MAC value; '`s`' full stabilisation. Stabilisation thresholds for natural frequency, damping ratio, and MAC value are 1%, 5%, and 2%, respectively.

The main difference between the two algorithms is related to the minimum model order corresponding to the full stabilisation of the four expected poles. In the G-OMA case, it corresponds to the theoretical one ($p = 8$), despite the added noise, while the classical pLSCF reaches an higher order because of the offsetting caused by the presence of a red noise among inputs.

		Natural Frequency (Hz)		Damping Ratio (%)	
		Estimated	$\|\Delta\|(\%)$	Estimated	$\|\Delta\|(\%)$
OMA	Mode 1	6.9546	0.0105	2.1848	0.0141
	Mode 2	13.2247	0.0386	4.1090	1.1366
	Mode 3	18.2272	0.0986	5.6881	0.5688
	Mode 4	21.4141	0.0365	6.8490	1.8439
G-OMA	Mode 1	6.9553	0.0001	2.2062	0.9646
	Mode 2	13.2410	0.0845	4.1338	0.5397
	Mode 3	18.2114	0.0115	5.6507	1.2228
	Mode 4	21.3902	0.0752	6.6298	1.4149

Table 3.3: Comparison between exact and estimated natural frequencies. Estimates computed by using classical and generalized OMA formulations are compared. Percentage relative error, $\Delta = 100 \times (v_{\text{th}} - v_{\text{est}})/v_{\text{th}}$, with respect to exact value is reported below each estimate.

Estimated natural frequencies and damping ratios exhibit negligible errors with respect to the theoretical values for both the approaches, see Table 3.3. In Figure 3.5, the MAC values show good consistency for the first four modes solely in the G-OMA case, in turn confirming the suitability of extended LMFD. Concerning the classical OMA results, it is highlighted how the wrong description of the ORV in the RMFD is reversed into the estimate of mode shape vectors made by the second step of the classical OMA. By looking at Figure 3.5, the estimated mode shapes' consistency gets worse especially for the most damped modes.

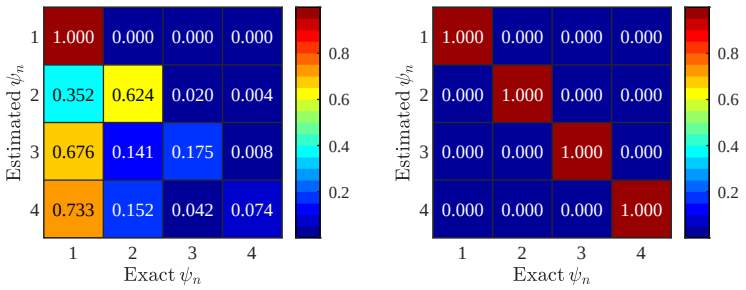

(a) OMA (b) G-OMA

Figure 3.5: MAC between exact and estimated modal vectors' sets estimated by following (a) the classical OMA procedure and (b) the generalized approach proposed in the paper.

3.4.1.1.2 Second identification step: LSFD

At this stage, the PSDs synthesized by the Least-Squares estimator, which minimizes the scatter in Eq. (3.61), and the classical LSFD, inspired to the model in Eq. (3.27), are compared. Figure 3.6 displays the four output PSD functions, in terms of magnitude and phase, comparing the non-parametric PSDs with the fitted ones resulting from OMA and G-OMA procedure. Legend reports the calculation of the correlation, Eq. (1.59), and normalized error coefficients, Eq. (1.60), for each curve in order to provide an evaluation of the consistency between data and fitted models. The visual match, together with a 100% correlation coefficient for all the PSDs, proves the goodness of the G-OMA process results as confirmed by error coefficients, which remain almost 0%. Furthermore it is pointed out that these improved results are mainly related to possibility to incorporate in the LSFD estimator the particular ORV expression, obtained in Eq. (3.65), where the red noise model can be taken into account. On the other hand, the classical OMA, relying on the NExT hypothesis here violated by coloration, is not able to capture the effect due to the presence of red noise resulting in high errors. These errors don't appear significant for some entries, such as $S^q_{31}(\omega)$ and $S^q_{41}(\omega)$, but the reason is purely justified by the accuracy around resonance peaks which have a major weight in the coefficients definition.

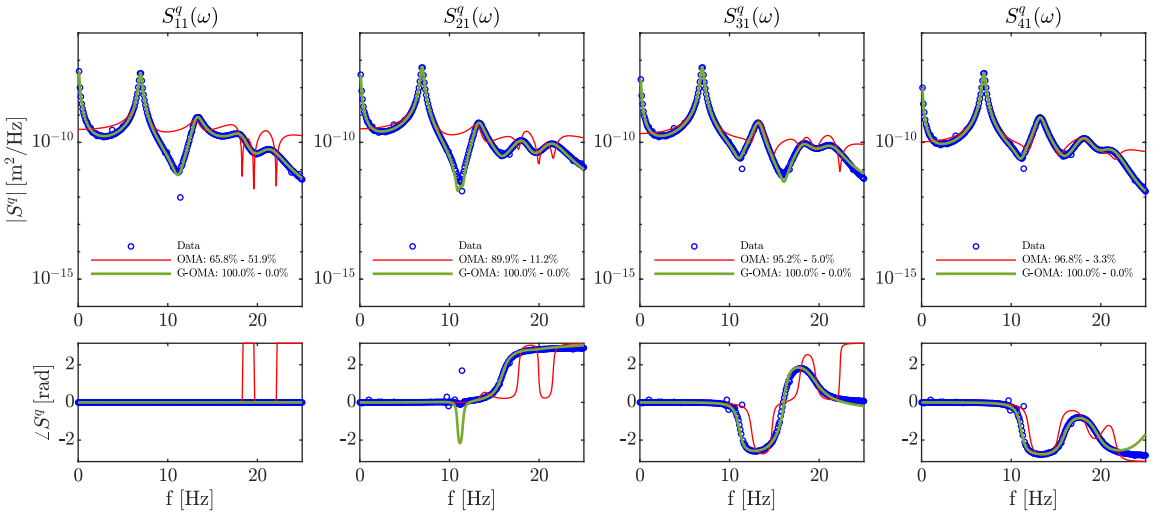

Figure 3.6: 4-DOF system: comparison between the measured output PSDs, blue dotted line, and syntheses by the classical OMA modal model, red solid line, and the G-OMA modal model, green solid line. The legend indicates, respectively, the correlation coefficients Eq. (1.59) and normalized errors Eq. (1.60) for both the LSFD approaches.

3.4.1.2 Effect of input temporal correlation

3.4.1.2.1 First identification step: pLSCF

In the case of time correlated white excitations, the knowledge of the temporal delay τ between the inputs, which is a parameter that is generally easily accessible by looking at the phase of the cross-correlation between the outputs [110], is included into the dedicated eLMFD model. By doing so, $\mathbf{N}^{(e)}(k)$ is designed as

$$\begin{aligned}\mathbf{N}^{(e)}(k) &= \sum_{r=0}^{p} S_1 z_k^{-r}\left(\boldsymbol{\beta}_r^{11}+\boldsymbol{\beta}_r^{22}\right)+\mathrm{e}^{-i\omega_k\tau}\sum_{r=0}^{p} z_k^{-r}\boldsymbol{\beta}_r^{12}+\mathrm{e}^{i\omega_k\tau}\sum_{r=0}^{p} z_k^{-r}\boldsymbol{\beta}_r^{21}= \\ &= \sum_{r=0}^{p} z_k^{-r}\bar{\boldsymbol{\beta}}_r^{0}+\mathrm{e}^{-i\omega_k\tau}\sum_{r=0}^{p} z_k^{-r}\boldsymbol{\beta}_r^{12}+\mathrm{e}^{i\omega_k\tau}\sum_{r=0}^{p} z_k^{-r}\boldsymbol{\beta}_r^{21},\end{aligned} \tag{3.73}$$

where $\bar{\boldsymbol{\beta}}_r^{0}$, $\bar{\boldsymbol{\beta}}_r^{12}$, and $\bar{\boldsymbol{\beta}}_r^{21}$ are the three numerator coefficient matrix unknowns. The classical pLSCF procedure produces a poor diagram, see Figure 3.7a, because of the time correlation terms. Pole selection is limited to the first two pole frequency lines which in turn reveal

a poor stabilisation in damping ratio. On the other hand, the usage of the proposed new method, based on the representation of the generalized output PSD model, leads to the computation of a stabilisation diagram where four stable columns are easily distinguishable even from the lowest model order, Figure 3.7b.

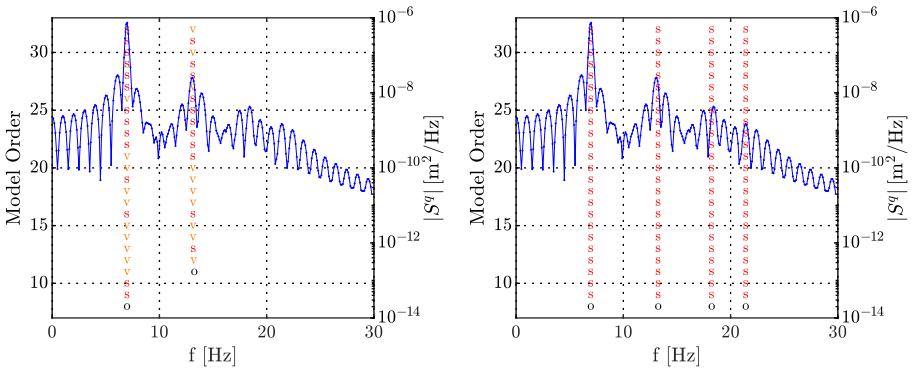

(a) OMA (b) G-OMA

Figure 3.7: Identification of the lumped parameter system: stabilisation diagram along with the magnitude of the PSDs sum function, blue line. The model order is indicated on the left ordinate axis. '`o`': new pole; '`f`' stabilisation in natural frequency; '`f`' extra stabilisation in damping ratio; '`v`' extra stabilisation in MAC value; '`s`' full stabilisation. Stabilisation thresholds for natural frequency, damping ratio, and MAC value are 1%, 5%, and 2%, respectively.

		Natural Frequency (Hz)		Damping Ratio (%)	
		Estimated	$\|\Delta\|$(%)	Estimated	$\|\Delta\|$(%)
OMA	Mode 1	6.9632	0.1137	0.9400	56.9816
	Mode 2	13.0962	1.0100	0.4960	88.0666
	Mode 3	-	-	-	-
	Mode 4	-	-	-	-
G-OMA	Mode 1	6.9553	0.0000	2.1851	0.0001
	Mode 2	13.2298	0.0000	4.1562	0.0012
	Mode 3	18.2092	0.0002	5.7208	0.0029
	Mode 4	21.4063	0.0001	6.7259	0.0131

Table 3.4: Comparison between exact and estimated natural frequencies. Estimates computed by using classical and generalized OMA formulations are compared. Percentage relative error, $\Delta = 100 \times (v_{\text{th}} - v_{\text{est}})/v_{\text{th}}$, with respect to exact value is reported below each estimate.

By employing the pLSCF based eLMFD algorithm, natural frequencies and damping ratios extracted exhibit negligible errors with respect to the theoretical values, as listed in Table 3.4.

Secondly, the OMA approach identifies two poles whose damping ratios tremendously differ from the expected ones.

Figure 3.8, shows the good consistency of the four mode shapes extracted by the G-OMA, while the classical OMA return the solely first two modes as well as the two ones less damped.

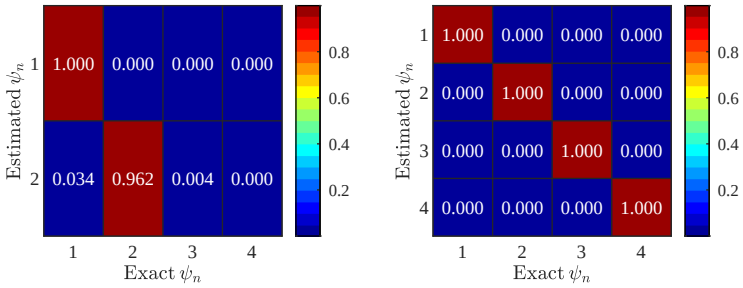

(a) OMA (b) G-OMA

Figure 3.8: MAC between exact and estimated modal vectors' sets estimated by following (a) the classical OMA procedure and (b) the generalized approach proposed in the paper.

3.4.1.2.2 Second identification step: LSFD

In violating the NExT assumption by temporal correlation between inputs, you still notice the good correlations of the G-OMA syntheses which turns out to be able to reproduce the typical humps in the magnitude of the cross-PSDs together with the saw-tooth trend in phases. This result is mainly due to the relevant definition of the frequency-dependent operational reference vector in Eq. (3.67) which takes into account the temporal delay τ as additional information to provide the modified LSFD. In addition, the classical LSFD offers a good fitting merely in the region around the first two resonance peaks, which are related to less damped modes with respect to the following two ones not identified by the classical pLSCF.

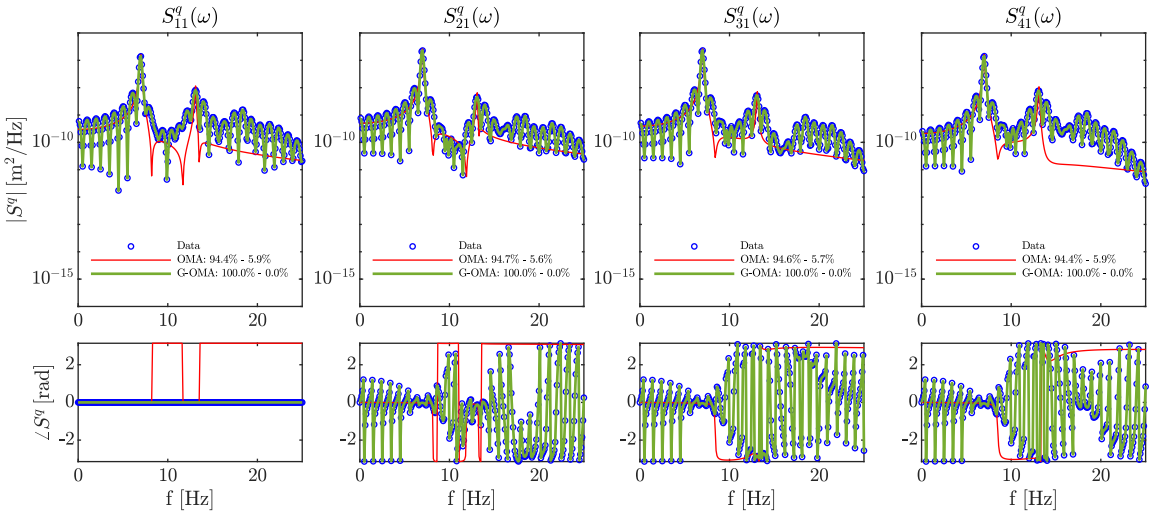

Figure 3.9: 4-DOF system: comparison between the measured output PSDs, blue dotted line, and syntheses by the classical OMA modal model, red solid line, and the G-OMA modal model, green solid line. The legend indicates, respectively, the correlation coefficients Eq. (1.59) and normalized errors Eq. (1.60) for both the LSFD approaches.

3.4.1.3 Effect of input coherence

3.4.1.3.1 First identification step: pLSCF

In the case of coherent white noises, the coherence model is incorporated in designing $\mathbf{N}^{(e)}(k)$ as

$$\mathbf{N}^{(e)}(k) = \sum_{r=0}^{p} z_k^{-r} \bar{\boldsymbol{\beta}}_r^0 + \mathrm{e}^{-\alpha|\omega_k|} \sum_{r=0}^{p} z_k^{-r} \bar{\boldsymbol{\beta}}_r^1, \tag{3.74}$$

with the unknowns $\bar{\boldsymbol{\beta}}_r^0$ and $\bar{\boldsymbol{\beta}}_r^1$ which contribute to the specific eLMFD in producing the stabilisation diagram reported in Figure 3.10b. As in the loading case of colored noise, the modified pLSCF shows full stabilisation of the four poles since the minimum polynomial model order, while the classical OMA reaches an higher order for achieving the all-poles stabilisation, as depicted in Figure 3.10a.

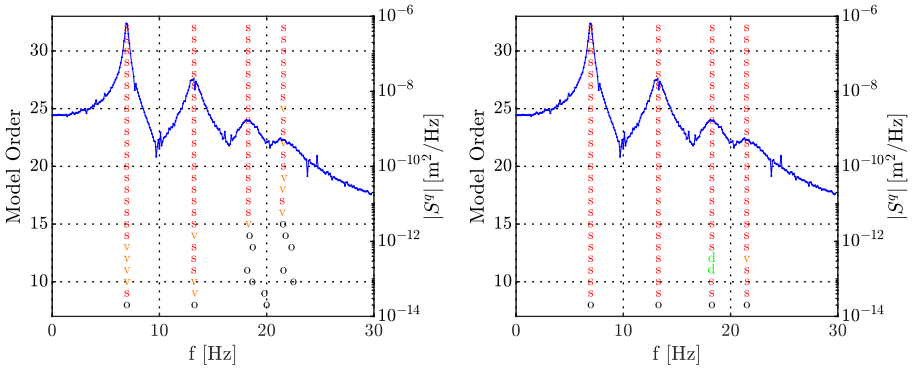

(a) OMA (b) G-OMA

Figure 3.10: Identification of the lumped parameter system: stabilisation diagram along with the magnitude of the PSDs sum function, blue line. The model order is indicated on the left ordinate axis. '`o`': new pole; '`f`' stabilisation in natural frequency; '`f`' extra stabilisation in damping ratio; '`v`' extra stabilisation in MAC value; '`s`' full stabilisation. Stabilisation thresholds for natural frequency, damping ratio, and MAC value are 1%, 5%, and 2%, respectively.

As suggested by Table 3.5, the two identification procedures produce similar results implying that the chosen coherence model doesn't significantly affect the modal parameters estimation except for the damping ratios that generally exhibit higher errors than the ones extracted by G-OMA approach. In Figure 3.11, the consistency of the estimated mode shapes is good for both the mode shape sets but more accurate in the case G-OMA for the third and fourth mode, i.e. the most damped.

		Natural Frequency (Hz)		Damping Ratio (%)	
		Estimated	$\lvert\Delta\rvert$(%)	Estimated	$\lvert\Delta\rvert$(%)
OMA	Mode 1	6.9545	0.0121	2.1904	0.2417
	Mode 2	13.2272	0.0197	4.0226	3.2167
	Mode 3	18.2641	0.3012	4.1063	28.2199
	Mode 4	21.5769	0.7972	4.2888	36.2258
G-OMA	Mode 1	6.9572	0.0264	2.2736	4.0511
	Mode 2	13.2553	0.1923	4.2419	2.0614
	Mode 3	18.2784	0.3798	5.3638	6.2367
	Mode 4	21.4801	0.3449	5.8158	13.5189

Table 3.5: Comparison between exact and estimated natural frequencies. Estimates computed by using classical and generalized OMA formulations are compared. Percentage relative error, $\Delta = 100 \times (v_{\text{th}} - v_{\text{est}})/v_{\text{th}}$, with respect to exact value is reported below each estimate.

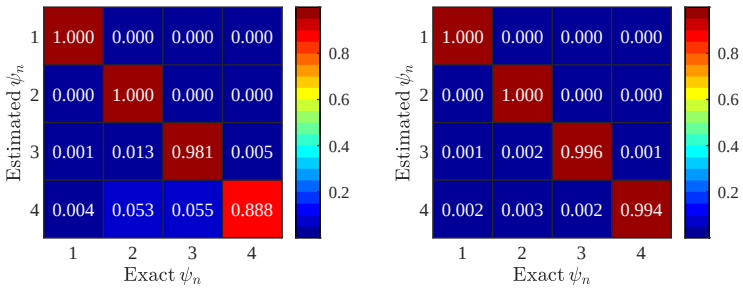

(a) OMA (b) G-OMA

Figure 3.11: MAC between exact and estimated modal vectors' sets estimated by following (a) the classical OMA procedure and (b) the generalized approach proposed in the paper.

3.4.1.3.2 Second identification step: LSFD

The loading case, defined by the particular coherence model $\Gamma(\omega) = \mathrm{e}^{-\alpha|\omega|}$, produces similar identification results for both the OMA and G-OMA syntheses. We notice how correlation and error coefficients remain almost the same in the two approaches.

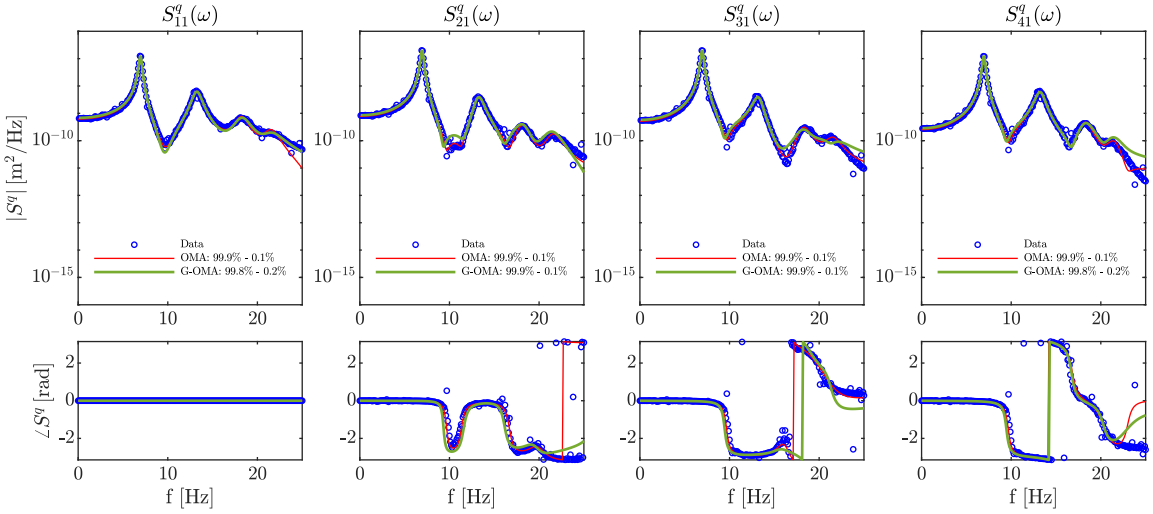

Figure 3.12: 4-DOF system: comparison between the measured output PSDs, blue dotted line, and syntheses by the classical OMA modal model, red solid line, and the G-OMA modal model, green solid line. The legend indicates, respectively, the correlation coefficients Eq. (1.59) and normalized errors Eq. (1.60) for both the LSFD approaches.

3.4.1.4 Effect of time-correlated, coherent, coloured inputs

3.4.1.4.1 First identification step: pLSCF

By combining coherence, temporal correlation and coloration effect, the fourth loading case is reproduced. It corresponds to a dedicated eLMFD whose extended numerator is

$$\mathbf{N}^{(e)}(k) = \frac{1}{\omega_k^2}\sum_{r=0}^{p} z_k^{-r}\bar{\boldsymbol{\beta}}_r^0 + \frac{1}{\omega_k^2}\mathrm{e}^{-\alpha|\omega_k|}\mathrm{e}^{-i\omega_k\tau}\sum_{r=0}^{p} z_k^{-r}\bar{\boldsymbol{\beta}}_r^{12} + \frac{1}{\omega_k^2}\mathrm{e}^{-\alpha|\omega_k|}\mathrm{e}^{i\omega_k\tau}\sum_{r=0}^{p} z_k^{-r}\bar{\boldsymbol{\beta}}_r^{21}, \quad (3.75)$$

where the temporal delay τ and the frequency dependence of coloration and coherence models are embedded into the extended numerator definition. The two stabilisation diagrams in Figure 3.13 are built up, which in turn reveal the robustness of the modified pLSCF in distinguish the four expected poles. Secondly, the classical algorithm offers three stable lines but lacking in strong damping ratio stabilisation.

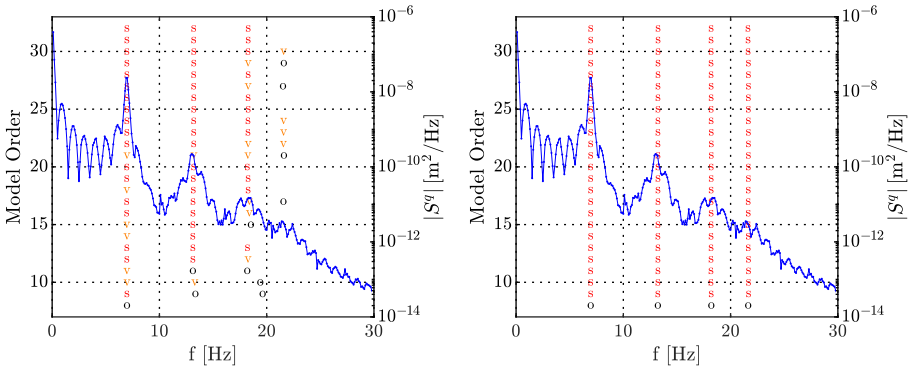

(a) OMA (b) G-OMA

Figure 3.13: Identification of the lumped parameter system: stabilisation diagram along with the magnitude of the PSDs sum function, blue line. The model order is indicated on the left ordinate axis. '`o`': new pole; '`f`' stabilisation in natural frequency; '`f`' extra stabilisation in damping ratio; '`v`' extra stabilisation in MAC value; '`s`' full stabilisation. Stabilisation thresholds for natural frequency, damping ratio, and MAC value are 1%, 5%, and 2%, respectively.

Table 3.6 and Figure 3.14 summarize the MPE results showing negligible errors for the natural frequency estimates and better performance of the eLMFD base pLSCF in terms

of damping ratio identification. The last mode is not captured by the classical procedure which is significantly affected by the infringements of the NExT assumption especially in the estimation of mode shape vectors, as confirmed by poor MAC values.

		Natural Frequency (Hz)		Damping Ratio (%)	
		Estimated	$\|\Delta\|(\%)$	Estimated	$\|\Delta\|(\%)$
OMA	Mode 1	6.9597	0.0629	1.3704	37.2817
	Mode 2	13.1870	0.3233	2.4909	40.0692
	Mode 3	18.2665	0.3143	1.5497	72.9096
	Mode 4	-	-	-	-
G-OMA	Mode 1	6.9529	0.0351	2.3641	8.1939
	Mode 2	13.2299	0.0008	4.3201	3.9414
	Mode 3	18.1758	0.1841	5.3951	5.6898
	Mode 4	21.6134	0.9675	5.7914	13.8818

Table 3.6: Comparison between exact and estimated natural frequencies. Estimates computed by using classical and generalized OMA formulations are compared. Percentage relative error, $\Delta = 100 \times (v_{\text{th}} - v_{\text{est}})/v_{\text{th}}$, with respect to exact value is reported below each estimate.

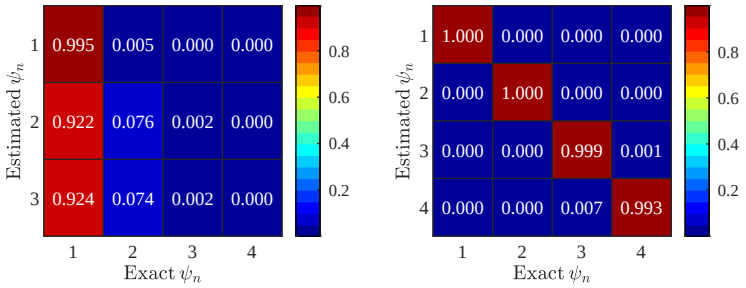

(a) OMA (b) G-OMA

Figure 3.14: MAC between exact and estimated modal vectors' sets estimated by following (a) the classical OMA procedure and (b) the generalized approach proposed in the paper.

3.4.1.4.2 Second identification step: LSFD

Regarding the second identification step, Figure 3.15 reveals the robustness of the G-OMA method which continues giving good fitting as turned out by the visual match and the correlation coefficients, almost 100%. As before, this result is mainly due to the proper expression of the frequency-dependent operational reference vector in Eq. (3.71) which allows

to capture the different effect violating the NExT assumption. In addition, the classical LSFD offers a poor fitting as confirmed by huge error coefficients.

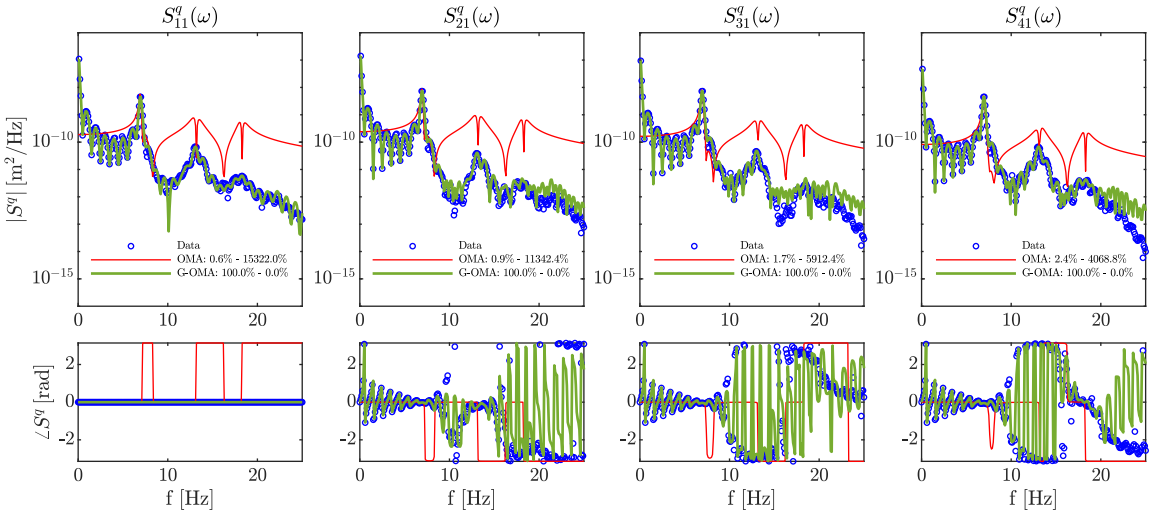

Figure 3.15: 4-DOF system: comparison between the measured output PSDs, blue dotted line, and syntheses by the classical OMA modal model, red solid line, and the G-OMA modal model, green solid line. The legend indicates, respectively, the correlation coefficients Eq. (1.59) and normalized errors Eq. (1.60) for both the LSFD approaches.

3.4.2 Experimental example: a PTFE beam

In Figure 3.16, the slender beam used to perform the MIMO environmental testing experiments, is represented. Specifically, the specimen is a PTFE beam of length, width, and thickness equal to 610 mm, 100 mm, and 10 mm, respectively. The set-up consists in free-free boundary conditions achieved by suspending the beam through extremely flexible elastic cords. The beam is forced by exerting random loads through two modal exciters, acting along the x-direction, attached to the structure through steel stingers and mechanical impedance sensors screw mounted. The output responses are even measured by eight accelerometers, attached to the beam's center-line, as shown in Figure 3.16, and by two impedance heads at the driving point locations. These latter sensors also provide the force measurements employed as control signals for the source driving.

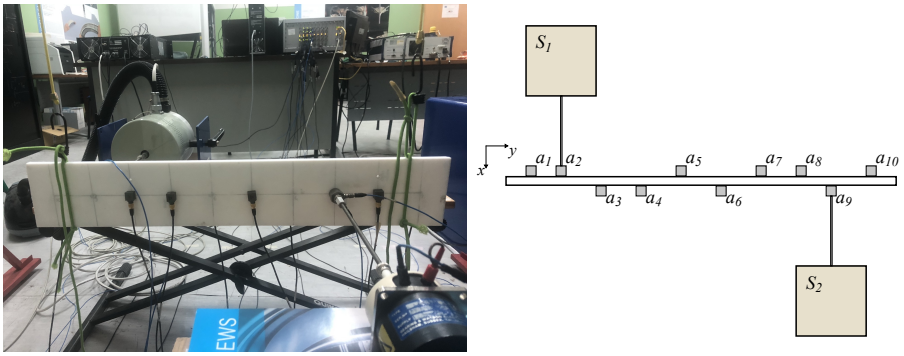

Figure 3.16: Experimental case study: PTFE beam in free-free boundary conditions. Forces are simulated by two modal shakers attached by stinger.

The experimental setup is, therefore, composed of (i) eight B&K 4535-B-001 triaxial accelerometers, (ii) two PCB 288D01 mechanical impedance sensors, (iii) Dongling ESD-045 and GW-V2/PA30E modal shakers, (iv) a LMS SCADAS III SC310-UTP mobile, equipped with DAC shutdown control box, PC based multichannel analyzer platform, running the LMS Test.Lab 14A software suite for acquiring and recording the time histories of output and input signals, measured by the accelerometers and the impedance head transducers. It is exploited the software module designed for environmental testing specifically for multi-axis random control. By doing so, you are allowed to drive two exciters targeting reference profiles of force PSDs, $S_1^f(\omega)$ and $S_2^f(\omega)$, including also a reference coherence $\Gamma(\omega)$ and a cross-PSD phase angle $\angle S_{12}^f(\omega)$ which determine the cross-correlation term $S_{12}^f(\omega)$, as described in Eq. (3.62). Three loading cases are explored represented in Figure 3.17 which aim at introducing different infringements of NExT assumption.

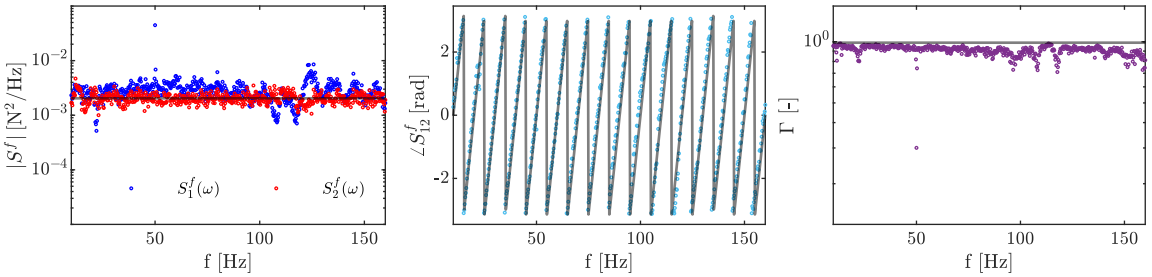

(a) Temporal correlation: $S_1^f(\omega) = S_2^f(\omega) = S_0$, $\angle S_{12}^f(\omega) = \omega\tau$, and $\Gamma(\omega) = 0.98$

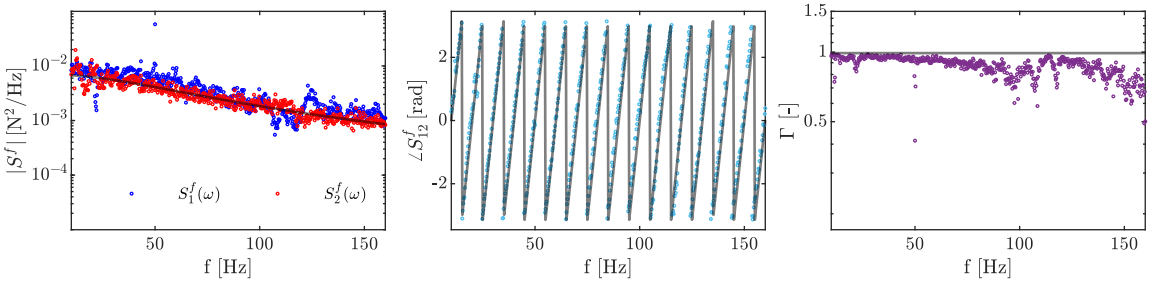

(b) Temporal correlation and coloration: $S_1^f(\omega) = S_2^f(\omega) = \dfrac{S_0}{\omega^2 + \omega_0^2}$, $\angle S_{12}^f(\omega) = \omega\tau$, and $\Gamma(\omega) = 0.98$

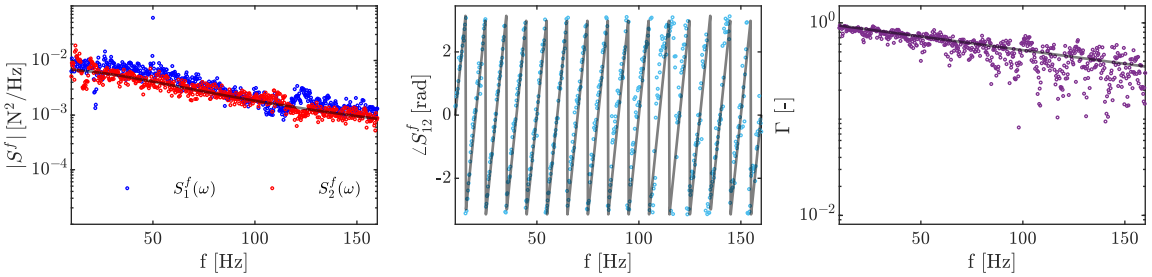

(c) Temporal correlation, coloration, and coherence: $S_1^f(\omega) = S_2^f(\omega) = \dfrac{S_0}{\omega^2 + \omega_0^2}$, $\angle S_{12}^f(\omega) = \omega\tau$, and $\Gamma(\omega) = \mathrm{e}^{-\alpha|\omega|}$

Figure 3.17: Experimental case study: three loading cases under no-NExT hypothesis. The dotted coloured lines display quantities derived from impedance head force measurements. On the other hand, black lines show the chosen target profiles whose analytical expression is reported in captions.

Signals are acquired in the time domain, adopting a sampling frequency, a time period, and a number of repetitions equal to 800 Hz, 4 s, and $M = 50$, respectively. Figure 3.18 offers the magnitude of cross-PSD between the 10^{th} and 5^{th} acceletometer signals, obtained by processing the system responses by means of the weighted correlogram when a 0.001% exponential window is applied.

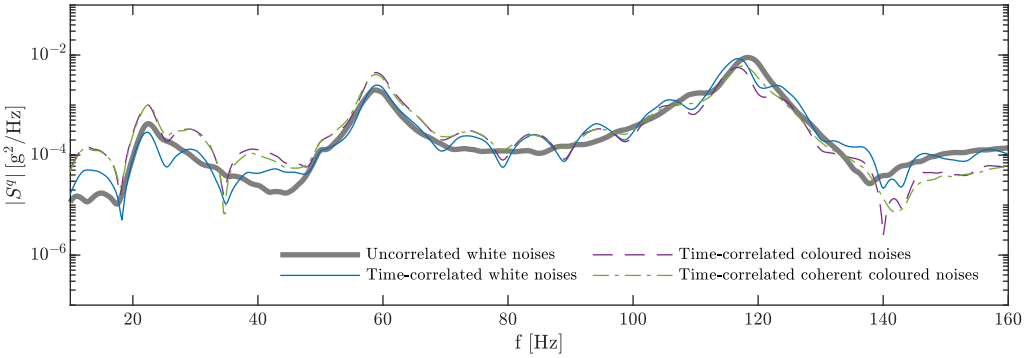

Figure 3.18: Experimental case study: magnitude of output crossPSD relating the 10$^{\text{th}}$ and 5$^{\text{th}}$ acceleration signals. The classical NExT loading case, black line, is compared with the three different loading cases, described in Figure 3.17, where temporal correlation, coloration, and coherence between forces is introduced, colored lines.

The time delay between the loads, acting at the 3$^{\text{rd}}$ and 9$^{\text{th}}$ location, introduces humps in the magnitude of the cross-PSDs, see the relevant distortion comparing the black line, referred to uncorrelated white noises case, and the blue one, where temporal correlation is reproduced. The coloration effect arises looking at the energy distribution in frequency of the blue and purple line, corresponding to the colored case. Coherence between the excitations, simulated according to an exponential law, produces the expected attenuation of humps with increasing frequency.

	Natural Frequency (Hz)	Damping Ratio (%)
Mode 1	22.1102	1.9463
Mode 2	58.5501	2.0002
Mode 1T	109.655	1.4797
Mode 3	117.967	1.4875

Table 3.7: PTFE beam system: natural frequencies and damping ratios extracted by classical modal analysis techniques [152].

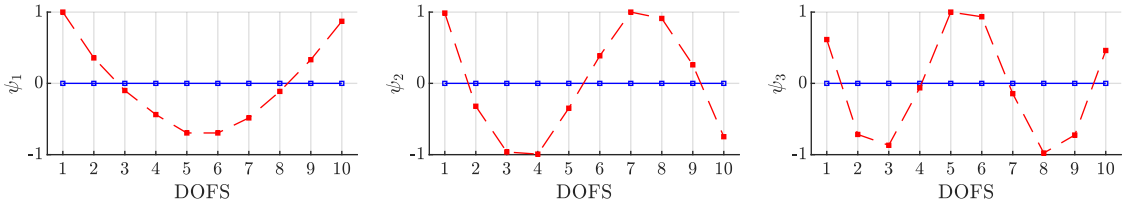

Figure 3.19: PTFE beam system: mode shapes extracted by classical modal analysis techniques. Blue dots: underformed nodes; red squares: deformed nodes.

In the following sections, the identification procedure is performed operating in the frequency band $10 - 160$ Hz that contains the first three flexural modes (along with a torsional one, around 110 Hz, which further emerges in some loading conditions despite sensor and force locations) extracted by classical modal analysis techniques [152] and collected in Table 3.7 and Figure 3.19. Three loading cases are investigated each focused on verifying the coloration, temporal correlation, and coherence impact on the two OMA procedures put into real-world experimental scenarios.

3.4.2.1 Effect of temporal correlation

3.4.2.1.1 First identification step: pLSCF

Starting from the loading case of temporal correlated white noises, one can write the eLMFD embedding in the numerator matrix the knowledge of τ, as done in Eq. (3.73) for the equivalent numerical case study.

In violating the NExT assumption by temporal correlation, it is observe an extremely confusing stabilisation diagram, see Figure 3.20a, which doesn't allow the analyst to easily select stable poles. For this reason poles' selection is forced in correspondence of the expected natural frequencies, in order to follow up on the identification procedure with estimated modal parameter comparison. On the other hand, the pLSCF solution based on the eLMFD leads to a stabilisation diagram extremely clean, allowing an easily selection of the stable poles, as evident is Figure 3.20b. Furthermore, it is noticed how the stabilisation of the first

pole requires an high model order because of the low signal level (the first mode results less excited in the particular loading case), that's another story for the two subsequent modes who show full stabilisation since the lowest model order.

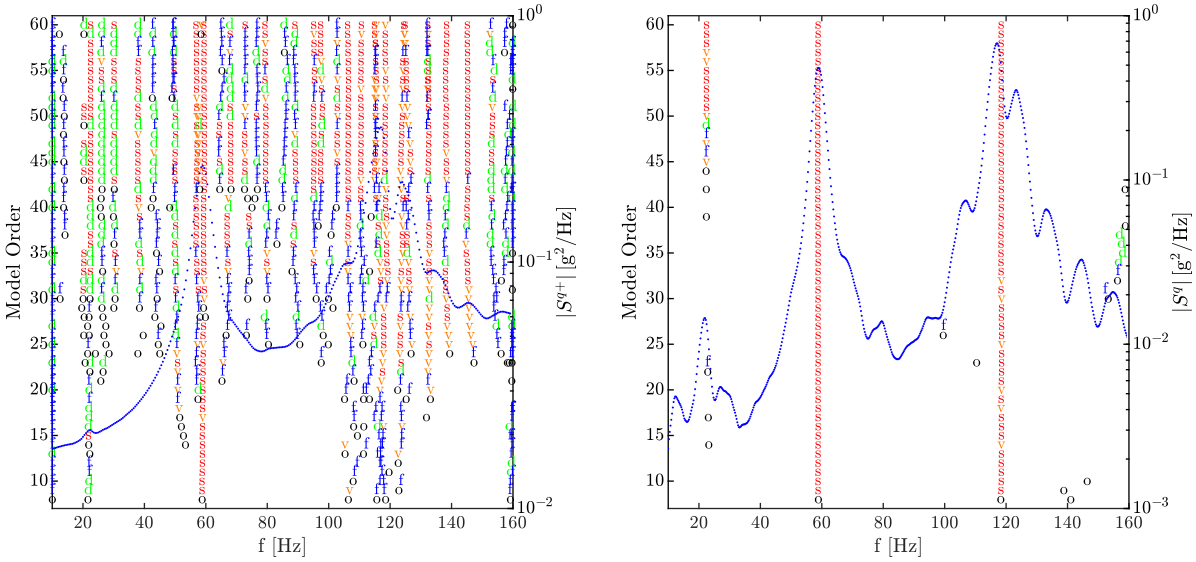

(a) OMA (b) G-OMA

Figure 3.20: Identification of the experimental system: stabilisation diagram along with the magnitude of the PSDs sum function, blue dotted line. The model order is indicated on the left ordinate axis. '`o`': new pole; '`f`' stabilisation in natural frequency; '`f`' extra stabilisation in damping ratio; '`v`' extra stabilisation in MAC value; '`s`' full stabilisation. Stabilisation thresholds for natural frequency, damping ratio, and MAC value are 1%, 5%, and 2%, respectively.

Once pole selection is performed, results are collected in Table 3.8. Estimated natural frequencies show low error values (less than 2%) with respect to the theoretical ones for both the approaches. Errors related to damping ratios are significantly improved by the G-OMA procedure exhibiting deviation below 10% from the estimates found by classical modal analysis techniques.

		Natural Frequency (Hz)		Damping Ratio (%)	
		Estimated	$\lvert\Delta\rvert$(%)	Estimated	$\lvert\Delta\rvert$(%)
OMA	Mode 1	22.5207	1.8565	6.0627	211.4992
	Mode 2	59.3786	1.4150	2.8176	40.8662
	Mode 3	118.4341	0.3960	1.2571	15.4929
G-OMA	Mode 1	22.3420	1.0484	2.1091	8.3643
	Mode 2	58.7194	0.2892	2.1525	7.6143
	Mode 3	118.5647	0.5066	1.4129	5.0145

Table 3.8: Comparison between exact and estimated natural frequencies. Estimates computed by using classical and generalized OMA formulations are compared. Percentage relative error, $\Delta = 100 \times (v_{\text{ref}} - v_{\text{est}})/v_{\text{ref}}$, with respect to reference value is reported nearby each estimate.

Figure 3.21 displays the pertinent MAC between reference and estimated modal vector sets: good values arise for both modal vectors' sets. However, it is relevant to highlight that the OMA results are strictly related to a forced selection on the stabilisaton chart in Figure 3.20a, that becomes cumbersome in practice.

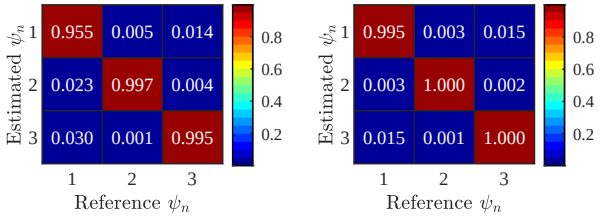

(a) OMA (b) G-OMA

Figure 3.21: MAC between reference and estimated modal vectors' sets estimated by following (a) the classical OMA procedure and (b) the generalized approach proposed in the paper.

3.4.2.1.2 Second identification step: LSFD

In this loading case, the frequency-dependent operational vector, referred to the n-th pole, can be written as

$$\boldsymbol{\rho}_n(\mathrm{i}\omega) = \bar{\boldsymbol{g}}_n^0 + \mathrm{e}^{\mathrm{i}\omega\tau}\bar{\boldsymbol{g}}_n^{12} + \mathrm{e}^{-\mathrm{i}\omega\tau}\bar{\boldsymbol{g}}_n^{21}, \tag{3.76}$$

where τ, temporal delay between the loads, is assumed to be a known feature. As in the numerical scenario, the G-OMA method achieves good fitting as turned out by the visual match, see Figure 3.22b, and by the high correlation coefficients and low normalized errors

shown in Figure 3.23b. The suitable definition of the operational reference vector in Eq. (3.76) guarantees positive results of the generalized LSFD. Instead, the classical LSFD leads to smaller correlation coefficients and higher errors than the proposed approach, Figure 3.23a, owing to a lack of description of the time delay terms in the modal decomposition, as can be seen in Figure 3.22a.

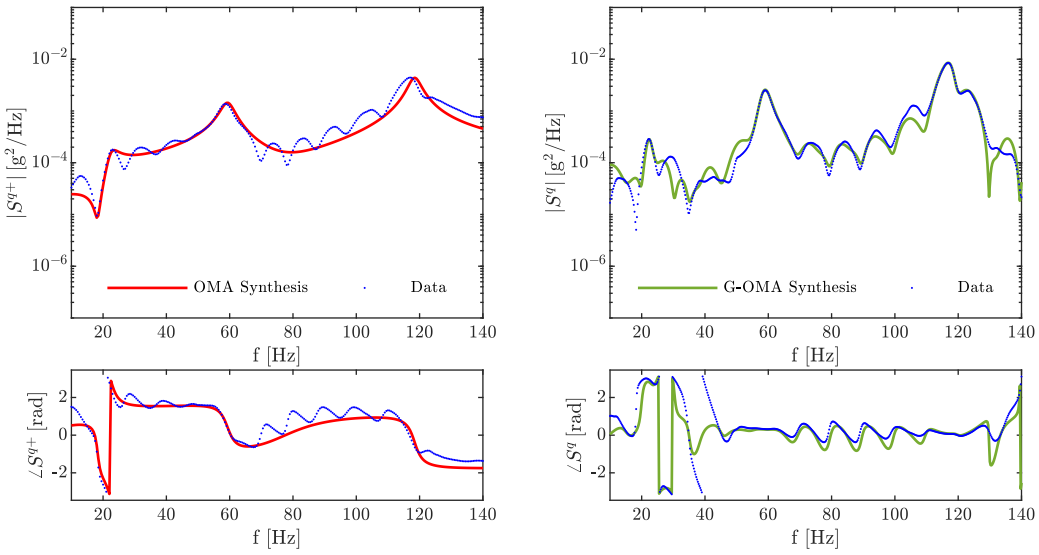

(a) OMA (b) G-OMA

Figure 3.22: Experimental beam under temporal-correlated white noises: (a) comparison between one measured positive power spectrum, blue dotted line, and the relevant synthesis obtained by the OMA modal model, red solid line; (b) G-OMA modal model synthesis, green solid line, of one measured output PSD, blue dotted line. The chosen matrix entry relates the 10^{th} and 5^{th} accelerations in the both plots.

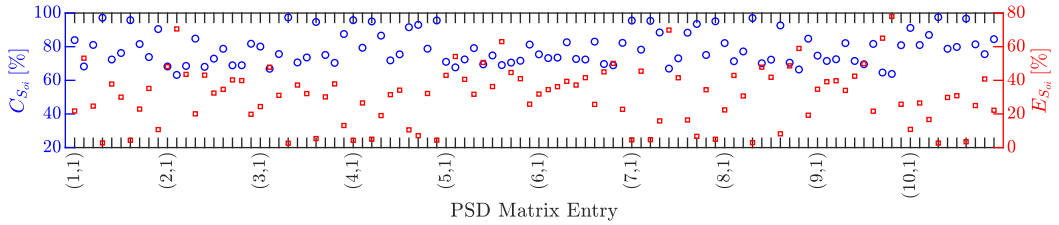

(a) OMA

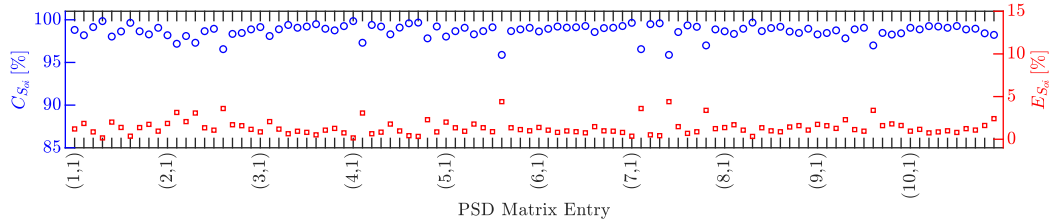

(b) G-OMA

Figure 3.23: Experimental beam under temporal-correlated white noises: correlation coefficients Eq. (1.59), blue circles, and normalized errors Eq. (1.60), red squares, related to one hundred spectra employed in the identification tackled by the (a) OMA and (b) G-OMA approach.

3.4.2.2 Effect of temporal correlation and coloration

3.4.2.2.1 First identification step: pLSCF

As a second loading case, it is explored that of temporal correlated colored noises that corresponds to the following definition of extended numerator matrix $\mathbf{N}^{(e)}(\omega)$

$$\mathbf{N}^{(e)}(k) = \frac{1}{\omega_k^2 + \omega_0^2} \sum_{r=0}^{p} z_k^{-r} \bar{\boldsymbol{\beta}}_r^0 + \frac{1}{\omega_k^2 + \omega_0^2} \mathrm{e}^{\mathrm{i}\omega_k \tau} \sum_{r=0}^{p} z_k^{-r} \bar{\boldsymbol{\beta}}_r^{12} + \frac{1}{\omega_k^2 + \omega_0^2} \mathrm{e}^{-\mathrm{i}\omega_k \tau} \sum_{r=0}^{p} z_k^{-r} \bar{\boldsymbol{\beta}}_r^{21}, \quad (3.77)$$

where the three unknowns $\bar{\boldsymbol{\beta}}_r^0$, $\bar{\boldsymbol{\beta}}_r^{12}$ and $\bar{\boldsymbol{\beta}}_r^{21}$ appear. As previously experienced, pole selection is quite challenging when applied on the stabilisation diagram obtained by the classical OMA procedure, see Figure 3.24a. But instead, the eLMFD reaches higher quality chart with three emerging stable pole lines. The stabilisation of the first pole starts from a lower model order, with respect to Figure 3.20b, because of the different energy distribution induced by the colored forces.

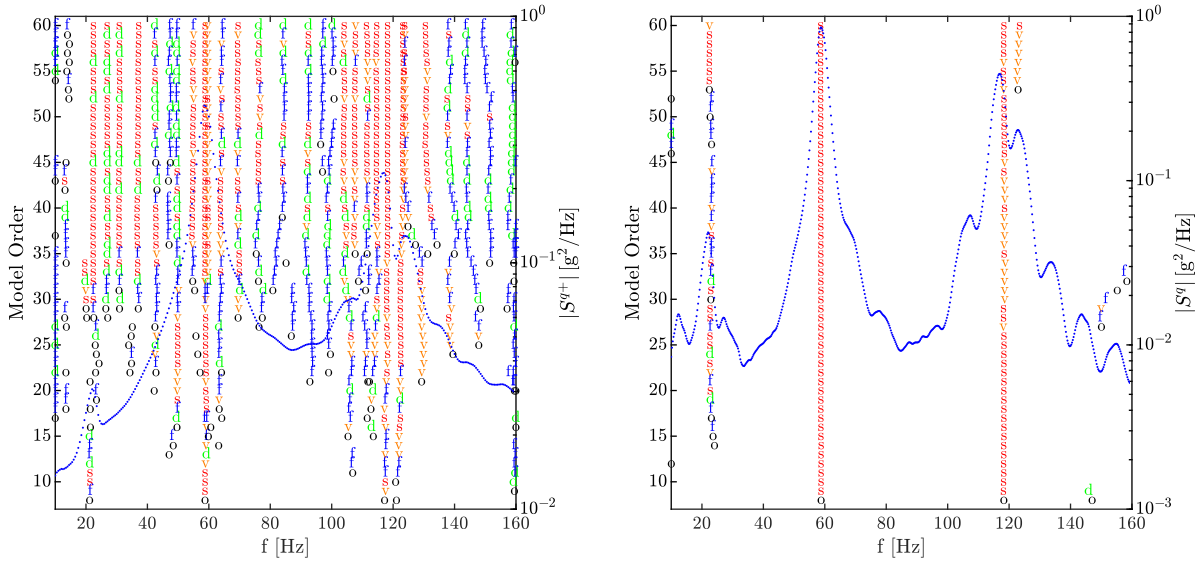

(a) OMA (b) G-OMA

Figure 3.24: Identification of the experimental system: stabilisation diagram along with the magnitude of the PSDs sum function, blue dotted line. The model order is indicated on the left ordinate axis. '`o`': new pole; '`f`' stabilisation in natural frequency; '`f`' extra stabilisation in damping ratio; '`v`' extra stabilisation in MAC value; '`s`' full stabilisation. Stabilisation thresholds for natural frequency, damping ratio, and MAC value are 1%, 5%, and 2%, respectively.

By analyzing results in Table 3.9, you notice similar performances of the two approaches in the natural frequency estimation but the G-OMA procedure enhances damping ratios achievement. Figure 3.25 reports the relevant MAC values revealing comparable mode shapes estimate. In practical case, the poles selection with classical OMA still remains challenging.

		Natural Frequency (Hz)		Damping Ratio (%)	
		Estimated	$\lvert\Delta\rvert$(%)	Estimated	$\lvert\Delta\rvert$(%)
OMA	Mode 1	22.4333	1.4611	5.7523	195.5505
	Mode 2	58.8215	0.4635	2.4538	22.6786
	Mode 3	118.2021	0.1993	1.4239	4.2745
G-OMA	Mode 1	22.4464	1.5208	1.9669	1.0593
	Mode 2	58.7111	0.2749	2.1759	8.7851
	Mode 3	118.3506	0.3252	1.3659	8.1741

Table 3.9: Comparison between exact and estimated natural frequencies. Estimates computed by using classical and generalized OMA formulations are compared. Percentage relative error, $\Delta = 100 \times (v_{\text{ref}} - v_{\text{est}})/v_{\text{ref}}$, with respect to reference value is reported nearby each estimate.

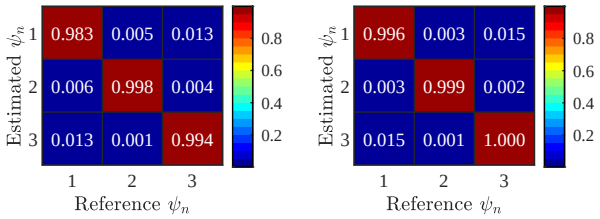

(a) OMA (b) G-OMA

Figure 3.25: MAC between reference and estimated modal vectors' sets estimated by following (a) the classical OMA procedure and (b) the generalized approach proposed in the paper.

3.4.2.2.2 Second identification step: LSFD

In this second loading case, the following definition of extended frequency-dependent operational vector is revealed

$$\boldsymbol{\rho}_n(\mathrm{i}\omega) = \frac{1}{\omega^2+\omega_0^2}\bar{\boldsymbol{g}}_n^0 + \frac{1}{\omega^2+\omega_0^2}\mathrm{e}^{\mathrm{i}\omega\tau}\bar{\boldsymbol{g}}_n^{12} + \frac{1}{\omega^2+\omega_0^2}\mathrm{e}^{-\mathrm{i}\omega\tau}\bar{\boldsymbol{g}}_n^{21}, \tag{3.78}$$

where again the three unknown vectors $\bar{\boldsymbol{g}}_n^0$, $\bar{\boldsymbol{g}}_n^{12}$, and $\bar{\boldsymbol{g}}_n^{21}$ are accessed by the modified LSFD. In Figure 3.26b, the good agreement between the measured and synthesized PSDs is confirmed by the correlation coefficients and errors in Figure 3.27b. On the other hand, the classical OMA second identification step achieves slightly poorer results in terms of errors and correlation coefficients as reflected in Figure 3.27a. This deficiency finds reason in the usual approximation introduced by the definition of constant operational reference vectors which doesn't fit the typical distorsion caused by the temporal correlation in both phase and magnitude of the postive spectra, as shown Figure 3.26a.

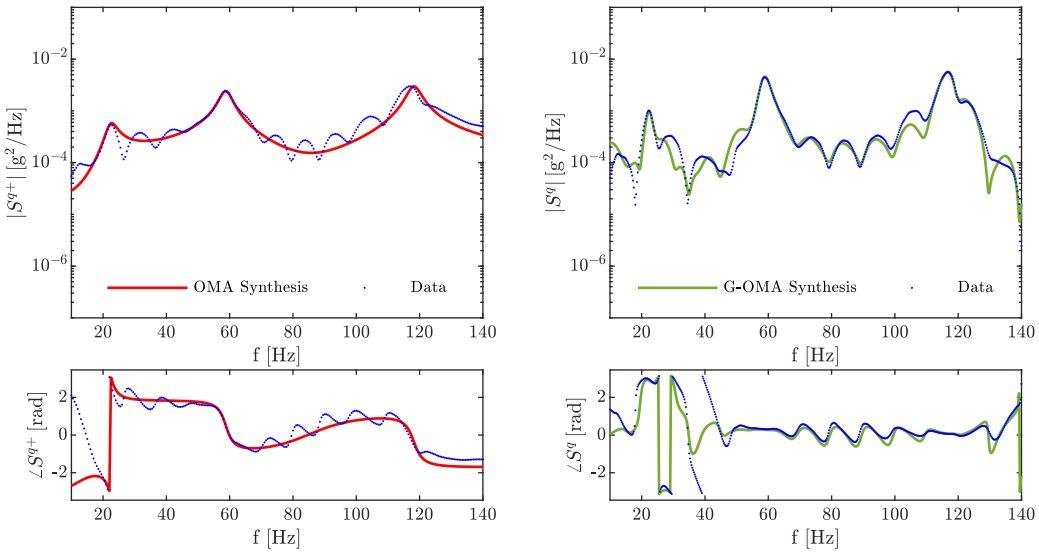

(a) OMA (b) G-OMA

Figure 3.26: Experimental beam under temporal-correlated colored noises: (a) comparison between one measured positive power spectrum, blue dotted line, and the relevant synthesis obtained by the OMA modal model, red solid line; (b) G-OMA modal model synthesis, green solid line, of one measured output PSD, blue dotted line. The chosen matrix entry relates the 10^{th} and 5^{th} accelerations in the both plots.

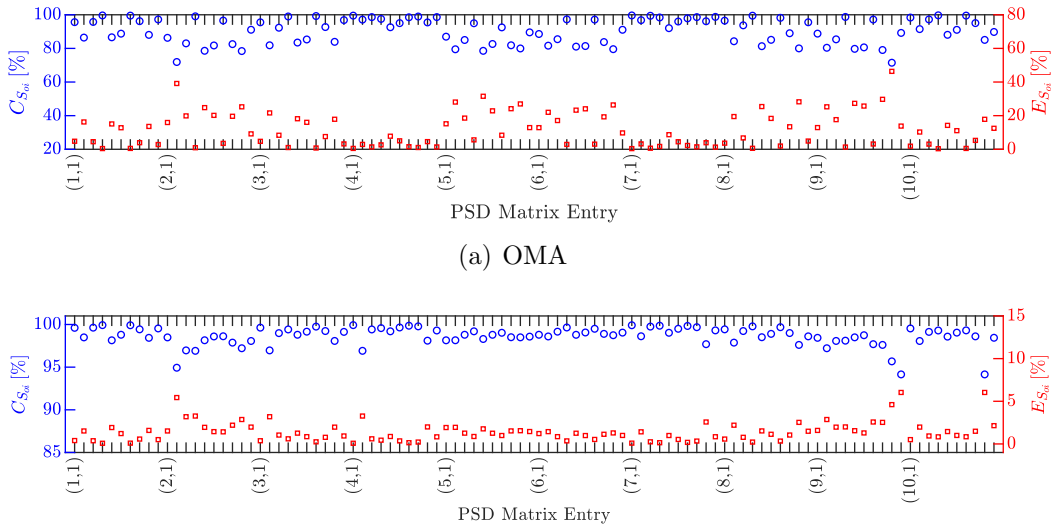

(a) OMA

(b) G-OMA

Figure 3.27: Experimental beam under temporal-correlated colored noises: correlation coefficients Eq. (1.59), blue circles, and normalized errors Eq. (1.60), red squares, related to one hundred spectra employed in the identification tackled by the (a) OMA and (b) G-OMA approach.

3.4.2.3 Effect of temporal correlation, coloration, and coherence

3.4.2.3.1 First identification step: pLSCF

Finally, the three no-NExT effects here investigated ae combined. So, in this loading condition the designed $\mathbf{N}^{(e)}(\omega)$ is expressed as

$$\mathbf{N}^{(e)}(k) = \frac{1}{\omega_k^2+\omega_0^2}\sum_{r=0}^{p} z_k^{-r}\bar{\boldsymbol{\beta}}_r^0 + \frac{1}{\omega_k^2+\omega_0^2}\mathrm{e}^{-\alpha|\omega_k|}\mathrm{e}^{\mathrm{i}\omega_k\tau}\sum_{r=0}^{p} z_k^{-r}\bar{\boldsymbol{\beta}}_r^{12} + \frac{1}{\omega_k^2+\omega_0^2}\mathrm{e}^{-\alpha|\omega_k|}\mathrm{e}^{-\mathrm{i}\omega_k\tau}\sum_{r=0}^{p} z_k^{-r}\bar{\boldsymbol{\beta}}_r^{21}, \tag{3.79}$$

where one can include the knowledge of the temporal delay τ together with the frequency dependence of coloration and coherence models.

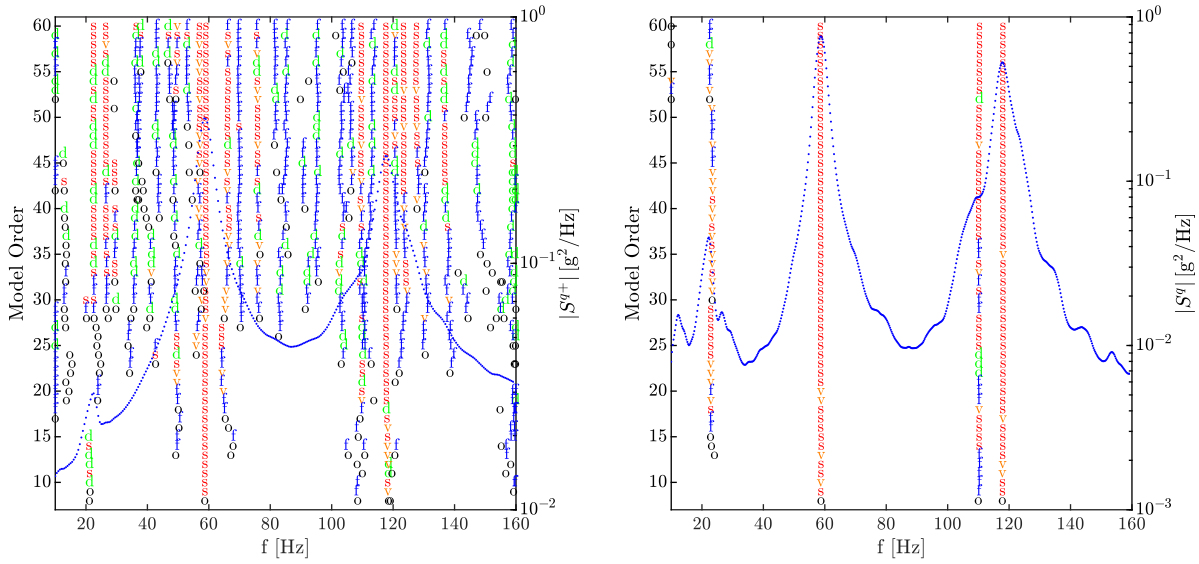

(a) OMA (b) G-OMA

Figure 3.28: Identification of the experimental system: stabilisation diagram along with the magnitude of the PSDs sum function, blue dotted line. The model order is indicated on the left ordinate axis. '`o`': new pole; '`f`' stabilisation in natural frequency; '`f`' extra stabilisation in damping ratio; '`v`' extra stabilisation in MAC value; '`s`' full stabilisation. Stabilisation thresholds for natural frequency, damping ratio, and MAC value are 1%, 5%, and 2%, respectively.

The two stabilisation diagrams in Figure 3.28 reveal different clarity highlighting the more accuracy of the G-OMA approach. The effect of coherence is reversed into the presence of a

fourth peak, see Figure 3.28b, related to the first torsional mode of the PTFE beam, that result more excited when the two loads loose correlation (as it happens at high frequency due to the effect of the coherence term $e^{-\alpha|\omega|}$). By looking at Figure 3.28a, pole selection is still quite challenging due to the stabilisation lines related to spurious mathematical poles deriving from the violation of the NExT assumption. By forcing selection in correspondence of the expected natural frequencies for the OMA stabilisation diagram, a comparison of the MPE results is established in Table 3.10 and Figure 3.29. The proposed identification procedure generally offers a better estimation for both frequencies and damping ratios as confirmed by the error values. Worse results are reached for the less excited modes, first flexural and torsional ones, because of the measurement noise effect. The MAC values reveal similar performances in terms of mode shapes estimate and they confirm the poor observability of the torsional mode related to force and sensor locations.

		Natural Frequency (Hz)		Damping Ratio (%)	
		Estimated	$\|\Delta\|$(%)	Estimated	$\|\Delta\|$(%)
OMA	Mode 1	22.4837	1.6893	5.1303	163.5944
	Mode 2	59.0800	0.9050	2.9887	49.4195
	Mode 1T	109.5787	0.0696	1.6697	12.8399
	Mode 3	117.6550	0.2645	2.0689	39.0821
G-OMA	Mode 1	22.5279	1.8890	0.9353	51.9459
	Mode 2	58.8164	0.4548	2.2579	12.8852
	Mode 1T	110.0922	0.3987	1.0549	28.7080
	Mode 3	117.9556	0.0097	1.3484	9.3519

Table 3.10: Comparison between exact and estimated natural frequencies. Estimates computed by using classical and generalized OMA formulations are compared. Percentage relative error, $\Delta = 100 \times (v_{\text{ref}} - v_{\text{est}})/v_{\text{ref}}$, with respect to reference value is reported nearby each estimate.

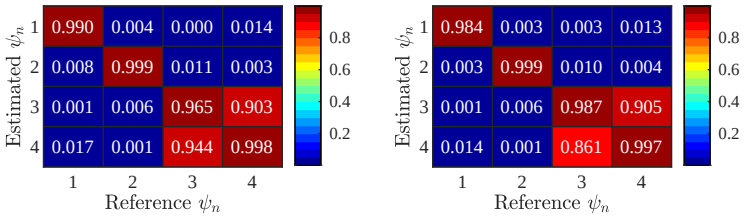

(a) OMA (b) G-OMA

Figure 3.29: MAC between reference and estimated modal vectors' sets estimated by following (a) the classical OMA procedure and (b) the generalized approach proposed in the paper.

3.4.2.3.2 Second identification step: LSFD

This last loading case is characterized by the frequency-dependent operational reference vector as

$$\boldsymbol{\rho}_n(\mathrm{i}\omega) = \frac{1}{\omega^2+\omega_0^2}\bar{\boldsymbol{g}}_n^0 + \frac{1}{\omega^2+\omega_0^2}\mathrm{e}^{-\alpha|\omega|}\mathrm{e}^{\mathrm{i}\omega\tau}\bar{\boldsymbol{g}}_n^{12} + \frac{1}{\omega^2+\omega_0^2}\mathrm{e}^{-\alpha|\omega|}\mathrm{e}^{-\mathrm{i}\omega\tau}\bar{\boldsymbol{g}}_n^{21}, \tag{3.80}$$

which embeds some a priori known features regarding input correlation and coloration, such as the temporal delay τ and the frequency dependence of coloration and coherence models. In doing so, the generalized LSFD is exploited in order to estimate the three extended operational reference vectors $\bar{\boldsymbol{g}}_n^0$, $\bar{\boldsymbol{g}}_n^{12}$, and $\bar{\boldsymbol{g}}_n^{21}$ for each n-th pole.

It is highlighted the suitability of the G-OMA method emphasised by low errors, below 5%, and high correlation coefficients, greater than 95%, in Figure 3.31b. Furthermore, the classical LSFD shortcomings relapse into slightly greater errors, Figures 3.30a and 3.31a, whereas the poles' selection is enforced having poor stabilization charts.

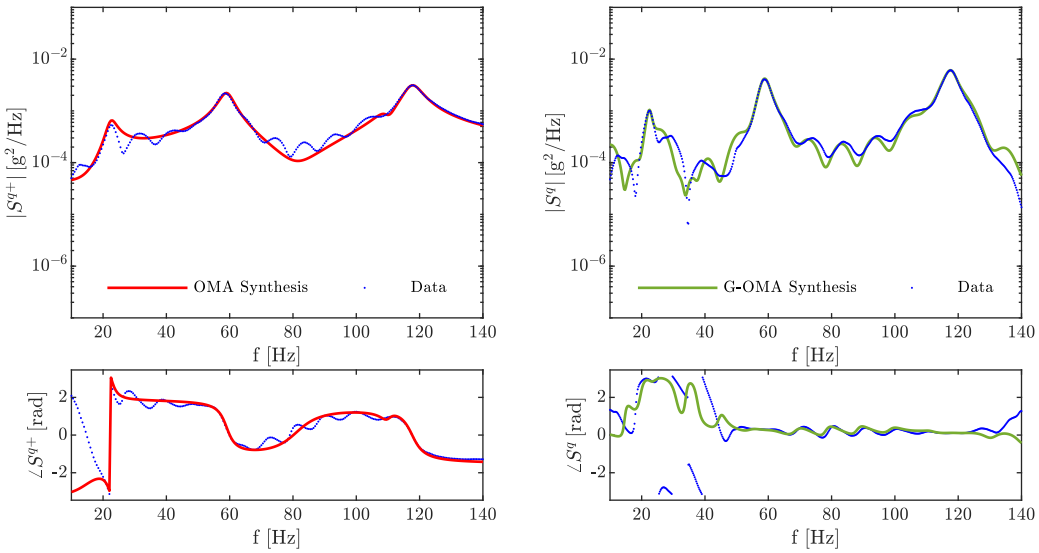

(a) OMA (b) G-OMA

Figure 3.30: Experimental beam under temporal-correlated colored coherent noises: (a) comparison between one measured positive power spectrum, blue dotted line, and the relevant synthesis obtained by the OMA modal model, red solid line; (b) G-OMA modal model synthesis, green solid line, of one measured output PSD, blue dotted line. The chosen matrix entry relates the 10^{th} and 5^{th} accelerations in the both plots.

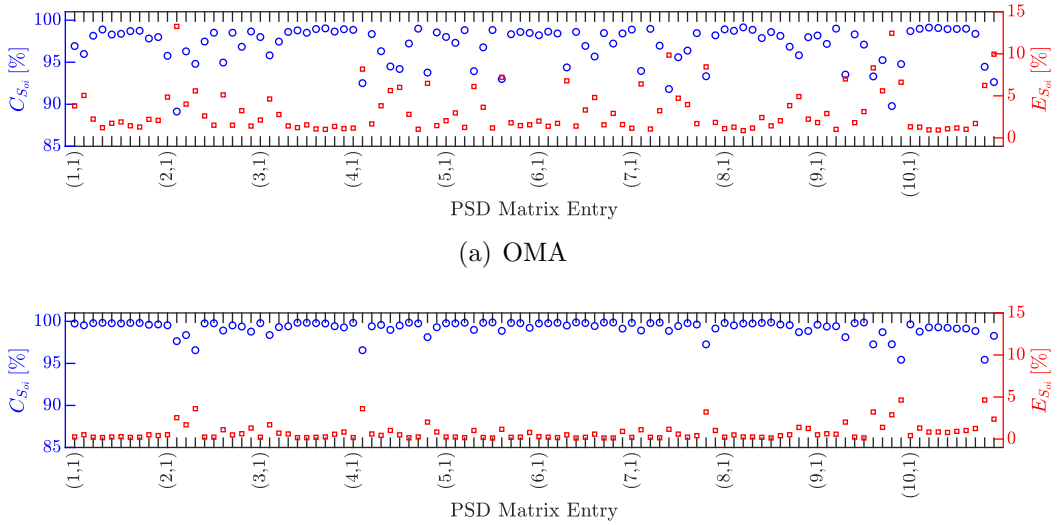

(a) OMA

(b) G-OMA

Figure 3.31: Experimental beam under temporal-correlated colored coherent noises: correlation coefficients Eq. (1.59), blue circles, and normalized errors Eq. (1.60), red squares, related to one hundred spectra employed in the identification tackled by the (a) OMA and (b) G-OMA approach.

In a nutshell

1. *Development of an OMA framework which overcomes the NExT assumption: generalized modal formulation of both the output cross-correlation and power spectral density functions.*
2. *The role of the frequency-dependent operational reference vectors as a generalization of the classical ORV embedding some a priori known input correlation features.*
3. *Identification technique in the frequency domain: the introduction of an extended left matrix fraction description, realization into the state-space and pLSCF solution for coefficient matrices calculation. The LSFD step for extended operational reference vectors achievement.*
4. *Modal parameter estimation in numerical and experimental case studies: investigating the effects of different infringements of the NExT assumption, such as coloration, temporal correlation, and coherence.*

Part II

On the role of a particular class of global transmissibility functions: the R-FRFs

Chapter 4

R-FRFs: definition and estimation

Contents

4.1 Introduction

Many different modal analysis besed protocols have been developed over the last four decades in the area of system dynamics with unconnected aims, from model updating to diagnostics. With regards to only the last-mentioned, also commonly named structural health monitoring (SHM) or damage detection, an extraordinarily important number of

research efforts has been made available. A reasonable citation base could be found, for example, in refs. [61, 62, 63, 107, 137], where devices, physical quantities, methods and perspectives involved in the numerous numerical and / or experimental protocols proposed in the scientific literature are illustrated and discussed. The devices comprise all possible transducers (typically, but not exhaustively, accelerometers and load cells) and the relevant conditioning systems followed by A/D digital boards. Transfer functions appear to be the most representative and commonly adoptred physical quantities, computed by measurements' processing, and, specifically, frequency response functions (FRFs), generally in the form of the ratio of forces and output accelerations (accelerances or apparent masses). However, FRFs could be seen, from a wider perspective, as functions relating different outputs of a linear time invariant system. In such a latter perspective, during the last two decades, researchers have started investigating transmissibility functions (see e.g. [38, 39, 100, 101, 134, 135, 138, 160]). In particular, Ribeiro [134] started generalizing a transmissibility concept from one degree of freedom systems to structures with multiple degrees of freedom. Specifically, he obtained a relationship between vectors of unknown responses and measurable responses, along with a pseudo-inversion when certain conditions between the number of interesting responses (known/measured and unknown) are not fulfilled. By his theoretical analyses, Ribeiro introduced a new concept that seemed to be promising not only as a monitoring tool, but even for its predictive capability. The results of this effort were also extended to a wider audience two years later (see Ribeiro et al. [135]). Sampaio et al. [138], used the transmissibility concept in the area of damage detection. They noticed that more research efforts would have been needed to better understand and explore all the possible improvements in the usage of the technique. With regards to this topic, other interesting contributions [38, 39, 100, 138] have been produced in the following years. Maia et al. [101] presented a general overview on the transmissibility concept and on pros and cons, and on possible applications; they also recognized that no simple relationships (if any) could be stablished

between peaks and anti-peaks of transmissibility functions and FRFs. The recent paper from Yan et al. [160] certainly testifies the great interest on transmissibility-based system identification in the area of structural health monitoring, by discussing existing studies dealing with the concept and the usage of transmissibility functions; they, specifically conclude that proving the capabilities of employing transmissibilities in an unsupervised manner, in the field of damage localization, can be tough.

In addition, Messina [102] followed a different formal approach for defining a new class of transmissibility functions (the R-FRFs), specifically designed to enrich the intrinsic modal database of the system under study and to allow for analyzing the system in a local sense. Based on the definitions given by Yan et al. [160], the R-FRFs, similarly to TFs, are global transmissibility functions. However, R-FRFs offer important and indisputable advantages if compared to the TFs. Firstly, while R-FRFs relate sets of responses in a rectangular way, but no pseudo-inversion is requested to recover $\mathbf{R}(\omega)$ (e.g. see experimental procedure suggested in [102]). Secondly, $\mathbf{R}(\omega)$, as discussed in reference [102] and experimentally proved in reference [103], is clearly correlated with the system under investigation with an easily understandable property: each transmissibility function in $\mathbf{R}(\omega)$ provides poles of the original structure when some of its degrees of freedom are, virtually, considered constrained to ground; thus, such a local sense is achieved when one virtually hampers the vibration of a specific part of the structure, but letting the remaining (and local) part to freely vibrate.

Of course, the evaluation of the output-only matrix $\mathbf{R}(\omega)$ does not require, in principle, the measurement of the exciting forces, even though we could take advantage of this information, if available, in an input-output manner. However, further insights, specifically aimed at improving R-FRFs estimation, are provided. To this aim, it is useful to recall the problem of classical FRF estimation, well established in the relevant literature [1, 10, 61]. Several estimators have been developed for MIMO linear systems and each estimator turns out to be optimal depending upon the balance of noise existing between inputs and outputs of the

system. In [70, 72], further nonparametric FRF estimators based on nonlinear averaging techniques are proposed. Some of them are the so-called H_{EV} and $H_{\log}$ estimators, which show better performance in reducing the bias caused by noisy data with respect to the classical H_1 and H_2. Global transmissibility functions, including the case of the RFRFs, are generally estimated from output-only measurements, by using H_1 like approaches; the possibility of using H_2 and H_s has been also investigated in [93].

The rest of the chapter is organized as follows. In Section 4.2, the theoretical background is presented regarding the response-based frequency response functions of the linear time invariant systems herein we deal with; such a theoretical background is formulated and illustrated with the view to the estimation of R-FRFs. In Section 4.3, RFRFs' estimators are introduced by redefining classical MIMO systems' estimators for FRFs and the possibility of exploiting input-output estimators, where exciting force are measured, is shown. In Section 4.4, numerical and experimental case studies are implemented, to evaluate the performance of estimators presented in Section 4.3.

4.2 R-FRFs definition

A linear, time-invariant, damped, vibrating system having N degrees of freedom (dofs) is considered. The set of second order motion equations for this system, is formulated in matrix notation as

$$\mathbf{M}\ddot{\mathbf{x}}(t) + \mathbf{C}\dot{\mathbf{x}}(t) + \mathbf{K}\mathbf{x}(t) = \mathbf{f}(t), \tag{4.1}$$

where $\mathbf{M}$, $\mathbf{C}$, and $\mathbf{K}$ are the mass, damping, and stiffness matrices, respectively, and $\mathbf{f}(t)$ and $\mathbf{x}(t)$ are the force and displacement vectors as functions of the time t. Assuming that the forces exerted on the system are applied only to a given subset of n forced or driving dofs and that the remaining $m = N - n$ measured dofs are not forced, and Laplace-transforming Eq. (4.1), with s the Laplace variable, we obtain the well-known input-output relationship:

$\mathbf{B}(s)\,\mathbf{X}(s) = \mathbf{F}(s)$, in which the dynamic stiffness matrix $\mathbf{B}(s)$, and the displacement $\mathbf{X}(s)$ and force $\mathbf{F}(s)$ vectors can be partitioned as

$$\left[\begin{array}{c|c} \mathbf{B}_{11}(s)_{n\times n} & \mathbf{B}_{12}(s)_{n\times m} \\ \hline \mathbf{B}_{21}(s)_{m\times n} & \mathbf{B}_{22}(s)_{m\times m} \end{array}\right] \left(\begin{array}{c} \mathbf{Z}(s)_{n\times 1} \\ \hline \mathbf{Y}(s)_{m\times 1} \end{array}\right) = \left(\begin{array}{c} \mathbf{Q}(s)_{n\times 1} \\ \hline \mathbf{0}_{m\times 1} \end{array}\right). \tag{4.2}$$

Specifically, the displacement vector $\mathbf{Z}(s)$ includes the n output response dofs in which the input forces described by the vector $\mathbf{Q}(s)$ are applied (we define such dofs as forced or driving), whilst the $\mathbf{Y}(s)$ vector contains the output displacements of the m unforced dofs (we define such dofs as guided or free). In this regard, Figure 4.1 clarifies the arrangement that we assume on the specific system under investigation, by stressing the fact that no hypothesis is made neither on the place of both the classes of dofs (driving and guided), nor on their respective number n and m, which can be arbitrarily different.

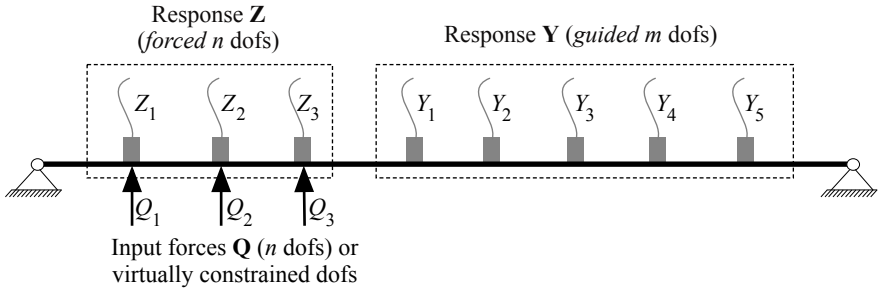

Figure 4.1: Sets of responses for a structure.

Therefore, the choice of which dofs are considered driving or free is absolutely arbitrary; moreover, the force applied to a certain driving dof can even be equal to zero, and, nonetheless, included in vector $\mathbf{Q}(s)$. By rephrasing the subset of motion equations related to the m free dofs, the following linear relationship, involving the sole output responses $\mathbf{Y}(s)$ and $\mathbf{Z}(s)$, is obtained

$$\mathbf{Y}(s) = \mathbf{R}(s)\mathbf{Z}(s), \tag{4.3}$$

where

$$\mathbf{R}(s) = -\mathbf{B}_{22}^{-1}(s)\mathbf{B}_{21}(s) \tag{4.4}$$

with $(.)^{-1}$ denoting an inverse matrix. $\mathbf{R}(s)$ is a $m \times n$ response-based transfer matrix containing the R-FRFs, connecting driving and free dofs. Since the analyst does not usually know in advance $\mathbf{R}(s)$ in situ, the objective of the study is to achieve its best estimation, through measurable entities, as the responses $(\mathbf{Y}, \mathbf{Z})$ appearing in Eq. (4.3). Moreover, different estimation procedures, both by accounting for the measurements of forces or not, will be exploited. To this end, Eq. (4.3) is reformulated in terms of classical transfer functions (i.e., FRFs). Thus, by rephrasing Eq. (4.2) as $\mathbf{X}(s) = \mathbf{H}(s)\mathbf{F}(s)$, where $\mathbf{H}(s) = \mathbf{B}(s)^{-1}$ is the system transfer function matrix, and specifying, as before, the matrix and vector partitions related to driving and free dofs, it is found

$$\left(\begin{array}{c} \mathbf{Z}(s)_{n\times 1} \\ \hline \mathbf{Y}(s)_{m\times 1} \end{array}\right) = \left[\begin{array}{c|c} \mathbf{H}_{11}(s)_{n\times n} & \mathbf{H}_{12}(s)_{n\times m} \\ \hline \mathbf{H}_{21}(s)_{m\times n} & \mathbf{H}_{22}(s)_{m\times m} \end{array}\right] \left(\begin{array}{c} \mathbf{Q}(s)_{n\times 1} \\ \hline \mathbf{0}_{m\times 1} \end{array}\right), \tag{4.5}$$

from which, by considering the subset of motion equations related to the n driving dofs, it is first derived

$$\mathbf{Q}(s) = \mathbf{H}_{11}^{-1}(s)\mathbf{Z}(s). \tag{4.6}$$

By substituting this expression of force vector $\mathbf{Q}(s)$ in the subset of motion equations related to the m free dofs, Eq. (4.3) is re-obtained in the form

$$\mathbf{Y}(s) = \mathbf{H}_{YQ}(s)\mathbf{H}_{ZQ}^{-1}(s)\mathbf{Z}(s) = \mathbf{R}(s)\mathbf{Z}(s), \tag{4.7}$$

where $\mathbf{H}_{11}(s)$ and $\mathbf{H}_{21}(s)$ are, respectively, indicated as $\mathbf{H}_{ZQ}(s)$ and $\mathbf{H}_{YQ}(s)$, to better highlight the existing connections between each partition matrix and the corresponding related subsets of output responses. As elucidated later, Eq. (4.7) provides the possibility of estimating, within the framework of MIMO systems' procedures, the $\mathbf{R}(s)$ matrix even

by taking into account the exciting forces. Eq. (4.3) can be easily derived from Eq. (4.7) recalling the relation between the system transfer function matrix, $\mathbf{H}(s)$, and the dynamic stiffness matrix, $\mathbf{B}(s)$, written in the following partitioned form

$$\left[\begin{array}{c|c} \mathbf{B}_{11}(s) & \mathbf{B}_{12}(s) \\ \hline \mathbf{B}_{21}(s) & \mathbf{B}_{22}(s) \end{array}\right] \left[\begin{array}{c|c} \mathbf{H}_{11}(s) & \mathbf{H}_{12}(s) \\ \hline \mathbf{H}_{21}(s) & \mathbf{H}_{22}(s) \end{array}\right] = \left[\begin{array}{c|c} \mathbf{I} & \mathbf{0} \\ \hline \mathbf{0} & \mathbf{I} \end{array}\right], \tag{4.8}$$

from which we obtain the partition $\mathbf{H}_{YQ}(s) = \mathbf{H}_{21}(s)$ as

$$\mathbf{H}_{21} = -\mathbf{B}_{22}^{-1}\mathbf{B}_{21}\mathbf{H}_{11}. \tag{4.9}$$

By substituting the expression of $\mathbf{H}_{YQ}(s)$ in Eq. (4.7), the definition of $\mathbf{R}(s)$ matrix is readily recovered in terms of dynamic stiffness matrix partitions, reported in Eq. (4.3).

Equation (4.3), translated in the Fourier domain by imposing $s = \mathrm{i}\omega$, can be even written in terms of cross-power spectral densities (cPSDs), as

$$\mathbf{S}_{YZ}(\mathrm{i}\omega) = \mathbf{R}(\mathrm{i}\omega)\mathbf{S}_{ZZ}(\mathrm{i}\omega), \tag{4.10}$$

$$\mathbf{S}_{YY}(\mathrm{i}\omega) = \mathbf{R}(\mathrm{i}\omega)\mathbf{S}_{ZY}(\mathrm{i}\omega), \tag{4.11}$$

with ω which refers to the radian frequency and the matrices $\mathbf{S}_{YZ}(\mathrm{i}\omega)$, $\mathbf{S}_{ZZ}(\mathrm{i}\omega)$, $\mathbf{S}_{YY}(\mathrm{i}\omega)$, $\mathbf{S}_{ZY}(\mathrm{i}\omega)$ are the partitions of the cross-power spectral density matrix of system displacements, which reads

$$\mathbf{S}_{XX}(\mathrm{i}\omega) = \left[\begin{array}{c|c} \mathbf{S}_{ZZ}(\mathrm{i}\omega)_{n\times n} & \mathbf{S}_{ZY}(\mathrm{i}\omega)_{n\times m} \\ \hline \mathbf{S}_{YZ}(\mathrm{i}\omega)_{n\times n} & \mathbf{S}_{YY}(\mathrm{i}\omega)_{n\times m} \end{array}\right], \tag{4.12}$$

while the entries of $\mathbf{R}(\mathrm{i}\omega)$ are transmissibility functions, here referred to as R-FRFs, as introduced in [102, 103].

4.3 Non-parametric estimation process

To perform the estimation of the $\mathbf{R}(\mathrm{i}\omega)$ matrix by directly using Eqs. (4.10) or (4.11), generally does not represent a workable option, owing to the required inversion of $\mathbf{S}_{ZZ}(\mathrm{i}\omega)$ and $\mathbf{S}_{ZY}(\mathrm{i}\omega)$ matrices, that rarely are of full rank or well conditioned [93]. A viable solution consists in gathering information from several different forcing conditions. Specifically, by considering a number of independent force vectors equal to that of the exciting dofs, and, thus, n independent experiments, relying on the linear relationship Eq. (4.3), which holds in each loading condition, the $\mathbf{R}(\mathrm{i}\omega)$ matrix is obtained as

$$\mathbf{R}(\mathrm{i}\omega) = \bar{\mathbf{Y}}(\mathrm{i}\omega)\bar{\mathbf{Z}}(\mathrm{i}\omega)^{-1}, \tag{4.13}$$

whereby $\bar{\mathbf{Y}}(\mathrm{i}\omega)$ indicates the $m \times n$ matrix of collected displacements of the not loaded, free dofs, that is $\bar{\mathbf{Y}}(\mathrm{i}\omega) = \begin{bmatrix} \mathbf{Y}_1(\mathrm{i}\omega) & \dots & \mathbf{Y}_n(\mathrm{i}\omega) \end{bmatrix}$, and $\bar{\mathbf{Z}}(\mathrm{i}\omega) = \begin{bmatrix} \mathbf{Z}_1(\mathrm{i}\omega) & \dots & \mathbf{Z}_n(\mathrm{i}\omega) \end{bmatrix}$ is the $n \times n$ matrix containing the output of the exciting dofs. By looking at Eq. (4.6), the invertibility of $\bar{\mathbf{Z}}(\mathrm{i}\omega)$ matrix is ensured by the fact that both the matrix partition $\mathbf{H}_{ZQ}(\mathrm{i}\omega)$ and the matrix collecting the n independent force vectors $\mathbf{Q}_i(\mathrm{i}\omega)$ are invertible [93, 102]. Thus, being the $\mathbf{R}(\mathrm{i}\omega)$ matrix a special case of FRF matrix, it can be assessed by applying the classical FRF estimators for MIMO linear systems. Transmissibility matrices are generally estimated by using an H_1 like approach and the possibility of using H_2 and H_s based procedures have also been investigated [93]. Here, the definitions of H_1 and H_2 estimators are reformulated and extended to the case of interest the $H_{\log}$, H_{EV}, and H_v measuring methods, derived from the literature of nonparametric FRF estimators [1, 72, 140].

4.3.1 Input-output estimation of the R matrix

The attractiveness of the $\mathbf{R}(\mathrm{i}\omega)$ matrix, expressed by its definition is related to the possibility of retrieving it from system responses only. It is, in fact, natively an output-only quantity. If the force signals are measured, an input-output estimator becomes available that we indicate $\mathbf{R}_{\mathrm{def}}$, suggested by Eq. (4.7)

$$\mathbf{R}_{\mathrm{def}}(\mathrm{i}\omega) = \tilde{\mathbf{H}}_{YQ}(\mathrm{i}\omega)\tilde{\mathbf{H}}_{ZQ}^{-1}(\mathrm{i}\omega), \tag{4.14}$$

where $\tilde{(.)}$ denotes estimated quantities and the matrix $\tilde{\mathbf{H}}(\mathrm{i}\omega)$ is the classically estimated FRF matrix of the system. In what follows, the estimator defined by Eq. (4.14) is used as a basis for the assessment of the presented output-only nonparametric estimators.

4.3.2 Classical FRF estimators applied to the R matrix

In a noisy environment, Eq. (4.13) allows for computing the empirical $\mathbf{R}_m$ estimate of the $\mathbf{R}(\mathrm{i}\omega)$ matrix, that differs from the exact one owing to the noises perturbing the responses at the exciting and free dofs. In fact, by assuming that the perturbation noises are additive, the linear relationship expressed by Eq. (4.13) can be rephrased as

$$\bar{\mathbf{Y}}(\mathrm{i}\omega) + \mathbf{n}_Y(\mathrm{i}\omega) = \mathbf{R}_m(\mathrm{i}\omega)\left(\bar{\mathbf{Z}}(\mathrm{i}\omega) + \mathbf{n}_Z(\mathrm{i}\omega)\right), \tag{4.15}$$

where $\mathbf{n}_Y$ and $\mathbf{n}_Z$ stand for the contribution of noises spectra at the free and exciting outputs, respectively.

The effect can be decreased by using generally nonlinear averaging techniques [72], which allow for introducing different estimators, obtained by performing the nonlinear mean associated with M independent observations of the matrices $\bar{\mathbf{Y}}(\mathrm{i}\omega)$ and $\bar{\mathbf{Z}}(\mathrm{i}\omega)$. A simple illustrative example is obtained by performing the arithmetic average of the M measured

$\mathbf{R}_{m,i}$, which leads to the following definition of the $\mathbf{R}_{\text{ar}}$ estimator

$$\mathbf{R}_{\text{ar}}(\mathrm{i}\omega) = \frac{1}{M}\sum_{i=1}^{M}\mathbf{R}_{m,i}(\mathrm{i}\omega). \tag{4.16}$$

Similarly, the $\mathbf{R}_{\log}$ estimator is computed by evaluating the logarithmic average of the M measured $\mathbf{R}_{m,i}$:

$$\mathbf{R}_{\log}(\mathrm{i}\omega) = \exp\left(\frac{1}{M}\sum_{i=1}^{M}\log\left(\mathbf{R}_{m,i}(\mathrm{i}\omega)\right)\right), \tag{4.17}$$

which allows for implementing the principle of the geometric mean. Moreover, it is introduced the unbiased errors-in-variables (EV) estimator, indicated as $\mathbf{R}_{\text{EV}}$, computed by preliminarily averaging out the matrices $\bar{\mathbf{Y}}_i$ and $\bar{\mathbf{Z}}_i$, as

$$\mathbf{R}_{\text{EV}}(\mathrm{i}\omega) = \left(\frac{1}{M}\sum_{i=1}^{M}\mathbf{Y}_i(\mathrm{i}\omega)\right)\left(\frac{1}{M}\sum_{i=1}^{M}\mathbf{Z}_i(\mathrm{i}\omega)\right)^{-1}, \tag{4.18}$$

where the convergence of the sums is ensured by the deterministic character of the excitation [70]. The three estimators Eqs. (4.16), (4.17) and (4.18) come from a re-conceptualization of the nonparametric FRF estimators proposed in [72].

The classical H_1, H_2, and H_v like approaches applied to Eq. (4.13) allow for introducing further output-only nonparametric estimators for the $\mathbf{R}(\mathrm{i}\omega)$ matrix. Specifically, by following an H_1 like route, applied to the matrix relationship Eq. (4.15), you obtain:

$$\begin{aligned}\sum_{i=1}^{n}\Big(\mathbf{S}_{Y_iZ_i}(\mathrm{i}\omega) + \mathbf{S}_{n_{Y_i}Z_i}(\mathrm{i}\omega) + \mathbf{S}_{Y_in_{Z_i}}(\mathrm{i}\omega) + \mathbf{S}_{n_{Y_i}n_{Z_i}}(\mathrm{i}\omega)\Big) = \\ \mathbf{R}_1(\mathrm{i}\omega)\sum_{i=1}^{n}\Big(\mathbf{S}_{Z_iZ_i}(\mathrm{i}\omega) + \mathbf{S}_{n_{Z_i}Z_i}(\mathrm{i}\omega) + \mathbf{S}_{Z_in_{Z_i}}(\mathrm{i}\omega) + \mathbf{S}_{n_{Z_i}n_{Z_i}}(\mathrm{i}\omega)\Big),\end{aligned} \tag{4.19}$$

where the present summands are cPSD matrices, evaluated considering noises and theoretical responses, and the sums are performed over the n different loading cases. Hypothesizing that the terms describing the correlation between the noises and the exact signals can be

considered negligible, it gets

$$\mathbf{R}_1(\mathrm{i}\omega) = \sum_{i=1}^{n} \mathbf{S}_{Y_i Z_i} \left(\sum_{i=1}^{n} \mathbf{S}_{Z_i Z_i} \right)^{-1} \left(\mathbf{I}_n + \sum_{i=1}^{n} \mathbf{S}_{n_{Z_i} n_{Z_i}} \left(\sum_{i=1}^{n} \mathbf{S}_{Z_i Z_i} \right)^{-1} \right)^{-1}, \tag{4.20}$$

where $\mathbf{I}_n$ is the $n \times n$ identity matrix, while the first term is equal to the exact $\mathbf{R}(\mathrm{i}\omega)$ written in terms of PSDs, for which the dependence on the radian frequency ω is omitted for brevity. Therefore, the $\mathbf{R}_1$ estimator is defined as

$$\mathbf{R}_1(\mathrm{i}\omega) = \mathbf{R}(\mathrm{i}\omega) \left(\mathbf{I}_n + \sum_{i=1}^{n} \mathbf{S}_{n_{Z_i} n_{Z_i}} \left(\sum_{i=1}^{n} \mathbf{S}_{Z_i Z_i} \right)^{-1} \right)^{-1}. \tag{4.21}$$

As in the case of the H_1 approach for the estimation of classical FRFs, $\mathbf{R}_1(\mathrm{i}\omega)$ produces a biased estimation due to noises perturbing the responses at the exciting dofs, which act as the inputs in the linear relation Eq. (4.13).

In a analogous manner, following an H_2 like path, the $\mathbf{R}_2$ estimator is introduced in the form

$$\mathbf{R}_2(\mathrm{i}\omega) = \left(\mathbf{I}_n + \sum_{i=1}^{n} \mathbf{S}_{n_{Y_i} n_{Y_i}} \left(\sum_{i=1}^{n} \mathbf{S}_{Y_i Y_i} \right)^{-1} \right) \mathbf{R}(\mathrm{i}\omega), \tag{4.22}$$

with similar meaning of adopted symbols; it even produces a biased estimation, owing to the noises on output responses at the not loaded, free dofs, which play the role of outputs in Eq. (4.13).

The above presented estimators are interpreted as the result of the solution of a linear regression problem, in which $\mathbf{R}_1(\mathrm{i}\omega)$ and $\mathbf{R}_2(\mathrm{i}\omega)$ minimise the overall vertical and horizontal squared error, respectively. In this context, the $\mathbf{R}_v$ estimator, that is interpreted as the Total Least Squares (TLS) solution, is obtained from the eigen-decomposition of the following

spectral correlation matrix [1, 158]:

$$\hat{\mathbf{R}}_{ZZY,p}(\mathrm{i}\omega) = \left[\begin{array}{c|c} \displaystyle\sum_{i=1}^{n} \mathbf{S}_{Z_i Z_i} & \left\langle \displaystyle\sum_{i=1}^{n} \mathbf{S}_{Y_i Z_i} \right\rangle_{p_{\mathrm{row}}} \\ \hline \left\{ \displaystyle\sum_{i=1}^{n} \mathbf{S}_{Z_i Y_i} \right\}_{p_{\mathrm{col}}} & \left(\displaystyle\sum_{i=1}^{n} \mathbf{S}_{Y_i Y_i} \right)_{pp} \end{array}\right]_{(n+1)\times(n+1)} = \mathbf{V}\boldsymbol{\Lambda}\mathbf{V}^{\mathrm{H}}, \tag{4.23}$$

where $(.)^{\mathrm{H}}$ indicates Hermitian transposition, $\boldsymbol{\Lambda}$ is the diagonal matrix of the eigenvalues and $\mathbf{V}$ is the matrix whose columns are the eigenvectors. The $p-$th row of the $\mathbf{R}(\mathrm{i}\omega)$ matrix is estimated, at each radian frequency ω, as the eigenvector associated with the smallest normalized eigenvalue, that we write as

$$\{\mathbf{V}\}_{\lambda_{\min}} = \left\{ \begin{array}{c} R_{p1} \\ R_{p2} \\ \vdots \\ R_{pn} \\ -1 \end{array} \right\}. \tag{4.24}$$

As for the previously presented estimators, the definition of $\mathbf{R}_1$, $\mathbf{R}_2$ and $\mathbf{R}_v$ estimators Eqs. (4.21), (4.22) and (4.24) is derived by means of a reformulation of the classical FRF estimators, when specifically applied to the case of the $\mathbf{R}(\mathrm{i}\omega)$ matrix.

4.4 Performance analysis of the R matrix estimators

In order to assess the performance of the presented estimators, two case studies are offered, the former employing the data achieved by numerically simulating a lumped-parameter system model, the latter processing the time records collected through real-world experiments of impact testing, performed on a slender beam of known geometry and material properties.

The considered discrete model, displayed in Figure 4.2, along with the pertinent nomenclature, consists in a 6-degrees-of-freedom system, comprising masses able to move only

along the horizontal direction, connected by springs and dashpots. The stiffness of all the springs is set to $10^4\,\mathrm{N\,m^{-1}}$, all the masses to 0.1 kg, and the system is subjected to a stiffness-proportional damping described by a damping matrix $\mathbf{C} = 5.0 \times 10^{-5}\,\mathbf{K}$. Thus, dashpots are not represented in the system sketch of Figure 4.2.

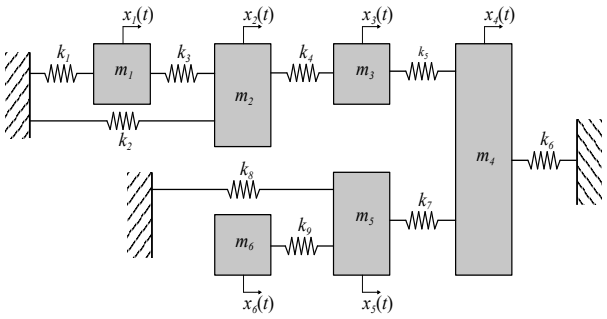

Figure 4.2: Schematic of the 6 degrees-of-freedom lumped-parameter system.

In Figure 4.3, the slender beam used to perform the impact testing experiments, is represented. Specifically, the specimen is a polymethyl methacrylate (Plexiglas, PMMA) beam of length, width, and thickness equal to 1000 mm, 60 mm, and 35 mm, respectively; material properties and resonance frequencies of the completely free PMMA beam are characterized and determined in [103]. In the adopted set-up, free-free boundary conditions are achieved by suspending the beam through extremely flexible elastic cords. The beam is forced by exerting impulsive loads through an instrumented impact hammer, hitting the beam along the x-direction, in ten equally spaced positions, where the output responses are even measured by ten accelerometers, attached to the beam's center-line, as shown in Figure 4.3.

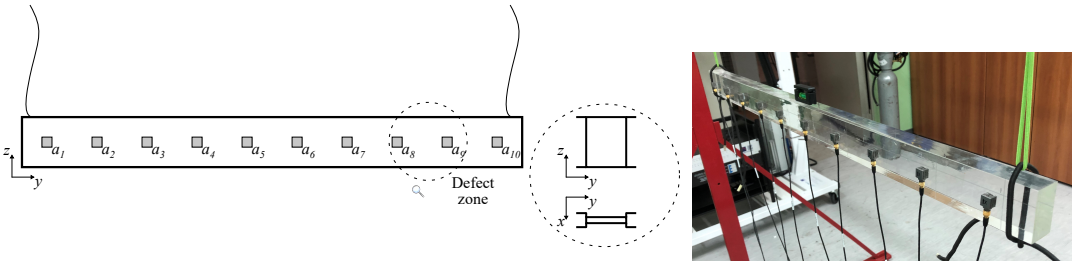

(a) (b)

Figure 4.3: Schematic of the experimental setup for the free-free beam structure. Geometry and position of the artificial damage introduced by locally reducing the cross-section thickness, are sketched in the highlighted area.

The experimental setup is composed of (i) ten B&K 4535-B-001 triaxial accelerometers, (ii) a PCB T086C03 instrumented impact hammer, (iii) a LMS SCADAS 310 mobile PC based multichannel analyzer platform, running the LMS Test.Lab 14A software suite for acquiring and recording the time histories of output and input signals, measured by the accelerometers and the hammer force transducer.

It is provided a comparison of the lumped-parameter system virtually generated output responses, when processed to compute the different introduced $\mathbf{R}(\mathrm{i}\omega)$ matrix estimators, in presence of additive noise, as a preliminary assessment of their performance. Then, in the beam system case, real-world performance of the same estimators are investigated in the noisy experimental environment.

A further scope is related to the power of using R-FRFs for local damage diagnoses by means of the assessment of additional modal parameters, made available by the $\mathbf{R}(\mathrm{i}\omega)$ matrix [103], that show an enhanced sensitivity to damage detection with respect to classical FRFs' global modal parameters. To this purpose, in the next chapter, the beam has been analyzed in two different states: undamaged, as described above, and in a damaged state, for which we have designed an artificially introduced damage, located between the 8^{th} and the 9^{th} sensor location, as sketched in Figure 4.3. The damage is, specifically, obtained by reducing the beam's thickness of 3.5 mm per side, from 35 mm to 28 mm.

4.4.1 Case study on a lumped-parameter system

In the case of the lumped-parameter system, four different loading conditions are considered, each obtained by exerting an impulsive force on the i-th exciting dof. In this respect, the output displacements are divided into the following two subsets: the exciting $\mathbf{Z}_i(\mathrm{i}\omega)$ dofs including the displacements of 1^{st}, 2^{nd}, 5^{th}, and 6^{th} mass and the free $\mathbf{Y}_i(\mathrm{i}\omega)$ dofs comprising the displacements of 3^{rd} and 4^{th} mass. Therefore, the output-only linear relationship Eq. (4.7) is particularized as

$$\begin{pmatrix} Y_3(\mathrm{i}\omega) \\ Y_4(\mathrm{i}\omega) \end{pmatrix}_i = \begin{bmatrix} R_{31}(\mathrm{i}\omega) & R_{32}(\mathrm{i}\omega) & R_{35}(\mathrm{i}\omega) & R_{36}(\mathrm{i}\omega) \\ R_{41}(\mathrm{i}\omega) & R_{42}(\mathrm{i}\omega) & R_{45}(\mathrm{i}\omega) & R_{46}(\mathrm{i}\omega) \end{bmatrix} \begin{pmatrix} Z_1(\mathrm{i}\omega) \\ Z_2(\mathrm{i}\omega) \\ Z_5(\mathrm{i}\omega) \\ Z_6(\mathrm{i}\omega) \end{pmatrix}_i , \tag{4.25}$$

where the notation $(.)_i$, with i ranging from 1 to 4, indicates the i-th loading case, featuring the i-th mass as subjected to the impulse force. You, thus, have four independent vectors, each corresponding to one of the exciting dofs, by which the matrix problem of Eq. (4.13) is rephrased as

$$\begin{bmatrix} \mathbf{Y}_1 & \mathbf{Y}_2 & \mathbf{Y}_5 & \mathbf{Y}_6 \end{bmatrix} = \mathbf{R}\,(\mathrm{i}\omega) \begin{bmatrix} \mathbf{Z}_1 & \mathbf{Z}_2 & \mathbf{Z}_5 & \mathbf{Z}_6 \end{bmatrix}, \tag{4.26}$$

where the dependence of exciting and free displacement vectors from the radian frequency ω is omitted for brevity. The obtained $\mathbf{R}(\mathrm{i}\omega)$ is a 2×4 matrix, whose first and last columns' entries are all null, as proved in [102], owing to the absence of connecting elements both between the 3^{rd} and the 4^{th} mass, and between the 1^{st} and 6^{th} mass.

By preliminary computing the analytical impulse response functions of the system, the corresponding numerical Eq. (4.26) is built up, as follows. Measurement noise is simulated as Gaussian incoherent noise and added to all the exciting and free output dofs, as well as to the input force, adjusting the variance values to achieve a 50 dB signal-to-noise-ratio (SNR) for

all signals. Forces, responses and additive noise are simulated in the time domain, adopting a sampling frequency, a time period, and a number of repetitions equal to 512 Hz, 10 s, and $M = 10$, respectively. Figure 4.4 offers an example of the impacting force together with a generic exciting dof, when compared with the added noise. Specifically, a 1% exponential window is applied to all the response signals, while a combined 10% force and 1% exponential window is used in the case of the input signal [66].

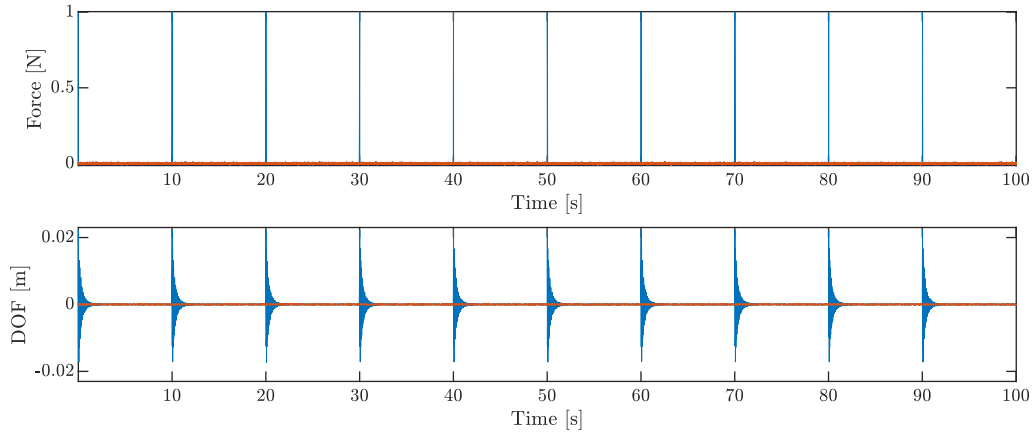

Figure 4.4: Example of an impacting force and of a generic exciting response dof, blue solid line, compared with the added noise, red solid line.

Once the noise-corrupted displacements are computed, they are collected to build up Eq. (4.26) and the previously defined estimators are used to correspondingly calculate the $\mathbf{R}(\mathrm{i}\omega)$ matrix. The aim of the study is to compare the estimates obtained by the five output-only nonparametric estimator $\mathbf{R}_{\mathrm{ar}}$, $\mathbf{R}_{\mathrm{EV}}$, $\mathbf{R}_{\log}$, $\mathbf{R}_1$, and $\mathbf{R}_v$ described in Eqs. (4.16), (4.18), (4.17), (4.21) and (4.22), respectively, with that from the input-output estimator $\mathbf{R}_{\mathrm{def}}$ introduced in Eq. (4.14), relying on the usage of the measured input forces and, in turn, on that of the classical FRFs estimated by the H_v method. In Figures 4.5 and 4.6, the comparison of the estimated four not null R-FRFs, is synoptically presented in terms of magnitude and phase angle.

A quantitative assessment of the agreement between estimated and theoretical values of each $\mathbf{R}(\mathrm{i}\omega)$ matrix entry is obtained by computing the FRF correlation coefficient $C_{R_{oi}}$ and

the normalised error $E_{R_{oi}}$ defined in Eqs. (1.59) and (1.60).

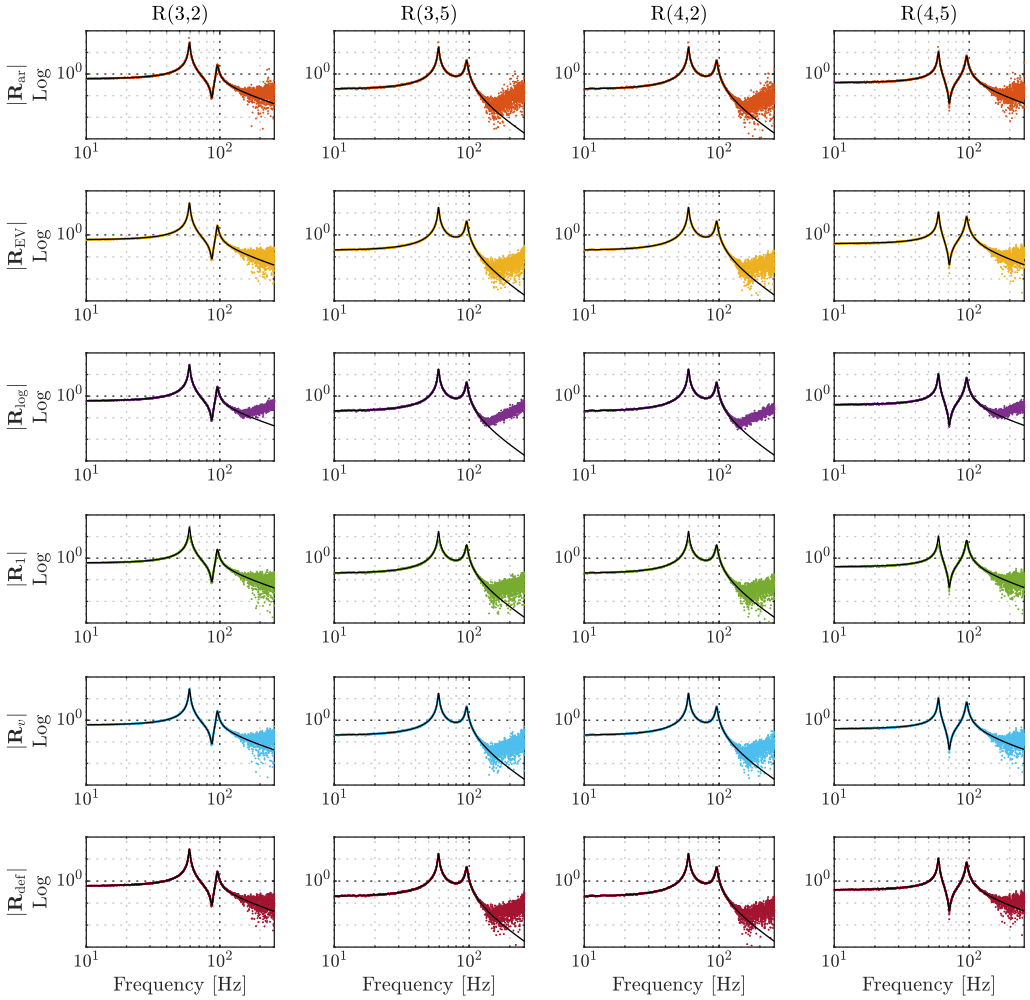

Figure 4.5: Magnitude of R-FRFs in the case of the lumped-parameter system: theoretical, black solid lines, and computed by using the different estimators, colored dotted lines.

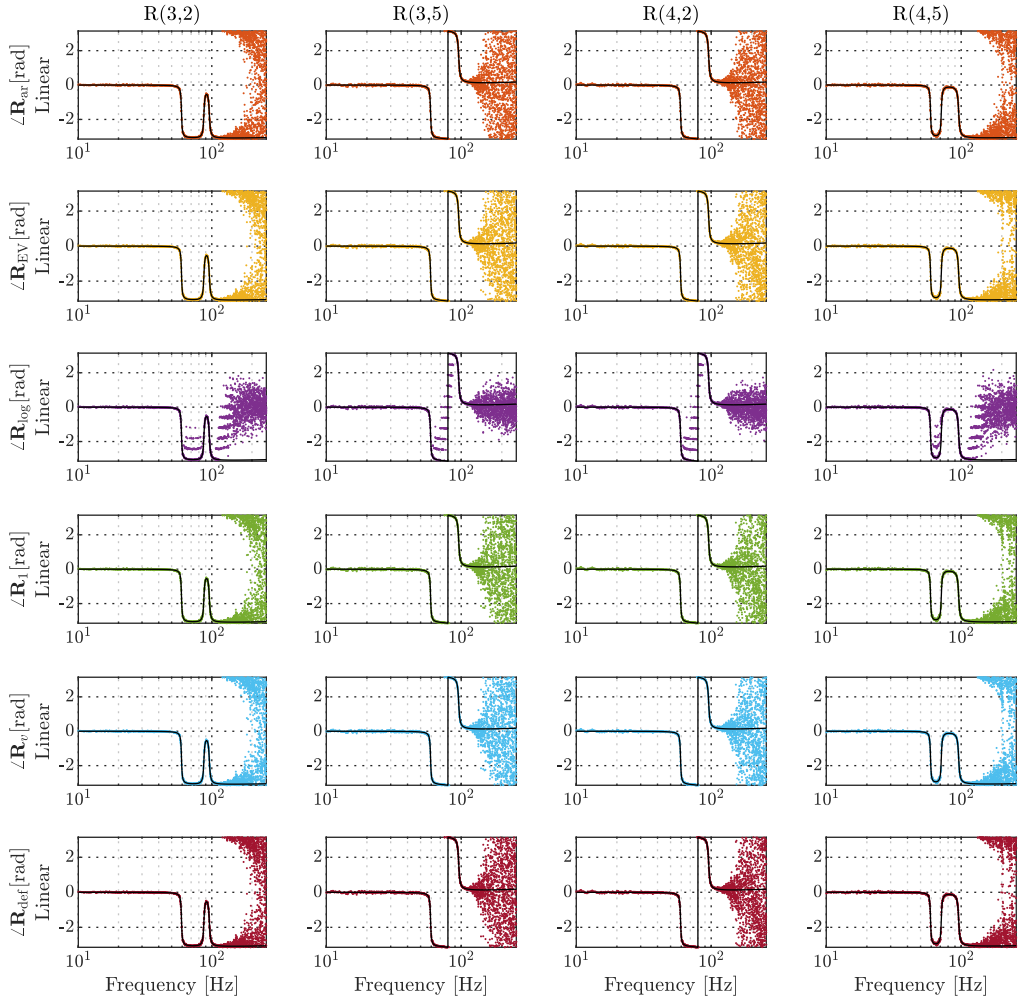

Figure 4.6: Phase of R-FRFs in the case of the lumped-parameter system: theoretical, black solid lines, and computed by the different estimators, colored dotted lines.

The two coefficients defined by Eqs. (1.59) and (1.60) provide a global evaluation, over the whole frequency range, of the linear relationship between the theoretical and estimated R-FRFs, so that a performance comparison of the different estimators is collected in Figure 4.7, where both quantities are represented.

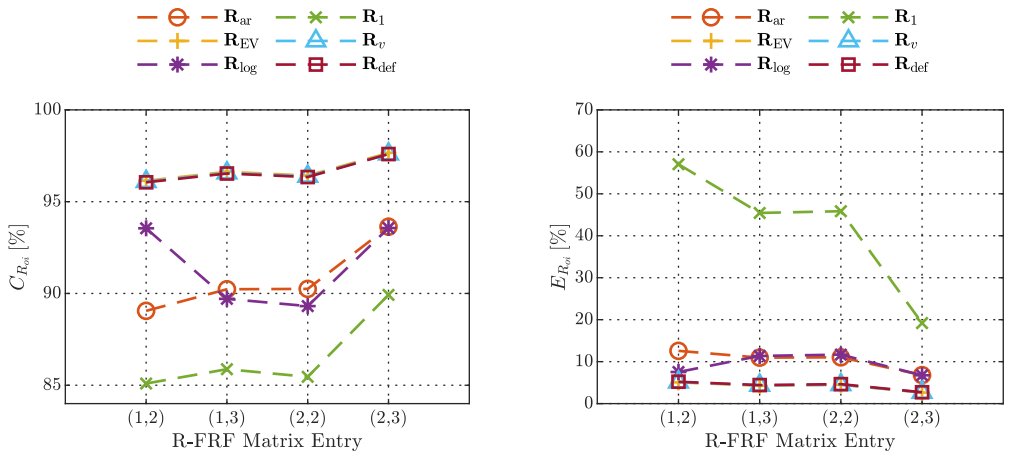

Figure 4.7: Performance analysis of the different estimators by using the correlation coefficient Eq. (1.59) and the normalised error Eq. (1.60), in the case of the lumped-parameter system. Points belonging to each dashed line represent the assessment of the R-FRF components indicated on the x-axis.

From error point of view, it is noticed that, excluding the case of $\mathbf{R}_1$, for which very high global error values, up to 60 %, are achieved, in the cases of $\mathbf{R}_{\text{def}}$, $\mathbf{R}_{\text{EV}}$, and $\mathbf{R}_v$, the error values remain lower than or equal to about 5%, while in those of $\mathbf{R}_{\text{ar}}$ and $\mathbf{R}_{\text{log}}$, values of about 10% maximum are reached. The values of the correlation coefficient confirm this assessment. Specifically, in the cases of $\mathbf{R}_{\text{def}}$, $\mathbf{R}_{\text{EV}}$, and $\mathbf{R}_v$, the correlation coefficient exhibits values greater than 95%, that decrease up to about 10% in the case of the $\mathbf{R}_1$ estimator. The highlighted better results are particularly related to the estimation accuracy achieved around the resonance peaks, see Figure 4.5. Since an equal amount of noise is added to all outputs, exciting and free ones, the unsatisfactory behaviour of $\mathbf{R}_1$ estimator has to be explained by considering that this formulation explicitly suffers for measurement errors present on the exciting dofs.

4.4.2 Case study on a PMMA experimental beam

In the case of the PMMA beam, the examined loading conditions are obtained by impacting the structure in correspondence of five different sensor locations, along the x-direction, as

anticipated. The acceleration signals, measured along the same direction, are divided into two subsets, classifying as exciting dofs, which contribute to the $\ddot{\mathbf{Z}}_i(\mathrm{i}\omega)$ vector, the signals acquired from the 1^{st} to the 5^{th} sensor, and as free dofs, contributing to the $\ddot{\mathbf{Y}}_i(\mathrm{i}\omega)$, the measured outputs from the 6^{th} to the 10^{th} sensor. The following matrix linear relationship is thus built up

$$\begin{bmatrix} \ddot{\mathbf{Y}}_6 & \ddot{\mathbf{Y}}_7 & \ddot{\mathbf{Y}}_8 & \ddot{\mathbf{Y}}_9 & \ddot{\mathbf{Y}}_{10} \end{bmatrix} = \mathbf{R}\,(\mathrm{i}\omega) \begin{bmatrix} \ddot{\mathbf{Z}}_1 & \ddot{\mathbf{Z}}_2 & \ddot{\mathbf{Z}}_3 & \ddot{\mathbf{Z}}_4 & \ddot{\mathbf{Z}}_5 \end{bmatrix}, \tag{4.27}$$

where the matrix $\mathbf{R}(\mathrm{i}\omega)$ is, in this case a squared 5×5 matrix, and the double dots' notation is utilised to highlight the fact that acceleration Fourier transforms are involved instead of displacement ones, although Eq. (4.3) remains unchanged if the considered outputs are displacements, velocities or accelerations

The signals are acquired in the time domain with a sampling frequency of 2048 Hz and a time period of 16 s. In order to apply averaging techniques, $M = 10$ repetitions are carried out in each loading condition. A 0.001% exponential window is used to reduce noise contamination, yielding smooth R-FRFs.

The estimation is performed by employing the different six estimators, as in the simulated discrete case. The whole matrix $\mathbf{R}(\mathrm{i}\omega)$, obtained by $\mathbf{R}_{\text{ar}}$ and $\mathbf{R}_{\text{def}}$ is reported in terms of magnitude and phase angle in Figures 4.8 and 4.9. Some differences are visible in the frequency range below 100 Hz, where the input-output estimators allows for a better identification of the first resonance peak, see Figure 4.8. The generally lower estimation quality of the first three columns' entries, already singled out in [103], is here confirmed, as related to lower intensity signals. This behaviour has been interpreted in [103], in view of the physical meaning of R-FRFs and, specifically, by accounting for the fact that the structure, in correspondence of the exciting dofs, is virtually constrained, as those dofs were grounded. Owing to these considerations, the last column of $\mathbf{R}(\mathrm{i}\omega)$ is used for the following performance assessment.

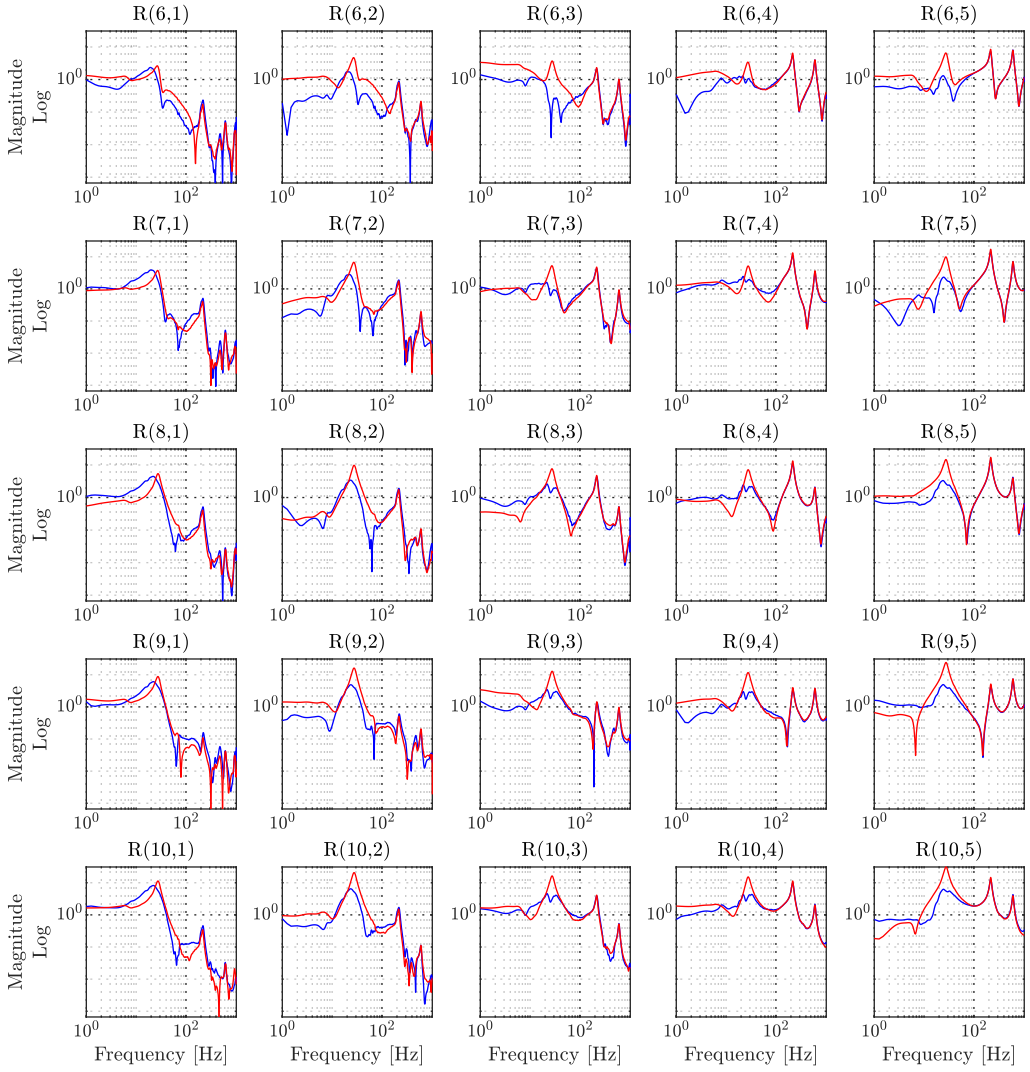

Figure 4.8: Magnitude of R-FRFs in the case of the PMMA beam: estimated by R_{ar}, blue solid line, estimated by R_{def}, red solid line.

Even in the beam's case, the performance of the considered estimators are compared in terms of correlation coefficient and normalized error, as defined in Eqs. (1.59) and (1.60), by using the estimated input-output $\mathbf{R}_{\text{def}}$ matrix as the reference quantity to assess the performance of all the other output-only estimators. The comparison analysis, thus, limited to the sole entries of the 5^{th} column of $\mathbf{R}(\text{i}\omega)$ is offered in Figure 4.10.

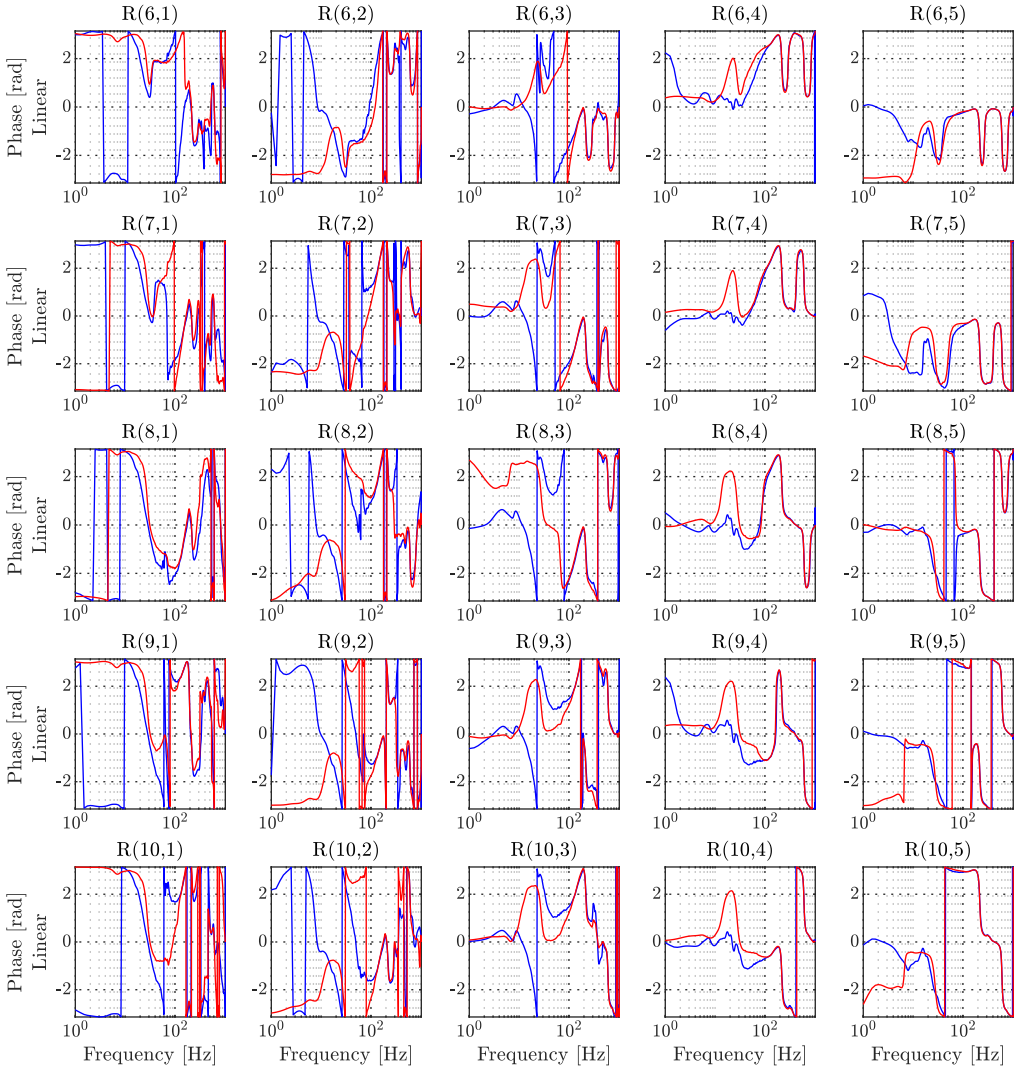

Figure 4.9: Phase of R-FRFs in the case of the PMMA beam: estimated by R_{ar}, blue solid line, estimated by R_{def}, red solid line.

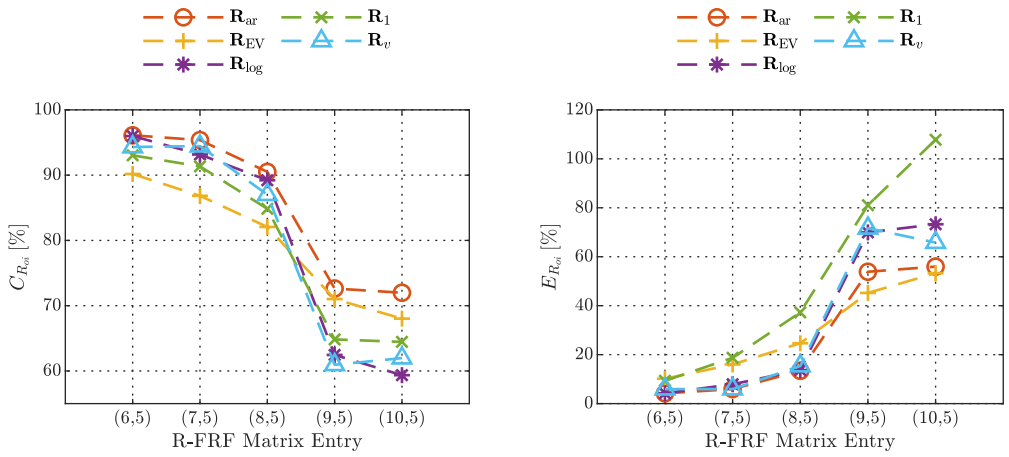

Figure 4.10: Performance analysis of the different estimators by using the correlation coefficient (1.59) and the normalised error (1.60), in the case of the PMMA beam. Points belonging to each dashed line represent the assessment of the R-FRF components indicated on the x-axis.

The higher global error values and the corresponding lower correlation coefficients affecting the $\mathrm{R}(9,5)$ and $\mathrm{R}(10,5)$ entries are due to the increasing distance of the related free and exciting dofs. The first peak estimation accuracy results especially affected. With regards to the other entries, $\mathbf{R}_{\mathrm{ar}}$, $\mathbf{R}_v$, and $\mathbf{R}_{\log}$ allow for achieving a satisfactory agreement with the reference estimator $\mathbf{R}_{\mathrm{def}}$, which is computed by accounting for the input force measurement. Being $\mathbf{R}_{\mathrm{ar}}$, in particular, the most promising in this specific case of interest, it is used to report on the comparison presented in Figures 4.8 and 4.9. In general, the unsatisfactory behaviour of $\mathbf{R}_1$ is confirmed, since, as already seen in the simulated discrete system case, the usage of this estimator leads to higher errors owing to its biased nature with respect to noises affecting the exciting dofs.

In a nutshell

1. *Definition of Response based Frequency Response Functions, R-FRFs: a transfer matrix between the so-called forced and guided dofs. The possibility for analyzing the system in a local sense (i.e., the original structure when some of its degrees of freedom are, virtually, considered constrained to ground).*
2. *Redefinition of the classical MIMO system estimators for the assessment of R-FRFs:* $\mathbf{R}_{\mathrm{def}}$ *as an input-ouput estimator, and* $\mathbf{R}_{\mathrm{ar}}$, $\mathbf{R}_{\mathrm{EV}}$, $\mathbf{R}_{1}$, $\mathbf{R}_{v}$, *and* $\mathbf{R}_{\log}$ *representing five output-only nonparametric estimators.*
3. *Estimators performance comparison exploiting data from a 6-dof discrete system and impact testing carried out on a slender PMMA beam.*

Chapter 5

Modal analysis through R-FRFs

Contents

5.1 Introduction

In the present chapter, a parametric model of R-FRFs, as a specific class of global TFs, is provided showing how these functions comprise additional local modal parameters. Such an objective is worth to be pursued, since structural modifications or damage, occurring in specific locations of the system under test, often need processing of both modal parameter kinds, that is poles and modes.

The possibility of adding those new modes comes from the fact that they are inherently related to the original system, even though it is partially, virtually, constrained. In this context, "virtually" means that no physical locks are actually needed to be added, whilst new boundary conditions are obtained simply by measuring the R-FRFs, through performing a feasible and attractive experimental procedure, aimed at investigating local structural modifications, potentially occurring on the system. Such a dual nature (of being local and additional) of the modal parameteres identifiable from R-FRFs, will be theoretically and experimentally proved in the following.

Basically, it is extended the application of curve fitting methods, classically used in the cases of EMA and OMA, to that of R-FRFs, whose parametric model is derived in terms of perturbated original system's modal parameters, combined with matrices whose entries are transmission elements in the form of combinations of physical lumped parameters relating defined groups of degrees of freedom. Usually, transmissibility-driven stochastic identification techniques [52] elaborate scalar transmissibility measurements, retrieved over different loading conditions, in order to obtain rational functions with poles equal to those of the original system. Specifically, in [156] poly-reference transmissibility-based OMA, uninfluenced by the content of the input spectrum, is introduced proposing a parametric model of the transmissibility functions exploited by an identification approach which only catches the eigenstructure of the system of interest. Similarly, in [50] multivariable transmissibilities, also known as global TFs, are related to scalar transmissibilities to obtain pseudo scalar trasmissibility functions, which system poles can be extracted from.

The rest of the chapter is organized as follows. In Section 5.2, the modal partial fraction decomposition of R-FRFs is derived for a linear time invariant system, containing the additional / local poles and mode shapes. Moreover, it is proposed an alternative theoretical approach to obtain the modal partial fraction decomposition of R-FRFs. In Section 5.3, a specialised algorithm to identify such additional / local poles and modes is developed. In

Section 5.4, numerical and experimental case studies are exploited; the former are used to evaluate the performance of the obtained algorithm on differently estimated R-FRFs, by comparing the computed modal parameters; the latter allow for performing a full damage detection analysis of a slender beam, to elucidate and highlight the additional / local nature of modal parameters estracted by R-FRFs' estimates.

5.2 Derivation of R-FRFs modal model

The linear output-output relationship, defined extracting the last m equations referred to the free dofs' motion in Eq. (4.2) [160], is here reintroduced:

$$\mathbf{Y}(s) = -\mathbf{B}_{22}^{-1}(s)\mathbf{B}_{21}\mathbf{Z}(s) = \mathbf{R}(s)\mathbf{Z}(s), \tag{5.1}$$

where matrix $\mathbf{R}(s)$ is expressed in terms of dynamic stiffness partitions and represents a $m \times n$ response-based transfer matrix containing the R-FRFs, connecting driving and free dofs. The entries $R_{ij}(s)$ in $\mathbf{R}(s)$ have poles corresponding to those of the system under investigation with its forced dofs grounded as it will be easily demonstrated. In fact, the first partition $\mathbf{B}_{22}^{-1}(s)$ in Eq. (5.1) stands for the specific transfer function matrix $\mathbf{H}_g(s)$. The system represented by the $\mathbf{H}_g(s)$ is here named virtually grounded system: it arises from the partitioning of the original dynamic stiffness $\mathbf{B}(s)$ and assumes the physical meaning of the original system, characterized by the $\mathbf{H}(s) = \mathbf{B}^{-1}(s)$ transfer matrix of Eq. (4.2), subjected to virtual constraints on the m driving dofs $\mathbf{Z}(s)$ [102].

Indeed, Eq. (5.1) could be rephrased in the following form

$$\mathbf{Y}(s) = \mathbf{B}_{22}^{-1}(s)\mathbf{F}_{eq}(s) = \mathbf{H}_g(s)\mathbf{F}_{eq}(s), \tag{5.2}$$

where $\mathbf{F}_{eq}(s) = -\mathbf{B}_{21}(s)\mathbf{Z}(s)$ is a $m \times 1$ vector containing the forces, induced by the motion

of the n driving dofs, which cause the free dofs' displacements $\mathbf{Y}(s)$ and are related to the restoring forces of elements connecting the two group of dofs as indicated by the partition $\mathbf{B}_{21}(s)$. Forces in $\mathbf{F}_{eq}(s)$ can be interpreted as the equivalent forces one should apply to the n free dofs location of the original system subjected to the virtual boundary constraint $\mathbf{Z}(s) = 0$ which is represented by the the transfer matrix $\mathbf{H}_g(s)$.

From the modal analysis theory [80], $\mathbf{H}_g(s)$ can be modally decomposed as

$$\mathbf{H}_g(s) = \sum_{r=1}^{N_p} \left(\frac{\boldsymbol{\psi}_r \boldsymbol{L}_r^{\mathrm{T}}}{s - \lambda_r} + \frac{\boldsymbol{\psi}_r^* \boldsymbol{L}_r^{\mathrm{H}}}{s - \lambda_r^*} \right) = \sum_{r=1}^{2N_p} \left(\frac{\boldsymbol{\psi}_r \boldsymbol{L}_r^{\mathrm{T}}}{s - \lambda_r} \right), \tag{5.3}$$

and

$$\lambda_r = -\zeta_r \omega_{u_r} + \mathrm{i}\omega_{u_r} \sqrt{1 - \zeta_r^2}, \tag{5.4}$$

where N_p is the number of modes, λ_r are the roots of the system characteristic equation $|\mathbf{B}_{22}(s)| = 0$ with ω_{u_r} the undamped natural frequency and ζ_r the damping ratio, $\boldsymbol{\psi}_r$ is the modal vector and $\boldsymbol{L}_r$ is the so-called modal participation factor vector. These additional poles and modes, referred to the virtually grounded system, are involved in the matrix $\mathbf{R}(s)$ giving it the character of a response-based frequency response functions. Indeed, $\mathbf{R}(s)$ is achieved multiplying the transfer matrix in Eq. (5.3) by the partition $\mathbf{B}_{21}(s)$ which could be expressed in terms of $\mathbf{M}$, $\mathbf{C}$ and $\mathbf{K}$ sub-matrices as

$$\mathbf{B}_{21}(s) = s^2 \mathbf{M}_{21} + s\mathbf{C}_{21} + \mathbf{K}_{21}, \tag{5.5}$$

where $\mathbf{M}_{21}$, $\mathbf{C}_{21}$ and $\mathbf{K}_{21}$ describe the mass, damping and stiffness relation between the two subsets of responses $\mathbf{Y}$ and $\mathbf{Z}$. Rewriting the $m \times n$ matrix $\mathbf{R}(s)$ in terms of the virtually grounded system modal parameters of Eq. (5.3) together with the transmission elements of

Eq. (5.5), you obtain

$$\mathbf{R}(s) = \sum_{r=1}^{2N_p} \left(-\frac{\boldsymbol{\psi}_r \boldsymbol{L}_r^{\mathrm{T}} s^2 \mathbf{M}_{21}}{s - \lambda_r} - \frac{\boldsymbol{\psi}_r \boldsymbol{L}_r^{\mathrm{T}} s \mathbf{C}_{21}}{s - \lambda_r} - \frac{\boldsymbol{\psi}_r \boldsymbol{L}_r^{\mathrm{T}} \mathbf{K}_{21}}{s - \lambda_r} \right). \tag{5.6}$$

Looking at the fractional terms of Eq. (5.6), the following Laplace transform of derivatives arise

$$\frac{s^2}{s - \lambda_r} - s - \lambda_r = \mathcal{L}\left(\frac{d^2 \mathrm{e}^{\lambda_r \tau}}{d\tau^2} \right) = \mathcal{L}\left(\lambda_r^2 \mathrm{e}^{\lambda_r \tau} \right) = \frac{\lambda_r^2}{s - \lambda_r}, \tag{5.7}$$

and, similarly,

$$\frac{s}{s - \lambda_r} - 1 = \mathcal{L}\left(\frac{d\mathrm{e}^{\lambda_r \tau}}{d\tau} \right) = \mathcal{L}\left(\lambda_r \mathrm{e}^{\lambda_r \tau} \right) = \frac{\lambda_r}{s - \lambda_r}, \tag{5.8}$$

where $\mathcal{L}(.)$ indicates the Laplace transform, $\frac{d(.)}{d\tau}$ and $\frac{d^2(.)}{d\tau^2}$ are respectively the first and the second derivative with respect to the time variable τ, and $\mathrm{e}^{(.)}$ is the exponential function. Starting from Eqs. (5.7) and (5.8), we rewrite Eq. (5.6) as

$$\begin{aligned} \mathbf{R}(s) = & \sum_{r=1}^{2N_p} \left(\frac{\boldsymbol{\psi}_r \boldsymbol{L}_r^{\mathrm{T}} \left(-\lambda_r^2 \mathbf{M}_{21} - \lambda_r \mathbf{C}_{21} - \mathbf{K}_{21} \right)}{s - \lambda_r} \right) + \\ & - s \left(\sum_{r=1}^{2N_p} \boldsymbol{\psi}_r \boldsymbol{L}_r^{\mathrm{T}} \right) \mathbf{M}_{21} - \left(\sum_{r=1}^{2N_p} \lambda_r \boldsymbol{\psi}_r \boldsymbol{L}_r^{\mathrm{T}} \right) \mathbf{M}_{21} - \left(\sum_{r=1}^{2N_p} \boldsymbol{\psi}_r \boldsymbol{L}_r^{\mathrm{T}} \right) \mathbf{C}_{21}, \end{aligned} \tag{5.9}$$

where certain additional terms find the meaning in post-initial condition produced by an impulsive force. In fact, we write the inverse Laplace transform of Eq. (5.3) as

$$\mathbf{h}_g(\tau) = \sum_{r=1}^{2N_p} \boldsymbol{\psi}_r \boldsymbol{L}_r^{\mathrm{T}} \mathrm{e}^{\lambda_r \tau}, \tag{5.10}$$

obtaining the so-called impulse response function (IRF) matrix whose derivative is

$$\dot{\mathbf{h}}_g(\tau) = \sum_{r=1}^{2m} \boldsymbol{\psi}_r \boldsymbol{L}_r^{\mathrm{T}} \lambda_r e^{\lambda_r \tau} \tag{5.11}$$

where the generic entries $h_{g,ij}(\tau)$ and $\dot{h}_{g,ij}(\tau)$ represent respectively the i-th dof displacement and velocity, valid for $\tau > 0$, to an impulsive force acting in the j-th dof at $\tau = 0$. Since the unit impulse produces the following set of post-initial conditions

$$\mathbf{h}_g\left(0^+\right) = \mathbf{0} = \sum_{r=1}^{2N_p} \boldsymbol{\psi}_r \boldsymbol{L}_r^{\mathrm{T}}, \tag{5.12}$$

and

$$\dot{\mathbf{h}}_g\left(0^+\right) = \mathbf{M}_{22}^{-1} = \sum_{r=1}^{2N_p} \lambda_r \boldsymbol{\psi}_r \boldsymbol{L}_r^{\mathrm{T}}, \tag{5.13}$$

Eq. (5.9) can be rewritten as in Eq. (5.14)

$$\mathbf{R}(s) = \sum_{r=1}^{2N_p} \left(\frac{\boldsymbol{\psi}_r \boldsymbol{L}_r^{\mathrm{T}} \left(-\lambda_r^2 \mathbf{M}_{21} - \lambda_r \mathbf{C}_{21} - \mathbf{K}_{21}\right)}{s - \lambda_r} \right) + \mathbf{M}_{22}^{-1} \mathbf{M}_{21}. \tag{5.14}$$

Thus, a novel modal transmission vector is defined

$$\boldsymbol{T}_r = \left(-\lambda_r^2 \mathbf{M}_{21} - \lambda_r \mathbf{C}_{21} - \mathbf{K}_{21}\right)^{\mathrm{T}} \boldsymbol{L}_r, \tag{5.15}$$

in order to express the modal decomposition of $\mathbf{R}(s)$ along the frequency axis $s = \mathrm{i}\omega$ as

$$\mathbf{R}(\mathrm{i}\omega) = \sum_{r=1}^{2N_p} \left(\frac{\boldsymbol{\psi}_r \boldsymbol{T}_r^{\mathrm{T}}}{\mathrm{i}\omega - \lambda_r} \right) + \mathbf{M}_{22}^{-1} \mathbf{M}_{21}, \tag{5.16}$$

where the vector $\boldsymbol{T}_r$ derives from the combination of the mass, stiffness, damping transmission elements in between the exciting and guided dofs and the modal participation factors $\boldsymbol{L}_r$ of the virtually grounded system. In addition to these modal vectors, a constant residue is found resulting related to the mass matrix of the virtually grounded system and the inertial coupling between guided and driving dofs.

This is how Eq. (5.16) proves that matrix $\mathbf{R}(\mathrm{i}\omega)$ collects several modal features: poles and modes shapes of the virtually grounded system in addition to the novel modal transmission

vector $\boldsymbol{T}_r$. To corroborate the existence of additional local mode shapes in R-FRFs matrix, an algebraic identification is expounded in the following subsection, leading to a polynomial model of $\mathbf{R}(\mathrm{i}\omega)$ closely related to the modal model in Eq. (5.16). It is remarked how these additional modal parameters are suitable for carrying out local diagnoses. Indeed, they show an higher sensitive to local damages with respect to modal parameters accessed by the estimation of the classical FRFs which have a global meaning [103]. It is also emphasized how the choice of exciting and free dofs, depending on the loading condition, leads to different definitions of $\mathbf{R}(\mathrm{i}\omega)$ and represents the virtually constraining of certain movements. This aspect have the makings of being a powerful tool also in the model updating field as an alternative to the use of the anti-resonant frequencies to update numerical models [160].

5.2.1 Algebraic identification of additional local mode shapes

The alternative theoretical approach to obtain the modal partial fraction decomposition of R-FRFs, Eq. (5.16), starts by expressing matrix $\mathbf{R}(s)$ as

$$\mathbf{R}\left(s\right) = -\frac{\mathrm{adj}\left(\mathbf{B}_{22}\left(s\right)\right)}{\left|\mathbf{B}_{22}\left(s\right)\right|}\mathbf{B}_{21}\left(s\right). \tag{5.17}$$

where poles λ_r of $\mathbf{R}(s)$ matrix are related to characteristic polynomial of $\mathbf{B}_{22}(s)$, indicated by $|\mathbf{B}_{22}(s)|$ that is a real coefficient polynomial of degree $2m$. These poles represent the virtually grounded system poles, obtained starting from the original system of Eq. (4.2) when subjected to $\mathbf{Z}(s) = \mathbf{0}$ condition. In order to find the mode shape vector for the generic λ_r of the virtual grounded system, the following equations are used

$$\mathbf{B}_{22}\left(\lambda_r\right)\mathbf{Y}_r = \mathbf{0}, \tag{5.18}$$

where $\mathbf{Y}_r = \boldsymbol{\psi}_r \in \mathbb{C}^{m\times 1}$ is the r-th eigenvector of the system represented by the transfer matrix $\mathbf{H}_g(s) = \mathbf{B}_{22}^{-1}(s)$. The main idea is to retrieve these additional modal parameters,

referred to the virtual system $\mathbf{H}_g(s)$, from matrix $\mathbf{R}(s)$ which is strongly related to $\mathbf{B}_{22}$ as expressed in Eq. (5.1). Looking at $\mathbf{R}(s)$ matrix entries from a polynomial point of view, it is stated

$$R_{ij}(s) = \frac{\sum_{q=0}^{2(m-1)} \beta_{ij,q}^{22} s^q}{\sum_{p=0}^{2m} \alpha_p s^p} \sum_{r=0}^{2} \beta_{ij,r}^{21} s^r, \tag{5.19}$$

where $\beta_{ij,q}^{22} \in \mathbb{R}$ are the real-valued polynomial coefficients of matrix $\text{adj}\,(\mathbf{B}_{22}(s))$ entries, $\alpha_p \in \mathbb{R}$ that of the characteristic equation, and $\beta_{ij,r}^{21} \in \mathbb{R}$ refer to $\mathbf{B}_{21}(s)$ entries which can be easily expressed as

$$-B_{ij}^{21}(s) = \sum_{v=0}^{2} \beta_{ij,v}^{21} s^v = -m_{ij}^{21} s^2 - c_{ij}^{21} s - k_{ij}^{21}. \tag{5.20}$$

where m_{ij}^{21}, c_{ij}^{21}, k_{ij}^{21} respectively indicate the ij entry of matrices $\mathbf{M}^{21}$, $\mathbf{C}^{21}$, $\mathbf{K}^{21}$. By multiplying the two numerator polynomials in Eq. (5.19), one can generally express

$$R_{ij}(s) = \frac{\sum_{k=0}^{2m} \beta_{ij,k} s^k}{\sum_{p=0}^{2m} \alpha_p s^p}, \tag{5.21}$$

where $\beta_{ij,k} \in \mathbb{R}$ are a combination of $\beta_{ij,q}^{22}$ and $\beta_{ij,r}^{21}$. By using the partial fractions method in the case of numerator degree equal to that of denominator, $R_{ij}(s)$ is expanded in partial fractions as

$$R_{ij}(s) = a_{ij}^{(0)} + \sum_{k=1}^{2m} \frac{a_{ij}^{(k)}}{s - \lambda_k}, \tag{5.22}$$

with a_{ij}^k are complex-valued coefficients and a_{ij}^0 is a constant term related to certain mass matrix entries which represent the coefficients of highest degree terms and embody the

remainder of the polynomial long division. By using matrix notation

$$\mathbf{R}\left(s\right)=\begin{bmatrix} a_{11}^{(0)} & \cdots & a_{n1}^{(0)} \\ \vdots & \ddots & \vdots \\ a_{m1}^{(0)} & \cdots & a_{mn}^{(0)} \end{bmatrix}+\sum_{k=1}^{2m}\begin{bmatrix} \dfrac{a_{11}^{(r)}}{s-\lambda_k} & \cdots & \dfrac{a_{1n}^{(k)}}{s-\lambda_k} \\ \vdots & \ddots & \vdots \\ \dfrac{a_{m1}^{(k)}}{s-\lambda_k} & \cdots & \dfrac{a_{mn}^{(k)}}{s-\lambda_k} \end{bmatrix}=\mathbf{A}^{(0)}+\sum_{k=1}^{2m}\frac{\mathbf{A}^{(k)}}{s-\lambda_k}, \tag{5.23}$$

where $\mathbf{A}^{(k)}\in\mathbb{C}^{m\times n}$ are the so-called residual matrices and $\mathbf{A}^{(0)}$ is a constant residue. Pre-multiplying both terms in Eq. (5.23) by $(s-\lambda_r)\mathbf{B}_{22}(s)$, referring to a generic r-th pole, we obtain

$$\left(s-\lambda_r\right)\mathbf{B}_{22}\left(s\right)\mathbf{R}\left(s\right)=\left(s-\lambda_r\right)\mathbf{B}_{22}\left(s\right)\mathbf{A}^{(0)}+\sum_{k=1,\,k\neq r}^{2m}\frac{\left(s-\lambda_r\right)\mathbf{B}_{22}\left(s\right)\mathbf{A}^{(k)}}{s-\lambda_k}+\mathbf{B}_{22}(s)\mathbf{A}^{(r)}, \tag{5.24}$$

and by making the limit of both terms as s approaches λ_r

$$\lim_{s\to\lambda_r}\left(s-\lambda_r\right)\mathbf{B}_{22}\left(s\right)\mathbf{R}\left(s\right)=\mathbf{0}=\mathbf{B}_{22}\left(\lambda_r\right)\mathbf{A}^{(r)}, \tag{5.25}$$

it is noticed that, similarly to the definition in Eq. (5.18), each column of $\mathbf{A}^{(r)}$ is proportional to the r-th eigenvector of the system $\mathbf{H}_g(s)$.

Until now, the existence of mode shapes, relative to virtually grounded system, is demonstrated in the algebraic structure of the R-FRFs matrix. In fact, as derived in Section 5.2, we can express the generic r-th residue matrix from the modal model in Eq. (5.16), equivalent to the polynomial representation in Eq. (5.23) as

$$\boldsymbol{\psi}_r\boldsymbol{T}_r^{\mathrm{T}}=\begin{bmatrix} \phi_{1,r}T_{1,r} & \cdots & \phi_{1,r}T_{n,r} \\ \vdots & \ddots & \vdots \\ \phi_{m,r}T_{1,r} & \cdots & \phi_{m,r}T_{n,r} \end{bmatrix}=\mathbf{A}^{(r)}, \tag{5.26}$$

where, specifically, entries of the modal transmission vector could be expounded as

$$\begin{aligned}\boldsymbol{T}_r =&\left(-\lambda_r^2\mathbf{M}_{21} - \lambda_r\mathbf{C}_{21} - \mathbf{K}_{21}\right)^{\mathrm{T}}\boldsymbol{L}_r = \\ =&\left\{\begin{array}{c}\sum_{k=1}^{m}\left(-\lambda_r^2 m_{k1}^{21} - \lambda_r c_{k1}^{21} - k_{k1}^{21}\right)\dfrac{\phi_{k,r}}{m_{ar}} \\ \vdots \\ \sum_{k=1}^{m}\left(-\lambda_r^2 m_{kn}^{21} - \lambda_r c_{kn}^{21} - k_{kn}^{21}\right)\dfrac{\phi_{k,r}}{m_{ar}}\end{array}\right\} = \left\{\begin{array}{c}T_{1,r} \\ \vdots \\ T_{n,r}\end{array}\right\},\end{aligned} \tag{5.27}$$

and the division remainder

$$\mathbf{A}^{(0)} = \mathbf{M}_{22}^{-1}\mathbf{M}_{21}, \tag{5.28}$$

assume the meaning of a constant residue related to virtually grounded system mass matrix and to the inertial coupling between driving and guided dofs.

5.3 R-FRFs identification technique

The similarity between the modal decompositions in Eqs. (5.3), (1.24) and (1.33) allows the application of the classical modal parameters estimation schemes to extract modal parameters from the PSDs matrix with the only difference represented by the operational participation vectors. By comparing Eqs. (5.16) and (1.33), the analogy between the half-spectrum modal model and the R-FRFs decomposition emerges. Indeed, the modal transmission vectors $\boldsymbol{T}_r$, similarly to the operational participation vectors $\boldsymbol{K}_r$, are a combination of the modal participation vectors and some physical parameters related to the transmission elements in between the guided and driving dofs, that are generally unknown. In order to estimate the modal parameters of the R-FRFs, one can apply identification techniques developed for OMA. Here, it is made the choice to use a frequency domain parametric modal method based on the Least Squares Frequency Domain (LSFD) estimator, relied on the modal model in Eq. (5.16), in combination with the poly-reference Least Squares Complex Frequency (pLSCF) method [114]. The LSFD method is employed to obtain a global estimate of the mode shapes in

combination with the pLSCF providing poles and modal transmission vectors.

Once the poles and the modal transmission factors have been computed by means of a stabilization diagram, the virtually grounded system mode shapes can be found, at last, by solving in a linear least square sense Eq. (5.16) through the well-known LSFD estimator. The virtually grounded system mode shapes consistency has been validated using the Modal Assurance Criterion (MAC).

5.4 MPE from R-FRFs

Modal parameter estimation, MPE, is performed following the procedure described in Section 5.3 for two case studies. Firstly, the 6-DOF lumped parameter system of Figure 5.1 is analyzed in the case-based R-FRFs matrix of Eq. (4.26). Retrieved matrix $\mathbf{R}(\mathrm{i}\omega)$ by means of six different estimators proposed in Section 4.3, MPE is performed exploiting each of the measured $\mathbf{R}(\mathrm{i}\omega)$. This example gives the possibility to compare the modal parameters referred to $\mathbf{R}(\mathrm{i}\omega)$ modal decomposition with respect to the theoretical ones of the system virtually grounded on exciting masses shown in Figure 5.1.

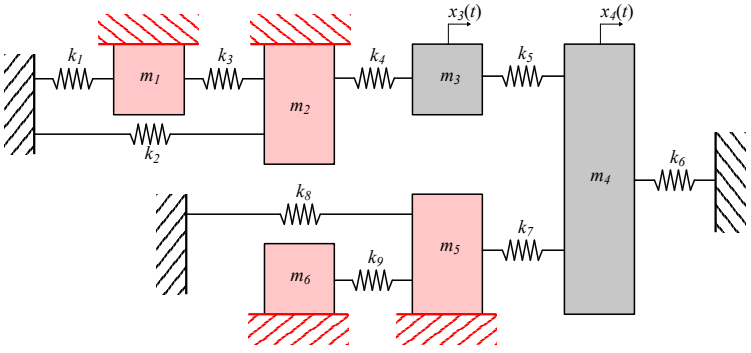

Figure 5.1: Schematic of the 6 DOF lumped parameter system virtually grounded on the exciting dofs.

Secondly, an experimental slender PMMA beam is examined in healthy and damaged state: the case-based R-FRFs matrix is that of Eq. (4.27) which ensures to virtually support the left undamaged part of the beam at a_{1-5} locations, where the impacts occur, how sketched

in Figure 5.2. This choice allows to compare the modal parameters, extracted from the several $\mathbf{R}(\mathrm{i}\omega)$ measurements in the two beam states, showing the local meaning of the R-FRFs in addition to the good sensitivity of the R-FRFs modal parameters with respect to the damage occurrence. This point is corroborated by performing a further analysis based on nine different $\mathbf{R}(\mathrm{i}\omega)$ definitions, focusing on several local portion of the beam, aimed at localizing the damage.

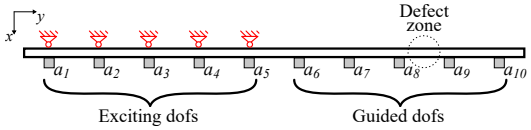

Figure 5.2: Schematic of the experimental beam with the classification of guided and exciting dofs. The red virtual supports correspond to the impact locations.

5.4.1 Identification of a lumped-parameter model

The identification procedure is shown in the case of the $\mathbf{R}_v$ measurement of the R-FRFs matrix. From the pLSCF, the stabilization diagram is built up in Figure 5.3 assuming subsequently an increasing number of the model order p of Eq. (1.35). The stabilisation diagram gives a strong indication of the two physical modes allowing the selection of the corresponding stable poles, indicated with '`s`'.

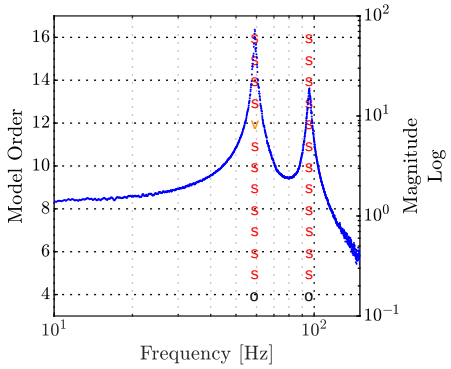

Figure 5.3: Identification of the lumped parameter system by using R_v estimated R-FRFs: stabilization diagram along with the magnitude of the R-FRFs sum function, blue line. The stable poles are indicated with '`s`' and the model order is indicated on the left ordinate axis.

The pair of natural frequencies and damping ratios, computed from the two selected

stable poles, are reported in Table 5.1 in addition to the exact modal parameter of the system grounded in the exciting dofs. The relative percentage error $\Delta = 100 \times (v_{\text{th}} - v_{\text{est}})/v_{\text{th}}$ is also provided for both natural frequencies and damping ratios.

	Natural Frequency (Hz)			Damping Ratio (%)		
	Exact	Estimated	$\lvert\Delta\rvert(\%)$	Exact	Estimated	$\lvert\Delta\rvert(\%)$
Mode 1	59.17	59.19	0.0408	0.929	0.8797	5.340
Mode 2	95.73	95.78	0.0530	1.504	1.365	9.223

Table 5.1: Identification of the lumped parameter system by using by using R_v estimated R-FRFs: comparison between exact and estimated modal parameters.

Achieved poles and modal transmission vectors from the first step, the MPE ends by deploying the LSFD estimator in order to compute the unscaled mode shapes.

Once the modal parameters are computed, the data synthesized from the modal model of Eq. (5.16) are compared with the measured data as shown in Figure 5.4. The visual match, together with an high correlation coefficient for all the R-FRFs, proves the goodness of the MPE process results.

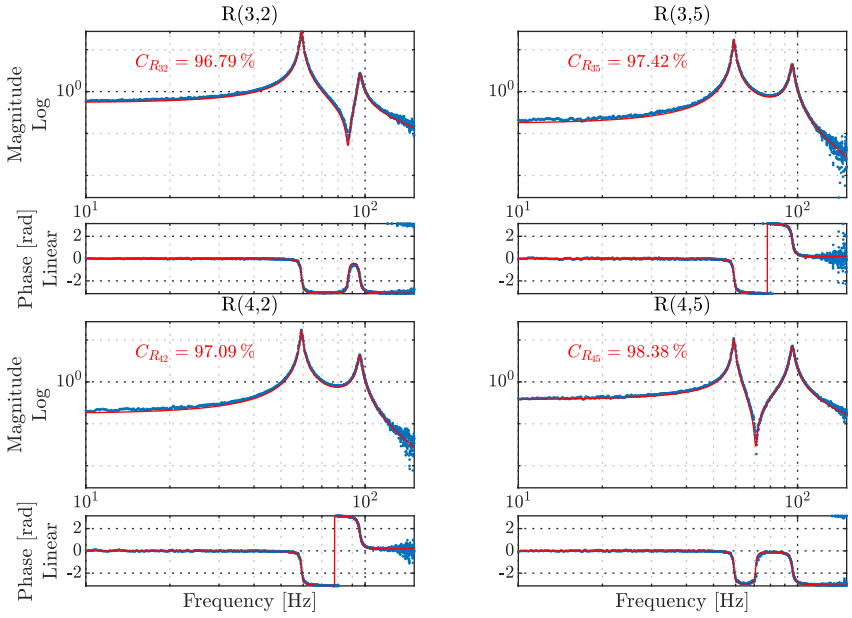

Figure 5.4: R-FRFs in the case of the lumped parameter system: comparison between R_{v} estimated R-FRFs, dotted lines, and syntheses by modal model, solid lines.

The identification process is repeated starting from each of the six different $\mathbf{R}(\mathrm{i}\omega)$ estimates. In Table 5.2, the computed natural frequencies and damping ratios are collected together with the relative percentage error obtained referring to the exact values of Table 5.1. Figure 5.5 shows the estimated modal parameter errors of Table 5.2 in a graphical fashion.

		Natural Frequency (Hz)		Damping Ratio (%)	
		Estimated	$\lvert\Delta\rvert$(%)	Estimated	$\lvert\Delta\rvert$(%)
R_{ar}	Mode 1	59.15	0.0243	0.7636	17.84
	Mode 2	95.77	0.0355	1.342	10.78
R_{EV}	Mode 1	59.19	0.0367	0.8726	6.110
	Mode 2	95.78	0.0524	1.366	9.174
R_{log}	Mode 1	59.11	0.0966	0.9924	6.782
	Mode 2	95.89	0.1737	1.192	20.71
R_1	Mode 1	59.21	0.0735	1.263	35.89
	Mode 2	95.79	0.0620	1.460	2.916
R_v	Mode 1	59.19	0.0408	0.8797	5.340
	Mode 2	95.78	0.0530	1.365	9.223
R_{def}	Mode 1	59.19	0.0331	0.8727	6.095
	Mode 2	95.78	0.0532	1.365	9.249

Table 5.2: Identification of the lumped parameter system: comparison between exact and estimated modal parameters computed by using the different R-FRFs estimators.

The identification results show a very good agreement between the theoretical poles of the virtually grounded system of Figure 5.1 and the ones extracted from the $\mathbf{R}(\mathrm{i}\omega)$ matrix by means of the pLSCF estimator. Negligible errors are observed for the identified natural frequencies, higher errors characterize the estimated damping ratios. The MPE performed on $\mathbf{R}_{\mathrm{EV}}$, $\mathbf{R}_v$, and $\mathbf{R}_{\mathrm{def}}$ measurements leads to better results in terms of damping ratios showing errors less the 10% for both the system modes. Figure 5.5 points out the total agreement between the modal parameter accuracy and the performance of the different R-FRFs estimators. The proposed comparison is a further check of the R-FRFs modal model formulation, derived in Section 5.3, and its strong analogy with the modal expression of the half spectrum matrix.

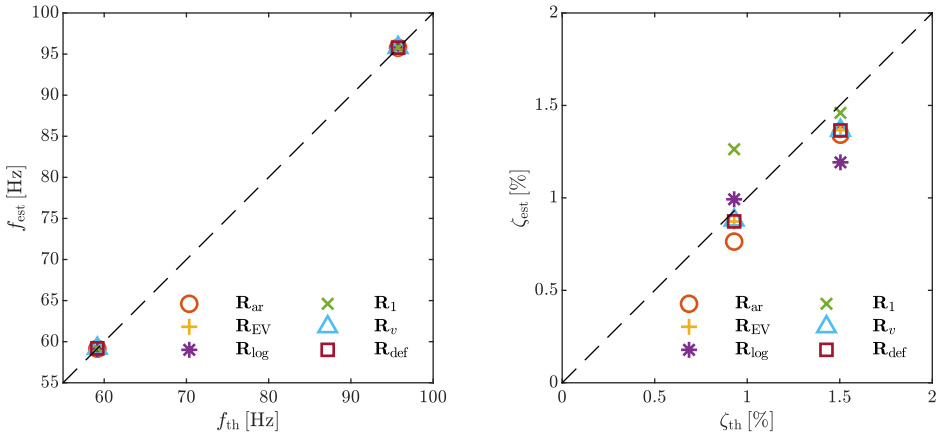

Figure 5.5: Representation of estimated modal parameters' deviations from corresponding theoretical values, in the case of the lumped parameter system, as collected in Table 5.2.

5.4.2 Identification of a PMMA experimental beam and damage detection

In the experimental case study, the identification process is performed considering a slender PMMA beam in two state: an healthy reference state and a damaged one realised introducing a thickness reduction as depicted in Figure 5.2. The particular $\mathbf{R}(\mathrm{i}\omega)$ matrix involved in Eq. (4.27) is processed: it relates the guided x-accelerations from sensor a_6 to a_{10} with the exciting ones from a_1 to a_5. Figures 5.6 and 5.7 show the $\mathbf{R}_{\text{def}}$ estimate of this particular R-FRFs in terms of magnitude and phase angle. Sliding effects on the R-FRFs exist due to the damage occurrence on the beam side that includes the free dofs. This frequency shifting is more evident for the second and third peak owing to the measurement accuracy in the low frequency range. The virtually constrained system defined by the particular $\mathbf{R}(\mathrm{i}\omega)$ matrix is schematized in Figure 5.2 where virtual supports are introduced on the left undamaged part of the beam in correspondence of the impact loads y-coordinates.

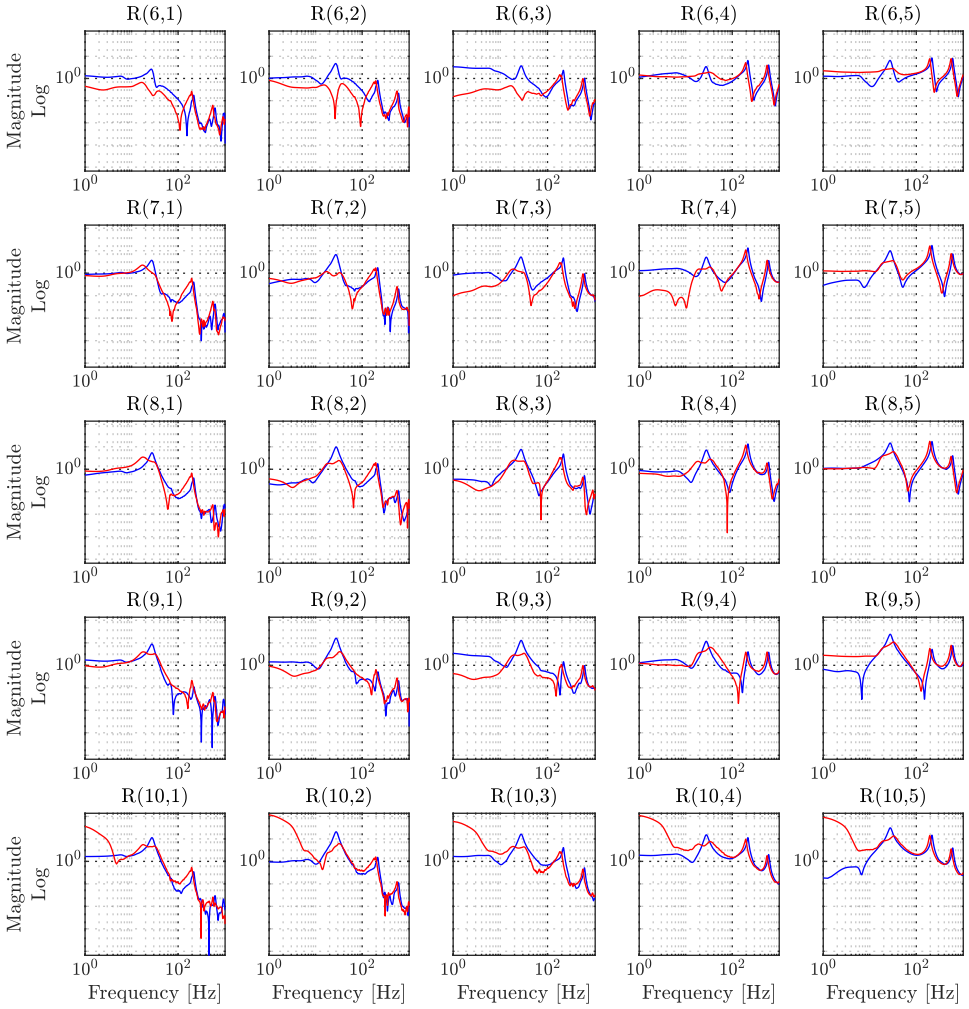

Figure 5.6: Magnitude of R-FRFs, computed by using R_{def} estimator, in the case of the PMMA beam: healthy state, blue line, and damaged state, red line.

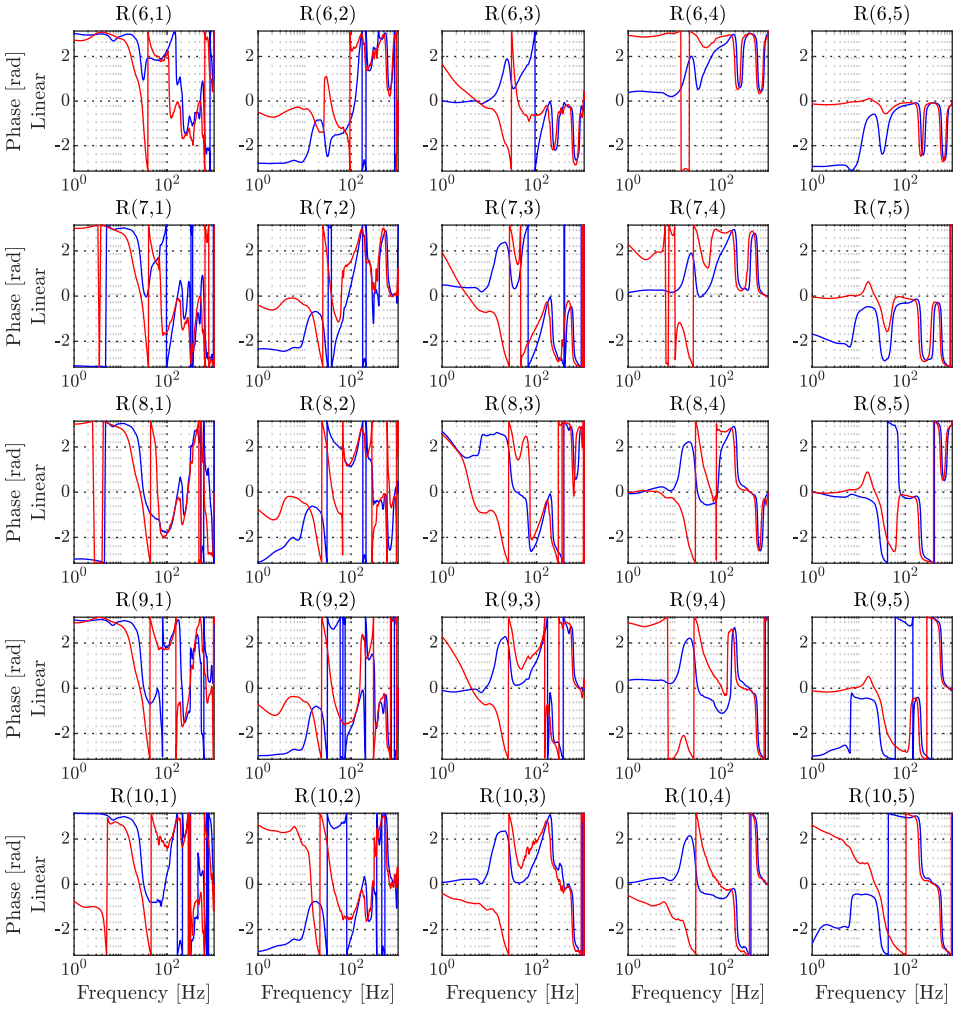

Figure 5.7: Phase of R-FRFs, computed by using R_{def} estimator, in the case of the PMMA beam: healthy state, blue line, and damaged state, red line.

The MPE procedure is performed starting from the $\mathbf{R}_{\text{def}}$ measurements of the beam in the healthy and damaged states. In this respect, the last column of the $\mathbf{R}(\mathrm{i}\omega)$ matrix is processed ensuring the estimation of the only 5^{th} component of the modal transmission vector $\boldsymbol{T}_r$ for each r^{th} mode, see Eq. (5.16). From the pLSCF estimator, the stabilization diagrams are built up in Figure 5.8. The stabilisation diagrams give a strong indication of the three physical modes allowing the selection of the corresponding stable poles. The stability of the

first potential mode is affected by the poor R-FRFs first peak quality as visible especially in the damaged beam state. Natural frequencies and damping ratios computed from the selected poles are shown in Table 5.3.

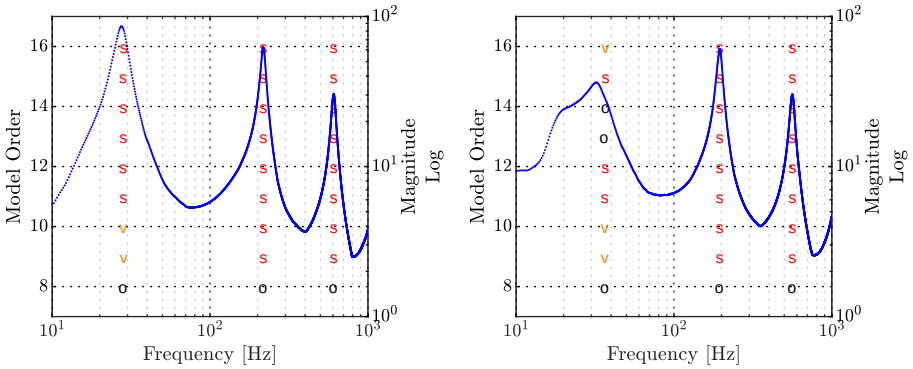

(a) Healthy: stabilization diagram (b) Damaged: stabilization diagram

Figure 5.8: (a) Identification of the healthy (a) and damaged (b) PMMA beam by using R_{def} estimated R-FRFs: stabilization diagram along with the magnitude of the R-FRFs sum function, blue line.

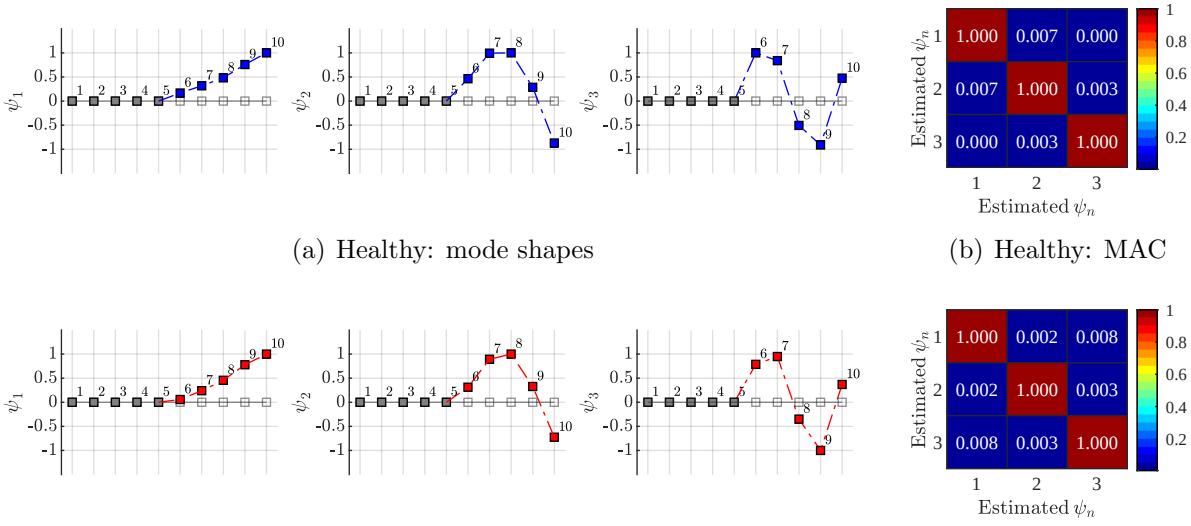

(a) Healthy: mode shapes (b) Healthy: MAC

(c) Damaged: mode shapes (d) Damaged: MAC

Figure 5.9: Identification of the healthy (a)-(b) and damaged (c)-(d) PMMA beam by using R_{def} estimated R-FRFs: (a)-(c) estimated modal vectors, (b)-(d) autoMAC from the estimated modal vectors' set.

From the second identification step, a modes shape vectors estimate is accessed by means of the LSFD estimator. In Figure 5.9 the three unscaled mode shapes, real part, are reported

for the two beam states. The mode vector $\boldsymbol{\psi}_r$ is defined in its m components corresponding to the guided dofs locations represented by the five accelerometers from a_6 to a_{10}. The corresponding autoMAC values are reported for each set of modes showing their orthogonality. As demonstrated in Section 5.3 and reported in [102] for the case of a finite-element beam model, the mode shapes extracted from matrix $\mathbf{R}(\mathrm{i}\omega)$ consist in the physical ones of the original system virtually constrained at the exciting dofs locations. The particular constraint condition depends on the signal considered: in the present case the y-accelerations from sensors a_1 to a_5 play the role of the grounded dofs.

As for the previous case study, the identification process is repeated involving each of the six different $\mathbf{R}(\mathrm{i}\omega)$ estimates regarding the two beam states. The relative percentage variation, $\Delta = 100 \times (v_\mathrm{h} - v_\mathrm{d})/v_\mathrm{h}$, between the healthy and damaged state is also reported for both frequencies and damping ratios.

		Natural Frequency (Hz)			Damping Ratio (%)		
		Healthy	Damaged	Δ(%)	Healthy	Damaged	Δ(%)
R_ar	Mode 1	28.98	33.65	16.132	14.69	8.195	−44.23
	Mode 2	218	196.9	−9.649	3.776	3.739	−0.976
	Mode 3	608	563.2	−7.378	2.995	3.217	7.401
R_EV	Mode 1		33.90			3.789	
	Mode 2	217.3	195.2	−10.159	4.674	3.725	−20.30
	Mode 3	606.9	564.1	−7.055	2.802	2.942	5.013
R_log	Mode 1						
	Mode 2	218.3	196.4	−9.996	3.179	3.166	−0.399
	Mode 3	607.9	563.6	−7.296	2.981	3.354	12.486
R_1	Mode 1						
	Mode 2	216.9	194.7	−10.24	4.532	4.800	5.903
	Mode 3	607.3	562.2	−7.422	3.160	3.3127	4.826
R_v	Mode 1						
	Mode 2	218.4	197.5	−9.555	3.139	3.087	−1.664
	Mode 3	607.5	562.6	−7.391	3.017	3.291	9.113
R_def	Mode 1	28.11	36.55	30.02	4.265	12.10	183.8
	Mode 2	217.6	194.9	−10.40	3.172	3.168	−0.141
	Mode 3	607.4	562.6	−7.373	3.003	3.207	6.795

Table 5.3: Identification of the PMMA beam: comparison between the estimated modal parameters, in the cases of the healthy and the damaged state, computed by using the different R-FRFs estimators.

The MPE procedure leads to the identification of all three modes only in the case of $\mathbf{R}_{\text{ar}}$ and $\mathbf{R}_{\text{def}}$ processing, the other estimators show less accuracy in the low frequency range baldy affecting the stability of the first pole. The 2$^{\text{nd}}$ and 3$^{\text{rd}}$ mode natural frequencies undergo a significant negative shift, around 10%, which, as reported in [103], is almost double than the frequency changes of the original system poles. The 1$^{\text{st}}$ mode, when available, presents an opposite frequency shift. Looking at the damping ratios in Table 5.3, it seems more difficult to inspect significant symptoms owing to the higher uncertainty of the estimates. Generally the 2$^{\text{nd}}$ mode damping ratio decreases, except for results from $\mathbf{R}_1$ processing, and the 3$^{\text{st}}$ one increases. The relevant aspect is the local meaning of the additional poles and modes that compose $\mathbf{R}(\text{i}\omega)$ matrix, suitably changing the exciting dofs, together with the loading conditions, it becomes possible to make different analyses based on several $\mathbf{R}(\text{i}\omega)$ matrices each containing modal parameters of a particular virtual subsystem. These additional modal parameters exhibit different sensitivity with respect to the damage location allowing SHM with a local approach. In the beam case, ten different loading conditions are collected, each defined by the presence of the impulsive load on the i-th accelerometer position along the x-direction. This allows to easily change the two responses subsets definition, exciting dofs and free ones, making possible the statement of several version of the matrix relationship in Eq. (5.1). We classify two accelerometers as guided dofs, and the remaining eight as exciting, in order to inspect different free beam portion. Changing the pair of sensors classified as free, nine analyses are performed following the identification procedure described in Section 5.3. The first natural frequency of each of the nine virtually grounded system is accessed both in the healthy and damaged state. The percentage relative variation $\Delta(\%)$ is used to compare this modal parameter in the two beam state. In Table 5.4 and Figure 5.10, the results derived by the MPE process on the nine $\mathbf{R}(\text{i}\omega)$ measurements are collected.

		Natural Frequency (Hz)		
Guided dofs	Exciting dofs	Healthy	Damaged	$\lvert\Delta\rvert(\%)$
1, 2	3, 4, 5, 6, 7, 8, 9, 10	145.0	141.1	−2.666
2, 3	1, 4, 5, 6, 7, 8, 9, 10	458.2	451.2	−1.526
3, 4	1, 2, 5, 6, 7, 8, 9, 10	594.9	588.6	−1.067
4, 5	1, 2, 3, 6, 7, 8, 9, 10	604.6	605.3	0.1266
5, 6	1, 2, 3, 4, 7, 8, 9, 10	613.3	604.3	−1.463
6, 7	1, 2, 3, 4, 5, 8, 9, 10	606.8	582.4	−4.016
7, 8	1, 2, 3, 4, 5, 6, 9, 10	604.5	593.0	−1.894
8, 9	1, 2, 3, 4, 5, 6, 7, 10	465.9	432.5	−7.163
9, 10	1, 2, 3, 4, 5, 6, 7, 8	147.8	120.6	−18.42

Table 5.4: Local diagnoses of the PMMA beam: comparison between the estimated first natural frequency, in the cases of the healthy and the damaged state, extracted from the several R-FRFs obtained by changing the definition of guided and exciting dofs.

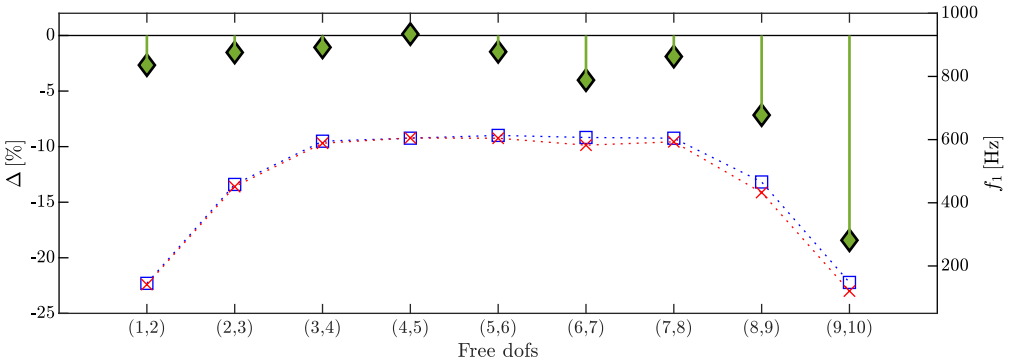

Figure 5.10: Local diagnoses of the PMMA beam: comparison between the estimated first natural frequency, in the cases of the healthy, blue square, and the damaged state, red cross. The green stems indicate the relative percentage frequency variation. The frequency value is indicated on the right ordinate axis and the percentage relative shift on the left one.

The damage occurrence, located in between the accelerometers 8^{th} and 9^{th}, becomes affecting more significantly the first natural frequency of the virtual system as its unconstrained dofs get closer to the artificially introduced damage. Indeed, the 8^{th} and 9^{th} cases, that focuses on a beam portion that includes the reduced beam sections, exhibit a frequency shift $\Delta(\%)$ remarkably greater than the one of the other cases. In this sense, the local meaning of the additional modes, which compose the R-FRFs, provides the possibility to develop indicators and strategies designated for local structural diagnoses.

In a nutshell

1. *R-FRFs modal structure in terms of perturbed original system's modal parameters: a modal partial fraction decomposition containing additional poles and mode shapes of the original system, when considered virtually constrained to ground at the exciting dofs locations.*
2. *The role of modal transmission vectors deriving from the combination of some transmission elements, existing between the exciting and free dofs, and the modal participation factors of the virtually constrained (or perturbed) system.*
3. *Modal parameter estimation, based on frequency-domain estimators from the field of experimental and operational modal analysis, applied to the R-FRFs, measured by several estimators, from numerical and experimental case studies.*
4. *Local diagnosis on an experimental PMMA beam, aimed at inspecting the sensitivity of the additional poles, estimated from R-FRFs, with respect to the damage location.*

Concluding Remarks

In the thesis, here presented, novel contributions in the field of Operational Modal Analysis are proposed with a view at system identification, monitoring, and damage detection in challenging engineering applications. The main research efforts tackle specific challenging problems, belonging to the field of structural identification, such as microsystems dynamic characterization, innovative OMA framework formulations that fit operational scenarios violating the NExT assumption, definition of nonparametric estimators and derivation of the relevant modal structure of global transmissibility matrices, R-FRFs, pointing out the role of their modal content in damage detection.

In the first part, Chapter 1 develops the modal formulations of two of stochastic identification techniques major functions, such as output cross-correlations and power spectral densities, when the inputs are assumed to be realizations of white uncorrelated noise processes. A particular two step procedure, operating in the frequency domain, is invoked and briefly described. The classical RMFD polynomial model is presented together with its relevant least squares problem (called pLSCF) for coefficient matrices calculation. A conversion of the matrix fraction description into a state-space one is determined or, put another way, a contrallable canonical state-space realization of the RMFD model is adopted and the concept of stabilisation analysis, associated to the companion matrix eigenvalue decomposition at increasing polynomial model orders, is clarified as a tool for physical modes selection. So in closing the classical OMA method outline, the LSFD estimator, employed for mode shapes extraction, is recalled and common procedures for data pre-processing, i.e. the correlogram

approach, and modal parameters validation, such as synthesis and MAC, are provided. Once the fundamental aspects of output-only identification field are pointed out, the discussion is carried forward to some novel elements.

In Chapter 2, the vibro-acoustical Operational Modal Analysis (OMA) approach is presented as a valid methodology to perform dynamical identification on micro-devices. To this end, particular attention is paid to a particular case study, that is a quartz tuning fork (QTF) vibrating in a fluid environment. Specifically, two fundamental conditions are investigated: QFT fundamental in-plane skew-symmetric mode and the two first out-of-plane flexural modes. Furthermore, in order to reproduce excitation and measurement techniques suitable for modal testing on such a microelectromechanical system, an acoustic stationary random field, generated by two speakers, is exploited to acoustically excite the QTF and the resulting structural velocities are measured and recorded by using a single-point LDV, while an electronic microphone is employed to measure the acoustic pressure at a specific fixed point close to the sensor. The latter represents an acoustical output reference to be included in the mathematical formulation for the output-only modal decomposition of vibro-acoustical systems derived in [124]. We conduct a comparison between the results obtained by means of the identification performed on the positive cross-power spectra, PCPs, computed by using only structural responses (classical OMA approach) and those with PCPs, which include both structural and acoustical outputs (this is referred as vibro-acoustical OMA). Including the acoustic pressure reference is proved to be crucial to an accurate estimate of modal parameters. We underline that the convenience of vibro-acoustical OMA for MEMS is related to its simple setup that exploit non-contact measurement sensors, such as LDVs and microphones, together with an acoustical excitation overcoming the conventional modal testing limits when dedicated to microsystems. Furthermore, this approach remains firmly based on an OMA formulation for vibrating system coupled with a fluid medium. As a possible further development of the proposed analysis, one can include in the coupled system

dynamics the analytical model of the fluid-structure interaction proposed in [28], which accounts for the inertial, the purely viscous and the diffusive terms, to further extend the OMA formulation in the aim of include the fluid coefficients into the identification procedure.

Chapter 3 outlines the development of a generalized OMA framework, meaning an alternative approach aiming at overcoming the NExT assumption limitations, which occur when output-only modal analysis is performed on mechanical system, such as vehicles during road test or operating wind turbines. The G-OMA approach is designed to fix no-NExT effects (i.e. coloration, time correlation, coherence, harmonics, etc.) by including a priori known input correlation features in OMA modal structures. In fact, a generalized modal decomposition of CFs and PSDs matrix is clarified by making no assumptions about the forces correlation. In doing so, the concept of frequency (or time lag) dependent operational reference vectors arises as a class of modal vectors which in turn collects a combination of several contributions related to the forces acting on the system. Moving from the theoretical generalized PSD partial fraction decomposition, a specific two step identification procedure, operating in the frequency domain, is developed. The first step, resulting in poles and mode shapes estimation, is based upon an extended left matrix fraction description and its relevant state-space observable canonical realization. The second step is an LSFD-based estimator operating on the extended operational reference vectors calculation. The investigated no-NExT effects are the coloured nature of stochastic loads, the presence of temporal correlation and coherence between inputs. The proposed formulation is compared with the classical one, described in Chapter 1, by performing modal parameter estimation of a numerical 4-DOF lumped-parameter system and an experimental PTFE beam under different operating loading conditions, comprising a number of NExT assumption infringements. The suitability of the G-OMA method is confirmed by improved results in terms of stabilisation diagram and modal parameters accuracy. The usage of identification techniques, based on the modal structures here proposed, could inspire simple and cost-effective "ad hoc" tools able to compute the

modal parameters of mechanical systems under operating conditions that violate to a certain extent the hypothesis of the classical OMA techniques.

The second part of the thesis intends investigating the problem of estimation and identification by R-FRFs, as a specific class of global transmissibility functions that have proved to be of utmost importance in the fields of modal identification and health continuous monitoring of structures. In Chapter 4, the possibility of redefining the classical MIMO systems' estimators for the assessment of R-FRFs is, specifically, investigated. First, an input-output estimator $\mathbf{R}_{\text{def}}$ is introduced, whose definition is based on a combination of specific partitions of the classical FRF matrix of the system under test. Thus, the knowledge of the input forces is needed to this estimator computation and classical H_1, H_2, and H_v FRFs' estimators can be used for achieving, in a preliminary phase, the estimates of the needed classical FRFs. Second, five output-only nonparametric estimators, namely $\mathbf{R}_{\text{ar}}$, $\mathbf{R}_{\text{EV}}$, $\mathbf{R}_{\log}$, $\mathbf{R}_1$, and $\mathbf{R}_v$, are redefined; their performance, together with that of $\mathbf{R}_{\text{def}}$, are compared, exploiting (i) the numerical case of a 6-dof discrete system, whose input and output responses are simulated together with the presence of measurement noise, and (ii) the data collected during impact testing experiments, carried out on a slender PMMA beam. The global quantitative comparison of the performance of the proposed R-FRFs' estimators is conducted by using a normalised error and a correlation coefficient, through which the best strategies are elucidated in each considered case. With regards to the simulated case, the performance analysis of the different estimators show error values of about 5% maximum achieved for $\mathbf{R}_{\text{def}}$, $\mathbf{R}_{\text{EV}}$, $\mathbf{R}_v$ and 10% maximum for $\mathbf{R}_{\text{ar}}$ and $\mathbf{R}_{\log}$. Poor accuracy around the resonance peaks is reached with the $\mathbf{R}_1$ estimator which suffers for measurement errors present on the exciting dofs, generally comparable with that of the free ones. In the case of the real-world experimental data, $\mathbf{R}_{\text{ar}}$, $\mathbf{R}_v$, and $\mathbf{R}_{\log}$ allows for achieving a good agreement with the reference estimator $\mathbf{R}_{\text{def}}$, which takes into account the input force measurements. These three output-only estimators prove to be the most promising. In particular, $\mathbf{R}_v$, which treats errors on exciting and free dofs

in similar manner, is expected to be the estimator most commonly used in the applications. As a possible further development of the proposed analysis, one could adapt additional nonparametric FRF estimators, which exploit errors-in-variables stochastic noise models or involve an iterative improvement strategy, to the case of the RFRFs.

In order to extend the usage of the MPE methods, employed in EMA and OMA, to global transmissibilities, Chapter 5 offers an innovative modal partial fraction decomposition of the R-FRFs, containing additional poles and mode shapes of the original system, when considered virtually constrained to ground at the exciting dofs locations. Specifically, those new, virtual boundary conditions depend on the signals classified as exciting dofs and, moreover, the virtually constrained to ground system responses are observed in correspondence of the free dofs. In addition to poles and modes of the virtual subsystem, the proposed modal model of the R-FRFs involves novel modal transmission vectors, which derive from the combination of some physical lumped parameters, related to the transmission elements existing between the exciting and the free dofs, and the modal participation factors of the virtually constrained system. The strong similarity between the R-FRFs modal model and that of the positive power spectrum matrix is highlighted: this aspect allows for performing MPE from R-FRFs, by making usage of the pLSCF algorithm combined with the LSFD method, both typically employed, in tandem, in the OMA field. By presenting different numerical and experimental case studies, the fundamental aspect of the local meaning of the estimated modal parameters is underlined. Actually, by suitably changing the exciting dofs' locations, it becomes possible to make different analyses based on independent R-FRFs, each containing modal features of a particular virtual subsystem. This key point is elucidated and corroborated by performing local diagnoses on an experimental PMMA beam, aimed at inspecting the sensitivity of the additional poles estimated from R-FRFs with respect to damage location. Furthermore, the corresponding additional modes are effectively usable in SHM, relying on their higher sensitivity to local changes with respect to that of classical modes. This magnification of a

structural change results from processing the R-FRFs related to different virtually constrained sub-structures, all including the damage to be detected. Further developments of this work will focus on relaxing the definition and the number of usable exciting dofs' locations and on including the usage of the modal transmission vectors, with the aim of scaling the mode shapes.

Bibliography

[1] R. Allemang, D. L. Brown, and R. Rost. Experimental Modal Analysis and Dynamic Component Synthesis. Volume 2. In *Measurement Techniques for Experimental Modal Analysis*, 1987.

[2] R. J. Allemang. The modal assurance criterion - Twenty years of use and abuse. *Sound and Vibration*, 37(8):14–21, 2003.

[3] R. J. Allemang and A. W. Phillips. The unified matrix polynomial approach to understanding modal parameter estimation: An update. In *Proceedings of the 2004 International Conference on Noise and Vibration Engineering, ISMA*, pages 2373–2401, 2004.

[4] M. S. Allen, M. W. Sracic, S. Chauhan, and M. H. Hansen. Output-only modal analysis of linear time-periodic systems with application to wind turbine simulation data. *Mechanical Systems and Signal Processing*, 25(4):1174–1191, 2011.

[5] P. Andersen. *Identification of civil engineering structures using vector ARMA models*. PhD thesis, University of Aalborg, Aalborg, 2003.

[6] P. Andrén. Power spectral density approximations of longitudinal road profiles. *International Journal of Vehicle Design*, 40(1-3):2–14, 2006.

[7] J. Antoni and S. Chauhan. A study and extension of second-order blind source separation to operational modal analysis. *Journal of Sound and Vibration*, 332(4):1079–1106, 2013.

[8] I. G. Araújo, J. A. G. Sánchez, and P. Andersen. Modal parameter identification based on combining transmissibility functions and blind source separation techniques. *Mechanical Systems and Signal Processing*, 105:276–293, 2018.

[9] H. Atuike. Stochastic theory of minimal realization. *IEEE Transactions on Automatic Control*, 19(6):667–674, 1974.

[10] J. S. Bendat and A. G. Piersol. *Random Data*. John Wiley & Sons, Inc., jan 2010.

[11] K. Bogsjö. Evaluation of stochastic models of parallel road tracks. *Probabilistic Engineering Mechanics*, 22(4):362–370, 2007.

[12] K. Bogsjö, K. Podgórski, and I. Rychlik. Models for road surface roughness. *Vehicle System Dynamics*, 50(5):725–747, 2012.

[13] K. Bogsjö. Coherence of road roughness in left and right wheel-path. *Vehicle System Dynamics*, 46(SUPPL.1):599–609, 2008.

[14] S. Bouwstra, J. van Rooijen, H. Tilmans, A. Selvakumar, and K. Najafi. Thermal base drive for micromechanical resonators employing deep-diffusion bases. *Sensors and Actuators: A. Physical*, 37-38(C):38–44, 1993.

[15] A. Brandt, M. Berardengo, S. Manzoni, M. Vanali, and A. Cigada. Global scaling of operational modal analysis modes with the OMAH method. *Mechanical Systems and Signal Processing*, 117:52–64, 2019.

[16] R. Brincker. Recent advances of Operational Modal Analysis and applications in Structural Health Monitoring. *Aalborg University*, 2010.

[17] R. Brincker. Some elements of operational modal analysis. *Shock and Vibration*, 2014, 2014.

[18] R. Brincker. On the application of correlation function matrices in OMA. *Mechanical Systems and Signal Processing*, 87(July 2014):17–22, 2017.

[19] R. Brincker and P. Andersen. Method for vibration analysis, 2001.

[20] R. Brincker and P. Andersen. Understanding Stochastic Subspace Identification. In *Conference Proceedings of the Society for Experimental Mechanics Series*, 2006.

[21] R. Brincker, P. Andersen, and N. Moller. Indicator for separation of structural and harmonic modes in output-only modal testing. *Proceedings of the International Modal Analysis Conference - IMAC*, 2:1649–1654, 2000.

[22] R. Brincker and C. Ventura. *Introduction to Operational Modal Analysis*. Wiley, 2015.

[23] R. Brincker, L. Zhang, and P. Andersen. Modal identification of output-only systems using frequency domain decomposition. *Smart Materials and Structures*, 10(3):441–445, 2001.

[24] J. Burdess, A. Harris, D. Wood, R. Pitcher, and D. Glennie. A system for the dynamic characterization of microstructures. *Journal of Microelectromechanical Systems*, 6(4):322–328, 1997.

[25] D. Burns and H. Helbig. System for automatic electrical and optical characterization of microelectromechanical devices. *Journal of Microelectromechanical Systems*, 8(4):473–482, 1999.

[26] J. M. Caicedo, S. J. Dyke, and E. A. Johnson. Natural Excitation Technique and Eigensystem Realization Algorithm for Phase I of the IASC-ASCE Benchmark Problem: Simulated Data. *Journal of Engineering Mechanics*, 130(1):49–60, 2004.

[27] H. N. Cambraia, L. M. Contini, and P. R. Kurka. Operational modal parameters

identification using the ARMAV model. In *Proceedings of DINAME 2017*. Springer International Publishing, 2018.

[28] A. Campanale, C. Putignano, S. De Carolis, P. Patimisco, M. Giglio, and L. Soria. A theoretical-experimental framework for the analysis of the dynamic response of a QEPAS tuning fork device immersed in a fluid medium. *Mechanical Systems and Signal Processing*, 149, 2021.

[29] E. M. Cárdenas and L. U. Medina. Non-Parametric Operational Modal Analysis Methods in Frequency Domain: A Systematic Review. *International Journal of Engineering and Technology Innovation*, 11(1):34–44, 2021.

[30] T. Carne and G. James III. The inception of oma in the development of modal testing technology for wind turbines. *Mechanical Systems and Signal Processing*, 24(5):1213–1226, 2010.

[31] T. Carne, D. Martinez, and A. Nord. A comparison of fixed-base and driven-base modal testing of an electronics package. *Sandia report*, 1989.

[32] B. Cauberghe. *Applied frequency-domain system identification in the field of experimental and operational modal analysis*. PhD thesis, Dept. of Mechanical Engineering, Vrije Universiteit Brussel, Belgium, 2004.

[33] B. Cauberghe, P. Guillaume, P. Verboven, and E. Parloo. Identification of modal parameters including unmeasured forces and transient effects. *Journal of Sound and Vibration*, 265(3):609–625, 2003.

[34] B. Cauberghe, P. Guillaume, P. Verboven, S. Vanlanduit, and E. Parloo. On the influence of the parameter constraint on the stability of the poles and the discrimination capabilities of the stabilisation diagrams. *Mechanical Systems and Signal Processing*, 19(5):989–1014, 2005.

[35] C.-M. Chang, T.-K. Lin, and C.-W. Chang. Applications of neural network models for structural health monitoring based on derived modal properties. *Measurement*, 129:457–470, 2018.

[36] S. Chauhan. Using the unified matrix polynomial approach (UMPA) for the development of the stochastic subspace identification (SSI) algorithm. *JVC/Journal of Vibration and Control*, 19(13):1950–1961, 2013.

[37] G. W. Chen, P. Omenzetter, and S. Beskhyroun. Operational modal analysis of an eleven-span concrete bridge subjected to weak ambient excitations. *Engineering Structures*, 151:839–860, 2017.

[38] L. Cheng and A. Cigada. An analytical perspective about structural damage identification based on transmissibility function. *Structural Health Monitoring*, 19(1):142–155, 2020.

[39] S. Chesné and A. Deraemaeker. Damage localization using transmissibility functions: A critical review. *Mechanical Systems and Signal Processing*, 38(2):569–584, 2013.

[40] Y.-F. Chou and L.-C. Wang. On the modal testing of microstructures: Its theoretical approach and experimental setup. *Journal of Vibration and Acoustics, Transactions of the ASME*, 123(1):104–109, 2001.

[41] H. Clarke, J. Stainsby, and E. Carden. Operational modal analysis of resiliently mounted marine diesel generator/alternator. In *Conference Proceedings of the Society for Experimental Mechanics Series*, volume 5, pages 237–244, 2011.

[42] S. Das, P. Saha, and S. Patro. Vibration-based damage detection techniques used for health monitoring of structures: a review. *Journal of Civil Structural Health Monitoring*, 6, 07 2016.

[43] S. De Carolis, G. De Filippis, D. Palmieri, and L. Soria. A generalized operational modal analysis framework for challenging no-NExT engineering applications. In *Proceedings of ISMA 2020 - International Conference on Noise and Vibration Engineering and USD 2020 - International Conference on Uncertainty in Structural Dynamics*, 2020.

[44] S. De Carolis, G. De Filippis, D. Palmieri, and L. Soria. Operational-modal-analysis-based processing of no-NExT engineering applications datasets: A generalized power spectral density modal model formulation. In *Advances in Acoustics, Noise and Vibration - 2021 Proceedings of the 27th International Congress on Sound and Vibration, ICSV 2021*, 2021.

[45] S. De Carolis, A. Messina, and L. Soria. On the estimation process of a particular class of global transmissibility functions: the R-FRFs. *Mechanics of Advanced Materials and Structures*, 2021.

[46] G. De Filippis, L. Mangialardi, D. Palmieri, and L. Soria. Method for determining the modal parameters of road or rail vehicles and for the indirect characterization of road or rail profiles, 2017.

[47] G. De Filippis, D. Palmieri, L. Soria, and L. Mangialardi. System and source identification from operational vehicle responses: A novel modal model accounting for the track-vehicle interaction. *arXiv e-prints*, page arXiv:1702.08325, 2017.

[48] G. De Filippis, D. Palmieri, L. Soria, L. Mangialardi, B. Peeters, and H. Van der Auweraer. Operational modal analysis of passenger cars: Effect of the correlation between front and rear inputs. In *Proceedings of the 11th International Conference on Recent Advances in Structural Dynamics (RASD), Pisa, Italy*, 1st–3rd July 2013.

[49] G. De Pasquale and A. Somà. Dynamic identification of electrostatically actuated mems

in the frequency domain. *Mechanical Systems and Signal Processing*, 24(6):1621–1633, 2010.

[50] C. Devriendt, G. De Sitter, and P. Guillaume. An operational modal analysis approach based on parametrically identified multivariable transmissibilities. *Mechanical Systems and Signal Processing*, 24(5):1250–1259, 2010.

[51] C. Devriendt, G. De Sitter, S. Vanlanduit, and P. Guillaume. Operational modal analysis in the presence of harmonic excitations by the use of transmissibility measurements. *Mechanical Systems and Signal Processing*, 23(3):621–635, 2009.

[52] C. Devriendt and P. Guillaume. The use of transmissibility measurements in output-only modal analysis. *Mechanical Systems and Signal Processing*, 21(7):2689–2696, 2007.

[53] C. Devriendt and P. Guillaume. Identification of modal parameters from transmissibility measurements. *Journal of Sound and Vibration*, 314(1):343–356, 2008.

[54] B. Dickinson, T. Kailath, and M. Morf. Canonical matrix fraction and state-space descriptions for deterministic and stochastic linear systems. *Automatic Control, IEEE Transactions on*, 19(6):656–667, Dec 1974.

[55] C. J. Dodds and J. D. Robson. The description of road surface roughness. *Journal of Sound and Vibration*, 31(2):175–183, 1973.

[56] C. J. Dodds and J. D. Robson. Partial coherence in multivariate random processes. *Journal of Sound and Vibration*, 42:243–249, 1975.

[57] X. Dong, J. Lian, M. Yang, and H. Wang. Operational modal identification of offshore wind turbine structure based on modified stochastic subspace identification method considering harmonic interference. *Journal of Renewable and Sustainable Energy*, 6(3), 2014.

[58] A. Edelman and H. Murakami. Polynomial roots from companion matrix eigenvalues. *Mathematics of Computation*, 64(210):763–776, 1995.

[59] M. El-Kafafy, P. Guillaume, and B. Peeters. Modal parameter estimation by combining stochastic and deterministic frequency-domain approaches. *Mechanical Systems and Signal Processing*, 35(1-2):52–68, 2013.

[60] M. El-Kafafy, B. Peeters, T. Geluk, and P. Guillaume. The MLMM modal parameter estimation method: A new feature to maximize modal model robustness. *Mechanical Systems and Signal Processing*, 120:465–485, 2019.

[61] D. Ewins. *Modal Testing: Theory, Practice and Application*. Engineering dynamics series. Wiley, 2000.

[62] W. Fan and P. Qiao. Vibration-based damage identification methods: A review and comparative study. *Structural Health Monitoring*, 10(1):83–111, 2011.

[63] C. Farrar, S. Doebling, and D. Nix. Vibration-based structural damage identification. *Philosophical Transactions of the Royal Society A: Mathematical, Physical and Engineering Sciences*, 359(1778):131–149, 2001.

[64] P. Fernández, P. Reynolds, and M. López-Aenlle. Scaling mode shapes in output-only systems by a consecutive mass change method. *Experimental Mechanics*, 51(6):995–1005, 2011.

[65] S. Filiz and O. Burak Ozdoganlar. Experimental modal analysis of micro-drills. In *Transactions of the North American Manufacturing Research Institution of SME*, volume 36, pages 185–192, 2008.

[66] B. Fladung. Windows used for impact testing. In *Proceedings of the International Modal Analysis Conference - IMAC*, volume 2, pages 1662–1666, 1997.

[67] S. Gade, N. B. Møller, H. Herlufsen, and H. Konstantin-Hansen. Frequency domain techniques for operational modal analysis. In *Proceedings of the 1st International Operational Modal Analysis Conference, IOMAC 2005*, 2005.

[68] M. Ghalishooyan and A. Shooshtari. Operational modal analysis techniques and their theoretical and practical aspects: A comprehensive review and introduction. In *6th International Operational Modal Analysis Conference, IOMAC 2015*, 2015.

[69] S. Gres, P. Andersen, C. Hoen, and L. Damkilde. Orthogonal projection-based harmonic signal removal for operational modal analysis. In *Conference Proceedings of the Society for Experimental Mechanics Series*, volume 6, pages 9–21, 2019.

[70] P. Guillaume. *Identification of Multi-Input Multi-Output Systems Using Frequency-Domain Models*. PhD thesis, Vrije Universiteit Brussel, 06 1992.

[71] P. Guillaume, T. De Troyer, C. Devriendt, and G. De Sitter. OMAX - A combined experimental-operational modal analysis approach. In *Proceedings of ISMA2006: International Conference on Noise and Vibration Engineering*, volume 5, pages 2985–2996, 2006.

[72] P. Guillaume, R. Pintelon, and J. Schoukens. Nonparametric frequency response function estimators based on nonlinear averaging techniques. *IEEE Transactions on Instrumentation and Measurement*, 41(6):739–746, 1992.

[73] P. Guillaume, P. Verboven, S. Vanlanduit, H. Van der Auweraer, and B. Peeters. A poly-reference implementation of the least-squares complex frequency-domain estimator. *Proceedings of IMAC*, 21, 01 2003.

[74] P. Göransson. Acoustic finite elements. *Advanced Techniques in Applied and Numerical Acoustics*, VI, 1993.

[75] M. Hart, R. Conant, K. Lau, and R. Muller. Stroboscopic interferometer system for dynamic mems characterization. *Journal of Microelectromechanical Systems*, 9(4):409–418, 2000.

[76] M. D. A. Hasan, Z. A. Ahmad, M. S. Leong, and L. M. Hee. Enhanced frequency domain decomposition algorithm: A review of a recent development for unbiased damping ratio estimates. *Journal of Vibroengineering*, 20(5):1919–1936, 2018.

[77] H. Herlufsen, P. Andersen, S. Gade, and N. Møller. Identıfıcatıon technıques for operatıonal modal analysıs – an overvıew and practıcal experıences. In *Proceedings of the 1st International Operational Modal Analysis Conference, IOMAC*, page 13, 2005.

[78] L. Hermans and H. Van Auweraer. Modal testing and analysis of structures under operational conditions: Industrial applications. *Mechanical Systems and Signal Processing*, 13(2):193–216, 1999.

[79] L. Hermans, H. Van Der Auweraer, and P. Guillaume. A frequency-domain maximum likelihood approach for the extraction of modal parameters from output-only data. In *Proceedings of the 23rd International Conference on Noise and Vibration Engineering, ISMA*, pages 963–972, 1998.

[80] W. Heylen, S. Lammens, and P. Sas. *Modal Analysis Theory and Testing*. Katholieke Universteit Leuven, Departement Werktuigkunde, Leuven, Belgium, 2007.

[81] S. A. Hosseini Kordkheili, S. H. Momeni Massouleh, S. Hajirezayi, and H. Bahai. Experimental identification of closely spaced modes using NExT-ERA. *Journal of Sound and Vibration*, 412:116–129, 2018.

[82] S. Ibrahim and E. Mikulcik. Method for the direct identification of vibration parameters from the free response. *Shock Vib Bull*, 1977.

[83] G. James, T. Carne, and J. Lauffer. The natural excitation technique (NExT) for modal parameter extraction from operating structures. *Modal Analysis-the International Journal of Analytical and Experimental Modal Analysis*, 10(4):260, 1995.

[84] K. Jamroziak and M. Kosobudzki. Determining the torsional natural frequency of underframe of off-road vehicle with use of the procedure of operational modal analysis. *Journal of Vibroengineering*, 14(2):472–476, 2012.

[85] J.-N. Juang and R. Pappa. An eigensystem realization algorithm for modal parameter identification and model reduction. *Journal of Guidance Control and Dynamics*, 8, 11 1985.

[86] S. Kalicinski, H. Tilmans, M. Wevers, and I. De Wolf. A new characterization method for electrostatically actuated resonant mems: Determination of the mechanical resonance frequency, quality factor and dielectric charging. *Sensors and Actuators, A: Physical*, 154(2):304–315, 2009.

[87] J. Kang, L. Liu, S. D. Zhou, and Y. P. Shao. A novel time-domain representation of transmissibility and its applications on operational modal analysis in the presence of non-white stochastic excitations. *Journal of Sound and Vibration*, 457:157–180, 2019.

[88] M. Khatibi, M. Ashory, A. Malekjafarian, and R. Brincker. Mass–stiffness change method for scaling of operational mode shapes. *Mechanical Systems and Signal Processing*, 26:34–59, 2012.

[89] H. Kim and M. Kaouk. Flight test, modal analysis, and model refinement of the mir space station. *AIAA Journal*, 40(8):1589–1595, 2002.

[90] A. A. Kosterev, Y. A. Bakhirkin, R. F. Curl, and F. K. Tittel. Quartz-enhanced photoacoustic spectroscopy. *Opt. Lett.*, 27(21):1902–1904, 2002.

[91] A. A. Kosterev, F. K. Tittel, D. V. Serebryakov, A. L. Malinovsky, and I. V. Morozov. Applications of quartz tuning forks in spectroscopic gas sensing. *Rev. Sci. Instrum.*, 76:1902–1904, 2005.

[92] E. Lawrence and C. Rembe. Mems characterization using new hybrid laser doppler vibrometer / strobe video system. In *Proceedings of SPIE - The International Society for Optical Engineering*, volume 5343, pages 45–54, 2004.

[93] Q. Leclère, N. Roozen, and C. Sandier. On the use of the Hs estimator for the experimental assessment of transmissibility matrices. *Mechanical Systems and Signal Processing*, 43(1-2):237–245, 2014.

[94] F. Liu, J. Wu, F. Gu, and A. Ball. An Introduction of a Robust OMA Method: CoS-SSI and Its Performance Evaluation through the Simulation and a Case Study. *Shock and Vibration*, 2019, 2019.

[95] X. Liu, H. Wang, Y. Shan, and T. He. Construction of road roughness in left and right wheel paths based on psd and coherence function. *Mechanical Systems and Signal Processing*, 60-61:668–677, 2015.

[96] L. Ljung. *System Identification: Theory for User*. Prentice Hall; 2 edition (January 8, 1999), 1999.

[97] X. Lu, X. He, H. Chen, and R. Zheng. Operational modal parameter identification with colored noise excitation. *Chinese Journal of Aeronautics*, 34(2):288–300, 2021.

[98] L. F. Lyu and W. D. Zhu. Operational modal analysis of a rotating structure under ambient excitation using a tracking continuously scanning laser Doppler vibrometer system. *Mechanical Systems and Signal Processing*, 152:107367, 2021.

[99] F. Magalhães, A. Cunha, and E. Caetano. Vibration based structural health monitoring of an arch bridge: From automated oma to damage detection. *Mechanical Systems*

and Signal Processing, 28:212–228, 2012. Interdisciplinary and Integration Aspects in Structural Health Monitoring.

[100] N. M. Maia, R. A. Almeida, A. P. Urgueira, and R. P. Sampaio. Damage detection and quantification using transmissibility. *Mechanical Systems and Signal Processing*, 25(7):2475–2483, 2011.

[101] N. M. M. Maia, A. P. V. Urgueira, and R. A. B. Almei. Whys and wherefores of transmissibility. In *Vibration Analysis and Control - New Trends and Developments*. InTech, 09 2011.

[102] A. Messina. Local diagnoses in modal analysis through additional poles. *Mechanics of Advanced Materials and Structures*, 28(9):928–937, 2021.

[103] A. Messina, L. Soria, and G. Mantriota. Experimental analyses on local diagnoses through additional poles extracted by R-FRFs. *Mechanics of Advanced Materials and Structures*, 28(17):1765–1774, 2021.

[104] N. Mohammadi and M. Nasirshoaibi. Modal parameter identification of a three-storey structure using frequency domain techniques FDD and EFDD and time domain technique SSI: Experimental studies and simulations. *Journal of Vibroengineering*, 19(4):2759–2776, 2017.

[105] P. Mohanty and D. Rixen. Operational modal analysis in the presence of harmonic excitation. *Journal of Sound and Vibration*, 270:93–109, 2004.

[106] P. Mohanty and D. J. Rixen. Modified ERA method for operational modal analysis in the presence of harmonic excitations. *Mechanical Systems and Signal Processing*, 20:114–130, 2006.

[107] D. Montalvão, N. M. M. Maia, and A. Ribeiro. A review of vibration-based structural

health monitoring with special emphasis on composite materials. *The Shock and Vibration Digest*, 38:295–324, 2006.

[108] S. M. Moore, J. C. Lai, and K. Shankar. ARMAX modal parameter identification in the presence of unmeasured excitation-I: Theoretical background. *Mechanical Systems and Signal Processing*, 21(4):1601–1615, 2007.

[109] S. M. Moore, J. C. Lai, and K. Shankar. ARMAX modal parameter identification in the presence of unmeasured excitation-II: Numerical and experimental verification. *Mechanical Systems and Signal Processing*, 21(4):1616–1641, 2007.

[110] D. Newland. *An introduction to random vibrations, spectral and wavelet analysis*. Longman Scientific & Technical (Harlow, Essex, England and New York), 1993.

[111] B. Ngoi, K. Venkatakrishnan, B. Tan, N. Noël, Z. Shen, and C. Chin. Two-axis-scanning laser doppler vibrometer for microstructure. *Optics Communications*, 182(1-3):175–185, 2000.

[112] O. Ozdoganlar, B. Hansche, and T. Carne. Experimental modal analysis for microelectromechanical systems. *Experimental Mechanics*, 45(6):498–506, 2005.

[113] B.-H. Park and K.-J. Kim. Vector armax modeling approach in multi-input modal analysis. *Mechanical Systems and Signal Processing*, 3(4):373–387, 1989.

[114] E. Parloo. *Application of Frequency-domain system identification techniques in the field of operational modal analysis*. PhD thesis, Dept. of Mechanical Engineering, Vrije Universiteit Brussel, Belgium, 2003.

[115] M. Pastor, M. Binda, and T. Harčarik. Modal assurance criterion. *Procedia Engineering*, 48:543–548, 2012.

[116] P. Patimisco, A. Sampaolo, M. Giglio, S. Dello Russo, V. Mackowiak, H. Rossmadl, A. Cable, F. K. Tittle, and V. Spagnolo. Tuning forks with optimized geometries for quartz-enhanced photoacoustic spectroscopy. *Opt. Express*, 27:1401–1415, 2019.

[117] P. Patimisco, A. Sampaolo, M. Giglio, S. Russo, V. Mackowiak, H. Rossmadl, A. Cable, F. Tittel, and V. Spagnolo. Tuning forks with optimized geometries for quartz-enhanced photoacoustic spectroscopy. *Optics Express*, 27(2):1401–1415, 2019.

[118] P. Patimisco, G. Scamarcio, and V. Spagnolo. Quartz-enhanced photoacoustic spectroscopy: a review. *Sensors*, 4:6165–6206, 2014.

[119] B. Peeters. *System Identification and Damage Detection in Civil Engineering*. PhD thesis, Katholieke Universiteit Leuven, Belgium, 2000.

[120] B. Peeters. Stochastic system identification for operational modal analysis: A review. *Journal of Dynamic Systems, Measurement, and Control*, 123(4):659–667, 2001.

[121] B. Peeters, M. El-Kafafy, and P. Guillaume. The new PolyMAX plus method: Confident modal parameter estimation even in very noisy cases. In *International Conference on Noise and Vibration Engineering 2012, ISMA 2012, including USD 2012: International Conference on Uncertainty in Structure Dynamics*, volume 4, pages 2801–2813, 2012.

[122] B. Peeters and H. Van der Auweraer. Polymax: A revolution in operational modal analysis. In *Proceedings of the 1st International Operational Modal Analysis Conference, IOMAC 2005*, 2005.

[123] B. Peeters, H. Van der Auweraer, F. Vanhollebeke, and P. Guillaume. Operational modal analysis for estimating the dynamic properties of a stadium structure during a football game. *Shock and Vibration*, 14(4):283–303, 2007.

[124] E. Pierro, E. Mucchi, L. Soria, and A. Vecchio. On the vibro-acoustical operational

modal analysis of a helicopter cabin. *Mechanical Systems and Signal Processing*, 23(4):1205–1217, 2009.

[125] F. Pioldi, R. Ferrari, and E. Rizzi. Output-only modal dynamic identification of frames by a refined FDD algorithm at seismic input and high damping. *Mechanical Systems and Signal Processing*, 68-69:265–291, 2016.

[126] C. Rainieri and G. Fabbrocino. *Operational Modal Analysis of Civil Engineering Structures, An introduction and a guide for applications*. Springer, 06 2014.

[127] R. B. Randall, J. Antoni, and W. A. Smith. A survey of the application of the cepstrum to structural modal analysis. *Mechanical Systems and Signal Processing*, 118:716–741, 2019.

[128] R. B. Randall and W. A. Smith. New cepstral techniques for operational modal analysis. In *WCCM 2017 - 1st World Congress on Condition Monitoring 2017*, 2017.

[129] C. Rembe, B. Tibken, and E. Hofer. Analysis of the dynamics in microactuators using high-speed cine photomicrography. *Journal of Microelectromechanical Systems*, 10(1):137–145, 2001.

[130] E. Reynders, D. Degrauwe, M. Schevenels, G. De Roeck, P. Van den Broeck, K. Deckers, and P. Guillaume. OMAX testing of a steel bowstring footbridge. In *Conference Proceedings of the Society for Experimental Mechanics Series 7*, volume 4, pages 357–364, 2011.

[131] E. Reynders, J. Houbrechts, and G. De Roeck. Fully automated (operational) modal analysis. *Mechanical Systems and Signal Processing*, 29:228–250, 2012.

[132] E. Reynders and G. D. Roeck. Reference-based combined deterministic-stochastic subspace identification for experimental and operational modal analysis. *Mechanical Systems and Signal Processing*, 22(3):617–637, 2008.

[133] M. Rezaee, V. Shaterian-Alghalandis, and A. Banan-Nojavani. Development of the smooth orthogonal decomposition method to derive the modal parameters of vehicle suspension system. *Journal of Sound and Vibration*, 332(7):1829–1842, 2013.

[134] A. Ribeiro. On the generalization of the transmissibility concept. In *Proceedings of NATO/ASI Conference on Modal Analysis and Testing*, pages 757–764, Sesimbra, Portugal, 05 1998.

[135] A. Ribeiro, J. Silva, and N. Maia. On the generalisation of the transmissibility concept. *Mechanical Systems and Signal Processing*, 14(1):29–35, 2000.

[136] A. Richard. Orthogonal polynomials and special functions. In *Regional Conference Series in Applied Mathematics 21*, 1975.

[137] O. Salawu. Detection of structural damage through changes in frequency: a review. *Engineering Structures*, 19(9):718–723, 1997.

[138] R. Sampaio, N. Maia, A. Ribeiro, and J. Silva. Damage detection using the transmissibility concept. In *Proceedings of Sixth International Congress on Sound and Vibration*, pages 2559–2568, Copenhagen, Denmark, 07 1999.

[139] J. Samuel, M. B. G. Jun, O. B. Ozdoganlar, A. Honegger, M. Vogler, and S. G. Kapoor. Micro/Meso-Scale Mechanical Machining 2020: A Two-Decade State-of-the-Field Review. *Journal of Manufacturing Science and Engineering*, 142(11), 09 2020.

[140] J. Schoukens and R. Pintelon. Measurement of Frequency Response Functions in Noisy Environments. *IEEE Transactions on Instrumentation and Measurement*, 39(6):905–909, 1990.

[141] M. Sheibani and A. K. Ghorbani-Tanha. Obtaining mass normalized mode shapes of

motorway bridges based on the effect of traffic movement. *Structures*, 33(June):2253–2263, 2021.

[142] F. Shen, M. Zheng, D. Feng Shi, and F. Xu. Using the cross-correlation technique to extract modal parameters on response-only data. *Journal of Sound and Vibration*, 259(5):1163–1179, 2003.

[143] M. Shinozuka and C.-M. Jan. Digital simulation of random processes and its applications. *Journal of Sound and Vibration*, 25(1):111–128, 1972.

[144] P. Skjoldan and M. Hansen. On the similarity of the coleman and lyapunov-floquet transformations for modal analysis of bladed rotor structures. *Journal of Sound and Vibration*, 327(3-5):424–439, 2009.

[145] K. Song, X. Chen, and Y. Lin. Wheelbase filtering effect on vehicle ride dynamics. In *Proceedings of the FISITA 2012 World Automotive Congress*, pages 1183–1195. Springer, 2013.

[146] L. Soria, B. Peeters, and J. Anthonis. Operational modal analysis and the performance assessment of vehicle suspension systems. *Shock and Vibration*, 19(5):1099–1113, 2012.

[147] G. Sternharz and T. Kalganova. Current methods for operational modal analysis of rotating machinery and prospects of machine learning. *Conference Proceedings of the Society for Experimental Mechanics Series*, 6:155–163, 2020.

[148] D. Styles and C. Dodds. Simulation of random environments for structural dynamics testing. *Experimental Mechanics*, 16(11):416–424, 1976.

[149] D. Tcherniak, S. Chauhan, and M. H. Hansen. Applicability limits of operational modal analysis to operational wind turbines. In *Conference Proceedings of the Society for Experimental Mechanics Series*, volume 1, pages 317–327, 2011.

[150] P. Vacher, B. Jacquier, and A. Bucharles. Extensions of the MAC criterion to complex modes. *Proceedings of ISMA 2010 - International Conference on Noise and Vibration Engineering, including USD 2010*, pages 2713–2725, 2010.

[151] P. Verboven, P. Guillaume, B. Cauberghe, E. Parloo, and S. Vanlanduit. Stabilization charts and uncertainty bounds for frequency-domain linear least squares estimators. In *IMAC XXI*, 2003.

[152] P. Verboven, P. Guillaume, B. Cauberghe, S. Vanlanduit, and E. Parloo. A comparison of frequency-domain transfer function model estimator formulations for structural dynamics modelling. *Journal of Sound and Vibration*, 279(3-5):775–798, 2005.

[153] X. Wang, G. Zhang, X. Wang, and P. Ni. Output-only structural parameter identification with evolutionary algorithms and correlation functions. *Smart Materials and Structures*, 29(3):035018, 2020.

[154] W. Weijtjens. *Advanced methods for estimating and monitoring the modal parameters of operational systems subjected to non-white excitation.* PhD thesis, Vrije Universiteit Brussel, 2014.

[155] W. Weijtjens, G. De Sitter, C. Devriendt, and P. Guillaume. Automated transmissibility based operational modal analysis for continuous monitoring in the presence of harmonics. *Proceedings of the International Conference on Structural Dynamic , EURODYN*, 2014-Janua(July):2231–2238, 2014.

[156] W. Weijtjens, G. De Sitter, C. Devriendt, and P. Guillaume. Operational modal parameter estimation of MIMO systems using transmissibility functions. *Automatica*, 50(2):559–564, 2014.

[157] P. Welch. The use of fast fourier transform for the estimation of power spectra: A

method based on time averaging over short, modified periodograms. *IEEE Transactions on Audio and Electroacoustics*, 15(2):70–73, 1967.

[158] P. White, M. Tan, and J. Hammond. Analysis of the maximum likelihood, total least squares and principal component approaches for frequency response function estimation. *Journal of Sound and Vibration*, 290(3-5):676–689, 2006.

[159] K. Wyckaert, F. Augusztinovicz, and P. Sas. Vibro-acoustical modal analysis: Reciprocity, model symmetry, and model validity. *Journal of the Acoustical Society of America*, 100(5):3172–3181, 1996.

[160] W.-J. Yan, M.-Y. Zhao, Q. Sun, and W.-X. Ren. Transmissibility-based system identification for Structural Health Monitoring: Fundamentals, approaches, and applications. *Mechanical Systems and Signal Processing*, 117:453–482, 2019.

[161] F. B. Zahid, Z. C. Ong, and S. Y. Khoo. A review of operational modal analysis techniques for in-service modal identification. *Journal of the Brazilian Society of Mechanical Sciences and Engineering*, 42(8):1–18, 2020.

[162] M. Zalalutdinov, A. Zehnder, A. Olkhovets, S. Turner, L. Sekaric, B. Ilic, D. Czaplewski, J. Parpia, and H. Craighead. Autoparametric optical drive for micromechanical oscillators. *Applied Physics Letters*, 79(5):695–697, 2001.

[163] L. Zhang, R. Brincker, and P. Andersen. An overview of operational modal analysis: Major development and issues. In *Proceedings of the 1st International Operational Modal Analysis Conference, IOMAC 2005*, 2005.

[164] P. Zhang, X. Tang, B. Shan, J. Brandon, and A. Kwan. Analytical and experimental modal analysis for operational validation and calibration of a miniature silicon sensor. *Journal of Sound and Vibration*, 214(5):903–913, 1998.

[165] P. Zhang, Q. Wang, X. Wu, and T. Huang. Experimental modal analysis of miniature objects by optical measurement technique. *The International journal of analytical and experimental modal analysis*, 7(4):243–253, 1992.

[166] Y. Zhang, D. Xie, J. Yu, and H. Chu. Analysis on the harmonics and inter-harmonics of a variable speed wind turbine. *Journal of Renewable and Sustainable Energy*, 7(4), 2015.